A Refined Method for Quantitation of Divalent Metal Ions in Metalloproteins and Local Stability and Conformational Heterogeneity of Amyotrophic Lateral Sclerosis-Associated Cu, Zn Superoxide Dismutase

by

Colleen Doyle

A thesis
presented to the University of Waterloo
in fulfillment of the
thesis requirement for the degree of
Master of Science
in
Chemistry

Waterloo, Ontario, Canada, 2014

AUTHOR'S DECLARATION

I hereby declare that I am the sole author of this thesis. This is a true copy of the thesis, including any required final revisions, as accepted by my examiners.

I understand that my thesis may be made electronically available to the public.

Abstract

Amyotrophic lateral sclerosis (ALS) is a devastating and progressive disease that results in selective death of motor neurons in the cortex, brain stem and spinal cord. ALS is the most common adult onset motor neuron disease resulting in paralysis and death, commonly within 2 – 5 years of symptom onset, yet there remains no effective treatment for the disease. The majority of ALS cases show no hereditary link (referred to as sporadic ALS or sALS); however, ~10% of cases show a dominant pattern of inheritance (referred to as familial ALS or fALS). Over 170 different mutations in human Cu, Zn superoxide dismutase (SOD1) have been identified to account for ~20% of fALS. SOD1 is a ubiquitously expressed homodimeric antioxidant enzyme. It is widely accepted that mutations in SOD1 result in a gain of toxic function, rather than a loss of native function. A prominent hypothesis for the gain of function is the formation of protein aggregates, which have been shown to be toxic to motor neurons. Protein aggregation is observed in a number of neurodegenerative disorders, including Alzheimer's, Huntington's and Parkinson's disease.

Each β-rich monomer of SOD1 binds one catalytic Cu ion and one structural Zn ion. The metallation state of SOD1 significantly influences the structure, dynamics, activity, stability, and aggregation propensity. A similar trend has been observed in a number of metalloenzymes and as such a method to rapidly and accurately quantitate metal ions in proteins is of great importance. Here a review of previous methods using the chromogenic chelator PAR to quantitate metal ions in proteins is presented. Three methods are assessed for their accuracy, precision and ease of use. The methods vary in accuracy, which is highest only under the specific conditions it was designed for. A robust new method is presented here that uses spectral decomposition software to accurately resolve the absorption bands of Cu and Zn with high precision. This method may be successful as a more general method for metal analysis of proteins allowing for the quantitation of additional metal combinations (e.g. Zn/Co, Ni/Cu, Ni/Co).

Thermodynamic stability has widely been implicated as playing a major role in the aggregation of globular proteins. Metal loss significantly decreases the global stability of SOD1 and as such metal-depleted (apo) forms of SOD1 have largely been the focus of SOD1 investigations. Recent studies, however, suggest that complete global unfolding is not required for protein aggregation. Local unfolding has been investigated and proposed to be sufficient to induce irreversible protein aggregation in the absence of global destabilization. Enhanced local unfolding has been observed in a number of disease-related proteins. Since SOD1 aggregation may occur from partially unfolded forms, NMR temperature dependence studies have been carried out on the most abundant form of SOD1 *in vivo*, the fully metallated (holo) dimer, to provide a residue specific picture of subglobal structural changes in SOD1 upon heating.

Amide proton (N^1H) temperature coefficients report on the hydrogen bonding status of a protein. A curved N^1H temperature dependence indicates that the proton populates an alternative conformation generally within 5 kcal/mol of the ground state. NMR temperature dependence studies of pseudoWT indicate that the thermal unfolding process of holo pWT begins with "fraying" of the structure at its periphery. In particular, increased disorder is observed in edge strands β5 and β6, as well as surrounding the zinc binding site. The local stability and conformational heterogeneity of ALS-associated mutants G93A, E100G and V148I was also assessed. All mutants display similar local unfolding patterns to pseudoWT, but also show distinct differences in the hydrogen bonding network surrounding the mutation site. Interestingly, each mutation regardless of its structural context results in altered dynamics at the β-barrel plug, a key stabilizing element in SOD1. A significant proportion of residues (~30%) access alternative states in both pseudoWT and mutants, however, overall mutants appear to be able to access higher free energy alternative states compared to pseudoWT. The implications of these results for the mechanism of protein aggregation and disease are discussed.

Acknowledgements

I would like to thank my supervisor, Dr. Elizabeth Meiering, for giving me the opportunity to truly realize my passion for science. I will forever be grateful for the guidance and inspiration.

I would like to thank the members of the Meiering lab for their unwavering help and support. It is truly a rare experience to meet such an amazing group of people. I would specifically like to thank Heather Primmer for being such an amazing teacher. I would also like to thank Helen Broom, Duncan MacKenzie and Jessica Rumfeldt for not only teaching me so much about science but even more about life.

Lastly, I would like to thank my family and friends for their positive and loving influence on my life. Your support and encouragement means everything.

Table of Contents

List of Figures

List of Tables

List of Abbreviations

1D..... one dimensional
2D..... two dimensional
3D..... three dimensional
A..... absorbance
a ..... quadratic coefficient
AAS ..... atomic absorption spectroscopy
ALS ..... amyotrophic lateral sclerosis
apo SOD1 ..... human superoxide dismutase free of copper and zinc
CCS ..... Cu chaperone for SOD1
CPMG ..... Carr-Purcell-Meiboom-Gill ^{15}N nuclear spin relaxation experiment
d ..... pathlength
DSC..... differential scanning calorimetry
DTPA ..... diethylenetriaminepentaacetic
EDTA ..... ethylenediaminetetraacetic acid
FAC..... familial amyloidotic cardiomyopathy
fALS..... familial amyotrophic lateral sclerosis
FAP ..... familial amyloidotic polyneuropathy
g_1 ..... temperature coefficient of ground state
g_2 ..... temperature coefficient of alternative state
GB3 ..... third IgG-binding domain of protein G
GdnHCl ..... guanidine hydrochloride
HEPES ..... 4-(2-hydroxyethyl)-1-piperazineethanesulfonic acid
holo SOD1 ..... human superoxide dismutase with full copper and zinc incorporation
HSCQ..... heteronuclear single quantum correlation
ICP-AES ..... inductively coupled plasma atomic emission spectroscopy
ICP-MS ..... inductively coupled plasma mass spectrometry
IPTG..... isopropyethiogalactoside
K_d..... dissociation constant
LB ..... Luria broth
$m_{Cu,490}$ ..... increase in absorbance upon the formation of 1 μM PAR:Cu at 490 nm
$m_{Cu,520}$ ..... increase in absorbance upon the formation of 1 μM PAR:Cu at 520 nm
MD ..... molecular dynamics

$m_{Zn,490}$ ..... increase in absorbance upon the formation of 1 μM PAR2:Zn at 490 nm

$m_{Zn,520}$ ..... increase in absorbance upon the formation of 1 μM PAR2:Zn at 520 nm

N^1H ..... amide proton

NCS-1 ..... neuronal calcium sensor-1

NMR ..... nuclear magnetic resonance

NOE ..... Nuclear Overhauser effect

NOESY ..... Nuclear Overhauser effect spectroscopy

NTA ..... nitrilotriacetic acid

p_1 ..... population of ground state

p_2 ..... population of alternative state

PAR ..... 4-(2-pyridylazo)resorcinol

PAR:Co ..... PAR and cobalt complex

PAR:Cu ..... PAR and copper complex

PAR_2:Zn ..... PAR and zinc complex

ppb ..... parts per billion

ppm ..... parts per million

pWT ..... SOD1 double mutant (C6S111) used as the control protein

R ..... gas constant

ROS ..... reactive oxygen species

S^2 ..... square of the generalized order parameter

sALS ..... sporadic amyotrophic lateral sclerosis

SDS-PAGE ..... sodium dodecyl sulfate polyacrylamide gel electrophoresis

SlyD ..... sensitive to lysis D

SOD1 ..... human superoxide dismutase

SpLab ..... SpectraLab spectral

T_m ..... temperature where the fraction of unfolded protein is one half

TS ..... transition state

TTR ..... transthyretin

WT ..... wild-type

δ ..... chemical shift

δ_1 (T) ..... chemical shift of ground state at T

δ_2 (T) ..... chemical shift of alternative state at T

δ_1° ..... initial chemical shift of ground state

δ_2° ..... initial chemical shift of alternative state

δ_{obs} ..... observed chemical shift

ΔAbs_{500} ..... change in absorbance at 500 nm

$\Delta_{avg}HN$ ..... weighted average difference in chemical shift

ΔG ..... difference in Gibb's free energy between two states

ΔH ..... change in enthalpy between two states

ΔS ..... change in entropy between two states

ε_i^{PAR} ..... molar extinction coefficients of free PAR

$\varepsilon_i^{PAR:Co}$ ..... molar extinction coefficients of PAR bound to cobalt

$\varepsilon_i^{PAR:Zn}$ ..... molar extinction coefficients of PAR bound to zinc

Chapter 1

General Introduction

1.1 Protein folding

The ability of a protein to serve its biological purpose is most often dependent upon its ability to form a stable, three-dimensional structure referred to as the native state (*1*). Protein folding is a complex process that can begin even before the newly synthesized polypeptide chain is released from the ribosome. As the polypeptide folds it forms an intricate network of weak noncovalent interactions that stabilize the native state. Solving the "folding problem" and identifying the pathways between the unstructured and native state are key to understanding and predicting sequence to structure relationships. The ability to predict structure would be instrumental also in the design of novel polypeptides able to serve a diverse range of functions from biomaterials to drug delivery systems, highlighting the importance of further investigations in this area.

Many years ago, Levinthal proposed that if a protein were to sample all of the states available to the unfolded polypeptide it would take longer than the age of the universe for a protein to reach the native state (*2*). Protein folding has since been proposed to occur through a number of defined pathways. The framework model suggests that a protein may fold through a sequential process, first by rapidly forming secondary structure that serves as a scaffold for the subsequent formation of tertiary structure (*3*). Two mechanisms proposed for this process include nucleation and diffusion-collision. In the nucleation mechanism, it is believed that folding initiates from a small number of key residues around which the remainder of the structure can then pack. In the diffusion-collision mechanism, secondary structures are formed and then through diffuse movement, collide and combine to form the tertiary structure. An alternative model is hydrophobic collapse, which involves the collapse of the protein due to hydrophobic interactions and within the confined volume formation of secondary and tertiary structure (*3*). Computer simulations using lattices models and *in vitro* folding studies have further developed the folding model

(*4*). This new view describes protein folding via numerous parallel pathways along an energy landscape, often depicted using a protein folding funnel (Figure 1.1). The top of the funnel is very broad, representing the vast number of conformations the unfolded polypeptide can adopt. As native interactions are formed through dynamic movements, the number of possible conformations is reduced as indicated by narrowing of the funnel. The local minima represent transient, partially folded intermediate states populated in the folding process. The bottom of the funnel represents the lowest energy, native state of the protein.

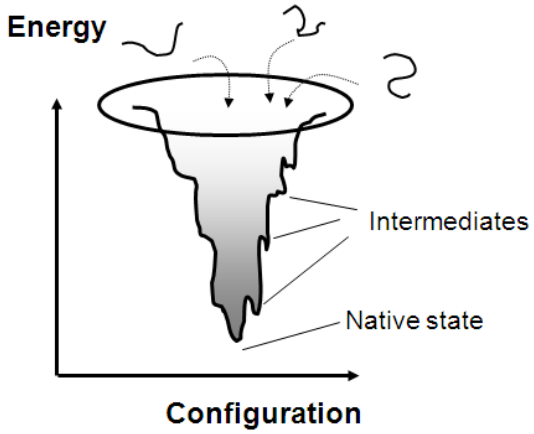

Figure 1.1 – Schematic depiction of the protein folding energy landscape adapted from Radford (2000)(*5*). An ensemble of different protein conformations all fold via multiple parallel pathways to reach the lowest energy native state. The jagged edges represent partially folded intermediates occupied along the folding pathway. Figure reproduced with permission from Rumfeldt, J., 2006 (*6*).

The Gibbs Helmholtz equation (Eq. 1.1) is often used to describe the thermodynamics of protein folding:

$$\Delta G = \Delta H - T\Delta S \qquad \text{Eq. 1.1}$$

where the differences in Gibbs free energy, enthalpy and entropy, of the folded state relative to the unfolded state, are given by ΔG, ΔH, and ΔS, respectively. The thermodynamics of solvent water also contribute to these terms. This is because as a protein unfolds many of the intramolecular hydrogen bonds and electrostatic interactions within the protein are replaced by intermolecular interactions with solvent water (*7*). Protein folding also involves overcoming at least one free energy barrier, with the highest point

of this barrier corresponding to the transition state (TS) and the rate determining step (Figure 1.2). Protein folding can and has been shown to exhibit both two-state and multi-state kinetics (*8*). Small monomeric proteins often fold via two-state kinetics, which involves the formation of the native protein from the unfolded peptide through one transition state (Figure 1.2) (*9*). Larger, more complex proteins tend to fold via multi-state kinetics with more elaborate mechanisms and parallel pathways (*10*). In multi-state kinetics there will be more than one of these barriers present and thus intermediates will be populated. The structure of the transition state cannot be observed directly, as it is formed transiently and does not build up to any significant concentration, however, it can be inferred through φ-value analysis, an experimental method that involves mutation of individual side chains to identify native-like interactions formed in the transition state (*11*).

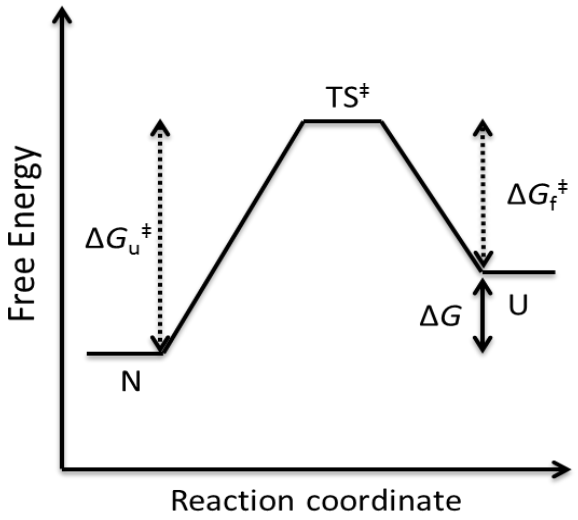

Figure 1.2 – Free energy diagram of two-state folding (N ↔ U). The highest energy point represents the transition state ($TS^{\ddagger}$). The difference in unfolded and folded free energy values is referred to as the free energy change of folding (ΔG). The kinetic folding and unfolded barriers are given by $\Delta G_f^{\ddagger}$ and $\Delta G_u^{\ddagger}$, respectively.

1.2 Protein misfolding and aggregation

Despite the vast number of conformations available to a polypeptide chain, remarkably, proteins are able to spontaneously fold into their native state. Anfinsen showed in 1961 that all of the information necessary for proper folding is contained in the amino acid sequence (*12*). The intracellular environment,

however, is a complex one that consists of a compartmentalized, inhomogeneous milieu of macromolecules (proteins, lipids, nucleic acids, etc.) at concentrations of 200-400 mg/mL (*13*). Macromolecular crowding can affect protein stability, the mechanisms of protein folding and kinetic rates associated with the process (*14*). In order to ensure proper folding *in vivo*, molecular chaperones often aid in the process (*15*). Some chaperones are involved early in the folding process to prevent protein aggregation, while others direct later stages of the process such as the binding of cofactors or the development of quaternary structure (*1*). In spite of this, and the fact that the native state of the protein is the most stable under physiological conditions, mistakes in protein folding occur.

Protein misfolding arises when a polypeptide acquires lasting non-native interactions that affect the overall structure and/or function of the protein (*1*). When misfolded or unfolded proteins cannot be prevented from forming or recovered they are often targeted for destruction through the ubiquitin-proteasome system (*16*). When all of these mechanisms to prevent the presence of misfolded or unfolded proteins in the cell fail, protein aggregation can occur. Aggregation involves the formation of non-native complexes of varied protein conformations containing many copies of the same protein. Aggregates are often formed through protein-protein interactions created by solvent exposed hydrophobic patches of misfolded or unfolded proteins (*1*). The type of aggregate structure formed depends on the specific protein as well as the environmental conditions; however, aggregates can range from small soluble oligomers to large, insoluble, well-ordered fibrils (*17*). The most well characterized type of aggregate is amyloid, a fibrillar aggregate with extensive beta-sheet structure suggested to be attainable by any protein under extreme conditions (*18, 19*). In some cases, protein aggregation may serve a physiological function, as in the case of F-actin filament formation in muscles; however, most often the result is toxic (*20*). Despite being the most fundamental process in molecular biology, there is still much to be learned about the mechanisms of protein folding, misfolding and aggregation.

1.3 Protein aggregation and disease

Protein aggregation has been linked to numerous peripheral diseases, such as renal amyloidosis, Type II diabetes and atherosclerosis, as well as many neurodegenerative diseases such as Alzheimer's disease, Parkinson's disease and amyotrophic lateral sclerosis (ALS) (*20*). Despite differing compositions of protein aggregates as well as varied disease symptoms, in general neurodegenerative diseases exhibit adult onset, extensive neuronal loss and the presence of cerebral protein aggregates suggesting a commonality in disease mechanisms (*21*). The exact mechanisms by which protein aggregates exert toxic effects on cells are not known. Various hypotheses have been proposed for the pathways by which intracellular aggregates lead to neuronal cell death, including decreased chaperone activity, sequestration of cellular components, enhanced oxidative stress, mitochondrial dysfunction, and impaired capabilities of the proteasome (*20, 22*). The involvement of aggregates in cell death is supported by studies that reveal the presence of abnormal protein aggregates in regions of the brain most damaged by disease, as well as *in vitro* studies showing that misfolded protein aggregates induce apoptosis in cells (*23, 24*). Recent studies however have shown that small, soluble oligomers are most toxic to cells (*25*). In some animal models, for example, disease symptoms appear well before insoluble aggregate formation(*21*). In addition, clinical studies have demonstrated that the presence of insoluble inclusions does not always correlated with disease symptoms (*21*). Rather, patient data for various neurodegenerative diseases show that neuronal cells containing large insoluble inclusion bodies are often healthier than surrounding cells lacking these structures(*21*). Taken together, these findings suggest that it is the earlier stages of aggregate formation are most toxic and likely the main causes of neurodegeneration.

1.4 Factors that affect protein aggregation

While not completely understood, there are a number of genetic and environmental factors that have been implicated in protein aggregation, such as point mutations, post-translational modifications and ionic strength (*17, 20*). The thermodynamic stability of proteins has widely been implicated as playing a

major role in the aggregation propensity of globular proteins (*26*). This theory has been supported by calorimetric analyses on a wide range of mutant proteins associated with protein misfolding diseases, which often show decreased conformational stability when compared to the wild-type (WT) protein and through *in vitro* studies revealing that aggregate formation generally requires at least mildly destabilizing conditions (*27-31*). An underlying assumption of the protein stability hypothesis is that the aggregation-prone state of a protein exists in the conformational ensemble in solution and is in equilibrium with the native state (*32*). With this model, destabilization of the native state will result in a higher population of the aggregation-prone species and thus an increase in observed aggregation (*32*). However, an increasing body of evidence shows that aggregation propensity cannot always be correlated well with protein global thermodynamic stability, challenging this theory.

It has been proposed that kinetic stability (*33*), as well as other factors, such as reduced global cooperativity (see below) (*34*), decreased net charge (*35*), and the pH-dependence of protein solubility (*36*), may also play vital roles in the misfolding and aggregation of proteins. The protein transthyretin (TTR) provides an example where the study of folding energetics has been instrumental in the understanding of protein aggregation. TTR is a homotetramer found in the cerebral spinal fluid and blood plasma. TTR has been implicated in 4 amyloid diseases: (1) familial amyloidotic polyneuropathy (FAP), (2) familial amyloidotic cardiomyopathy (FAC), (3) senile systemic amyloidosis and (4) the rare central-nervous-system-selective amyloidosis (*37*). Over 80 different point mutations have been identified to cause FAP and FAC (*38*). Different mutations have been associated with diversity in the age of onset, penetrance and tissues affected (*39*). Mutations destabilize the native state of TTR, however, decreases in thermodynamic stability alone (i.e. ΔG) do not correlate well with disease severity (*37*). For example, the most destabilized TTR mutants, D18G and A25T, are not the most pathogenic (*40, 41*). In contrast, when both kinetic and thermodynamic data are considered together, the effects of mutations can more reliably predict disease severity. TTR aggregation is believed to occur through a mechanism referred to as downhill polymerization (*42*). In this case, tetramer dissociation is the rate-limiting step and thus

mutations that decrease the kinetic barrier associated with dissociation may increase aggregation without destabilizing the native state. However, tetramer-monomer-unfolded monomer equilibria are strongly influenced by thermodynamic stability, as shown by urea denaturation studies (*43*), and thus destabilization of the tetramer or folded monomer can enhance aggregation propensity (*37*). The combined results of these studies indicate that there is a strong interplay between kinetic and thermodynamic stability in relation to aggregation and associated disease properties.

Recently, based on studies on dimeric T7 endonuclease I, the Eisenberg group proposed a different model for understanding the pathways of protein aggregation, called the prepared model (*32*). The new model suggests that the protein ensemble in solution is governed by both protein sequence and solution conditions and only under certain conditions, when the protein is said to be "prepared", does the protein ensemble in solution contain the aggregation-prone species. The authors propose that this model complements the protein stability hypothesis as it can account for cases where disease-causing mutations do not result in a decrease in protein stability. In this case the mutations prepare the protein by making the aggregation-prone state accessible without actually destabilizing the native state. This model also complements the conformational change hypothesis, suggesting that the preparation of a protein requires specific local conformational changes rather than complete unfolding (*32*).

1.4.1 The role of local unfolding in protein aggregation

Local unfolding, or localized increases in protein dynamics, have been investigated and proposed to be sufficient to induce irreversible protein aggregation in the absence of global destabilization (*34, 44*). In the native state, the globular fold of many proteins buries much of the main chain of the polypeptide within the structure preventing it from forming non-native interactions. Fluctuations, or breathing motions, of the protein can expose very local regions to solvent but such conformations are transient and unlikely to form strong intermolecular interactions (*45*). Rather, it may be more likely that conditions promoting the formation of a partially unfolded state exposing larger sections of the polypeptide

backbone to solvent induce aggregation (*46*). The generic building block model of protein aggregation postulates that the residual structured regions of a partially unfolded protein form non-native interactions, serving as building blocks for the formation of aggregates and as such these structured regions represent the core-forming segments (*47-49*). This theory suggests that variations in local unfolding patterns, due to genetic or environmental influences, can explain the different aggregate morphologies observed for proteins (*50*).

Enhanced local unfolding has been characterized in a number of disease-related proteins, such as human Cu,Zn superoxide dismutase (SOD1) (*47, 51, 52*), lysozyme (*45*), β_2-microglobulin (*30*), and γ-crystallin (*53*). Hydrogen-deuterium exchange studies on the WT and an amyloidogenic variant of human lysozyme (D67H) revealed that upon mutation two regions of the protein, the β-domain and the adjacent C-terminal region, showed marked decreases in stability (*45*). The transient unfolding of these two regions appeared to be cooperative, resulting in a partially structured intermediate with both of these regions simultaneously unfolded. When compared to WT, the population of this partially unfolded intermediate and the degree of cooperativity of partial unfolding were much greater for the mutant; both factors likely contribute to the increased aggregation propensity of D67H (*45*). Another study on β_2-microglobulin, the protein implicated in hemodialysis-related disorders, used nuclear magnetic resonance (NMR) spectroscopy to monitor that stability of the protein on an atomic level as a function of pH and urea (*30*). Again, the state proposed to be the amyloid precursor is a partially folded intermediate that has lost structure in 2 of the seven β-strands that make up the native fold (*30*). Molecular dynamics simulations also support the role of partially unfolded species in disease. Computational studies of γ-crystallin, linked to inherited cataract disease, suggest that a partially unfolded intermediate, with a structured C-terminus but a largely unstructured N-terminus, is the aggregation prone species (*53*). Together these studies demonstrate that complete unfolding of a protein is likely not necessary for pathogenesis and understanding of local unfolding patterns may be vital to elucidating protein aggregation mechanisms.

1.5 Amyotrophic lateral sclerosis

ALS is the most common adult onset motor neuron disease, with approximately 1 in 2000 people being affected. Patients with ALS exhibit selective death of motor neurons in the cortex, brain stem and spinal cord. This leads to total paralysis and death, often due to respiratory failure, usually within 2-5 years of disease onset (*54*). A universal characteristic of ALS is the appearance of protein deposits called inclusion bodies in degenerating neurons (*55*). Patients who have no genetic link are classified as having sporadic ALS (sALS), while those with family inheritance are classified as familial ALS (fALS). The majority of ALS cases show no hereditary link, however, ~10% show a dominant pattern of inheritance. In 1993, it was found that mutations in the gene SOD1 account for ~20% of the fALS (*56*). Knowledge of the mechanisms underlying SOD1 dysfunction is crucial to an understanding of the familial form of the disease, and since the phenotypes and molecular mechanisms of the sporadic and familial forms are similar, this suggests common therapies may be possible. Currently, there is no cure for ALS and very little available in terms of medical therapy, which is mainly limited to amelioration of disease symptoms (*57*).

1.6 Cu, Zn Superoxide dismutase

1.6.1 SOD1 structure

SOD1 is a 32 kDa homodimeric metalloenzyme with 153 amino acids per monomer. Each monomer consists of a Greek key beta barrel motif with eight antiparallel β-strands connected by a series of loops (Figure 3) (*54*). SOD1 undergoes a variety of post-translational modifications, including metal binding, the formation of a disulphide bond between Cys57 and Cys146 (Figure 3), and dimerization to form the mature protein (*58*). The dimer interface is formed by ~14 side chains from each subunit, with 8 of these being hydrophobic residues (*59*). Three residues, Gly51, Gly114 and Ile151, form the four hydrogen bonds that span the dimer interface (*58*). Dimerization buries approximately 8% of the total monomer surface area which is relatively small compared to other homodimeric proteins (*58, 60*).

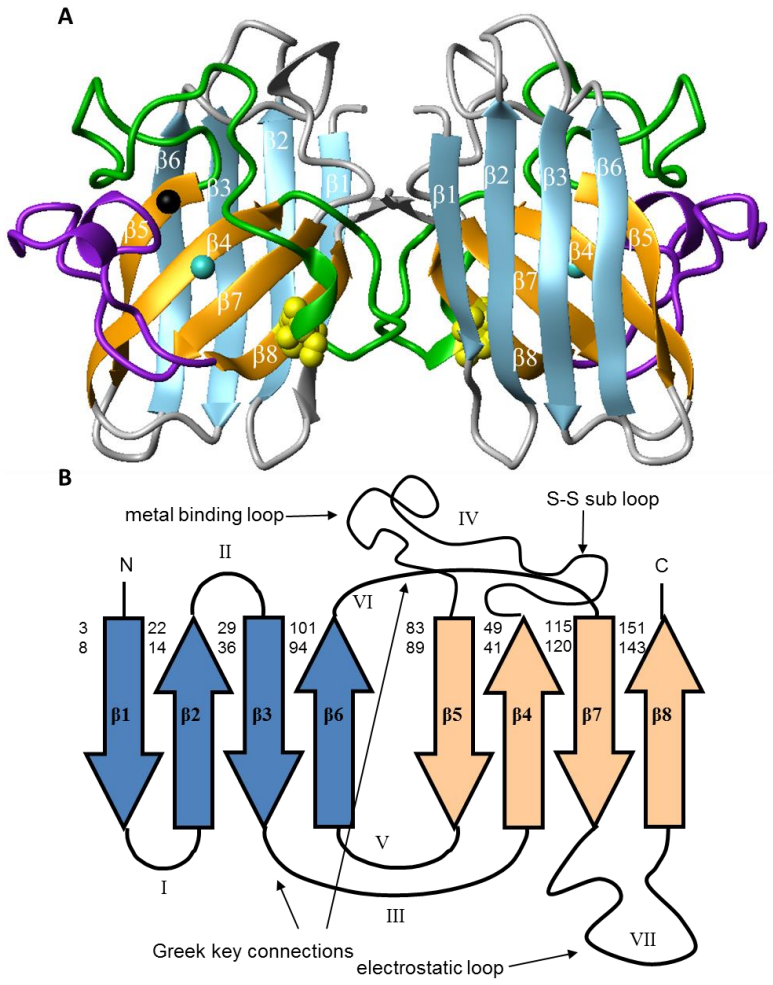

Figure 1.3 – Structure and topology of human SOD1. (A) Ribbon diagram of pWT SOD1. Copper and zinc atoms are shown by turquoise and black spheres, respectively. Cys57 and Cys 146 are shown in yellow space-filling representation. β-sheet 1 (strands β1, β2, β3 and β6) is coloured blue. β-sheet 2 (strands β4, β5, β7 and β8) is coloured orange. Loops IV and VII are coloured green and purple, respectively. Prepared using MOLMOL (*61*) and PDB coordinates 1SOS (*62*) (B) Topology diagram of SOD1 monomer illustrating the Greek-key barrel. β-strands are numbered and loops are labelled in roman numerals. The amino acid sequence is labelled numerically at the end of each β-strand. Figure adapted from Rumfeldt, J., 2006 (*6*).

Each monomer binds one copper and one zinc ion (Figure 1.4). The copper ion is coordinated by four histidine residues (His46, His48, His63, and His120) and one water molecule. The imidazole group of His63 bridges the copper and zinc ions. The zinc ion is coordinated by two other histidine residues (His71 and His80) and the aspartyl group of Asp83 forming a tetrahedral geometry (*62, 63*). The copper ion is essential for the enzyme's catalytic activity while the both copper and zinc contribute to the

stability of the enzyme (*54*). Excess free copper within cells can be damaging and thus the concentration within the cytoplasm is highly regulated. Transfer into the cell and between compartments often involves metallochaperones, which bind to the ion to reduce its toxic effects (*31*). *In vivo*, SOD1 has been shown to obtain copper through an interaction with the metallochaperone, Cu chaperone for SOD1 (CCS), which catalyzes both copper insertion and disulphide formation. In yeast, it has been shown that zinc must be bound to SOD1 in order for it to interact with CCS (*64*). SOD1 has been shown to obtain copper through alternative mechanisms in the absence of CCS, such as through a glutathione dependent pathway (see section 2.1.2) (*65*). The mechanisms through which SOD1 acquires zinc remain unknown.

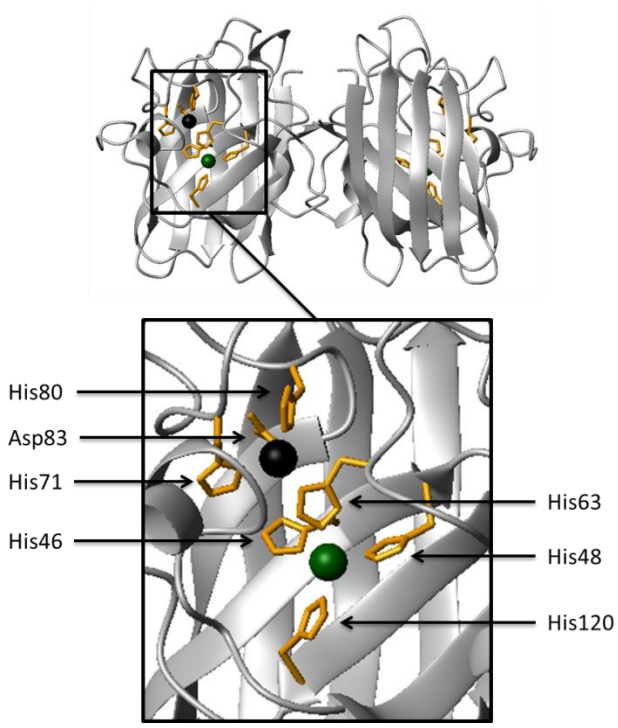

Figure 1.4 – Structure of human SOD1 metal binding site. Copper and zinc atoms are shown by green and black spheres, respectively. Side chains of meal binding ligands are shown in stick representation, coloured orange.

1.6.2 SOD1 activity

SOD1 is expressed in all tissue types but is found in higher concentrations within the central nervous system (*66*). The physiological concentration of SOD1 is approximately 40 μM in motor neurons

(*67*). Within the cell, SOD1 is found in the nucleus, peroxisomes, mitochondrial intermembrane space and most abundantly in the cytosol (*54*). SOD1 serves to reduce oxidative damage from reactive oxygen species (ROS) through the conversion of superoxide to hydrogen peroxide and oxygen:

$$2O_2^- + 2H^+ \rightarrow O_2 + H_2O_2 \qquad \text{Eq. 1.2}$$

The active site of SOD1 is located at the bottom of a long channel formed by the metal binding loop (loop electrostatic field that guides the negatively charged superoxide radical into the active site (*58*). The mechanism of SOD1 activity involves the successive oxidation and reduction of Cu^{2+} (*68*). In the first step copper is reduced converting the superoxide radical to molecular oxygen. In the second step the copper is reoxidized and a second superoxide radical is reduced and protonated to form hydrogen peroxide (*69*).

1.6.3 SOD1 stability

The fully metallated (holo) form of SOD1 is extremely stable with a melting temperature (T_m) of approximately 90°C (*70, 71*). This fully mature form of the protein is also highly resistant to chemical denaturation and proteolytic degradation (*70*). Partially and unmetallated (apo) SOD1 are considerably less stable (*72*) and have been reported to have an increased aggregation propensity (*72-74*). In the apo form of SOD1, reduction of the disulfide bond, which connects a portion of loop IV to the β-barrel (Figure 1.3 A), increases the rate of dimer dissociation, increasing the population of the apo monomer, a species that has been implicated in disease (*75*). Interestingly, reduction of the disulfide bond in the holo form has been reported to have no measurable effect on the monomer-dimer equilibrium (*76*). It has been proposed that in addition to the stability conferred by metal binding, the tight packing of the two halves of the β-barrel core and of the hydrophobic dimer interface in the holo state also confer greater stability (*77*).

1.6.4 SOD1 mutations

To date, 177 different mutations in SOD1 have been linked to ALS (http://alsod.iop.kcl.ac.uk/). Initially, it was proposed that mutations promote disease through a loss of protective function leading to

increased oxidative damage within the cell (*78*). This theory was later disproved using mice models. Mice lacking the SOD1 gene did not develop the disease but mice expressing both their endogenous SOD1 gene and a mutant form of the human SOD1 gene did develop disease symptoms (*66*). This finding and the autosomal dominant pattern of inheritance in patients indicate that mutant SOD1 promote disease through a toxic gain of function, which has yet to be elucidated. Current hypotheses for the mechanisms by which mutant SOD1 may cause disease include endoplasmic reticulum stress, excitotoxicity from failure to remove synaptic glutamate, mitochondrial damage and aberrant enzymatic activity (*22*). The most widely supported hypothesis for the gain of function is the formation of toxic intracellular protein aggregates (*21*). Patient data for both the sporadic and familial forms of ALS, as well as mice models, show that inclusions found in neuronal cells contain SOD1, as well as ubiquitin and neurofilament proteins (*79*). The non-native protein aggregates may form unfavourable interactions interfering with various cellular components, such as chaperones, protein trafficking and degradation machinery, and membranes (*22*).

The fALS SOD1 mutation sites span the entire polypeptide chain. It is noteworthy that despite the varying sites of mutation and differences in stability, hydrophobicity, metal binding status and susceptibility to post-translational modifications caused by mutation, each leads to the same fatal outcome (*80*). Most mutations do result in a decrease in conformation stability in both the holo and apo state; however this is not always true (*81*). The disease-associated mutant V148I has increased stability compared to WT, a low aggregation propensity compared to other mutants, and yet, surprisingly, a short average disease duration of ~1.7 years (Figure 1.5) (*80*). There does not appear to be a correlation between mutant destabilization and disease duration. DSC studies reveal that mutations can have differential effects on the stability of the holo and apo states while ITC studies show the same is true for the extent to which the dimer interface is destabilized (*81*). Thus, different mutations can increase the population of folded and/or unfolded monomers to varying extents depending on the combination of the varying effects on folding energetics. SOD1 aggregation is likely a multifactorial process that is

dependent on the concomitant alteration of a number of different factors in addition to mutation (*20*). Elucidation of these factors may help to understand the role, if any, of WT SOD1 in sALS.

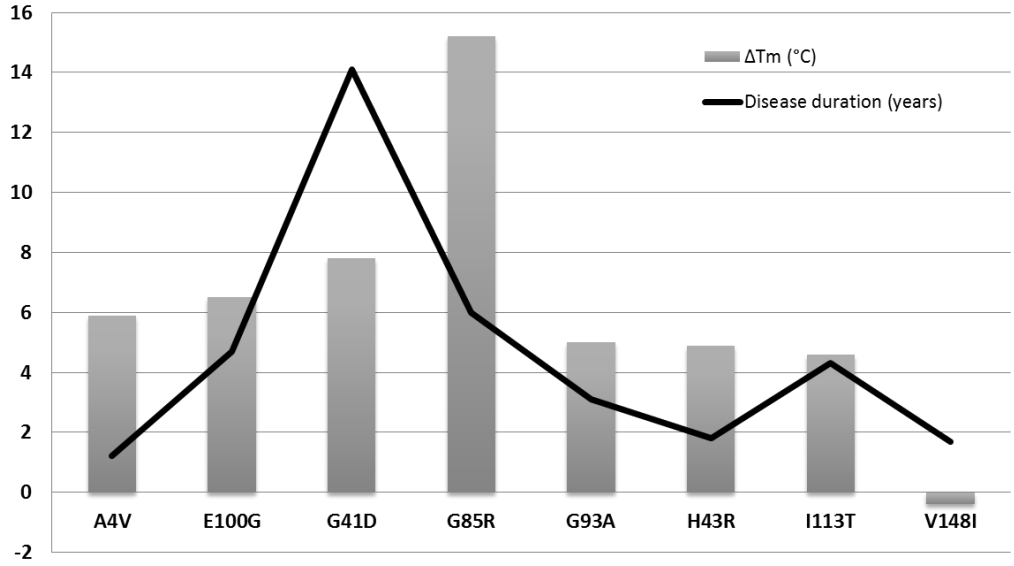

Figure 1.5 – Disease duration and global stability of mutant SOD1s. The global stability is given as a grey bar and is the difference in the temperature where half of the protein is unfolded (T_m; measured by DSC) from that for pWT ($\Delta T_m = T_{m(pwT)} - T_{m(mutant)}$). Disease durations are given as a black line and were obtained from Wang et al., 2008 (*80*).

1.6.5 SOD1 folding energetics

The observed folding mechanism of SOD1 depends on the conditions for denaturation. Thermal denaturation of holo SOD1 at relatively high protein concentration fits as a 2-state transition between folded dimers and unfolded monomers (*81, 82*). On the other hand, in chemical denaturation experiments at lower protein concentrations the observed transition is 3-state, as a monomeric intermediate also becomes populated (*70*). Similar behaviour is observed for apo SOD1 which again is well fit as a 2-state and 3-transition for thermal and chemical denaturation, respectively. However, at decreased concentrations it appears that the thermal denaturation of apo SOD1 becomes less cooperative as a monomeric intermediate is populated. Mutations also influence the observed unfolding of SOD1 as it has been shown that some mutants exhibit more 3-state behaviour (*81, 82*) (and unpublished). In the most

immature form (apo, disulfide reduced), SOD1 is monomeric and shows a 2-state transition between folded and unfolded monomers (*83*). The low heat capacity (ΔC_p) for unfolding suggests that the apo, disulfide reduced monomer is expanded compared to that in the holo, oxidized dimeric state (*81, 83*).

1.6.6 SOD1 gain of toxic function

It has been proposed that dimer dissociation and metal loss are required for SOD1 aggregation (*84-86*). However, the role of metal and/or disulfide deficient or misfolded forms of SOD1 in disease still remain unclear (*81, 87, 88*). Various factors have been suggested to promote SOD1 aggregation, including increased flexibility of loops IV and VII upon metal loss (*89*), the formation of intermolecular disulfide bonds between cysteine residues of SOD1 (*90*), a reduction in net charge upon mutation (*35*), and oxidation induced misfolding (*91*). There is evidence that some mutations weaken metal binding affinity resulting in an increased propensity to loose metals (*92*). Loss of metals will not only result in increased dynamics in the metal binding loop (loop IV) but can favour monomerization as the metal binding loop also forms a portion of the dimer interface, which is weakened in apo SOD1 compared to holo SOD1 (*92, 93*). Further, even in the holo state mutations have been shown to increase the global dynamics of SOD1 (*75, 94, 95*). Increased dynamics could provide non-native substrates access to the active site allowing for aberrant chemistry and oxidative damage to the protein (*95*) or increase the population of locally unfolded states.

Recent work on holo SOD1 shows that even from this most mature state aggregation can and does occur. Under physiologically relevant conditions, over time holo SOD1 can undergo changes in metallation and/or dimerization resulting in the formation of aggregates (*92*). This process is increased by but does not require mutation. Holo SOD1 is a remarkably stable protein and while mutations are destabilizing, in this form the extent to which mutations increase the population of unfolded protein under physiologically relevant conditions is very small (*81*). It is for this reason that the role of holo SOD1 in disease is often overlooked, with the focus often instead on the most immature, monomeric form of the

protein (*75, 84, 96-100*). However, even in the most immature reduced apo monomeric form, some disease associated variants, such as H48Q, H46R, D101N, and V148I, do not enhance global unfolding at physiological temperature (*83, 101*). This suggests that local unfolding, in both the holo and apo state, may play important roles in SOD1 aggregation.

Computational analyses on the conformational dynamics and aggregation propensity of WT and two fALS mutants (G37R and I149T) suggest that the apo monomer undergoes common modes of local unfolding (*49*). It was found that the two long loops (loop IV and VII), as well as strands 4, 5 and 7, which make up most of the C-terminal β-sheet 2, show a high degree of unfolding. Furthermore, mutations were shown to alter the local unfolding dynamics of SOD1 resulting in aggregates with different core-forming segments and structural polymorphism (*49*). Interestingly, recent experimental and computational studies have shown that the morphologies of protein aggregates affect the resulting disease phenotype which may help to explain the diversity in the age of onset and disease duration seen in ALS patients, for example (*49, 102, 103*). The β-barrel was identified early on as a key stabilizing element is SOD1 (*58, 78*). Leu38 is often referred to as the "plug" as it fills a cavity created by a number of residues (Val14, Ile35, Leu144 and His43) in the structure. With the exception of Ile35, all of these residues have been reported as disease-causing mutations (http://alsod.iop.kcl.ac.uk/). Molecular dynamics (MD) simulations on the apo dimer of WT and fALS mutants A4V, H46R and G37R, show that regardless of the mutation site and effect on stability, mutations commonly alter the dynamics in the β-barrel plug, suggesting that local destabilization may be sufficient to induce aggregation and could provide a general mechanism for SOD1 aggregation (*104*).

Experimental work further supports the presence of local unfolding in the apo monomer of SOD1. Edge-to-edge aggregation is commonly seen in *de novo* designed β-sheet proteins since edge strands are aligned perfectly to interact with any other β-strand they encounter (*105*). In nature, it appears proteins have evolved a number of ways to protect against this phenomenon, such as the β-barrel structure which has continuous H-bonding around the barrel cylinder or the placement of charged residues in edge

strands to avoid association (*105*). SOD1 employs both a β-barrel structure and as well as charged edge strands to avoid edge-to-edge aggregation (*52*). Charged strands β6 and β8 serve to protect the hydrophobic strands β1-3 from solvent exposure in the apo monomer. However, φ-value analysis reveals that these strands are largely unfolded in the transitions state, suggesting that these edge strands are more likely to unfold locally upon environmental perturbations (*52*).

Taken together, the data show that aggregation can occur from every form of SOD1 and the extent of unfolding required for aggregation in disease remains unknown. Mutations likely affect a number of factors that influence aggregation (i.e. stability, metal loss, monomerization, dynamics, etc.), which when combined may help explain the role of SOD1 in disease. Understanding of the early stages by which holo SOD1 may give rise to aggregation is of particular interest as holo SOD1 is the major form of SOD1 in cells (*54*).

1.6.7 Pseudo wild-type SOD1

There are 4 cysteine residues in the human SOD1 polypeptide. Two of these cysteines participate in the intramolecular disulphide bond (Cys57 and Cys146) (Figure 1.3 A); the remaining two free cysteine residues (Cys6 and Cys111) have the ability to form aberrant intermolecular disulphide bonds. For the purposes of thermodynamic analysis, protein denaturation must be reversible. It is for that reason that all experiments in this thesis have been carried out on pseudo wild-type SOD1 (pWT). In pWT, Cys6 is mutated to alanine and Cys111 to serine. Use of this variant also allows for comparison with DSC and ITC data previously obtained on pWT SOD1 in the Meiering lab. This construct has been characterized extensively, including in studies of SOD1 folding and is suitable for these experiments as it exhibits a much higher degree of reversibility of unfolding as well as essentially the same stability, enzymatic activity and structure as WT SOD1 (*6, 81, 88, 106*). Further, while it has been proposed that aberrant intermolecular reactions between Cys6 and Cys111 may play a role in protein aggregation and disease,

studies show that intermolecular bond formation is found only in later stages of disease in mice models and thus is likely a secondary effect (*107*).

1.7 Research objectives and outline

The main hypothesis for the toxic gain of function associated with SOD1 in ALS is protein aggregation (*54*). The Meiering lab focuses on gaining a deeper understanding of the physical and chemical properties of SOD1, of how mutations alter these properties, and how these alterations affect protein aggregation. Metal binding, for example, has a substantial influence on a number of physical and chemical properties (e.g. structure, activity, stability, aggregation propensity) (*54, 81, 88*), yet much remains to be learned about the effects of mutations on metal binding affinity and selectivity, and how these changes affect both local and global stability. It has been shown that changes in global stability do not always provide an accurate description of the local changes occurring within a protein (*108*), which may be important in understanding aggregation pathways. Recent studies on a number of disease related proteins suggest that the aggregation precursor is a partially folded form of the protein (*30, 45, 53*).

In Chapter 2, a review of previous methods using the chromogenic chelator PAR for quantitation of metal ions in proteins is presented. Three methods are assessed for their accuracy, precision and ease of use. A new, more general method using PAR is presented that uses spectral decomposition software to separate the absorption bands of Cu and Zn. Insights into the metallation state of pWT and mutant SOD1, as well as the successes and failures associated with the use of a chromogenic chelator for metal analysis are discussed. NMR temperature dependence experiments of pWT and three fALS mutants (G93A, E100G and V148I) are described in Chapter 3. The local stability and conformational heterogeneity of each variant is investigated, with each mutant showing both common and distinct changes relative to pWT. Implications for the role of observed local unfolding patterns in protein aggregation are discussed. Residues accessing alternative states close in free energy to the native state of SOD1 are identified and provide insight into the thermal unfolding pathway of SOD1.

Chapter 2

Spectrophotometric Metal Determination Assay

2.1 Introduction

2.1.1 Metalloproteins

Metal cofactors are naturally found in many proteins. In fact, approximately one third of all proteins are metalloproteins and ~40% of enzymes require metals for catalytic function (*109*). The incorporation of metals in proteins takes advantage of metals' small size, simple structure and positive charge, serving to create or enhance functionality as well as diversify proteins (*110*). The importance of metals is supported by their requirement for life. Bulk metals form 1-2% of the human body weight and include sodium, potassium, magnesium and calcium (*111*). Trace metals represent less that 0.01% of the human body weight and include vanadium, chromium, molybdenum, manganese, iron, cobalt, nickel, copper and zinc (*111*). Zn is the second most abundant trace metal, following iron, and is found in more than 300 enzymes (*112*). Zn is an interesting cofactor since it has a filled d orbital shell and thus only has a single redox state making it a stable ion (*112, 113*).

The concentration of metals in cells is strictly limited as excess free metals can be damaging (*109*). For example, free Cu is almost non-existent in the cytoplasm due to its redox potential as it can participate in or catalyze aberrant redox reactions which can result in oxidative damage of proteins, lipids and nucleic acids (*109*). Since the concentration of many metals is restricted in cells, chaperone proteins often aid in protein metallation. Some metals bind to the unfolded polypeptide providing local structure that aids in protein folding. Other metals do not bind until the structured active site is formed (*109*). Commonly metals stabilize the native state of the protein. Metals with only one redox state (e.g. Zn) are often used to counteract negative charges in protein. Metals with multiple redox states are often involved in enzymatic activity (*114*). A metal can participate in reactions in different ways depending on the local

environment. The iron in heme, for example, can act as a reversible electron carrier (cytochrome), a dioxygen carrier (hemoglobin) or an activator (cytochrome P450) (*115*). Further, it has been shown that undermetallation or the binding of non-native metals can promote protein aggregation (*110*).

The vast number of metalloproteins and the requirement of metals for native structure and function highlight the importance of knowledge of metal binding affinity and selectivity in proteins. This knowledge would be useful for investigating catalytic reactions, protein folding and aggregation, and signal transduction (*110*). Further, it is important to understand how flexibility in the metal-binding site may affect metal affinity and in contrast how metal binding affects protein flexibility, for example in Cu, Zn SOD1 (see also Chapter 3).

2.1.2 Metals and SOD1

The most immature form of SOD1 observed in cells is the reduced apo form. As described in Chapter 1 (section 1.6.1), SOD1 undergoes a number of post-translational modifications to reach the mature, fully active state (*58*). These maturation steps include the binding of one Cu and one Zn ion per monomer. Cu is believed to be transported into cells by the Ctr1 transmembrane protein through a Cu specific pore. Once inside the cell, Cu chaperones mediate transfer of the metal to its various targets, aiding in the efficiency of Cu metallation *in vivo* (*31*). SOD1 is understood to bind Cu through an interaction with the Cu chaperone, CCS. This metallochaperone consists of 3 domains: (1) a highly conserved N-terminal Cu binding domain located in a surface exposed loop, (2) a β-barrel domain that structurally resembles monomeric SOD1 and (3) a second highly conserved C-terminal Cu binding domain (*31, 116*). The second domain cannot bind Cu and thus it has been proposed that the main function of this domain is target recognition (*117*) (*118*).

One model for CCS activity proposes that Cu binding in domain 1 results in a conformational change within the protein that causes domain 3 to rotate and form a Cu binding complex with domain 1 (*118*). This reorientation allows domains 1 and 3 to interact with the active site residues of SOD1 and

facilitates Cu release. CCS has also been implicated in disulfide bond formation between Cys57 and Cys146. The interaction between CCS and SOD1 results in a disulfide bond between Cys57 and a cysteine residue in the third domain of CCS (*118*). Once Cu is transferred to SOD1, the intermolecular disulfide bond is replaced by an intramolecular bond with Cys146. This transfer is expected to help facilitate dissociation of the heterodimer. *In vitro* studies reveal that in both mammalian and yeast cells null of CCS, a glutathione-dependent pathway exists for copper insertion into SOD1. The role of this pathway in cells with CCS present remains unclear however it has been proposed that interaction with glutathione may damage or alter SOD1 and thus this pathway may play some role in toxicity of SOD1 (*65*). The mechanisms by which SOD1 obtains Zn remain unknown however it should be noted that the natural concentration of SOD1 in cells is on the order of 10-100 μM, which is much greater than the amount of free Zn present in the cytosol (*119*).

MD simulations reveal that metal binding has a greater influence on the thermostability of SOD1 than formation of the disulfide bond (*47*). The metal ions have been proposed to stabilize SOD1 monomers by holding together strands 4 and 7, which are disordered in apo SOD1 (*47*). Zn ions have been proposed to confer stability to proteins by counteracting negative charges within proteins (*114*). This occurs in SOD1 as the Zn ion binds at the C-terminal end of a helix located in loop VII with a negative dipole (*120*). Further, the conformation of loop VII has been shown to be strictly dependent upon the conformation of loop IV; the conformation of the latter is dependent upon Zn binding as loop IV contains key residues that coordinate the bound zinc (*120*). Interestingly, the binding of a Zn ion to one subunit of SOD1 will stabilize the second subunit in the dimer highlighting a propagating network of interactions between monomers (*121*).

The dissociation constants (K_d) for Cu and Zn binding to wild-type SOD1 have previously been measured using a competition assay (*122*). The results show that Cu binds more strongly to SOD1 than Zn with K_d values of 6.0×10^{-18} M^{-1} and 4.2×10^{-14} M^{-1}, respectively. The K_d values were also determined for 4 mutants (A4TV, A4T, I113T and L38V) and reveal that the affinity for Zn is reduced up to 30-fold

in mutants (*122*). In addition to the decreased affinity, *in vitro* studies show that mutants also have reduced metal binding selectivity and are more likely to be mismetallated (*123*). This lack of specificity has been attributed to irregularities in the Zn binding site (*123, 124*). Denaturation studies monitoring the metal status of SOD1 reveal that the major unfolding pathway involves rapid dimer dissociation and Zn loss, followed by a slow conformational rearrangement that results in Cu release before global unfolding (*125*). Unfolding kinetic experiments reveal that mutants favour increased formation of a Zn-free monomer intermediate; a state implicated in non-native protein association (*126*).

Zn deficiency has been proposed to play a role in disease for both WT and mutant SOD1 (*127*). Zn-deficient SOD1 has been shown to initiate apoptosis in motor neurons (*128, 129*). Loss of Zn alters the structure of SOD1 more than fALS mutations and results in the formation of a 4Å wide channel allowing non-native small molecules to the active site (*127*). Further, loss of Zn alters the coordination of Cu as they share a bridging histidine ligand (His63) decreasing Cu binding affinity (*130*). This connection between the metal binding affinities has also been observed in computational studies (*131, 132*). Previous studies reveal that in the absence of Zn, the catalytic activity of SOD1 can actually be reversed producing ROS which can damage the protein (*130*). It is clear that Zn binding significantly modulates the structure and activity of SOD1.

A study analyzing the metal content of WT and 14 different fALS mutants as-isolated from Sf21 insect cells revealed that Cu deficiency was much more common than Zn deficiency (*133*). Previous studies monitoring Cu and Zn release from SOD1 during unfolding found that while the major unfolding pathway involves Zn loss prior to Cu, mutant SOD1s showed a greater propensity to unfold using the minor pathway that involves Cu loss first (*134*). The role of Cu deficiency in disease is supported by the finding that Cu levels in the spinal cords of rats are increased which was proposed to likely be a consequence of reduced incorporation of Cu into SOD1 (*135*). On the other hand, studies of ALS-transgenic mice reveal that aggregated SOD1 found in spinal cords is not enriched in Cu or Zn (*136*). A few investigations have reported how the presence of bound metal affects aggregation. One study showed

that reduced apo SOD1 could recruit Zn-bound but not Cu-bond protein into aggregates (*121*). A contradicting study revealed that the presence of one equivalent of Zn per dimer was sufficient to eliminate the oligomerization of reduced and oxidized apo SOD mutants (*98*). The exact role of metal ions in disease still remains unclear.

The above-mentioned studies and others (*81, 88, 109*) provide strong evidence that metallation strongly influences the structure, stability, activity, dynamics and propensity of SOD1. It is therefore important to be able to accurately characterize the metal status of not just SOD1 but also other metalloproteins.

2.1.3 Common methods for metal quantitation of metalloproteins

Measurement of the metal content of proteins is complicated by a number of factors including the complex structure of proteins and the generally low metal content**.** For these reasons especially sensitive and selective methods are required. The most common methods for metal determination in proteins are often referred to as hybrid methods as they combine a chromatographic method for protein separation with a high sensitivity method for metal detection in solution (*137*). Well-known detection methods include atomic absorption spectroscopy (AAS), inductively coupled plasma atomic emission spectroscopy (ICP-AES) and inductively coupled plasma mass spectrometry (ICP-MS). ICP-MS is the most widely used technique due to its versatility, low detection limits and multi-element capabilities; however, for good separation of proteins buffers of high ionic strength are often required but high salt can also result in signal reduction (*137*). In general, hybrid methods are extremely accurate and reliable but most often they are also expensive, time-consuming, require fairly concentrated samples and are not always available. Alternatively, chromogenic chelators have been widely used for metal determination in solution, however, only more recently for the quantification of metals in proteins. Chromogenic chelators are rapid, inexpensive and sensitive but are not very selective (*138*). An example of a commonly used chromogenic chelator is 4-(2-pyridylazo)resorcinol (PAR; see below).

2.1.4 Metal quantitation using PAR

PAR is an azo dye that has been shown previously to from complexes with a variety of metal ions in solution (*122, 125, 139-141*). These complexes have high molar absorptivities making PAR a very sensitive indicator of metal ion concentrations. The free PAR absorption spectrum exhibits a symmetric peak with a maximum absorption at approximately 416 nm (λ_{max}). Upon metal binding the absorbance at 416 nm decreases and a shoulder appears at approximately 500 nm. The λ_{max} and shape of the shoulder is dependent upon the metal bound. Due to the low selectivity of PAR, its use in metal determination was initially restricted to solutions containing just one metal (*141*). The use of PAR for metal determination in proteins was first described in 1984 when it was used to quantify Zn by measuring changes in the absorption spectrum of PAR following denaturation of the protein (*141*). Denaturation of the protein was required to render the metal ions available for chelation by PAR. The non-selectivity of PAR can be either an advantage or a disadvantage. This property makes the quantification of a specific metal difficult if more than one is present in solution, however, if this limitation can be overcome it may allow for the simultaneous quantification of multiple metals in solution.

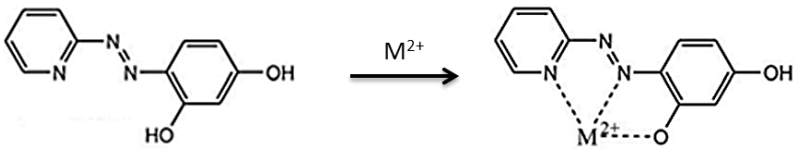

Figure 2.1 - Structure of free and metal-bound PAR. Transition metals are bound through the pyridyl nitrogen atom, the nitrogen of the azo moiety and the 2-phenolate oxygen of the resorcinol moiety.

The simultaneous quantification of two metals using PAR was described by Crow *et al*. in 1997 to measure the concentration of Cu and Zn in SOD1 (*122*). The binding stoichiometry is 1:1 for Cu and 2:1 for Zn (as long as PAR is in 2.5-fold molar excess over Zn) (*122*). In this study, the dissociation constants of the PAR and Cu complex (PAR:Cu) and PAR and Zn complex (PAR_2:Zn) were determined using a competition assay. The results reveal that PAR binds Cu more tightly than Zn with K_d values of 7.7×10^{-11} M^{-1} and 2.6×10^{-15} M^{-1}, respectively (*122*). For metal determination, SOD1 is denatured in

guanidine hydrochloride (GdnHCl) and the increase in absorbance at 500 nm upon metal release is monitored. When the absorbance no longer increases (~1-4 minutes), nitrilotriacetic acid (NTA) is added to selectively chelate Zn. It was believed that NTA binding is not strong enough to remove Cu from the tighter PAR:Cu complex. The decrease in absorption upon the addition of NTA is converted to a Zn concentration using the molar extinction coefficient for PAR_2:Zn and Beer-Lambert's law (given below).

$$A = \varepsilon lc \qquad \text{Eq. 2.1}$$

Ethylenediaminetetraacetic acid (EDTA), a stronger chelator, is then added to strip Cu from the PAR:Cu complex. The decrease in absorbance at 500 nm upon addition of EDTA is converted into a Cu concentration using of the PAR:Cu extinction coefficient. The aim of this method is to allow for the simultaneous quantitation of Cu and Zn in solution by using a chelator to mask one of the metals (*122*). Initial experiments in the Meiering lab suggested there were inaccuracies with this method (Bonner, Primmer, and Meiering). These are investigated further in this thesis.

An alternative PAR-based method later developed (Sabel *et al.* 2009) did not require of the second metal (*139*). In this case, the authors describe the simultaneous quantitation of Zn and cobalt (Co) in solution. The population of the three species contributing to absorbance (free PAR, PAR:Co and PAR_2:Zn) is analyzed using the equation:

$$A_i = d \times \left(\varepsilon_i^{PAR}[PAR] + \varepsilon_i^{PAR:Zn}[PAR_2{:}Zn] + \varepsilon_i^{PAR:Co}[PAR{:}Co]\right) \qquad \text{Eq. 2.2}$$

where d is the pathlength (cm), $\varepsilon_i^{PAR}, \varepsilon_i^{PAR:Zn}$ and $\varepsilon_i^{PAR:Co}$ are the molar extinction coefficients for the free and metal-bound states of PAR, and [PAR], [PAR_2:Zn] and [PAR:Co] are the concentrations for free and bound complexes of PAR (*139*). The sum of the concentrations of all PAR species in solution is equal to the initial amount of chelator present and as such:

$$A_i = d \times [PAR]_0\left(x\varepsilon_i^{PAR} + y\varepsilon_i^{PAR_2:Zn} + z\varepsilon_i^{PAR:Co}\right) \quad \text{with} \quad x + y + z = 1 \qquad \text{Eq. 2.3}$$

where $[PAR]_0$ is the total concentration of PAR, *x* is the molar fraction of free PAR, and *y* and *z* are the molar fractions of PAR complexing Zn and Co, respectively. The concentrations of Zn and cobalt can be obtained by fitting the experimental absorption spectrum to Eq. 2.3 with *x*, *y* and *z* as fitted parameters. To use this method the molar extinction coefficient of all three states must be known. These values can be obtained from the absorbance spectra of each species at a known concentration; however, a spectrum of metal-bound PAR with no interfering free PAR was not attainable. Therefore the spectral contribution of free PAR is manually removed from the PAR_2:Zn and PAR:Co spectra to create a 'clean' spectrum. After this, the 'clean' spectra are scaled to the same concentration the free PAR spectrum (50 μM). It is from these manipulated spectra that the extinction coefficients are determined. The experimental spectrum is fit by the least squares method as a linear combination of the component spectra using the Solver add-in in MS Excel (*139*).

A third method using PAR (Mulligan *et al.*, 2008) to simultaneously quantitate two metals in solution relies on the different shapes of PAR:Cu and PAR_2:Zn absorption peaks (*125*). More specifically, by monitoring the changes in absorbance at two wavelengths, 490 nm and 520 nm, the Cu and Zn signals can be resolved. Both metals have linear increases in absorbance with concentration at these two wavelengths however Cu has an almost identical increase at both wavelengths whereas Zn absorbance increases much more at 490 nm than 520 nm (*125*). Two linear equations can be applied:

$$A_{490} = m_{Cu,490}[PAR{:}\,Cu] + m_{Zn,490}[PAR_2{:}\,Zn] \qquad \text{Eq. 2.4}$$

$$A_{520} = m_{Cu,520}[PAR{:}\,Cu] + m_{Zn,520}[PAR_2{:}\,Zn] \qquad \text{Eq. 2.5}$$

where $m_{Cu,490}$ and $m_{Cu,520}$ represent the increase in absorbance upon the formation of 1 μM PAR:Cu at 490 nm and 520 nm, respectively and $m_{Zn,490}$ and $m_{Zn,520}$ represent the increase in absorbance upon the formation of 1 μM PAR_2:Zn at 490 nm and 520 nm, respectively (*125*). These values are obtained from plots of absorbance at 490 nm and 520 nm versus metal concentration. The linear equations can then be rearranged to solve for the concentration of Cu and Zn (*125*).

$$[PAR{:}\,Cu] = \frac{m_{Zn,520}A_{490} - m_{Zn,490}A_{520}}{m_{Cu,490}m_{Zn,520} - m_{Cu,520}m_{Zn,490}} \quad \text{Eq. 2.6}$$

$$[PAR_2{:}\,Zn] = \frac{m_{Cu,520}A_{490} - m_{Cu,490}A_{520}}{m_{Cu,520}m_{Zn,490} - m_{Cu,490}m_{Zn,520}} \quad \text{Eq. 2.7}$$

The methods described above each use a different approach to differentiate between the two metals in solution. The first relies on a chelator to render one of the metals spectroscopically silent, the second uses a designed fitting routine to separate absorbance bands of all three PAR species present in solution and the third relies on the differential shapes of the metal-bound PAR absorbance peaks.

2.1.5. Chapter overview

In this chapter the three methods outlined above will be for assessed for their accuracy, robustness and ease of use. A new method using PAR will be presented which does not require the determination of molar extinction coefficients or standard curves as a function of metal concentration. The focus will be on the quantification of Cu and Zn in SOD1 however the implications for more general use will be discussed. Insights into the metallation state of pWT and mutant SOD1, as well as complications will be addressed.

2.2 Methods

2.2.1 Solutions

All solutions were prepared using MilliQ ultrapure water (resistivity of 18.2 MΩ·cm; Millipore Ltd., Bedford, MA). All glassware was washed with nitric acid (50% (v/v)) then MilliQ water to remove any contaminating metals prior to use. Tips, eppendorf tubes and cuvettes were washed in a similar manor. All pH adjustments were made using either 1 M sodium hydroxide or 1 M hydrochloric acid.

Metal stock solutions (100 mM) of Cu^{2+} and Zn^{2+} were made by dissolving Cu sulfate (2.50 g; > 98.5% purity) and Zn sulfate (2.88 g; > 99% purity) in 100 mL of water, respectively. All stock solutions were

prepared in a volumetric flask. Working stock solutions (0.25 mM) were prepared by diluting 100 μL of the stock solution to 40 mL with MilliQ water.

A stock solution of GdnHCl (8 M) was prepared by dissolving the denaturant (229.2 g) in water to a final volume of 300 mL using a graduated cylinder.

A stock solution of PAR (10 mM) was prepared by dissolving 0.0215 g of the chelator in 10 mL of water in a volumetric flask. A working 4x PAR-HEPES solution was prepared by mixing 0.89 mL or 1.78 mL of the PAR stock solution (final concentration of 222.22 μM or 444.44 μM, respectively) with 2.12 g of HEPES (final concentration of 222.22 mM) and water to a final volume of 40 mL. The pH was adjusted to 8.0. A 1x PAR-HEPES-GdnHCl solution was prepared by mixing the 4x PAR-HEPES solution (112.5 μL) with 8M GdnHCl (337.5 μL) (total volume of 450 μL). The final assay volume is 500 μL (after addition of 50 uL of metals or protein sample) with a pH of 8.2 as measured by a standard electrode. The 4x PAR concentrations of 222.22 μM or 444.44 μM result in a final PAR concentration of 50 μM and 100 μM, respectively. The final concentrations of HEPES and GdnHCl in the assay solution are 50 mM and 5.4 M, respectively. All PAR solutions were stored in the dark at 4°C as PAR has been shown to have decreased stability with light exposure (*142*).

EDTA (292.24 g/mol) and NTA (191.14 g/mol) stock solutions were prepared by dissolving the appropriate amount of chelator in 15 mL of water using a graduated cylinder. The NTA solution also contained 16 mM sodium hydroxide (39.997 g/mol).

2.2.2 Sample preparation and measurement

Holo and apo pWT SOD1 were prepared using methods established in the Meiering lab (*6, 82*). EDTA bound to the apo protein was removed by unfolding the protein in 2M GdnHCl for 40 min followed by 5 exchanges against 2 M GdnHCl and then 5 exchanges against MilliQ water using a centricon (Ultracel 3K, MILLIPORE IRELAND, Ltd.). Protein concentration was determined by absorbance using the extinction coefficient at 280 nm ($\mathcal{E}_{280}$ = 5, 400 M^{-1}, cm^{-1}) (*124*).

Sample preparation and measurement for experiments using the Crow method were completed as outlined in Crow *et al.*, 1997 (*122*) with the exceptions that HEPES buffer (50 mM) was used instead of sodium borate (100 mM) and the final sample pH was 8.2 instead of 7.8. Briefly, 450 μL of 1x PAR-HEPES-GdnHCl was mixed 50 μL of sample metal solution to the desired metal concentration. After the initial absorbance scan, NTA was added (to a final concentration of 0.8 mM). The sample was incubated for at least 5 minutes in the dark before another absorbance scan was obtained. EDTA addition was completed in the same manner. Absorbance scans were measured from 200 to 800 nm. Trace metals present in solution are accounted for by measuring the decrease in absorbance at 500 nm upon the addition of NTA and EDTA in the absence of added metals. Observed decreases in absorbance at 500nm in the absence of added metal are subtracted from those observed in the presence of metal before calculating metal content. Dilution upon the addition of EDTA and NTA was not accounted for as the effect on calculated metal content was minimal (≤ 1.5%; data not shown).

For all other methods, 450 μL of 1x solution of PAR-HEPES-GdnHCl (final concentration of PAR is 100 μM unless otherwise specified) was mixed with 50uL of the desired concentration of metal-containing sample solution. For protein metal determination, the protein (50 μL) was first added to GdnHCl (337.5 μL) and incubated for 40 minutes to allow sufficient time for the protein to unfold. After incubation, 4x PAR-HEPES was added (112.5 μL) and the absorbance scan was acquired. Again, absorbance scans were measured from 200 to 800 nm. The final assay solutions generally contain 100 μM PAR, 50 mM HEPES, 5.4 M GdnHCl, pH 8.2.

2.2.3 Pyrogallol activity assay

The pyrogallol assay indirectly measures the activity of SOD1 by monitoring the autoxidation of pyrogallol by superoxide (the substrate for SOD1) (*143*). The assay involves a reference scan and an inhibition scan. The reference scan measures the autoxidation of pyrogallol in the presence of catalase. The inhibition scan measures the rate of autoxidation of pyrogallol in the presence of catalase and holo

SOD1. A unit is defined as the amount of SOD1 required to reduce the rate of autoxidation by 50% in 3 mL of buffer. Briefly, in a polystyrene cuvette, 30 μL of bovine liver catalase (Sigma, St. Louis MO) in 50 mM potassium phosphate buffer (pH 7.5) and 75 μM of 8 mM pyrogallol (Sigma, St. Louis MO) in 10 mM HCl, were added to 3 mL of assay buffer (50 mM Tris, 1 mM diethylenetriaminepentaacetic acid (DTPA), pH 8.2, 25 °C) just prior to addition of SOD1. The cuvette was covered with parafilm and mixed rapidly by inverting the cuvette 3 – 4 times. The absorbance at 450 nm was measured over 2 minutes providing the inhibition scan. The reference scan was obtained as described above without the addition of SOD1.

2.2.4 Differential scanning calorimetry

Differential scanning calorimetry (DSC) measurements were performed, as described previously (*6*), using a MicroCal LLC VP-DSC (MicroCal Inc., Northampton MA). SOD1 samples (0.4 – 0.7 mg mL^{-1}) were buffered in 20 mM HEPES, pH 7.8. Samples were degassed for 1 minute prior to loading. Buffer/buffer baselines were determined for each experiment and subtracted from protein/buffer scans. Data were normalized for protein concentration. Experiments used a scan rate of 1 °C min^{-1}.

2.3 Results and Discussion

2.3.1 Crow method

The Crow method for metal analysis involves the use of two chelators; NTA and EDTA (see section 2.1.4) (*122*). The difference in absorbance at 500 nm upon the addition of NTA and EDTA is proposed to represent the amount of Zn and Cu present in the sample, respectively (see above). However, the results here show that NTA is not entirely specific for Zn, as described below. Extinction coefficients were determined by measuring the absorbance at 500 nm as a function of known metal concentration in the absence of chelators. Under the assay conditions the extinction coefficients for Cu and Zn were determined as 36,397 $M^{-1}cm^{-1}$ and 83,240 $M^{-1}cm^{-1}$, respectively. The Cu extinction coefficient matches

very well with the value reported previously, however, the Zn extinction coefficient is larger (*122*) Different values for extinction coefficients have been reported previously (*122*, *139*). These values are sensitive to pH, which could account for the variability (*122*). It is for this reason that standard curves are often prepared daily when using a chromogenic chelator for metal analysis.

The changes in the absorption spectra of Cu and Zn in the presence of PAR upon the addition of NTA and EDTA are illustrated in Figure 2.2. Crow *et al*. (*122*), stated that NTA cannot remove Cu from PAR:Cu; however, in the presence of Cu (20 µM) NTA will chelate approximately 5% of the metal (Figure 2.2 A). On the other hand, in the presence of Zn (20 µM) NTA is only able to chelate approximately 93% of the metal (Figure 2.2 B), even though NTA is in 40-fold excess over Zn and 8-fold excess over PAR.

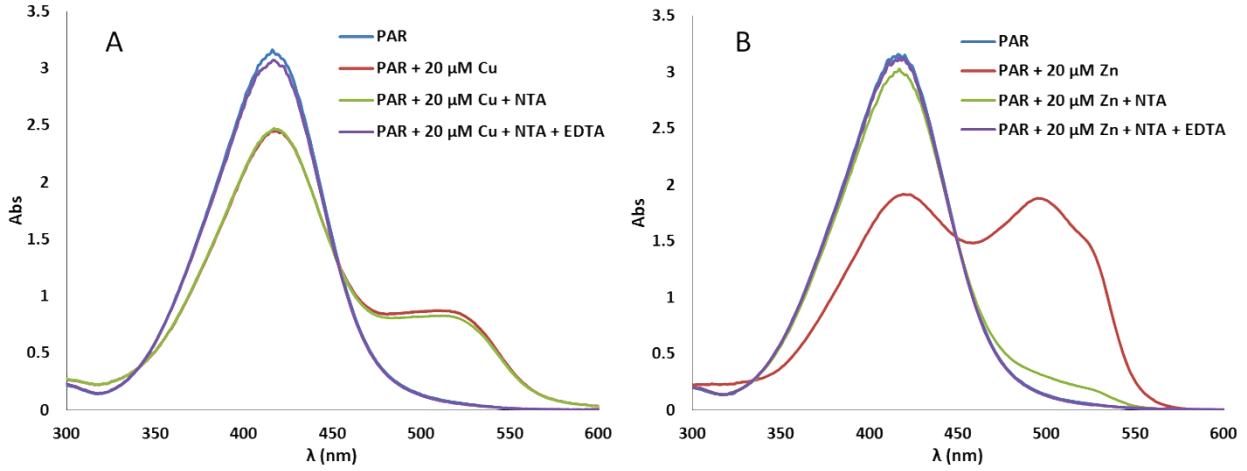

Figure 2.2 - Specificity of the chelators used in the Crow method. (A) Changes in the absorption spectrum of free PAR (100 µM) upon the addition of Cu (20 µM), NTA (0.8 mM) and EDTA (0.8 mM). (B) Changes in the absorption spectrum of free PAR upon the addition of Zn (20 µM), NTA (0.8 mM) and EDTA (0.8 mM). The decrease in absorbance at 500nm (ΔAbs_{500}) is converted to the concentration of metal bound by each chelator using equation 2.1 and the respective extinction coefficient. The percent of metal bound by each chelator is calculated as ([metal bound by chelator] / [total metal])*100%.

In the Crow assay, the difference in absorbance caused by NTA is converted to a Zn concentration using the Zn extinction coefficient and the difference caused by EDTA is converted to a Cu concentration using its extinction coefficient (*122*). It should be noted that for this analysis, when only

one metal is present (as in Figure 2.2), the extinction coefficient of that metal was used to calculate concentration in both steps. To analyze the generality of the chelating trend discussed above, the percent of total metal bound by each chelator was determined at 4 different concentrations of Cu and Zn independently (Table 2.1). Overall, it appears that in the presence of any concentration of Cu NTA will bind approximately 5% of the metal and EDTA will bind the remaining Cu. In the presences of Zn, NTA will bind approximately 94% of the metal and EDTA will chelate the remainder.

Total [Cu] (μM)	% bound by NTA	% bound by EDTA	Total [Zn] (μM)	% bound by NTA	% bound by EDTA
5	4.95	87.92	5	93.22	8.42
10	3.85	104.68	10	93.35	10.81
15	4.76	96.53	15	94.51	10.25
20	4.95	94.79	20	93.11	9.85
Average	**4.62**	**95.98**	**Average**	**93.55**	**9.83**

Table 2.1 - Chelating properties of NTA and EDTA in the presence of varying concentrations of Cu and Zn. The decrease ΔAbs_{500} is converted to the concentration of metal bound by each chelator using Eq. 2.1 and the respective extinction coefficient. The percent of metal bound by each chelator was calculated as ([calculated metal bound by chelator] / [total metal])*100%. The total calculated metal in some cases is greater than 100%. The reason for this is unknown as trace metals were accounted for (see section 2.2.2) however these data were obtained from only one experiment and should be completed in triplicate. All samples contain 100 μM PAR, 50 mM HEPES, 5.4 M GdnHCl, pH 8.2.

This method however was developed to test the metallation status of a protein that binds two different metals. To test its efficacy under these conditions it is applied to various combinations of both Cu and Zn in solution. When the concentration of Zn is much greater than the concentration of Cu the error, especially for Cu, is the largest. On the other hand, when the concentration of Zn is much smaller than Cu or the concentration of both metals is equal, the error is reduced. However in almost every condition the calculated Zn value is lower than expected and the Cu value is higher than expected.

Actual [Cu] (μM)	Actual [Zn] (μM)	Calculated [Cu] (μM)	Calculated [Zn] (μM)	Calculated % Cu	Calculated % Zn
5	20	9.81 ± 0.51	18.25 ± 0.56	196.17 ± 10.10	91.24 ± 2.80
10	15	12.79 ± 0.56	14.10 ± 0.04	127.90 ± 5.64	93.99 ± 0.28
15	10	16.27 ± 0.58	9.79 ± 0.03	108.44 ± 3.88	97.85 ± 0.25
20	5	19.64 ± 0.43	5.18 ± 0.15	98.22 ± 2.14	103.55 ± 3.06
5	5	5.84 ± 0.06	5.30 ± 0.08	116.77 ± 1.17	105.84 ± 1.53
10	10	11.46 ± 0.12	9.90 ± 0.17	114.57 ± 1.16	98.99 ± 1.70
12.5	12.5	14.38 ± 0.60	12.07 ± 0.12	115.07 ± 4.82	96.59 ± 0.95

Table 2.2 - Accuracy and precision of the simultaneous determination of Cu and Zn using the Crow PAR assay protocol. Each value represents the mean ± the standard deviation of two independent experiments. The percent metal was calculated as ([calculated metal] / [actual metal])*100%. All samples contain 100 μM PAR, 50 mM HEPES, 5.4 M GdnHCl, pH 8.2.

The results can be explained by the chelation trend identified above and the differences in the extinction coefficients of each metal. When the concentration of Zn is high, NTA does not bind all of it and the remaining Zn is bound by EDTA. This causes the decrease in absorbance upon the addition of EDTA to be greater than it should be. This error is then magnified in the metal calculation as the amount of Zn miscalculated as Cu is exaggerated. The decrease in absorbance upon stripping say 1 μM of Zn from PAR will be over 2-fold greater than the decrease caused by the removal of 1 μM of Cu since the extinction coefficient of PAR_2:Zn is over 2-fold larger than that of PAR:Cu. Therefore the concentration of Cu calculated will be equal to the amount of Cu present plus the amount of Zn not bound by NTA multiplied by a factor of 2.3 (this is equal to the ratio of the extinction coefficients). When the concentration of Zn is low relative to Cu, NTA will bind some of the Cu present. This will result in a lower than expected Cu value and a higher than expected Zn value. However, in this case the error in the Zn value will be underestimated again due to the relative magnitudes of the extinction coefficients of each metal. When the concentrations of both metals in solution is equal the calculated metal content is more accurate, although still generally some of the Zn is miscalculated as Cu likely because the NTA does not bind all the Zn.

Overall the results show that there is variability of the proportion of metals chelated by NTA depending on the sample conditions. The type and amount of metal bound by NTA is dependent upon the concentration of metals present in solution. As a consequence, the error in the calculated metal content follows a clear trend, illustrated in Figure 2.3. In the case of a protein that binds two metals in equal concentration this method is fairly accurate but as a more general method for metal quantitation it is not reliable. In terms of SOD1, mismetallated or undermetallated species have been implicated as playing a role in disease. It is therefore of great importance to characterize accurately the metallation state of these species, however by their nature the concentration of the two metals will not be equal limiting the applicability of this method.

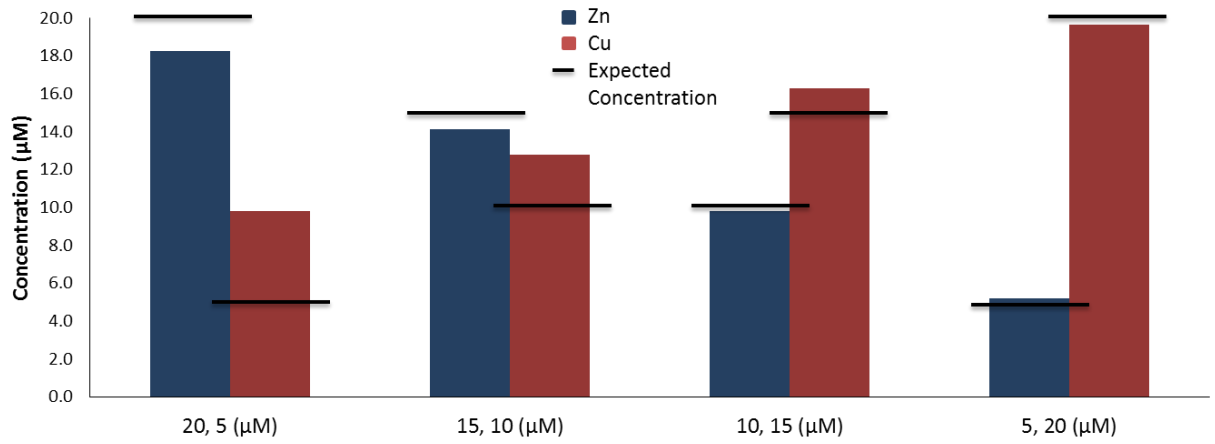

Figure 2.3 - Trend in the error of calculated metal using the Crow protocol with unequal metal concentrations. The actual concentrations of the metals are given by horizontal lines, and calculated concentrations are given by blue and red bars for Zn and Cu, respectively. When the Zn concentration is high relative to Cu concentration, Cu is greatly overestimated and Zn is underestimated. Conversely, at relatively high Cu levels, Cu is slightly underestimated and Zn slightly overestimated. All samples contained 100 μM PAR, 50 mM HEPES, 5.4 M GdnHCl, pH 8.2.

2.3.2 Säbel method

The fitting routine described by Säbel *et al.* (*139*) requires the determination of the extinction coefficient of all three PAR species (free PAR, PAR_2:Zn and PAR:Co) in solution. A number of manual processing steps (subtraction of the free PAR signal and multiplication to reflect the same concentration

of $[PAR]_0$) are required to do this and create sources of possible error. This method was optimized specifically for the determination of Zn and cobalt in solution. For this developed application, this method is fairly accurate with the expected and calculated values generally within 10% and the standard deviation usually below 10% (Figure 2.4) (*139*).

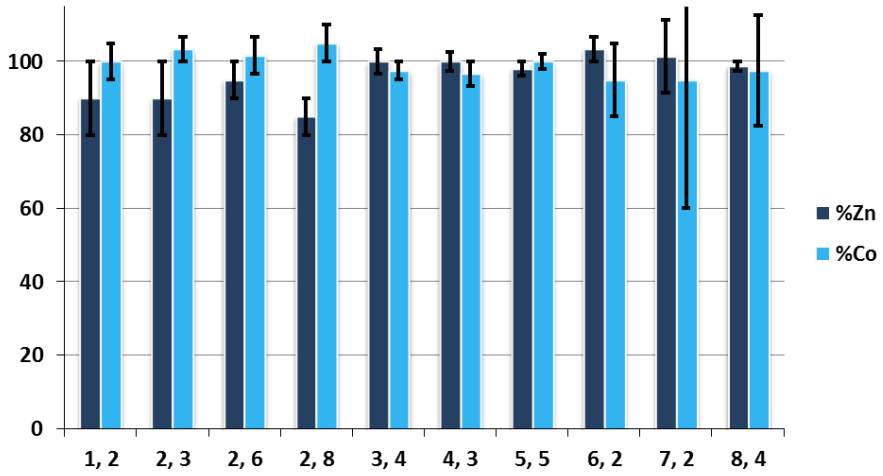

Figure 2.4 - Metal determination of Zn and Co with PAR using the Säbel Method. The concentrations of each metal in solution are given on the x-axis as Zn, Co (μM). Numbers were taken from Säbel et al., 2009 (*139*) and are the average of three independent trials. Shown off scale is the error bar for the 7 μM Zn and 2 μM cobalt condition at 130%.

One of the main factors contributing to the success of this method is the different spectral features of the PAR_2:Zn and PAR:Co complexes. At the same concentration, PAR_2:Zn has a significantly higher absorbance peak than PAR:Co, which exhibits a wider peak (Figure 2.5). Analysis of the efficacy of this method with Cu and Zn was not completed herein as it has already been completed in the Siemann lab. The fits, precision and accuracy were relatively poor, which was attributed to the PAR:Cu absorbance peak having more extensive overlap with the PAR_2:Zn peak (Figure 2.5), preventing good resolution of the two species (Stefan Siemann, personal correspondence).

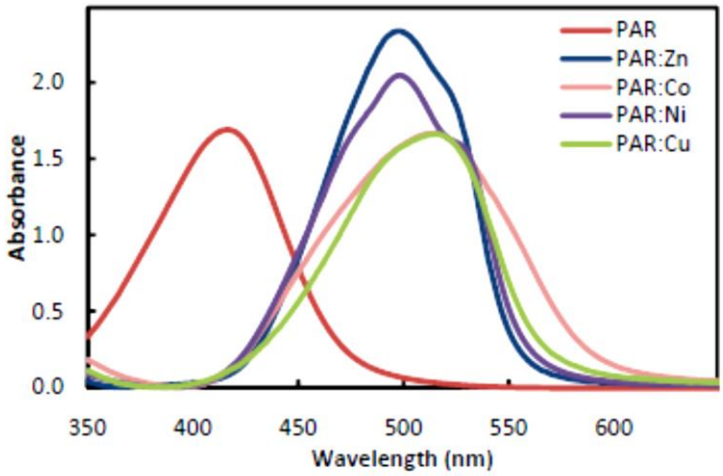

Figure 2.5 - The absorption spectra of PAR (50 µM) with in the presence of 10 µM Zn, Co, Ni or Cu. The absorbance of free PAR has been manually subtracted. Figure taken from Säbel, C.E. 2010 (*140*).

This method proves to be fairly accurate under the specific conditions for which it was developed; however as a more general method it is not ideal. It appears that this method is limited by the spectral features of some PAR-metal complexes. Further, the amount of manual processing reduces the ease of use and increases the possibility of introducing error.

2.3.3 Mulligan method

The linear equation-based method published by Mulligan *et al.* (*125*) did not provide any details on its accuracy but did state that the values obtained were similar to the those obtained using the Crow method. The results above (section 2.3.1) show that the Crow method is not always accurate. The accuracy of the Mulligan method is therefore analyzed below. For each experiment, the values of $m_{Cu,490}$, $m_{Cu,520}$, $m_{Zn,490}$ and $m_{Zn,520}$ (see section 2.1.4) were determined on the same day from a standard curve of the absorbance at each specified wavelength versus concentration. Representative determinations of $m_{Cu,490}$, $m_{Cu,520}$, $m_{Zn,490}$ and $m_{Zn,520}$ are shown in Figure 2.6. From day to day these values did not change significantly.

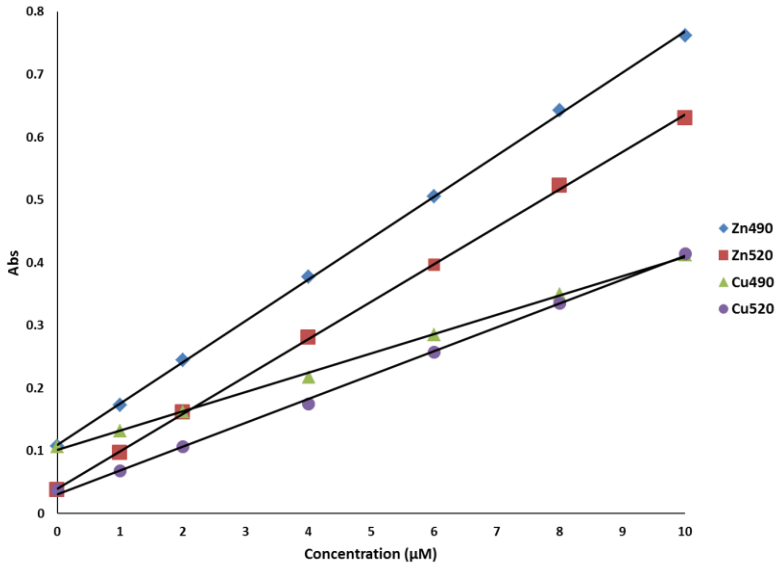

Figure 2.6 - Standard curves of PAR:Cu and PAR_2:Zn absorbance as a function of concentration for 490 nm and 520 nm. These representative curves are the average of 4 independent experiments. All samples contain 50 μM PAR, 50 mM HEPES, 5.4 M GdnHCl, pH 8.2.

To test the efficacy of this method, solutions of known concentrations of Cu and Zn (total metal equal to 10 μM) were analyzed (Table 2.3). This method proves to be quite accurate under these conditions as in most cases the calculated concentrations are within 5% of the expected values. The standard deviation of three independent trials is also quite low indicating a high level of precision. It should be noted that a change in the binding stoichiometry between PAR and Zn is clearly evident in standard curves when PAR is not in great enough excess (data not shown). For example, in the presence of 50 μM PAR the absorbance at both 490 and 520 nm increases linearly upon the addition of up to 25 μM Cu. On the other hand, under the same conditions the Zn standard curves begin to curve significantly above 15 μM. Therefore, one needs to be careful about the total metal present in solution in relation to the amount of PAR present. In this analysis, the total metal was not above 10 μM so the absorbance changes with concentration were linear; however, to test the assay at higher metal concentrations the PAR concentration was increased (100 μM).

Actual [Cu] (μM)	Actual [Zn] (μM)	Calculated [Cu] (μM)	Calculated [Zn] (μM)	Calculated % Cu	Calculated % Zn
0	10	-0.20 ± 0.15	10.19 ± 0.42	-	101.94 ± 4.18
2	8	1.80 ± 0.12	8.13 ± 0.35	90.04 ± 5.95	101.68 ± 4.37
4*	6*	3.79 ± 0.02	6.51 ± 0.11	94.67 ± 0.41	108.52 ± 1.84
6	4	5.87 ± 0.19	4.02 ± 0.07	97.88 ± 3.18	100.60 ± 1.84
8	2	7.81 ± 0.04	1.95 ± 0.08	97.61 ± 0.50	97.88 ± 4.16
10	0	9.22 ± 1.01	-0.01 ± 0.03	92.21 ± 10.08	-

Table 2.3 - Accuracy and precision of the simultaneous determination of Cu and Zn in solution using the Mulligan PAR assay protocol (*125*). Each value represents the mean ± the standard deviation of three independent trials with the exception of one condition where only two trials were completed (marked with an asterisk). All samples contain 50 μM PAR, 50 mM HEPES, 5.4 M GdnHCl, pH 8.2. The percent metal was calculated as ([calculated metal] / [actual metal])*100%.

At increased metal concentrations this method again proves to be quite accurate (total metal equal to 25 μM; Figure 2.7). Overall, this method is well suited to simultaneously quantitate Cu and Zn levels in proteins. One drawback is the requirement to construct standard curves for both Cu and Zn with at least 3 different concentrations daily, which is time consuming. Further, this method relies on the differences in absorbance increases at two wavelengths which may not provide good separation of signals for all metals (e.g. Cu and cobalt; Figure 2.5). Thus, as a general method, applicable to a wide variety of metals and easily conducted, this method is not ideal.

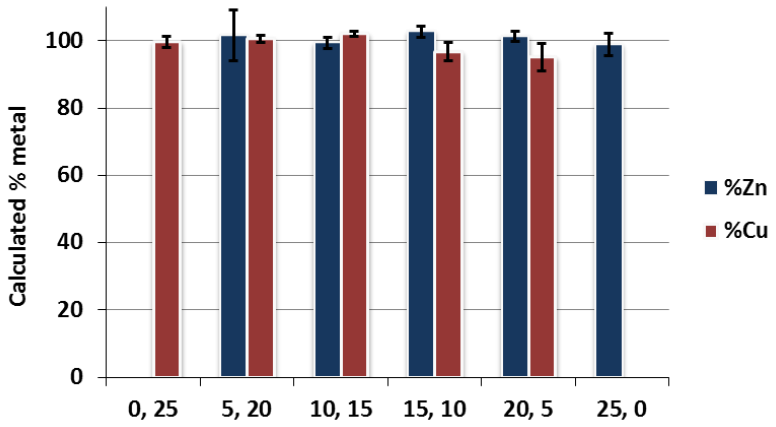

Figure 2.7 - Accuracy and precision of the simultaneous determination of Cu and Zn in solution using the Mulligan PAR assay protocol (*125*). The concentrations of each metal (25 μM total) in solution are given on the x-axis as Zn, Cu (μM). Each calculated value represents the mean ± the deviation of two independent trials. All samples contained 100 μM PAR, 50 mM HEPES, 5.4 M GdnHCl, pH 8.2. The average deviations are 2.62% and 1.75% for Zn and Cu, respectively. The percent metal was calculated as ([calculated metal] / [actual metal])*100%.

2.3.4 Modified PAR assay

2.3.4.1 Method

A new method was developed here that uses spectral software (SpectraLab or SpLab created by Dmitri Davydov, University of California at San Diego) to distinguish the PAR, PAR:Cu and PAR_2:Zn absorbance signals (*144*). This software is freely available for download (http://cyp3a4.ucsd.edu/spectralab.html). In SpLab, spectral decomposition is achieved using least squares fitting method. This is a mathematical approach that minimizes the sum of the squared deviations (or residuals) between the observed (experimental spectrum) and fitted value. Using this software the experimental spectrum is fit using a set of absorption spectra for three standards: free PAR, PAR:Cu and PAR_2:Zn (Figure 2.8 A). Any trace metals present in solution are accounted for in the free PAR standard spectrum.

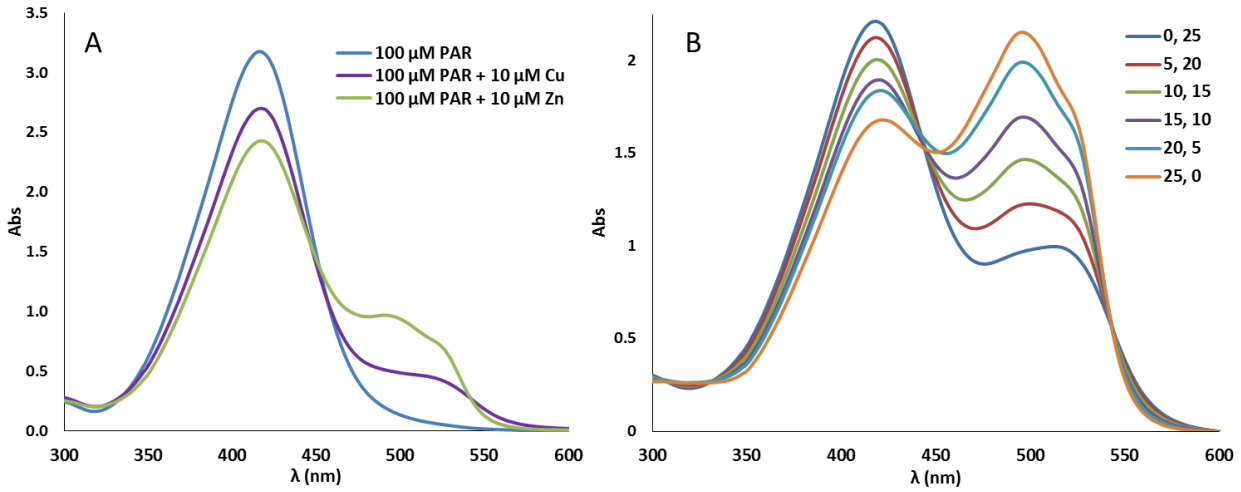

Figure 2.8 - Representative absorption spectra for PAR assay of Cu and Zn. All samples contained 100 µM PAR, 50 mM HEPES, 5.4 M GdnHCl, pH 8.2. (A) The three standards used to fit experimental spectra. (B) Experimental spectra for experiments on known mixtures of Cu and Zn with a total metal concentration of 25 uM. The concentration of each metal is given in the legend as Zn, Cu (µM).

A screenshot of the SpLab software is given in Figure 2.9 showing the fit of an experimental absorbance spectrum. Under the Data Analysis tab there is an option for "Spectral Decomposition". This

will open the SurFit tab where one can select the standard spectra (by row) for fitting the experimental spectrum and the destination for the fitted curve. Upon clicking `run` a SpectraLab window will appear which gives the percentage of each standard in the fitted spectrum. The quality of the fit is also given in this tab by the squared correlation coefficient. Since the concentration for each standard spectrum is known, simple multiplication of the concentration of each spectrum by its percentage in the fitted spectrum yields the concentration of each metal in the sample.

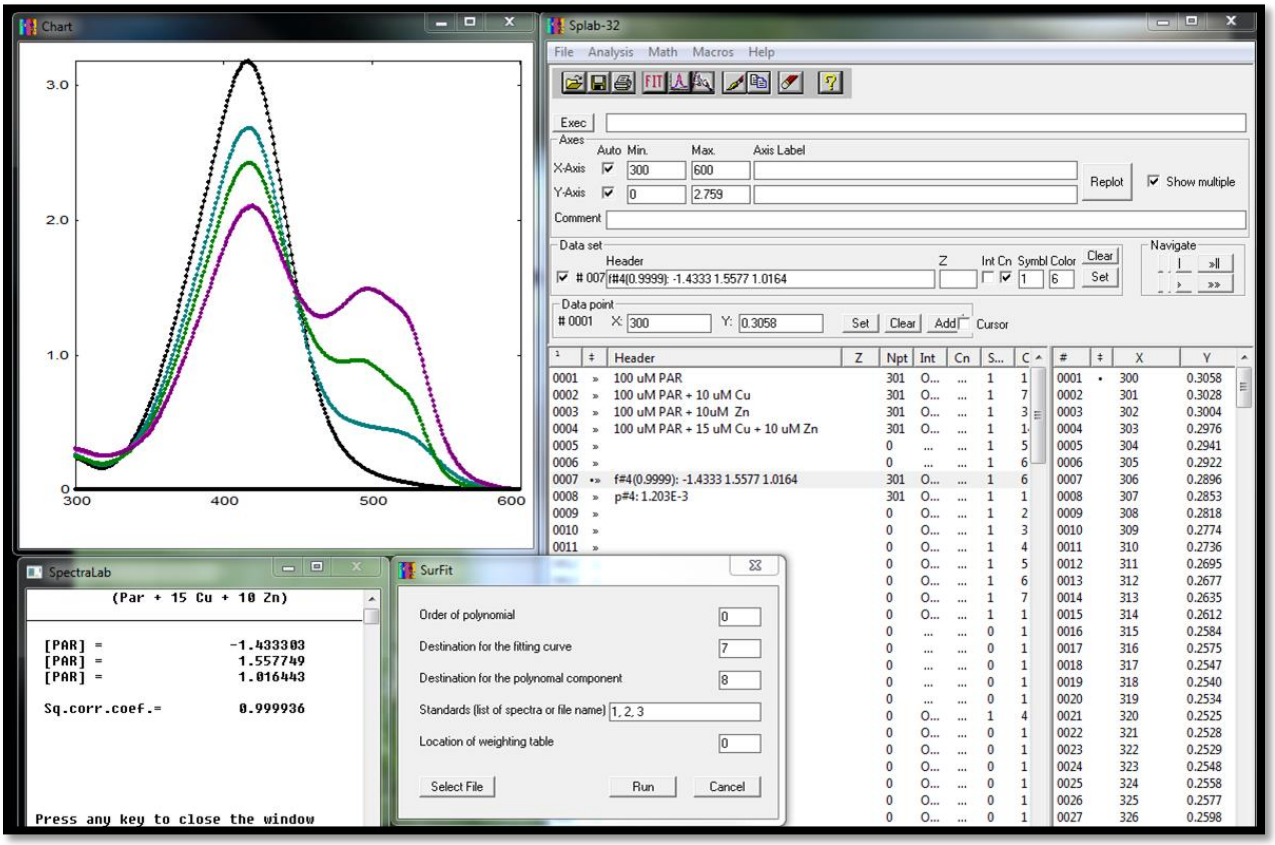

Figure 2.9 - Screenshot of SpLab software (*144*). The standard spectra of PAR, PAR:Cu and PAR_2:Zn are shown in the upper left panel in black, teal and green, respectively. The experimental spectrum is shown in purple (15 μM Cu, 10 μM Zn). The fitted spectrum is also plotted but is not visible as it lies directly under the experimental spectrum.

There are some key differences between the modified PAR assay and the one previously described by Säbel *et al.* (see section 2.1.4). First and foremost, this method does not require manually created `clean` absorption spectra or knowledge of extinction coefficients. In the Säbel method the

experimental spectrum is fit to Eq. 2.3. Instead in the current method the spectrum is simply fit to a linear combination of the three standard spectra. In order to have sufficiently large and proportional absorbance changes for accurate determination of metal while using minimal protein, the concentration of PAR was chosen to be 100 uM with the total metal concentration not exceeding 25 μM to avoid changes in the binding stoichiometry of PAR and Zn.

The most suitable metal concentrations for the PAR:Cu and PAR_2:Zn standard spectra was determined by fitting known metal samples with standards having a wide range of concentrations (5 – 25 μM), comparing the agreement with expected values and standard deviations (data not shown). Standards of 10 μM Cu and Zn were chosen, however, the differences caused by changing the concentration of the standard spectra (from 5 to 25 μM) are small. The corresponding sample proteins concentration for the most accurate analysis was determined by comparing the quality of the fit at various protein concentrations while also considering protein conservation. A protein concentration of 5 μM was chosen, although higher protein concentrations (up to 10 μM) have very little effect on the quality of the fit. The performance of the developed modified PAR assay is described further below.

2.3.4.2 Determination of the accuracy and precision of the modified PAR assay

The accuracy and precision of the modified PAR assay was assessed, as for the other assays described in the preceding sections, by analyzing sample solutions with known concentrations of metal (Table 2.4). In all cases the actual and calculated values are within 5% and in most cases the standard deviation is below 3%. These results reveal that, unlike the previous method that uses a fitting routine described above (*139*), this method is able to separate the signals of Cu and Zn with good accuracy and precision even though the absorbance bands of the two metals are not well resolved.

Actual [Cu] (μM)	Actual [Zn] (μM)	Calculated [Cu] (μM)	Calculated [Zn] (μM)	Calculated % Cu	Calculated % Zn
0	25	0.15 ± 0.21	24.87 ± 0.27	-	99.48 ± 1.08
5	20	4.89 ± 0.33	20.87 ± 0.48	97.71 ± 6.59	104.35 ± 2.41
10	15	9.68 ± 0.26	15.27 ± 0.11	96.83 ± 2.59	101.80 ± 0.73
15	10	15.14 ± 0.31	10.17 ± 0.03	100.96 ± 2.04	101.70 ± 0.26
20	5	20.29 ± 0.12	5.05 ± 0.01	101.47 ± 0.59	100.95 ± 0.16
25	0	24.87 ± 0.40	0.02 ± 0.06	99.47 ± 1.59	-

Table 2.4 - Accuracy and precision of the simultaneous determination of Cu and Zn in solution using the modified PAR assay with SpLab. Each value represents the mean ± the standard deviation of three independent experiments. All samples contain 100 μM PAR, 50 mM HEPES, 5.4 M GdnHCl, pH 8.2.

Previously developed methods describe the successive scanning of PAR absorption spectra as a function of time to monitor changes in absorbance upon the addition of chelators or protein unfolding, for example (*122, 125*). To determine if successive scanning has any effect on the modified PAR assay, the absorbance peak of PAR_2:Zn was monitored as a function of time. The results reveal that over a 20 minute period, the absorbance decreases. This was independently repeated over a 5 minute time frame and the results were the same. In the second case, the absorbance at λ_{max} decreased by 0.01 over the given time period equivalent to approximately 0.15 μM Zn. The exact reason for this decrease is unknown; however, since PAR has been shown to be unstable under light exposure it is likely that the successive scanning is causing photodamage of the PAR (*142*). For this reason, when sample protein is analyzed (described in the following section) it is first incubated in GdnHCl for 40 minutes to allow for full denaturation prior before it is mixed with PAR.

2.3.1.4 Analysis of holo SOD1 using the modified PAR assay

Using the optimized PAR assay described above and further detailed in the methods (sections 2.2.1 and 2.2.2), the metallation state of pWT and 11 different fALS SOD1 mutants obtained by overexpression in *E. coli* was investigated (Figure 2.10). In all cases, the results show that the proteins are undermetallated. On average, the proteins contain 66.8% (± 10.8%) Zn and 80.2% (± 11.5%) Cu. This result is surprising for three reasons. First, since there is no Cu chaperone present in the expression

system to facilitate Cu insertion into the protein it seems more likely that the variants would be deficient in Cu. Second, analysis of the activity and global stability of SOD1 (see sections 2.2.3, 2.2.4 and 2.3.1.6), which are significantly influenced by the presence of Cu and Zn, respectively, suggests that these samples have higher levels of metals than observed in Figure 2.10. For example, pWT which is calculated to have only 80% Zn by the PAR assay displays by DSC a T_m of 91.4°C which is comparable to that for fully metallated pWT (92°C) (see section 2.3.1.6). Third, ICP-AES metal analysis of SOD1 suggests that for typical protein preparations of both pWT and mutant SOD1 in the Meiering lab, Zn incorporation is generally equal to or greater than Cu (*92*). Analysis of the same pWT sample by both methods reveals 108% Zn and 89% Cu incorporation by ICP-AES and only 79% Zn and 91% Cu incorporation by the PAR assay. The calculated Cu is quite similar in both methods however the Zn is much lower in the PAR assay. The discrepancy between the methods can be explained by an effect of EDTA, described next.

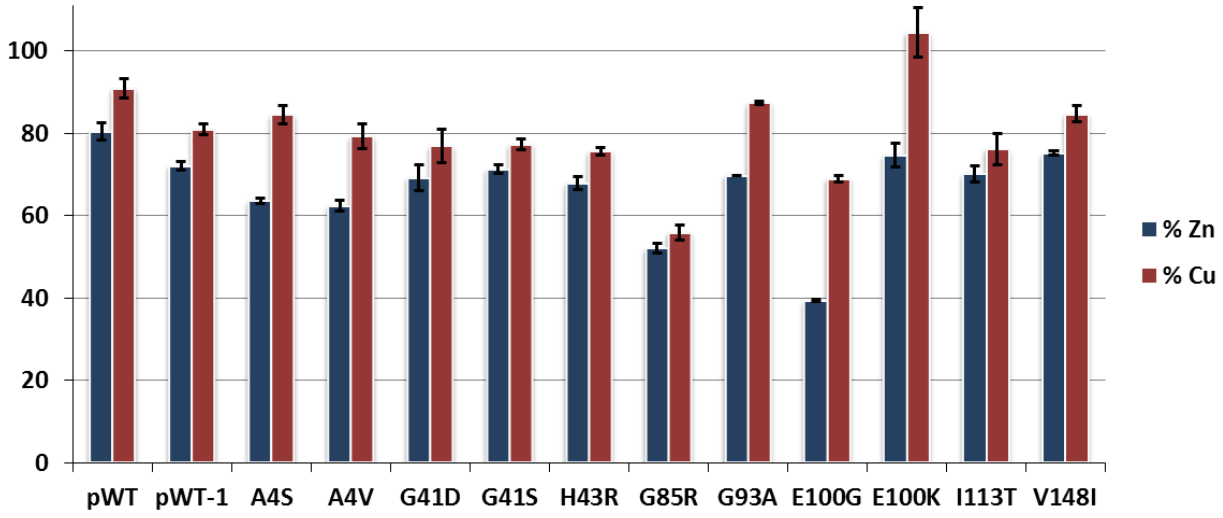

Figure 2.10 - Metal content of pWT and 11 fALS mutants. Values are calculated as % metal per protein subunit, where full metallation corresponds to 100%. All samples contain 100 µM PAR, 50 mM HEPES, 5.4 M GdnHCl, 5 µM SOD1, pH 8.2. Values are the average of three samples. The standard deviation is given as error bars.

In order to ensure that the presence of protein in solution does not interfere with the modified PAR assay, samples of known metal prepared with added denatured EDTA-free apo pWT were analyzed. EDTA is used to prepare apo SOD1, and it binds strongly to SOD1 at low ionic strength (*145*). EDTA can

be removed (see section 2.2.2) to ensure it does not interfere with the assay. Both Cu and Zn were tested at two different concentrations in two independent trials with added EDTA-free apo protein. The expected and calculated metal concentrations were generally within in 3% indicating that the presence of denatured protein does not interfere with the assay (data not shown).

Further inspection of the results revealed not every holo SOD1 sample had lower Zn levels compared to Cu. Rather, protein samples obtained using a different growth protocol involving a fermenter as well as remetallated EDTA-free apo pWT samples all had higher Zn levels. Both of these types of samples would not have contained EDTA bound to the protein because the chelator is not used in fermenter preparations and is removed from the apo samples before remetallation. The presence of EDTA bound to apo SOD1 samples would not be surprising since the chelator is directly added to purified protein; however, it was not thought previously that the chelator would also be bound to holo SOD1. In a typical purification of holo SOD1 using shaker flask culture growth, EDTA is used in an osmotic shock step to release the periplasmic fraction of SOD1 (*146*); at this point there are various proteins and cellular components present that may bind EDTA. Further, a number of subsequent purification steps are used to obtain pure holo SOD1, so it was not thought that EDTA would be present at any considerable level in final holo SOD1 samples. The results described above suggest otherwise.

2.3.1.5 Interference in the modified PAR assay by protein-bound EDTA

To further investigate the possibility of EDTA as the cause of the low measured levels of Zn for the holo SOD1 variants analyzed, the metal chelating preference of EDTA in the absence and presence of pWT was analyzed. EDTA has a stronger affinity for Cu (*147*) which is clearly illustrated by its preferential binding of Cu over Zn when only free metals are present in solution (Figure 2.11 A). In the presence of holo SOD1 (5 μM) however the opposite trend is observed, although the difference between metal preference is not as great (Figure 2.11 B). It has been shown previously that SOD1 binds Cu more tightly than Zn (*122*). In these experiments holo pWT is unfolded in ~7 M GdnHCl for 40 min prior to the

addition of PAR-HEPES and EDTA. Based on previous studies of the unfolding kinetics of pWT in the Meiering lab, the protein should be fully unfolded after the 40 min incubation. The results here suggest that even in the denatured state SOD1 has a strong enough affinity for Cu to alter the observed chelation by EDTA. Cu binding to the unfolded state of SOD1 is supported by studies monitoring the unfolding kinetics of SOD1 which found that adding Cu prior to unfolding had little to no effect on the unfolding rate (*126*). The results indicate that if EDTA is present in holo SOD1 samples, it would manifest as a lower than expected Zn concentration in agreement with what is observed (Figure 2.11 B).

Metal titrations with holo pWT also reveal an interesting trend that supports the above proposed interference of SOD1-bound EDTA in the modified PAR assay. When equimolar Cu and Zn were added to samples of holo SOD1, the observed Cu concentration actually decreases slightly and the observed Zn concentration is increased, beyond the added amount (by ~30%). One theory that could explain this behaviour is that upon the addition of free metals, the EDTA present releases some of the bound Zn to chelate the free Cu in solution, for which it has a higher affinity. Lastly, recent size-exclusion chromatography experiments on holo SOD1 in the Meiering lab display a characteristic EDTA peak for holo SOD1 samples obtained from typical flask preparations (Jessica Rumfeldt, unpublished data). Taken together, the results indicate that EDTA bound to holo SOD1 is the reason for the lower than expected calculated Zn concentrations. It should be noted that this does not mean that Cu is unaffected by EDTA but rather the effects on Zn are more pronounced.

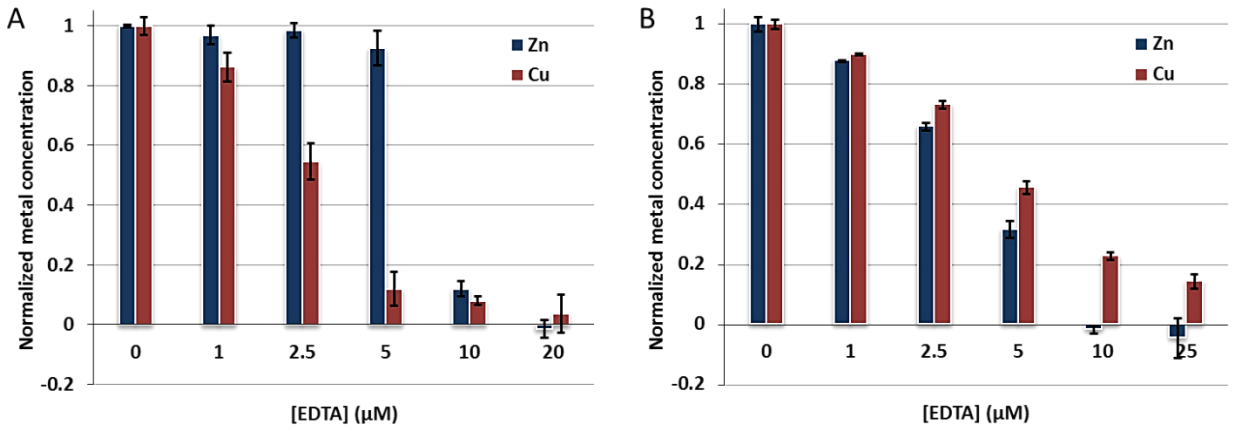

Figure 2.11 – Specific chelation of Cu and Zn by EDTA. (A) In the absence of protein with added free Cu (5 μM) and free Zn (5 μM). (B) In the presence of 5 uM holo pWT SOD1 at varied EDTA concentrations. All samples contain 100 μM PAR, 50 mM HEPES, 5.4 M GdnHCl, pH 8.2. All concentrations are normalized to the initial concentration of metal present in solution. The values are the average for three samples. The standard deviation is given as error bars.

Unfortunately, the presence of protein-bound EDTA greatly limits the use of the PAR assay for samples of SOD1 that have been exposed to and therefore bound EDTA. To try to circumvent this problem for samples of recombinant SOD1 which are routinely being produced and studied by various methods in the Meiering lab, osmotic shock in the absence of EDTA was attempted. This greatly reduced the protein yield. Different chelators (NTA and DTPA), as well as additional processing steps (such as dialysis of the purified SOD1 against perchlorate (*148*) were also attempted in hopes to reduce the amount of chelator bound to the protein or remove the chelator entirely. In all cases, the Zn levels remained lower than Cu and levels of both metals were lower than expected for full metal incorporation of SOD1.

2.3.1.6 Insights into SOD1 properties from PAR analyses

The ability to accurately, reliably and rapidly determine the metal bound to SOD1 is of importance for the sensitive comparison between metallation and various biophysical and biochemical properties including protein activity, stability and aggregation propensity. Decreased metal binding affinity has been proposed to be a general consequence of ALS associated SOD1 mutations and it was hoped that the PAR assay would allow for the comparison many mutants to test this theory. Even with the

inaccuracy introduced by the presence of EDTA some correlations were identified. DSC scans of pWT were completed to assess the stability of SOD1 variants (see section 2.2.4) and a pyrogallol assay was used to determine the activity (see section 2.2.3). It should be noted that some of these experiments were completed by previous students in the Meiering lab however for comparisons it was ensured that all experiments were completed on protein prepared from the same cell culture growth.

The temperature where half of the protein is unfolded, or T_m, provides a good measure of SOD1 stability. The results show that there is a fairly strong positive correlation between total metal and global stability (Figure 2.12 A). The metal binding mutant G85R (*54*) is a notable outlier in this correlation. In the holo state the T_m for G85R is significantly reduced compared to pWT (by 16.5°C) yet in the apo state the T_m is quite similar to pWT (reduced only by 3.8°C) (*149*). This suggests that the G85R mutation disrupts the metal binding region in such a way that the typical stability conferred by metal binding is lost. Altered metal binding in this mutant could explain the lower total metal content calculated for G85R compared to other mutants (by ~20%; Figure 2.10) and also the lower than expected T_m even when metal content is accounted for (Figure 2.12 A). There is also a strong positive correlation between measured Cu and specific activity (Figure 2.12 B). This is consistent with the Cu ion being required for catalytic activity (see section 1.6.2). In addition, the results indicate that almost every mutant analyzed has reduced total metal compared to pWT. This result only holds true if the amount of bound EDTA is comparable in each sample, however, the similar sample preparation procedures used for each mutant points to uniform EDTA levels. From Figure 2.10, it is clear that for some mutants (e.g. A4S, A4V, G93A, E100G and E100K) calculated Zn is considerable lower than calculated Cu (by ~20%). This difference is likely more than just the effect of bound EDTA. Decreased affinity for Zn has been observed for A4V (ref Crow), and NMR studies of G93A (see Chapter 3) reveal decreased local stability surrounding the zinc binding site in this mutant. The results therefore support the theory of altered metal binding in mutants, which may in part contribute to the decreased global stability.

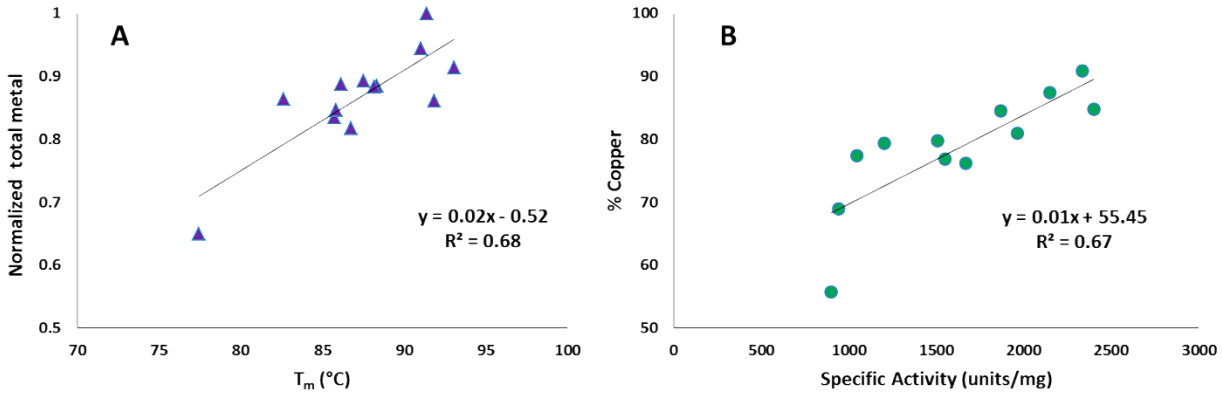

Figure 2.12 - Correlation plots of SOD1 metal status as calculated using PAR. (A) Correlation of total metal (normalized to pWT) and the T_m (measured by DSC with protein concentrations ranging from 0.2 – 1 mg/mL). Values are calculated as % metal per protein subunit, where full metallation corresponds to 100%. Total metal was calculated [(% Cu + % Zn)/2] and all values were then normalized to pWT having a total metal of 1. (B) Correlation of the % Cu and specific activity (measured by pyrogallol assay). The line of best fit is given by a solid black line. The associated equation and R^2 value is given in the plot area. Data points farthest to the lower left in both panels are for G85R, a known metal binding mutant (*54*).

2.3.1.7 Summary and future work

The optimized PAR assay described herein provides a method for the simultaneous quantification of Cu and Zn in solution. This method is accurate and precise and is very easy to use. Further, since the fitting routine uses a linear combination of three standard spectra accounting for changes in experimental condition is straightforward. One simply needs to obtain the three standard spectra under the new conditions and complete the rest of the analysis in a similar way. In good practice standards should be made daily. However, with the conditions outlined in the methods section for PAR solution storage and the fitting routine described, which uses the entire absorption spectrum instead of 1 or 2 specific wavelengths for analysis reducing variability, metal quantitation with standards from the same week has proven to be just as accurate as when using standards from the same day (data not shown). Analyses of holo SOD1 purified from the periplasm of E. *coli* (*149*) reveal that there is EDTA bound to the protein; unfortunately the EDTA interferes with the assay by masking metal ions resulting in lower than expected calculated metal concentrations. Despite this interference, the assay has proved to be very useful within the Meiering lab in many contexts. The assay provides fast and reliable confirmation of the removal of

metals for reduced apo preparations of pWT and mutant SOD1 samples used in aggregation studies (*83*). Further, the metal status of inclusion bodies (cytoplasmic aggregates) formed by over-expression of WT SOD1 in *E. coli* has been investigated indicating varying levels of metal incorporation (Johnathan Almey, unpublished data).

Potentially valuable future experiments may be to assess the robustness of this new PAR assay method for analyzing other combinations of metals in solution. Based on the absorption bands observed for different metals (Figure 2.5), this method should be easily be able to resolve mixtures of Zn and Cu (as shown above), Zn and Co, Ni and Cu, and Ni and Co in solution. Since this method is able to accurately separate the spectral signals of PAR:Cu and PAR_2:Zn, which a previous fitting method has failed to do, we are hopeful the accurate determination of other metals in solution will be possible. Further, an interesting future experiment using this assay will be to test the propensity of SOD1 mutants to loose metals over time compare to pWT. This experiment would be completed in the absence of denaturant to quantify the amount of metal released from the protein. The samples could be incubated at 37°C with aliquots tested as a function of time. If a mutant is more likely to lose metal then it may be more likely to populate an aggregation prone state (see section 2.1.2).

2.4 Conclusions

The importance of metalloproteins is reflected by the sheer number of proteins that bind metal cofactors (*109*). The presence or absence of metal cofactors can greatly influence the structure, function and flexibility of a metalloprotein. In some cases, such as SOD1, the loss of metal cofactors is proposed to lead to protein aggregation and disease (*88, 136*). It is therefore of utmost importance that when analyzing various biophysical and biochemical properties of a protein, or when making comparisons between proteins, that the metallation state is known.

The use of the chromogenic chelator PAR for metal determination in proteins was explored herein due its low cost and high sensitivity. The non-selectivity of PAR makes distinguishing between

metal ions in solution difficult. A number of methods have been developed to overcome this limitation. The Crow method (*122*) relies on the use of two chelators to mask one of the metals in solution, which is shown here to be only partially effective. We further show here that the selectivity of the chelators depends on the type and amount of metal in solution and thus only under specific experimental conditions is the Crow method reliable (Figure 2.3). The alternative Säbel method uses a linear addition of Beer-Lambert law to separate the spectral contributions of each metal (*139*). This method is fairly accurate for the determination of Zn and Co in solution but the resolution for Zn and Cu is low (Stefan Siemann, personal correspondence). Further, a number of manual processing steps decrease the ease of use and increase the possibility of introducing error. A third method developed by Mulligan *et al*. (*125*) relies on the differential absorbance of Cu and Zn at two specific wavelengths. This method proves to be quite accurate at distinguishing between Cu and Zn however use of only two-wavelengths for analysis is not compatible for quantification of metals with more similar spectral signals in solution.

An alternative method presented herein proves to be very accurate and precise in the determination of Cu and Zn in solution. This method uses the spectral software (*144*), to perform spectral decomposition separating the three species contributing to absorbance (PAR, PAR:Cu and PAR_2:Zn). Analysis only requires the input of three standard absorbance spectra at one concentration. This method is quite rugged as changes in the experimental conditions simply need to be accounted for using the standards. Comparison of results of the PAR assay using the Mulligan method and that described here reveal that while both methods are quite similar in terms of accuracy, more often the standard deviation is smaller for analyses using SpLab (Figure 2.13). A method that only uses two wavelengths is inherently prone to more errors that one that uses the entire absorption band for analysis and thus the increased precision observed in the PAR assay using the SpLab method would likely be more pronounced if there were any noise or greater uncertainty in absorbance values.

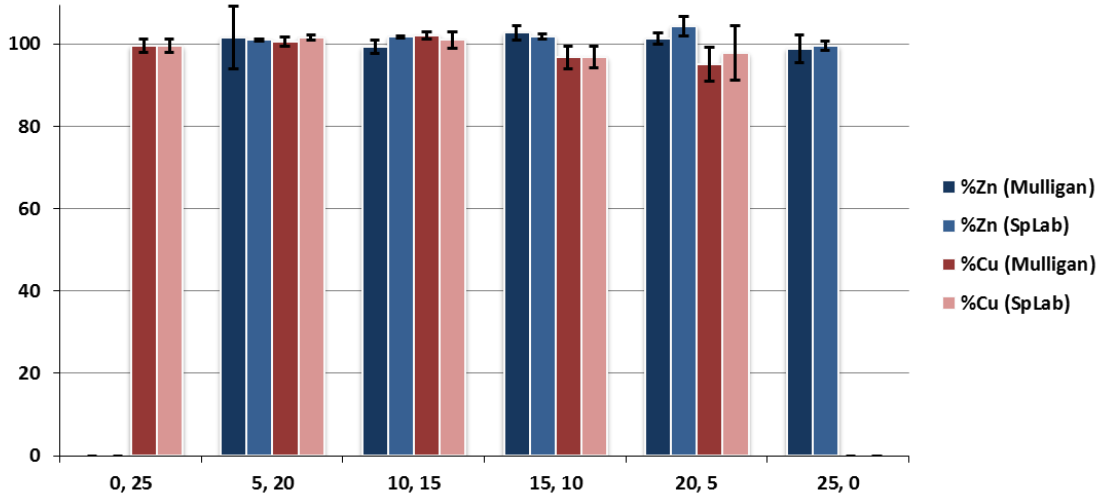

Figure 2.13 - Comparison of the accuracy and precision of metal quantitation using the PAR applying the Mulligan and SpLab methods. The concentrations of each metal (25 μM total) in solution are given on the x-axis as Zn, Cu (μM). Each calculated value represents the mean ± the deviation of two (Mulligan method) or three (SpLab method) independent experiments. All samples contained 100 μM PAR, 50 mM HEPES, 5.4 M GdnHCl, pH 8.2. The percent metal was calculated as ([calculated metal] / [actual metal])*100%. The average deviations are 2.62% and 1.80% for the Mulligan method and SpLab method, respectively.

The studies herein reveal three important points to consider for the use of PAR in the metal determination of proteins. (1) Avoid successive scanning of the protein as this will decrease the absorbance; instead let the protein unfold separately first. (2) Ensure that PAR is in at least 2.5 fold molar excess over the total metal present to avoid decreasing the PAR_2:Zn stoichiometry (*122*). (3) Be aware of the possibility of interfering substances that may spectroscopically silence metal ions. Overall, the results indicate that the use of PAR for the determination of Cu and Zn in solution is both accurate and useful for different applications.

Chapter 3

Local unfolding and conformational heterogeneity of holo SOD1

3.1 Introduction

3.1.1 Protein dynamics

The new view of protein folding occurring via parallel pathways along an energy landscape converging at the lowest energy conformation, or native state, can sometimes give the false impression that the native state of a protein is static. In reality, the native state generally consists of multiple microstates in equilibrium with one another. Each of these states may be close in energy to the lowest energy conformation but can have very different structures, due to diverse processes including the movement of secondary structural elements, changes in loop conformations and reorientation of side chains (*150*). The transition from ground to low populated excited states typically goes undetected using many standard techniques, however, recent advances in NMR spectroscopy have allowed for observation of these states (discussed further below) (*151, 152*). These transiently populated low-energy conformers may be important in function or pathology (*153, 154*).

Protein function is known to rely on the intricate relationship between sequence, structure, stability and flexibility. There is often a trade-off between protein stability and the flexibility required for function (*150*). This increased flexibility can be local or global. For example, the protein SlyD (sensitive to lysis D) is a protein folding helper enzyme that has two functional domains (*155*). The first domain acts as a peptidylprolyl isomerase and the second acts as a ubiquitous chaperone. The second domain has reduced stability compared to the first. It is believed that this is a consequence of its function and the requirement to accommodate a variety of different structures. Even so, the protein displays highly cooperative global unfolding and binding studies show that the stability of each domain is linked (*155*).

Thus, even proteins that show cooperative unfolding can have regions with different local stabilities which can be functional (described above) or pathogenic (see section 1.4.1).

Flexibility "hotspots" in proteins have been implicated as sites of protein aggregation (*150*), such as the M80 region in cytochrome *c* (*156*). The effects of mutations on the local and global stability of proteins are distinct, with even different mutations at the same position resulting in unique changes depending on the substituted residue. This phenomenon has been highlighted for a number of proteins, including position Y73 in acyl-coenzyme A binding protein (*157*) and position G93 in SOD1 (*82*). A complete understanding of the folding landscape, including folding intermediates, transition states, and high and low energy alternative states, is required to understand not only the relationship between mutation and protein stability, flexibility and function but also how protein dynamics may contribute to dysfunction and pathology.

3.1.2 NMR spectroscopy

Many advances in NMR spectroscopy, such as the development of multidimensional NMR methods and high field spectrometers, have made NMR a vital tool in the study of proteins at atomic resolution (*158*). One common use of NMR is the determination of high resolution three dimensional (3D) structures of biological molecules in solution. Other uses include measuring protein dynamics, protein-ligand interactions and temperature coefficients (*159-161*). The NMR experiment requires that the protein of interest be placed in a static magnetic field. The unique resonance frequencies of NMR active nuclei are detected (upon radiofrequency irradiation). Only nuclei with a non-zero spin quantum number have a magnetic dipole moment. The most commonly studied nuclei are of spin ½ such as ^{1}H, ^{13}C, ^{15}N and ^{31}P. The chemical shift, δ, is the difference between the absorption frequency of a given nucleus and a standard reference nucleus divided by the spectrometer frequency and is given in parts per million (ppm) (*158*).

In a one-dimensional (1D) NMR spectrum, chemical shift is plotted on the horizontal axis and the peak area is representative of the number of nuclei with the same chemical shift. One of the limitations of protein NMR is molecular size. The greater number of peaks and lower rotational correlation time associated with larger proteins will lead to peak overlap and line broadening , reducing sensitivity (*158*). One way to overcome this limitation is with multidimensional NMR experiments on high field spectrometers. In multidimensional NMR, cross peaks are observed between nuclei that are linked through bonds (J-coupling or correlation experiments) or are close in space (Nuclear Overhauser Effect experiments). Correlation experiments can be used to analyze through bond and through-space interactions between pairs of identical (homonuclear) or different (heteronuclear) nuclei. 3D experiments can further increase resolution by expanding a two dimensional (2D) spectrum into a third dimension allowing overlapping peaks to be separated into layers (*158*).

One of the most common 2D experiments is the $^{1}H,^{15}N$-heteronuclear single quantum correlation (HSQC) experiment, which provides the "fingerprint" of a protein (*158*). An HQSC experiment correlates protons to their covalently bonded nitrogen atoms producing a cross peak for each backbone amide, with the exception of proline. Cross peaks are also observed for the side chain NH groups of Trp and His, Asn, Gln, Arg and Lys. The HSQC experiment can be combined with a Nuclear Overhauser Effect experiment (NOESY) to separate the HSQC spectrum into a third dimension. Each plane of a NOESY-HSQC is a NOESY spectrum of amide protons attached to nitrogens which resonate at a particular frequency. Each cross peak in the NOESY spectrum represents protons within ~5 Å of the amide proton making this experiment very helpful for making sequence specific resonance assignments of ^{1}H-^{15}N cross peaks (*158*).

3.1.3 Temperature coefficients

The temperature dependence of chemical shift changes, known as the temperature coefficient, for an NMR active nucleus can be measured by acquiring spectra at a series of temperatures. Since chemical

shift values are sensitive to structural as well as environmental influences, monitoring the change in chemical shift with temperature can provide useful structural information at atomic resolution. The temperature dependence of amide protons was first described in 1969 (*162*) and since then much work has contributed to the understanding and interpretation of amide proton (N^1H) temperature coefficients (*160, 163, 164*). While great strides have been made in discerning the origins of N^1H temperature dependences; the contributing factors to ^{15}N and $C^{\alpha}H$ temperature coefficients still remain unclear (*165*).

Amide protons almost always show a negative temperature coefficient (normally falling within the range of -11 to 1 ppb/K) indicating the proton resonances shift upfield with increasing temperature (Figure 3.1) (*160*). Oshnini and Urry showed in 1969 that amide protons involved in intramolecular hydrogen bonds have more positive temperature coefficients indicating that their chemical shift is relatively less affected by temperature (*162*). It is suggested that the observed negative temperature coefficients of amide protons is a consequence of the downfield shift caused by hydrogen bonding (*163*). Upon heating, the magnitude of thermal fluctuations in solution becomes larger, causing the length of the hydrogen bond to increase. This weakens the hydrogen bond, reducing the associated downfield shift resulting in a negative temperature coefficient (upfield shifting resonance). It should be noted that almost all amide protons in a protein participate in hydrogen bonds; those that do not participate in an intramolecular hydrogen bond often hydrogen bond with bulk water (*166*). In the latter case, the hydrogen bond is weaker and thus the lengthening caused by temperature will be larger resulting in a more negative temperature coefficient (Figure 3.1).

The use of amide proton temperature coefficients for prediction of hydrogen bonds was initially analyzed for peptides (*167, 168*). The correlations between temperature coefficients and hydrogen bonding were poor however it was later proposed that the peptides, being less stable than globular proteins, were likely undergoing significant loss of secondary structure upon heating which influenced the temperature coefficients and reduced the correlation (*163, 164*). The reliability of temperature coefficients as hydrogen bond indicators in proteins was then investigated by analyzing the temperature coefficient of

793 amides protons from 14 different globular proteins in relation to hydrogen bonding determined from geometric criteria obtained from crystal and/or NMR structures (*160*). The observed correlations were much more convincing showing that if the temperature coefficient is more positive than -4.6 ppb/K there is an 85% probability that the amide participates in an intramolecular hydrogen bond (Figure 3.1). The reliability of predicting a hydrogen bond increases to 93% if the value is more positive than -4 ppb/K. It was found that 82% of all non-intramolecularly hydrogen bonded amides have temperature coefficients that fall between -5 and -11 ppb/K (Figure 3.1). Counterintuitively, amide protons participating in strong intramolecular hydrogen bonds have larger temperature coefficients than those in weaker intramolecular bonds (Figure 3.1). This is because amide chemical shifts are dependent on the inverse third power of hydrogen bond lengths (*160, 169*) and so increasing length has a larger effect on chemical shift for a shorter hydrogen bond. Nevertheless, in both cases the temperature coefficient will still most likely be more positive than -4.6 ppb/K. Overall, it appears that stable globular proteins provide a better system for using amide proton temperature coefficients to predict hydrogen bonds.

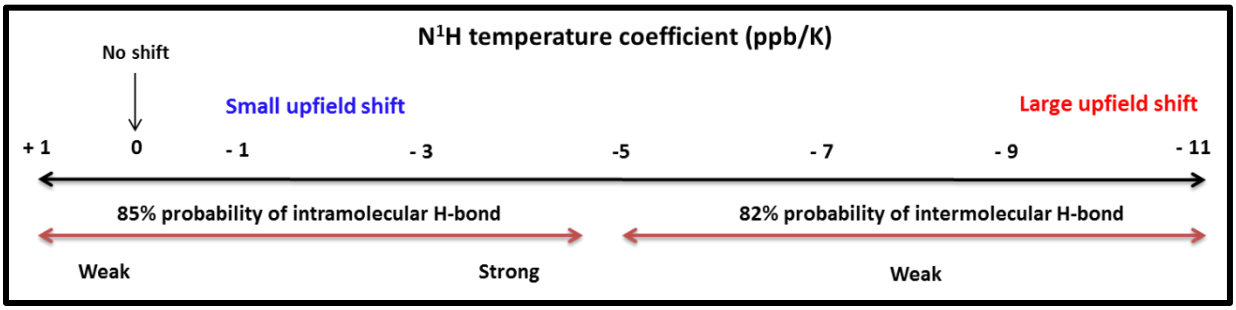

Figure 3.1 - Understanding N^1H temperature coefficients. A value more positive than -4.6 ppb/K (small upfield shift with temperature) indicates a high probability of an intramolecular hydrogen bond. Within this range a more positive value represents a weak intramolecular hydrogen bond and a more negative value represents a strong intramolecular hydrogen bond. A value more negative than -5 ppb/K (large upfield shift with temperature) indicates a high probability of a weak intermolecular hydrogen bond (with bulk water).

It should be noted that factors other than hydrogen bonding can also affect amide proton temperature coefficients. For example, the ring current of nearby aromatic side chains can deshield amide protons resulting in a temperature coefficient similar to that for a hydrogen bonded proton (*160*). In addition, secondary structure can influence the temperature coefficient, with amide protons in α-helices

showing coefficients approximately 1 ppb/K more negative than those in β-sheets. This is because amide protons in α-helices are less deshielded than in β-sheets (*170*). It has been shown that there is a weak correlation between amide proton temperature coefficients and amide exchange rates (*163, 171*). While both amide proton temperature coefficients and amide exchange rates are thought to be sensitive to hydrogen bonding status, the weak correlation could be due to different factors affecting the two methods. For example, amide exchange rates are very sensitive to both hydrogen bonding and surface exposure whereas temperature coefficients appear to be less sensitive to the surface exposure (*163*). Further, amide exchange rates are sensitive to pH while temperature coefficients do not appear to be affected unless the pH change induces conformational rearrangements in the protein (*160*).

Newer data reveal conflicting interpretations with regards to hydrogen bonding being the main determinant of amide proton temperature coefficients. NMR measurements of the third IgG-binding domain of protein G (GB3) show that amide proton temperature coefficients strongly correlate with the temperature coefficient of the through hydrogen bond J-coupling value (*172*), which provides a direct measure of amide proton hydrogen bonds (*173*) and has previously been used to study hydrogen bond expansion in ubiquitin (*174*). This suggests that the change in the strength of the hydrogen bond due to thermal expansion is the main contributor to the amide proton temperature coefficient. The authors propose that the temperature dependent shift between ordered and disordered states can also contribute to the observed coefficient, but to a lesser extent (*172*). In another study, the temperature coefficients of specific residues were studied at different pH values to probe the role of hydrogen bonding (*165*). Amide protons that hydrogen bond to carboxylate side chains are expected to participate in stronger hydrogen bonds above the pK_a of the carboxylate group. This should be reflected in the temperature coefficient of the amide proton however the correlation was poor. The authors concluded that the temperature dependence is determined mainly by local unfolding not the strength of the hydrogen bond (*165*). It was proposed that the tendency of amide protons participating in strong intramolecular hydrogen bonds to display larger temperature coefficients than those in weaker intramolecular hydrogen bonds is simply

because regions with strong hydrogen bonds are more structured, and thus the same fractional loss of structure will result in greater chemical shift changes when stronger hydrogen bonds are disrupted (*165*). In either case, whether the N^1H temperature coefficient is directly or indirectly related to the strength of a hydrogen bond, the value nevertheless provides useful information on hydrogen bonding and local structure in proteins.

The temperature coefficients of other nuclei, ^{15}N and $C^{\alpha 1}H$ for example, have been observed to be both positive and negative. The range of ^{15}N temperature coefficients is 2 times larger than that for amide protons, while the range of $C^{\alpha}H$ temperature coefficients is 2-3 times smaller (*163*). There does not appear to be any correlation between N^1H and $C^{\alpha 1}H$ temperature coefficients for the same residue, and only a very weak correlation between N^1H and ^{15}N coefficients. No clear relationship between ^{15}N temperature coefficients and structure has been found to date (*165*). Thus, temperature coefficients for N^1H remain the main resource for structural investigations of proteins.

3.1.4 Non-linear temperature dependence of N^1H

Chemical shift changes with temperature are commonly linear. This has been attributed to the thermal expansion coefficient of proteins being constant with temperature and thus any structural changes upon heating are linear (*163, 175*). Despite this fact, studies on a number of proteins have revealed that some amide protons do in fact show curved temperature dependences (*163, 176-180*). This curvature has been proposed to arise from the population of a low energy alternative state and therefore can report on the conformational heterogeneity of a protein (*180, 181*). This theory is supported by the high correlation observed between residues expected to be involved in an alternative conformation and those that show curved temperature dependences for the N-terminal domain of phosphoglycerate kinase, hen egg-white lysozyme and bovine pancreatic trypsin inhibitor (*180*).

The extent of curvature can provide useful information on a number of factors including the difference in free energy between the ground and excited state (discussed further in section 3.3.6.1) (*177,*

178). It is important to stress that lack of curvature does not necessarily mean that the amide proton does not access another state. It could be that the energy difference between the two states is simply too great or that the amide proton is in exchange with a large number of alternative states, both of which result in a linear temperature dependence (*180*). Thus, no conclusions can be made from lack of curvature. Interestingly, since temperature dependences can report on alternative states close in energy to the native state, it reports on conformations that may not be observed using amide exchange studies. It has been proposed that the high energy and likely extensive structural rearrangement required to allow water access into the protein interior make the conformations observed through amide exchange more like unfolding intermediates rather than alternative sates (*177, 180*).

Conformational heterogeneity within proteins has been suggested to arise from a variety of factors including alternative hydrogen bonding networks possibly due to buried water molecules, structural instability, disulphide bond isomerization, disruption of loops and loss or extension of secondary structural elements (*180*). Previous studies reveal that the proportion of N^1Hs displaying curved temperature dependences in proteins can range from, but by no means is limited to, 5 – 40% (*163, 176-180*). These residues are often spread throughout the polypeptide chain clustering at the ends of secondary structural elements and in loops (*178, 180*). A comparative study analyzing the streptococcal IgG binding B1 domain of proteins G and L showed that residues accessing alternative states do so independently based solely on local stability (*176*). The energy barrier for the local folding from the excited state back to the ground state was determined is most cases to be less than 1.5 kcal/mol. Further, analysis of the folding pathways of these two proteins reveals that their folding transition states have distinct structural differences. Interestingly, on closer inspection, residues displaying curvature were concentrated in regions unstructured in the transition state in both cases (*176*). Characterization of curved N^1H temperature dependences of non-myristoylated and myristoylated neuronal calcium sensor-1 (NCS-1) revealed that myristolation increases the number of residues accessing alternative states (*178*). Further, it was found that the distribution of residues populating alternative conformations in the Ca^{2+}-binding

loops myristoylated and non-myristoylated NCS-1 quite different which could explain, in part, the differences in their Ca^{2+} binding affinities (*178*). The identification of low energy alternative states can therefore be useful in the understanding the dynamics of the native state, folding pathways and local stability.

A very interesting study on horse cytochrome *c* found that at least 25% of residues access an alternative state under equilibrium conditions (*177*). These residues cluster in the most destabilized region of the protein expected to unfold first based on previous folding studies. In contrast, the most stable region expected to fold first and unfold last show very few amide protons with curved temperature dependences. Based on simulations, the author proposed that the residue displaying curvature is at the middle of a five consecutive amino acid cooperative unit populating a higher energy state. The results show that cytochrome c has many local alternative states that are less structured and again accessed independently. It was suggested that these alternative states may be the earliest cooperative units of unfolding with the unfolding pathway beginning from local breathing motions converging to create low energy alternative states, as identified by N^1H temperature dependences, merging to create higher energy states, such as those identified by amide exchange studies, which finally merge resulting in global unfolding (*177*). This model suggests that there may be many competing unfolding pathways involved in global denaturation.

3.1.5 Previous studies on the dynamics/conformational heterogeneity of SOD1

NMR relaxation experiments can provide information on the dynamics of a protein from the picosecond to millisecond time scale. These experiments were employed to monitor the dynamic properties of holo SOD1, showing that this very stable protein has a rigid structure (*182*). The most flexible loop is loop I, with most of the mobility being observed for Gly12. All 8 β-strands in the holo dimer show comparable flexibility. Relaxation rates suggest the occurrence of conformational exchange processes in the dimer (*182*). Of the residues showing this conformational heterogeneity, over half are

found in β-strands providing evidence for the existence of breathing motions in the holo dimer. This type of dynamic behaviour in β sheets has been proposed for other proteins (*183, 184*). Residues showing conformational exchange also appear to cluster close to Cys57 and Cys146 indicating that isomerization of the intramolecular disulfide bond may also contribute to the conformational heterogeneity in SOD1 (*182*).

The dynamics of monomeric holo SOD1 were also studied using a monomer variant containing three mutations (F50E, G51E, E133Q) that disrupt the dimer interface (*182*). The global fold of this variant is essentially the same as a single subunit of holo SOD1 however it should be noted that this variant is a model and may not behave exactly the same as the native monomer (*185*). Even in the monomeric state, holo SOD1 is fairly rigid. The residues that would normally make up the dimer interface have greater mobility in the monomeric variant, as expected. Notably, residues 76-86 and 88-95, which are far from the dimer interface, show altered mobility in the dimer compared to the monomer (Figure 3.2), highlighting propagating structural effects within the monomer (*182*). In addition, the dimer has increased flexibility at residues 131-142 (Figure 3.2) which are part of the active site channel and neighbour the catalytically important Arg143 (*186*). The authors proposed that increased flexibility in this region in the dimer may play a role in driving the superoxide anion toward the active site (*185*). Different fALS mutations show further increased flexibility in this region (*123, 187*) which on the other hand could allow non-native substrate access and lead to aberrant enzymatic reactions. It appears that the breathing motions observed in the dimer are hampered in the monomer, suggesting that joint motions of the two subunits may be involved in the breathing process (*182*). MD simulations indicated that these breathing motions are also hampered in mutants even in the dimeric state (*104*). The authors propose that these breathing motions allow for the release of excess energy and that without this ability energy perturbations may be more likely to result in local unfolding. This increased strain within mutant SOD1 favouring local unfolding may lead to the solvent exposure of aggregation-prone structural elements.

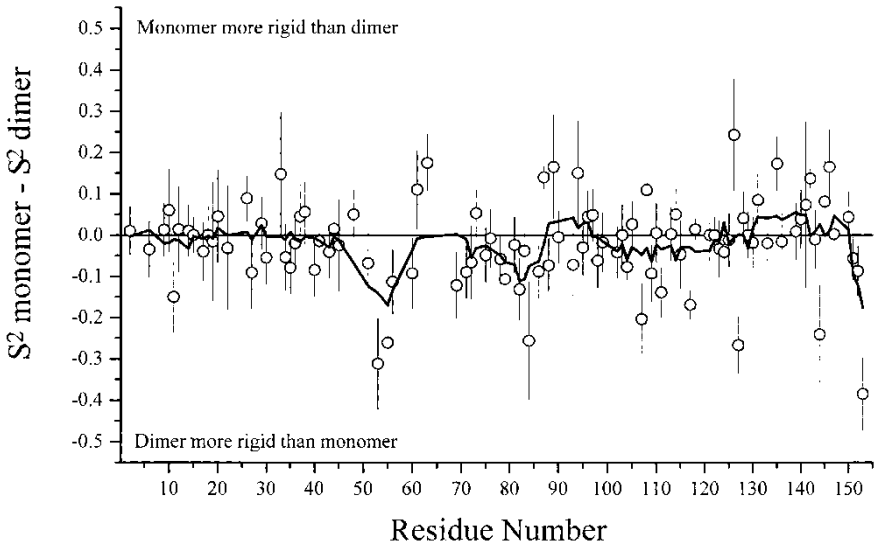

Figure 3.2 - Differences between the S^2 values of the monomer variant and dimeric holo SOD1. The S^2 value is the square of the generalized order parameter characterizing the amplitude of internal motions. Only residues where the S2 value was determined for both forms are included (represented as open circles). The thin black lines show the uncertainty of the differences. The thick black line represents a smoothing of the data by averaging over five adjacent points (centred at the point of interest). Figure taken from Banci *et al*., 2000 (*182*).

NMR relaxation experiments were also employed to analyze the dynamic properties of the fALS mutant G93A (*95*). The results show that holo G93A exhibits higher mobility than WT and significant chemical shift and Nuclear Overhauser effect (NOE) differences in loops III and V. These regions make up the β-barrel plug, a key stabilizing element in SOD1 (*58, 78, 188*). The increased mobility and lack of observed NOEs indicate deprotection of edge strands and an opening of the β-barrel, which could lead to edge-to-edge aggregation (see section 1.6.6). The most flexible β-strand in G93A is the charged edge strand β6 (*95*). Compared to WT, G93A has increased mobility at ~25% of residues throughout the structure again indicating that the mutation has propagating effects. Computational work also points to increased flexibility compared to WT as a general consequence of mutation, with mutants G37R, A4V, and H46R having increased mobility at 64%, 62%, and 53% of residues, respectively (*104*). It should be noted however, that while the G93A mutation appears to increase dynamics on both a local and global scale, there are also regions of the mutant, such as residues 76-84 near the zinc binding site, that are more rigid compared to WT (*95*). A similar trend has been observed computationally for A4V and H46R, which also display decreased flexibility in this region (res 70-80) (*104*). Therefore it appears that often

both increases and decreases in mobility are observed experimentally and computationally upon mutation of SOD1, as has been reported for other proteins (*108, 161*).

Amide exchange studies on holo SOD1 confirm the results of the relaxation experiments identifying a fairly rigid structure (*189*). The majority of amide protons in β-strands exhibit slow exchange with the exception of those at the β3–β6 and β5–β6 interfaces, again indicating increased dynamics at the edge strands. Amide exchange measurements on G93A show localized destabilization surrounding the mutation site, specifically in the β-barrel plug (*189*). The authors also report propagating destabilization of the metal binding site, which is interesting as a number of these residues fall in the region described above to be stabilized in mutants in the apo state (res 70-84). Therefore the results reveal altered behaviours in the metal binding region of SOD1 in apo and holo states. The results did not reveal any changes in the dimer interface which is intriguing as it has been proposed that mutations, regardless of the site, have propagating destabilizing effects on the dimer interface (*104, 189*). As seen in the NMR relaxation experiments, regions with increased amide protection in the mutants were observed (*189*). Amide exchange studies of apo A4V also show altered dynamics in the β-barrel plug (*51*). This is surprising as the A4V mutation is in the dimer interface far from the β-barrel plug indicating the presence of propagating structural effects. MD simulations confirm these results for A4V, and show the same for H46R and G37R (*104*). Thus, the β-barrel plug may represent a common region of destabilization among mutants, while the mutation effects on the dimer interface are more variable. Notably, the β-barrel plug is also 1 of 4 segments of SOD1 predicted to have a high aggregation propensity (*190*).

Another technique that allows for the determination of short-lived, weakly populated, excited states is the Carr-Purcell-Meiboom-Gill (CPMG) ^{15}N nuclear spin relaxation experiment (*191, 192*). This method was used to study the conformational heterogeneity of the monomeric apo SOD1 variant (*193*). These experiments provide information on the exchange rate between the native and the excited states, the relative populations and the chemical shift for each state. Regions of the protein perturbed in the excited state include loops IV, VI and VII, as well as β4, β5, β7, β8, which together make up the C-terminal β-

sheet. This sheet has been shown to be more dynamic in the apo state via previous computational work (*49*). Additionally, three mutants were studied using CPMG (A4V, G85R and D90A) revealing similar residues accessing alternative conformations however these residues showed enhanced structural distortion in the excited state and in some cases decreased kinetic barriers between the two states (*193*). The mutations altered local dynamics, with A4V showing increased conformational heterogeneity in β1 and G85R and D90A in the β-barrel plug. Overall, the authors conclude that the excited state, being common to all 4 variants and unstructured likely exposing hydrophobic side chains, may be the state responsible for non-native assembly. The conformational heterogeneity of zinc-bound SOD1 was also analyzed. Zinc binding confers a great deal of stability and the results reveal that this state does not undergo large scale conformational exchange however there is evidence for slow conformational exchange between states with small structural changes (*193*).

Taken together, the above-described experimental and computational studies show that holo SOD1 has a fairly rigid structure; however, there is a degree of conformational heterogeneity attributed to breathing motions. These breathing motions are reduced in the holo monomer indicating that concerted communication between the two subunits is involved in the process. Propagating structural effects upon monomerization and mutation are evidenced by alterations in the flexibility of residues far from the dimer interface and site of mutation, respectively. A number of mutations, studied by a variety of biophysical and computational methods, exhibit altered dynamics in the β-barrel plug, indicating a common pattern of destabilization. Further, residues that access alternative conformations in the apo monomer appear to correlate well with regions of decreased stability based on MD simulations, which has been reported for other proteins as well (*177*). It remains unknown whether residues accessing alternative states will follow the same pattern for other, more mature forms of the protein.

3.1.6 Chapter Overview

With the dimeric nature of SOD1 and the number of post-translational modifications the protein undergoes there are over 44 different states in which the protein can exist (*98*). Thus, it is important to focus on those states which are believed to be physiologically relevant. Holo SOD1 is often overlooked due to its high stability and resistance to denaturation. However, due to recent mounting evidence that local unfolding may play a role in protein aggregation and disease (see sections 1.4.1 and 1.6.6), holo SOD1 cannot be ruled out. Further, since the most mature state is the major form present in cells (*54*), understanding of altered processes in the holo state of mutants may provide information on the initial stages of protein aggregation.

The determination of N^1H and ^{15}N temperature coefficients has not been reported for any form of SOD1. The determination of low energy alternative states has been studied using CPMG experiments on the apo and zinc-bound monomer construct at 18°C, 25°C and 32°C (discussed above) but have not been described for the holo form. The identification of alternative states through non-linear temperature dependences has not been applied to any form of SOD1 to my knowledge. This chapter will describe the determination of N^1H and ^{15}N temperature coefficients, as well as the characterization of residues accessing low free energy alternative states, for holo-pWT SOD1 by acquiring 2D NMR spectra at a series of temperatures. The same studies are also carried out here for the ALS-mutants G93A, E100G and V148I in order to assess the differences in structure, dynamics, local stability and conformational heterogeneity caused by single site mutations, and the possible implications for protein aggregation. These mutants were chosen based on their differences in stability, aggregation propensity, site of mutation and change in net negative charge, highlighted in Table 3.1.

Mutant	Location of Mutation	Aggregation Propensity	Change in Net Negative Charge	Disease Duration (years)	Holo T_m (°C)	Holo ΔT_m (°C)
WT	n/a	n/a	n/a	n/a	96.3	n/a
G93A	Loop V (β-plug)	High	No Change	3.1	92.5	-3.8
E100G	β6 (edge strand)	High	Reduced	4.7	91.1	-5.2
V148I	β8 (dimer interface)	Low	No Change	1.7	97.0	+0.7

Table 3.1 – Summary of Mutant Characteristics. Aggregation propensities obtained from Prudencio et al., 2009 (*194*). Stability data obtained from DSC simulations at 30 mg/mL (see section 3.3.2). Disease durations obtained from Wang et al. 2008 (*80*).

3.1.7 Acknowledgements

I would like to thank Jan Venne, Michael Piazza and Dr. Thorsten Dieckmann for their assistance with NMR experiments. I would like to thank Joe Gaspar for his help with NMR processing and Dr. Jessica Rumfeldt for her help with protein expression and purification.

3.2 Methods

3.2.1 Expression and purification of labeled proteins

SOD1 variants were expressed in the *E. coli* strain BL21. The expression vector pHSOD1ASlacI^q contains the *sod1* gene (human cytosolic CuZnSOD) and a leader sequence from *Photobacterium leiognathi* which directs the translated protein to the periplasm. The expression vector contains the lac repressor and the tacI promoter, and an ampicillin resistance marker gene. Transformation was carried out by electroporation as previously described (*195*). To summarize, BL21 cells were prepared through the removal of salt (media) from 1 L of mid to log-phase culture through three centrifugation steps at 4000 x g. After each step the cells were resuspended in 1 L, 0.5 L, and 0.25 L of 10% glycerol, respectively. This was done to increase the resistance (5000 Ω) of the sample.

Approximately 1 μg of vector DNA was added to 40 μL of cells, mixed well and added to an electroporation cuvette (0.1 cm gap; BioRad Laboratories, Inc., Hercules, CA.). The DNA/cell mixture

was subjected to a high electric field (1.8 kV for ~1 s; Eppendorf Eporator, Eppendorf, Hamburg, Germany). The cells were immediately placed in 1 mL liquid medium (0.4% (w/v) glucose, 20.0 g tryptone, 5.0 g yeast extract, 0.5 g NaCl, 0.01 M $MgSO_4$, per litre) and incubated for ~ 1 hour at 37°C. The cells were then centrifuged and plated on Luria Broth (LB) agar containing ampicillin (100 µg/L) and incubated overnight at 37°C. Individual colonies were picked and grown in an overnight LB culture containing LB culture with ampicillin (100 µg/L). The overnight culture was diluted 1:100 into 1L of M9 minimal media (Na_2HPO_4 (6 g/L), KH_2PO_4 (3 g/L), NaCl (0.5 g/L), $^{15}NH_4Cl$ (0.5 g/L), $MgSO_4$ (2mM), glucose (4 g/L), thiamine (0.0005 g/L), $CaCl_2$ (0.1 mM)) with ampicillin (100 µg/L). Cultures were grown at 25°C with shaking (220 rpm) for ~10 hours until an optical density of ~0.6 absorbance units at 600 nm was reached. Protein expression was induced with isopropyethiogalactoside (IPTG, 0.5 mM final concentration). $CuSO_4$ (0.1 mM final concentration) and $ZnSO_4$ (0.05 mM final concentration) were added at induction. Cells were grown at 25°C for ~36 hours. Cells were harvested by centrifugation (4500 x g for 20 min) and were stored at -80°C before performing osmotic shock.

Osmotic shock was completed to release SOD1 from the *E. coli* periplasm as described previously (*146*). Briefly, cells were resuspended in 10 mM ice-cold Tris-HCl buffer (50 mL for pelleted cells from 1L of culture) containing EDTA (15 mM final concentration) and sucrose (20% (w/v) final concentration). Cells were gently agitated on ice for 20 minutes and pelleted by centrifugation at 4000 x g for 30 minutes. The cell pellet was resuspended in ice-cold deionized milliQ (Millipore Ltd., Bedford, MA) water (20 mL for cells pelleted from 1L of culture). Cells were again agitated on ice for 20 minutes and centrifuged at 4500 x g for 45 minutes. The soluble periplasmic fraction containing SOD1 was flash frozen in liquid nitrogen and stored at -80°C until further purification.

Hydrophobic interaction chromatography was used to separate SOD1 from native *E. coli* periplasmic proteins. The soluble fraction from osmotic shock was diluted to ~0.8 mg/mL total protein in 20 mM Tris-HCl, pH 7.0 and heated to 70°C in the presence of $CuSO_4$ (1.4 mM final concentration) to ensure full copper insertion into the active site. The heating also acts as a purification step since few

proteins are stable at this temperature. After heating, the precipitated protein is separated by centrifugation (10 000 x g for 20 minutes) and $(NH_4)_2SO_4$ was added to the supernatant (3 M final concentration). All buffers were filtered through a 0.2 micron low protein binding filter and degassed for ~20 minutes prior to chromatography. The protein in $(NH_4)_2SO_4$ was loaded onto a Waters column (2.2 cm diameter x 10 cm length; Waters Corporation, Mississauga, ON) packed with Poros 20 micron HP2 (polystyrene-divinylbenzene) hydrophobic interaction chromatography media. SOD1 was eluted using an ammonium sulphate (3M $(NH_4)_2SO_4$ in 20 mM Tris-HCl, pH 8) to buffer (20 mM Tris-HCL pH 8) gradient (65% to 35% 3M ammonium sulphate over 4 column volumes). Fractions containing SOD1 were pooled and dialyzed against milliQ water using dialysis tubing (Spectra/Por 6-8,000 Da cutoff membrane, regenerated cellulose membrane; Millipore, Ltd, Bedford, MA). The holo SOD1 was concentrated to ~6 mg/mL using an Amicon ultrafiltration device using a 10 000 Da cutoff membrane (Amicon ultrafiltration regenerated cellulose membrane, Millipore, Ltd, Bedford, MA). Aliquots of the protein were added to 1.5 mL Eppendorf tubes and flash frozen in liquid nitrogen and stored at -80°C.

The purity of SOD1 was >95% as determined by sodium dodecyl sulfate polyacrylamide gel electrophoresis (SDS-PAGE). Metal content was determined qualitatively from the NMR spectrum. For NMR experiments purified ^{15}N-labeled pWT or mutant SOD1 was exchanged into buffer (20 mM Hepes, pH 7.8; four 1:8 dilutions) using a Millipore centrifuge tube (Ultracel 3K, Millipore Ireland, Ltd.) to a final concentration of ~30 mg/mL and a final volume of ~450 µL. The copper was reduced by addition of 5 mM sodium isoascorbate. Reduction to Cu^{1+} avoids paramagnetic ling broadening caused by Cu^{2+}. After the addition of D_2O (37.5 µL) the sample was transferred to a 5 mm NMR tube.

3.2.2 NMR experiments

NMR experiments for three variants (pWT, G93A and E100G) were carried out on a Bruker Avance spectrometer operating at 600 MHz with a triple-resonance (TXI) 5 mm probe with pulse field gradients along the x, y and z-axes (Bruker, Billerica, MA, USA). The set temperature was varied from

25°C to 75°C at 10°C increments. The actual sample temperature was verified using a standard curve provided by Bruker (T= (4.218 -Δ)/0.009132) based on chemical shift separation of resonances in 80% ethylene glycol (DMSO-d6) and a thermocouple. The actual sample temperatures ranged from 24 - 84°C at ~12°C increments. Chemical shifts were referenced according to the internal spectrometry frequency calibrations. NMR data were processed using the Bruker software and analyzed using computer aided resonance assignment software (CARA) (*196*). For 2D heteronuclear experiments ^{15}N decoupling during acquisition was achieved using the GARP sequence (Shaka et al., 1985 jess). Water suppression was achieved using gradients until a set temperature of 55°C (actual sample temperature 61.5°C) (see A2.1 for pulse program). Above this temperature, water suppression was achieved using presaturation (see A2.2 for pulse program). Two-dimensional ^{1}H-^{15}N HSQC spectra were acquired using INEPT magnetization transfers (*197*).

NMR experiments for V148I were carried out on a Bruker Avance spectrometer operating at 500 MHz with a triple-resonance (TXI) 5 mm probe with pulse field gradients along the z-axis (Bruker, Billerica, MA, USA). The set temperature was varied from 25°C to 80°C at 5°C increments. The actual sample temperature was verified as described above and ranged from 24.5°C to 87.5°C at ~5.7°C increments. Spectra were acquired as described above with the exception that water suppression was achieved with a single z-gradient at all temperatures (see A2.3 for pulse program). A three-dimensional ^{15}N-NOESY-HSQC spectrum (see A2.4 for pulse program) of V148I was collected on the spectrometer operating at 600 MHz (as described above) with a mixing time of 125ms. The total time for the experiment was approximately 3 days.

3.2.3 Resonance assignments

Sequence specific resonance assignments were determined previously for pWT SOD1 and the mutants G93A and E100G at 25 °C, pH 7.8 (*6*). Resonance assignments for V148I were made in a similar way as for G93A and E100G by a ^{15}N-NOESY-HSQC experiment at 25°C, pH 7.8. NOE cross peaks

were used to assign the peaks that shifted upon mutation and confirm the assignment of those that did not shift. The uncertainties in N^1H and ^{15}N chemical shifts estimated as 0.005 and 0.03 ppm, respectively, by comparing chemical shift values of two independent experiments under the same conditions,

3.2.4 Temperature dependence of ^1H-^{15}N crosspeaks of holo SOD1s

NMR samples of pWT and mutant dimeric holo SOD1 (final concentration ~30 mg/mL) in D_2O were equilibrated at each temperature for a minimum of 20 minutes. Each spectrum took approximately 20 minutes with 8 scans. All peaks in the spectra were picked manually and the chemical shifts at each temperature were recorded. For each spectrum the N^1H chemical shifts were referenced to water, the resonance of which was independently determined at each temperature. The chemical shift of water has a strong temperature dependence of approximately -10.3 ppb/K (*198*)**.** For spectra acquired on the 600 MHz spectrometer, the resonance of water shifted linearly downfield with temperature by ~0.31 ppb/K. A water correction of -10.7 ppb/K was applied to the determined slopes (see below) to account for this downfield shift and the true temperature dependence of water. For spectra obtained on the 500 MHz spectrometer the resonance of water varied non-linearly with temperature. The chemical shift values were therefore referenced after acquisition so that the resonance of water was set to the same value of 4.69 ppm at each temperature. A water correction of -10.39 ppb/K was then applied. For each residue, the N^1H and ^{15}N chemical shifts were plotted as a function of temperature and fit to a straight line. The slope of this line represents the temperature coefficient, commonly given in ppb/K. Deviations from linearity (residuals) were calculated by subtracting the observed chemical shift from the straight line. Residuals were plotted against temperature and fit to a quadratic equation:

$$y = ax^2 + bx + c \qquad \text{Eq. 3.1}$$

The quadratic coefficient, *a*, provides a measure of the magnitude of curvature. The residuals for each residue were also examined visually for curvature. Simulations of experimental curvature were calculated

using Equation 3.5 as described in section 3.3.6.1, with individual parameters varied systematically (see figure legend for a full description).

3.3 Results

3.3.1 Backbone amide resonance assignments

Resonance assignments were previously obtained for pWT at pH 7.8, 25°C with 135 of the 148 non-proline backbone amides assigned (*6*). Due to peak overlap, only 117 were sufficiently well resolved to be followed with confidence with increasing temperature. A similar number of amides were definitively assigned and followed in G93A (128 amides) and E100G (108 amides). The spectrum of V148I at pH 7.8, 25°C has not previously been assigned. A NOESY-HSQC experiment was used to make assignments. Again 117 residues were adequately resolved to be assigned and followed with increasing temperature.

The $^{1}H,^{15}N$-HSQC spectra of mutants G93A, E100G and V148I are very similar to that of pWT. The effect of mutation on the chemical shift of each backbone amide at 24°C is illustrated in Figure 3.3 using the weighted average difference ($\Delta_{avg}HN$) in chemical shift between pWT and mutant.

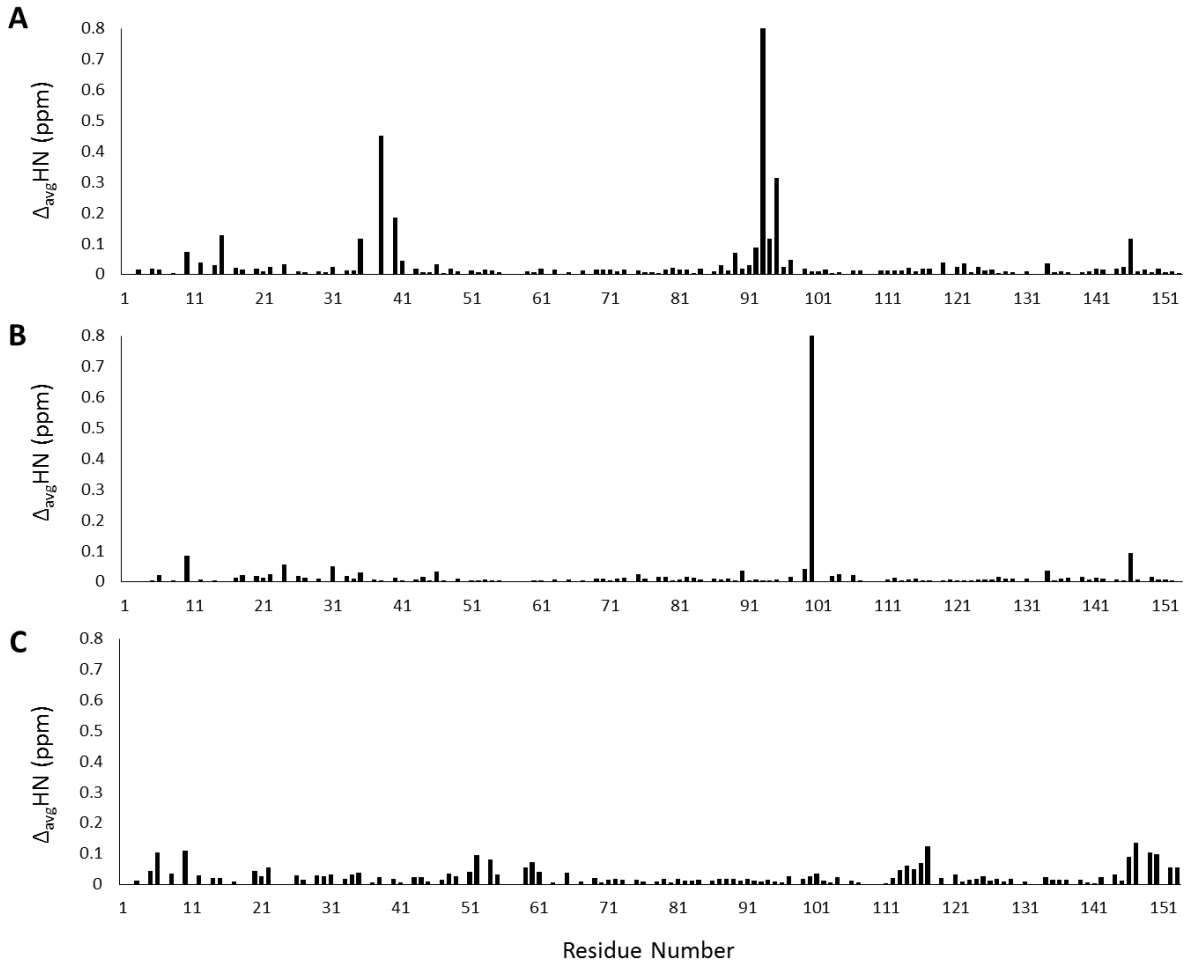

Figure 3.3 - Changes in chemical shift between pWT and mutants at pH 7.8, 24°C. (A) G93A (B) E100G and (C) V148I. Chemical shift changes, Δ_{avg}HN, are calculated as $[\{(\Delta N^1H)^2 + (\Delta^{15}N/5)^2)\}/2]^{1/2}$ and shown as vertical black bars. Shown off scale for G93A is residue 93 at 1.0 ppm, and for E100G residue 100 at 1.6 ppm.

Backbone amides with significant changes in electronic environment or conformation compared to pWT are for the most part in close to proximity to the mutation site. Residues with significant chemical shift changes are mapped onto the 3D ribbon structure (Figure 3.4). Predominantly, residues displaying the largest differences cluster near the site of the mutation with residues showing smaller changes propagating throughout the structure. There are 20 residues in G93A with significantly altered shifts (Δ_{avg}HN > 0.3) compared to pWT, 8 of which with Δ_{avg}HN > 1. This mutation is at a highly conserved site in loop V. E100G has the least variation with only 9 amides showing changes greater than 0.3 ppm, and the mutated residue being the only site with Δ_{avg}HN > 1. This is noteworthy as E100G is the most

destabilized of the three mutants studied. The site of the mutation is highly exposed on the monomer surface, far from the dimer interface. V148I is the most affected, with 32 amides significantly altered, 5 of which display $\Delta_{avg}HN > 1$. Residue 148 is located in the dimer interface, a region shown to have high connectivity with distal regions of the protein (*104*), and so it is perhaps not surprising that a mutation in this region results in increased propagating effects throughout the protein.

In all three mutants, two residues have consistently altered shifts: Cys 146 ($\Delta_{avg}HN \geq 0.9$) and Gly10 ($\Delta_{avg}HN \geq 0.7$). Cys146 is located in β8 close to the dimer interface and participates in an intermolecular disulfide bond that contributes to the stability of SOD1. It has been proposed that mutations predispose SOD1 to more easily undergo disulphide reduction (*199*). Gly10 is located in loop I. The amide proton of Lys9 participates in a hydrogen bond with the oxygen of Cys146. The chemical shift of Gly10 could be affected by an altered interaction between these two residues. While the observed structural changes around Cys146 in all three mutant cannot confirm that mutants are more prone to disulphide reduction it is an interesting result.

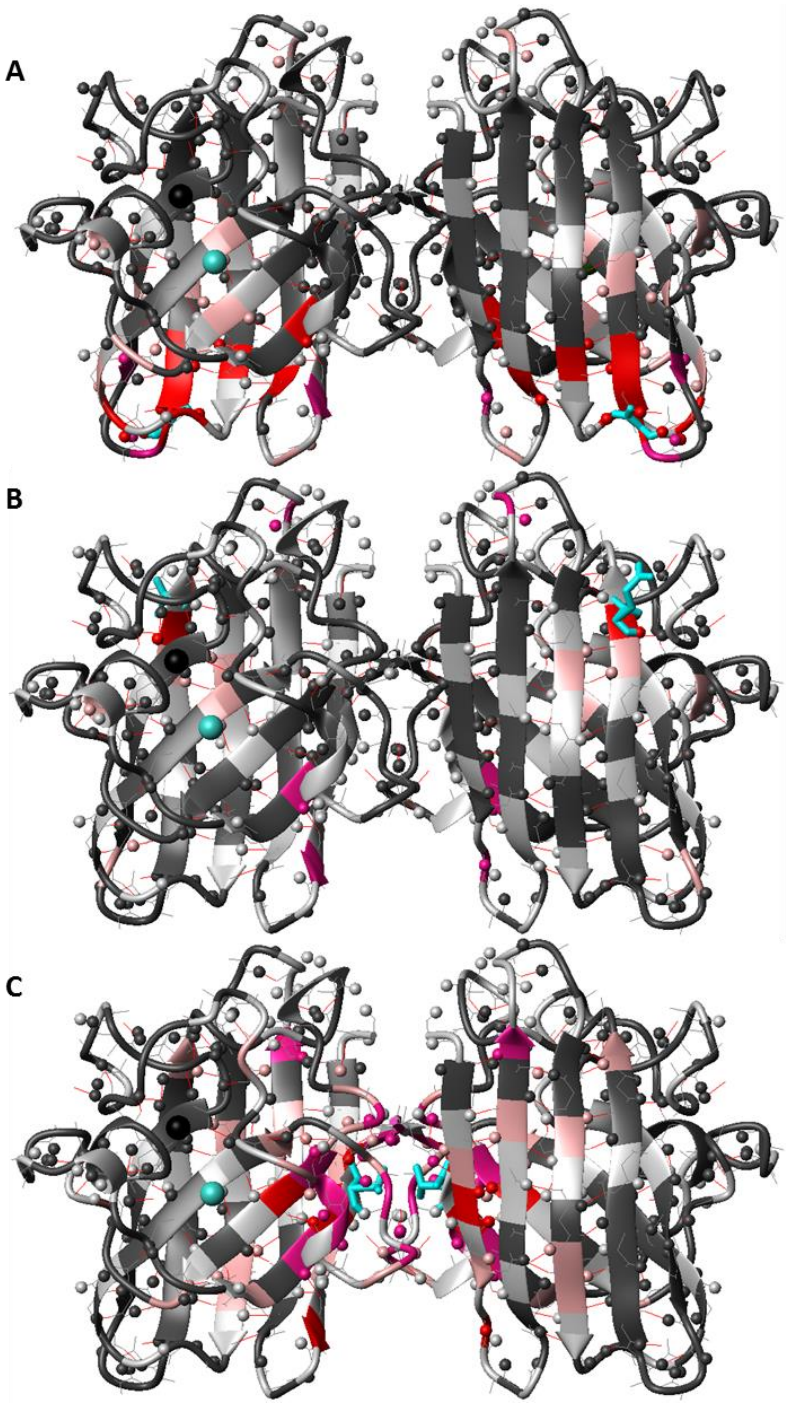

Figure 3.4 - Ribbon diagram of pWT SOD1 indicating significant chemical shift changes (Δ_{avg}HN > 0.3) caused by mutations at 24°C (A) G93A (B) E100G and (C) V148I. The main chain of the mutation site is coloured cyan. Pink is used to highlight residues with Δ_{avg}HN between 0.3 - 0.7. Deep pink is used to highlight residues with Δ_{avg}HN between 0.7 – 1. Red is used to highlight residues with Δ_{avg}HN > 1. Dark grey is used to highlight residues with no significant change (Δ_{avg}HN < 0.3). Light grey is used to highlight residues where no data is available. Bound copper (turquoise) and zinc (black) are represented as spheres. The ribbon diagram was generated using MOLMOL (*61*) and PDB file 1SOS (*62*).

3.3.2 DSC simulations

DSC allows for direct measurement of the heat associated with intra- and inter-molecular interactions in solution as a function of temperature providing information on the energetics (*ΔG*, *ΔH*, *ΔS*, etc.) of protein folding. The energetics of oligomeric protein folding are further complicated by the added step of protein association (*81*). For oligomeric proteins displaying 2-state behaviour, as is the case of SOD1 (see section 1.6.5.), the temperature where half of the protein is unfolded (T_m) is protein concentration dependent. Previous DSC analyses in the Meiering lab on holo pWT and mutants have been carried out at concentrations ranging from 0.1 – 5 mg/mL. In order to model the global stability of pWT, G93A, E100G and V148I under the conditions used in this study (~30 mg/mL), simulations of the unfolding energetics for each variant at the desired concentration were carried out (Figure 3.5; See the figure legend for thermodynamic parameters used). For pWT, G93A, E100G and V148I the T_m was found to be 96.3°C, 92.5°C, 91.1°C and 97.0°C, respectively (*6, 82*) (unpublished). Interestingly, the disease causing mutant V148I is more stable than pWT, again suggesting that global stability may not be the main determinant of protein aggregation, which has also been proposed for pathogenic lysozyme mutations (*34*). The simulations show that the fraction of globally unfolded protein at the highest temperature studied for the most destabilized mutant (E100G) is ~3%. One can therefore conclude that observed chemical shift changes in the NMR experiments are essentially exclusively caused by local and not global unfolding.

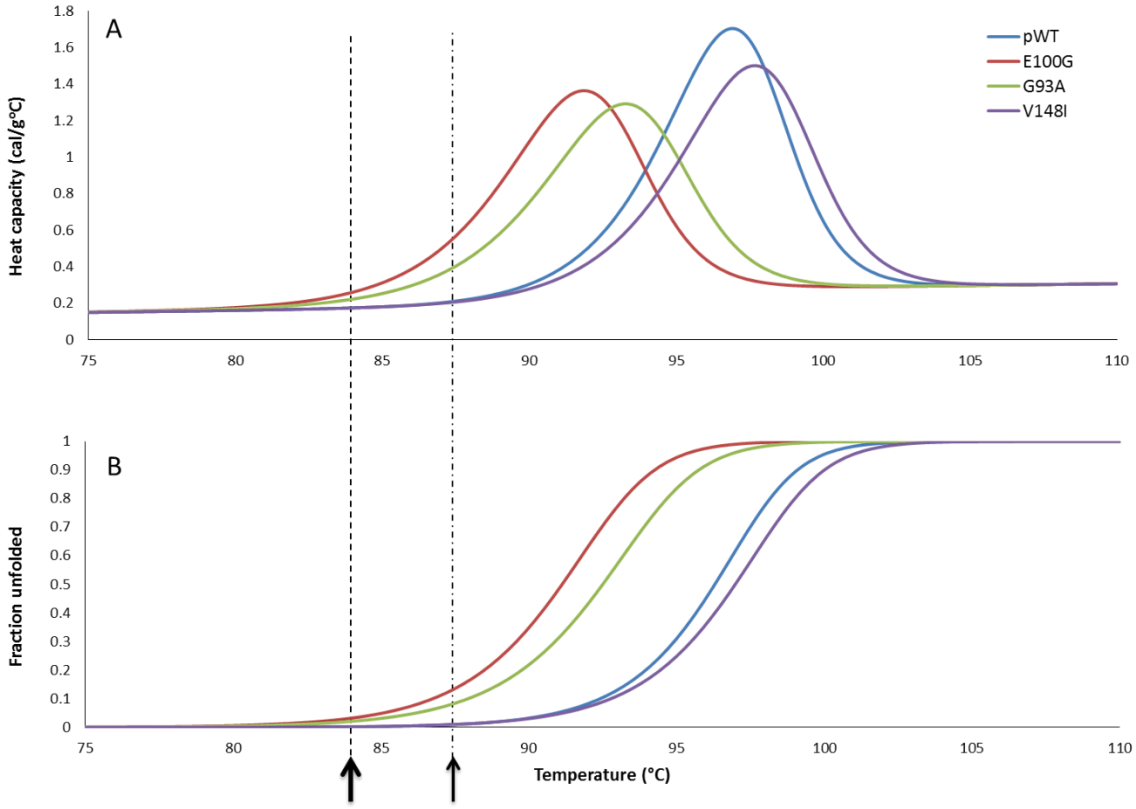

Figure 3.5 - Thermal denaturation of holo SOD simulated for 30 mg/mL protein. (A) $C_{p,total}$ vs. temperature. Thermal denaturation of holo pWT (*82*), G93A (*82*) and E100G (*6*) has been shown to fittable by a 2-state transition between folded dimer and 2 unfolded metal bound monomers, $N_2 \leftrightarrow 2U$ (between 0.1 and ~4 mg/mL). 2-state behaviour has not been confirmed for V148I due to lack of data but was assumed. Simulations were performed using equations 1-12 (*81*). In these simulations the reference temperature (T_{ref}) was defined as the temperature where the protein is half unfolded (T_m). The T_m and ΔH_{Tm} were interpolated for 0.5 mg/mL using data ranging from 0.1 to at least 2 mg/mL. For pWT T_m = 92.1°C, ΔH_{ref} = 256.3 kcal (mol dimer)$^{-1.}$ For E100G T_m = 86.4°C, ΔH_{ref} = 219.4 kcal (mol dimer)$^{-1}$. For G93A T_m = 87.6°C, ΔH_{ref} = 211.7 kcal (mol dimer)$^{-1}$. For V148I T_m = 92.5°C, ΔH_{ref} = 236.6 kcal (mol dimer)$^{-1}$. The ΔC_p = 2.75 kcal (mol dimer)$^{-1}$ °C^{-1} previously determined for holo pWT (*82*). (B) The fraction of unfolded protein vs. temperature. The thick black arrow and dashed line represents the highest temperature NMR spectrum recorded for pWT, G93A and E100G. The thin arrow and dash-dotted line represents the highest temperature acquired for V148I. The fraction of globally unfolded protein at the highest temperature studied is 0.2%, 2%, 3% and 1% for pWT, G93A, E100G and V148I, respectively. DSC simulations were completed by Dr. Jessica Rumfeldt.

3.3.3 N^1H temperature coefficients

3.3.3.1 pWT

Of the 117 backbone amides analyzed for pWT, at higher temperatures (≥36.5°C) the signals for 19 amides are no longer observable. This may occur due to increased chemical and/or conformational

exchange. Chemical exchange occurs when the amide proton exchanges with the protons of solvent water. Under conditions of fast chemical exchange (when the intrinsic exchange rate is much greater than the difference in frequency between the amide proton and solvent) (*158*), the observed resonance for the proton is a weighted average of the two exchanging states. Since water is in great excess (~55 M compared to ~1.9 mM protein), the averaged resonance becomes essentially that of bulk water and consequently the signal in the amide region is no longer observed. The amide protons of residues shielded from solvent will not show this behaviour (*200*). Thus, the loss of a proton signal at increased temperature due to chemical exchange can mean one of two things: (1) the intrinsic exchange rate of the amide proton with water has surpassed the threshold making it fast on the NMR timescale and thus the signal a weighted average dominated by bulk water or (2) a conformational change in the protein structure has increased the solvent accessibility of the amide proton allowing it to enter into fast exchange with water (*200*). If the amide proton is fully solvent accessible to begin with (at low temperature) then condition 1 is likely the reason for the disappearance of the cross peak at increased temperature. If it is not originally solvent accessible then both scenarios described above must be true in order for chemical exchange to be the cause of signal loss. The temperature at which a given amide proton may become in fast exchange with solvent can be estimated using predicted exchange rates for random coil peptides with the server program sphere (*201, 202*).

Conformational exchange occurs when the amide proton is populating two different conformational states (*158*). For the peak to disappear due to conformational exchange the amide proton would be in intermediate exchange on the NMR timescale. Intermediate exchange occurs when the exchange rate is similar to the difference between the resonance frequencies of the two exchanging conformations. This will cause significant line broadening and loss of the signal if the two conformations have sufficiently different chemical shifts (*158*). For experiments on holo SOD1, it is difficult to say whether signal loss is definitively due to chemical or conformational exchange. However, since the protein remains significantly structured at all temperatures studied (see above), and as such the chemical

shift difference between alternative conformations is likely small, it seems more plausible that chemical exchange is the cause of signal loss. From this point forward it will be said that the crosspeaks for these amide protons have disappeared, however the different factors contributing to the lack of observation will be considered.

An overlay of the acquired $^{1}H,^{15}N$-HSQC spectra as a function of temperature (Figure 3.6) illustrates the temperature dependences of the observed amide crosspeaks. The crosspeaks appear to move downfield (left) with temperature however this is a consequence of the $N^{1}H$ shifts being referenced to water (~4.7 ppm) at each temperature (see section 3.2.4). The chemical shift of water has a strong temperature dependence (*198*) which is not accounted for in the acquired spectra. When the appropriate water correction is applied the crosspeaks move upfield (right), as expected.

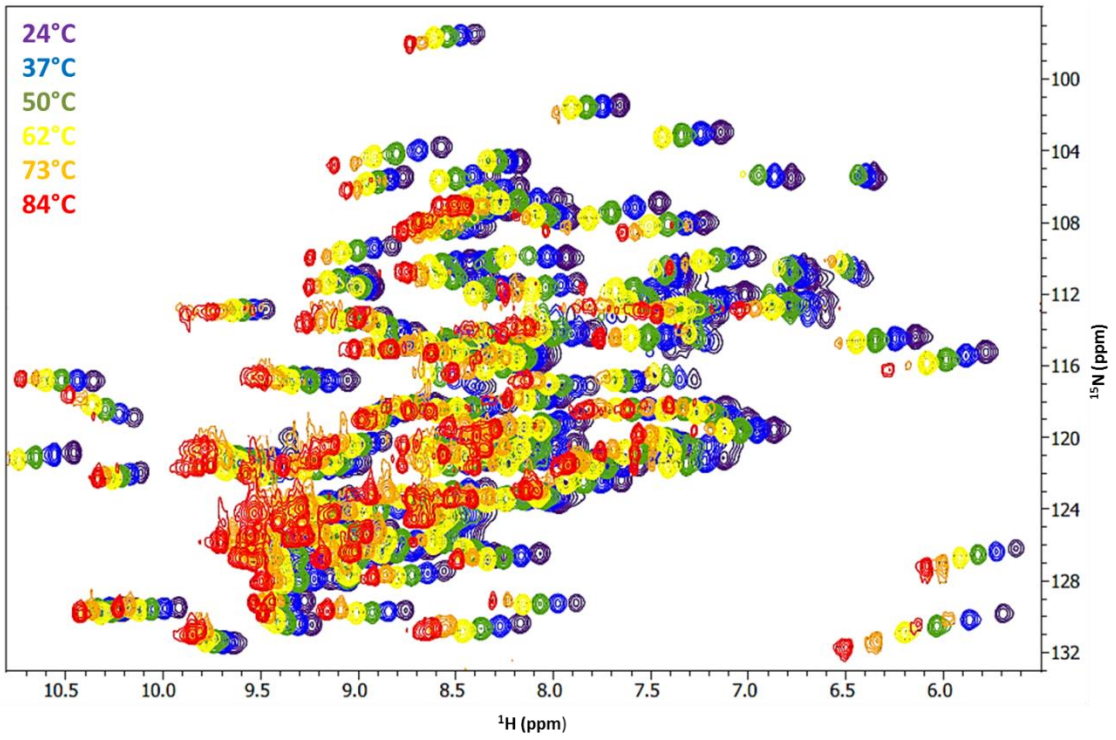

Figure 3.6 - Overlaid $^{1}H,^{15}N$-HSCQ spectra of holo pWT SOD1 (20mM Hepes, pH 7.8) acquired at different temperatures. Temperatures and associated peak colours are given on the left. The raw experimental data shows the amides shifting downfield (left) with temperature. This is a consequence of referencing the chemical shifts to water (~4.7 ppm) at each temperature, which has a strong temperature dependence. After acquisition, a water correction was applied resulting in a negative (upfield) shift with temperature (see section 3.2.4), as expected. Different amides show different temperature dependences, as can be observed for the well resolved crosspeaks.

Amide proton temperature coefficients were determined for 98 of the 148 non-proline residues (Table A1.1). The values range from -1.16 ppb/K to -11.04 ppb/K, all of which are within the limit of values that have been observed for other proteins (*160*). There does not appear to be a correlation between N^1H temperature coefficients and amino acid type or secondary structure. There is a correlation with hydrogen bonding based on crystal structure data (PDB 1SOS). Approximately 62% of all residues with amide protons predicted to participate in a hydrogen bond based on the crystal structure have temperature coefficients more positive than -5 ppb/K and those that do not cluster in regions of the protein thought to have reduced local stability (Table A1.1; section 3.1.5 and below). Comparison of temperature coefficients with amide exchange rates previously determined in the Meiering lab under the same buffer conditions at 25°C (*6*) does not reveal a correlation (Figure 3.7; see table A1.2 for amide exchange rates).

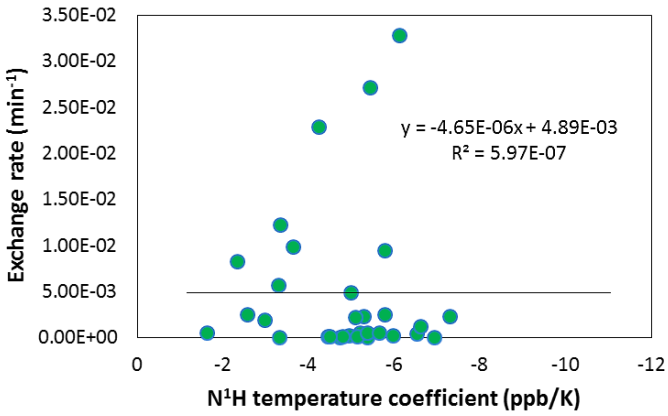

Figure 3.7 - Correlation between measurable amide exchange rates (min^{-1}) and N^1H temperature coefficients for pWT. The line of best fit obtained by linear regression is given by a black solid line. The associate equation and R^2 value is given in the plot area.

On further inspection there does appear to be a qualitative correlation with exchange behaviour, with the exception of the "too fast to measure category" which only has 6 residues (Table 1, Table A1.2.). Comparative analysis reveals that ~70% of residues with N^1H temperature coefficients more negative than -6 pbb/K, and 78% of residues that disappear at increased temperatures, exchange in the dead time (Table A1.1, Table A1.2). Amide protons that exchange in the dead time in most cases are solvent exposed and not protected by a hydrogen bond. Since most of the residues that disappear at increased

temperatures also exchange in the dead time, the disappearance of the cross peak is most likely to occur due to fast exchange with water. For pWT, there are four residues that disappear but do not exchange in the dead time: Ile18, His46, Cys146 and Gln153. The N^1H of each of these residues is expected to be hydrogen bonded. Since Ile18 and Gln153 are both surface exposed, it could be that loss of protective hydrogen bonds at increased temperature allows for the N^1Hs to enter into fast exchange with solvent resulting in signal loss. His46 and Cys146 on the other hand are both buried within the core of pWT and thus chemical exchange seems less plausible. Both of these residues partake in important stabilizing interactions within pWT as His46 is a copper binding ligand and Cys146 forms an intramolecular disulphide bond. For these two residues conformational exchange could be the cause of signal loss if altered metal interactions or disulphide bond isomerization is occurring. Conformational exchange in residues surrounding the disulphide bond has been observed in NMR relaxation experiments on the monomer construct (*182*).

Exchange Behaviour	**Average N^1H temperature coefficient**	**Number of Residues**
Too slow to measure	-4.40 ± 1.06 ppb/K	31
Measurable	-4.82 ± 1.38 ppb/K	36
Too fast to measure	-3.69 ± 1.66 ppb/K	6
Exchanged in the dead time	-5.81 ± 2.08 ppb/K	29

Table 3.2 - Average N^1H temperature coefficients for residues in pWT with different amide exchange behaviour. See table A1.2 for residue specific amide exchange rates and exchange behaviour classifications.

The N^1H temperature coefficient of each residue was mapped onto the 3D ribbon structure of pWT (Figure 3.8). Overall, 54% of the residues followed have coefficients more positive than -5 ppb/K indicating that holo pWT is still fairly structured even at 84°C. This is consistent with holo SOD remaining highly folded, as indicated by DSC experiments and simulations. Residues with N^1H temperature coefficients more negative than -5 ppb/K in pWT cluster at the ends of β-strands, in loops and specifically in edge strands β1, β5 (bottom half in Figure 3.8) and β6. The unfolding pathway of holo pWT has previously been described as 2-state with a cooperative transition from folded dimer to unfolded

monomers (*81*). The NMR experiments completed here provide a higher resolution picture of the initiation of the thermal unfolding transition, which appears to begin with partial loss of structure at various sites throughout the protein (discussed below).

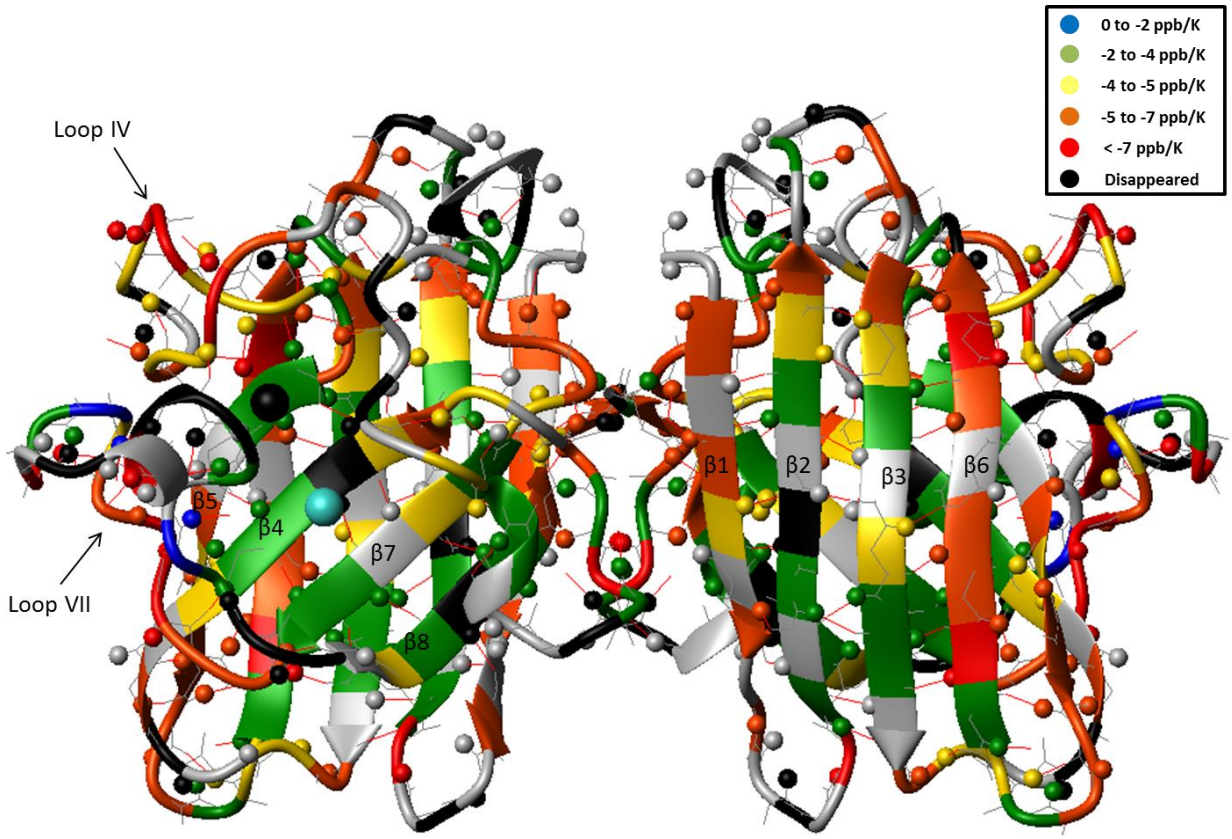

Figure 3.8 - N^1H temperature coefficients of pWT at pH 7.8. Hydrogen bonds are represented by thin red lines. The bond between the backbone carbonyl C and O is represented by thin grey lines. Description of the colour scheme is given in the legend on the right. Grey indicates residues for which no data are available. The ribbon diagram was generated using MOLMOL (*61*) and PDB file 1SOS (*62*).

It has been observed previously that ~82% of amide protons that do not participate in a hydrogen bond have a temperature coefficient between -5 and -11 ppb/K (*160*). Based on this cut-off and crystal structure data, pWT appears to lose 29 hydrogen bonds before global unfolding (Figure 3.9). The "loss" of a hydrogen bond suggests that it is either not present in solution to begin with (thus only present in the crystal structure) or that it is lost early in the unfolding pathway of pWT. The free energy of breaking one hydrogen bond has been estimated at ~1 kcal/mol (*203*). It should be noted that there is some inherent

error in using this cut-off, however, the clustering of residues with lost hydrogen bonds as well as the comparison with other residue-specific data (amide exchange and relaxation experiments; see below) is convincing. The structural implications are discussed next.

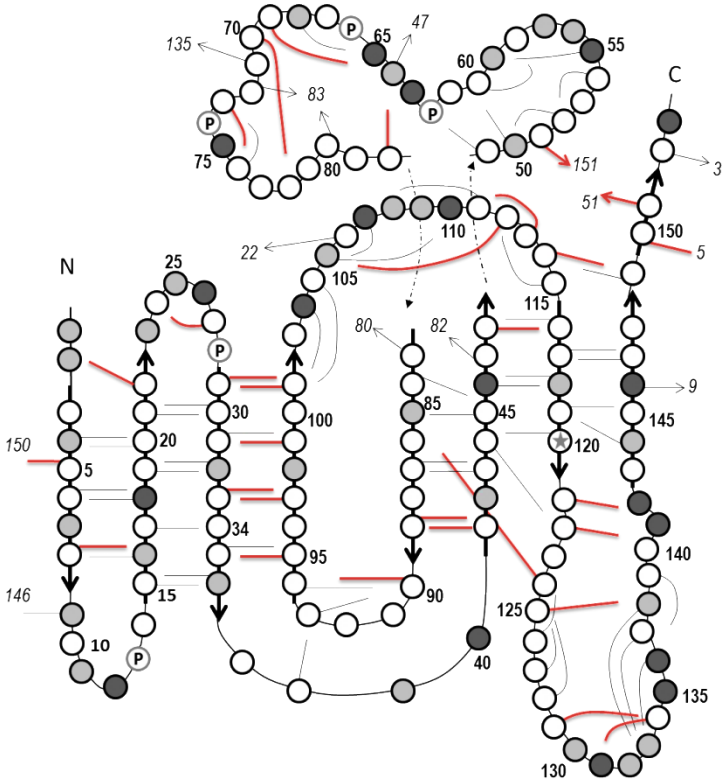

Figure 3.9 - Cartoon representation of hydrogen bonding in pWT SOD1. Each circle represents a residue in the protein. Circles that lie on arrows represent residues in β-strands. Circles with 'P' in the center represent proline residues. Hydrogen bonds (based on crystal structure data PDB 1SOS) are given by solid black lines connected to the NH and pointing towards the oxygen acceptor. Hydrogen bonds coloured red are expected to be lost in the pWT unfolding pathway prior to global unfolding based on N^1H temperature coefficients using a cut-off of -5 ppb/K. Dark grey circles represent residues that disappear at higher temperatures. Light grey circles represent residues that were not followed. In both cases no information on the hydrogen bonding status could be obtained.

Loop II in pWT only has one stabilizing hydrogen bond (Gly27). The loss of this hydrogen bond, as well as three others (Gln22 and Val29) at the ends of the β-strands before and after this loop, suggests increased mobility in this region. β5 runs from the hydrophobic interior of pWT out to the exterior wrapping around the β-sheet edge to help protect the core of the protein. β6 is a charged strand that is believed to help prevent edge-to-edge aggregation and again protect the hydrophobic core. The N^1H

temperature coefficients reveal significant loss of hydrogen bonding for the solvent-exposed protective portion of β5 and most of β6 suggesting early steps of the unfolding pathway may involve local unfolding at these edge strands and deprotection of the hydrophobic interior. In addition, the results suggest there is loss of hydrogen bonding at 5 (Gly51, Ile113, Gly114, Gly150 and Ile151) of the 15 residues that make up the dimer interface, as well as Ile112 which sits very close to the interface. The residues identified above form the top section of the dimer interface (as in Figure 3.8) indicating that there may be structural perturbations occurring early in the unfolding pathway in this region.

The long loops (loops IV and VII) also show a significant loss of structure. In loop IV, this loss is found mainly in the second half of the loop which forms the zinc binding site; approximately half of the stabilizing hydrogen bonds are lost. It should be noted that of the remaining 5 hydrogen bonds in this region, three (His71, Gly72 and His76) have N^1H temperature coefficients that are within 0.5 ppb/K of the cut-off. Loop VII is characterized by two segments, the N- and C-terminal, which lead into and out of a short α-helix, respectively. The C-terminal segment is tethered to the N-terminal segment through three main hydrogen bonds: Glu121-Ser142, Lys122-Ala140 and Asp125-Gly138. The N^1H temperature coefficients indicate that these hydrogen bonds are lost. In addition, there appears to be loss of hydrogen bonding with three residues disappearing near the helix suggesting loss or perturbation of this structure. In the native state, this helix creates a negatively charged dipole that is involved in binding the positively charged Zn^{2+} (*120*). The loss of structure in loops VI and VII point to significantly reduced shielding of the zinc-binding site in pWT at high temperatures. Overall, it appears that the monomer β-barrel core of pWT remains stable up to 84°C with local unfolding occurring at the periphery, specifically in edge strands, loops and the dimer interface.

The application of an algorithm that assesses the propensity for disorder within proteins, PONDR (*204*), reveals that β5, β6, loop VII and more significantly loop IV are expected to be natively disordered (*205*). This is noteworthy as these regions are essentially the same as those shown to have reduced local stability from the analysis of N^1H temperature coefficients. Further, amide exchange studies from our

and another lab also indicate decreased local stability at the edge strands (*6, 189*). Our studies reveal that many of the amides in β strands have exchange rates that are too slow to measure. However, in the protective half of β5 and in β6 the exchange rates are measureable (faster) suggesting reduced local stability. The transition state of the apo monomer variant has been analyzed using ϕ-value analysis. In this construct, β5 and β6 are also unstructured indicating that these regions are generally last to fold and so likely the first to unfold (*52*). This analysis also revealed that the long loops IV and VII are disordered in the apo transition state. It is known that upon metal binding these loops gain a significant amount of structure (*120*). Described earlier in Chapter 2 (section 2.1.2), experiments monitoring the unfolding kinetics of holo SOD1 indicate that the zinc binding site becomes unstructured early in the unfolding pathway (*52*) with zinc loss often preceding copper loss (*125, 126*). In another study which analyzed how the folding kinetics of SOD1 are affected by zinc binding, the authors alternatively proposed that the zinc binding site is formed in the transition state for both the apo and metal bound state of the monomer construct (*205*). This was based on zinc significantly increasing the rate of folding however the extent of structure formation is unclear. The N^1H temperature coefficients found here reveal that loop IV and VII become disordered early in the unfolding pathway, which points towards the zinc binding site likely being unstructured in the transition state of holo pWT, consistent with the previous kinetic studies of holo SOD1 (*125, 126*).

It should be noted that, since temperature coefficients are almost always negative and the sign of the coefficient is representative of directionality (upfield vs. downfield) not the magnitude of the shift, when comparing mutants to pWT a "larger or increased" temperature coefficient is one in which the absolute value is larger. Therefore, a coefficient of -7 ppb/K is larger than one of -3 ppb/K as it indicates a larger upfield shift with temperature.

3.3.3.2 G93A

G93 is located in the solvent-exposed β-barrel plug and more specifically is a conserved residue in a tight turn that has been found to be a hotspot for fALS mutations (*82*). Mutation decreases the T_m by 3.8°C. Of the 128 residues followed in G93A, 28 disappear at increased temperatures. Amide proton temperature coefficients were calculated for 100 of the 148 non-proline residues, 85 of which could be directly compared to pWT. Overall, comparison of N^1H temperature coefficients indicates that the local stability of G93A is very similar to that of pWT. There are, however, marked differences close to the site of the mutation. Most of these residues show increased N^1H temperature coefficients and are found in the β-barrel plug indicating decreased stability in this region upon mutation. In parallel to what has been seen both computationally and experimentally, G93A also exhibits sites with decreased temperature dependences indicating more stable regions compared to pWT. The site specific results are described in detail next.

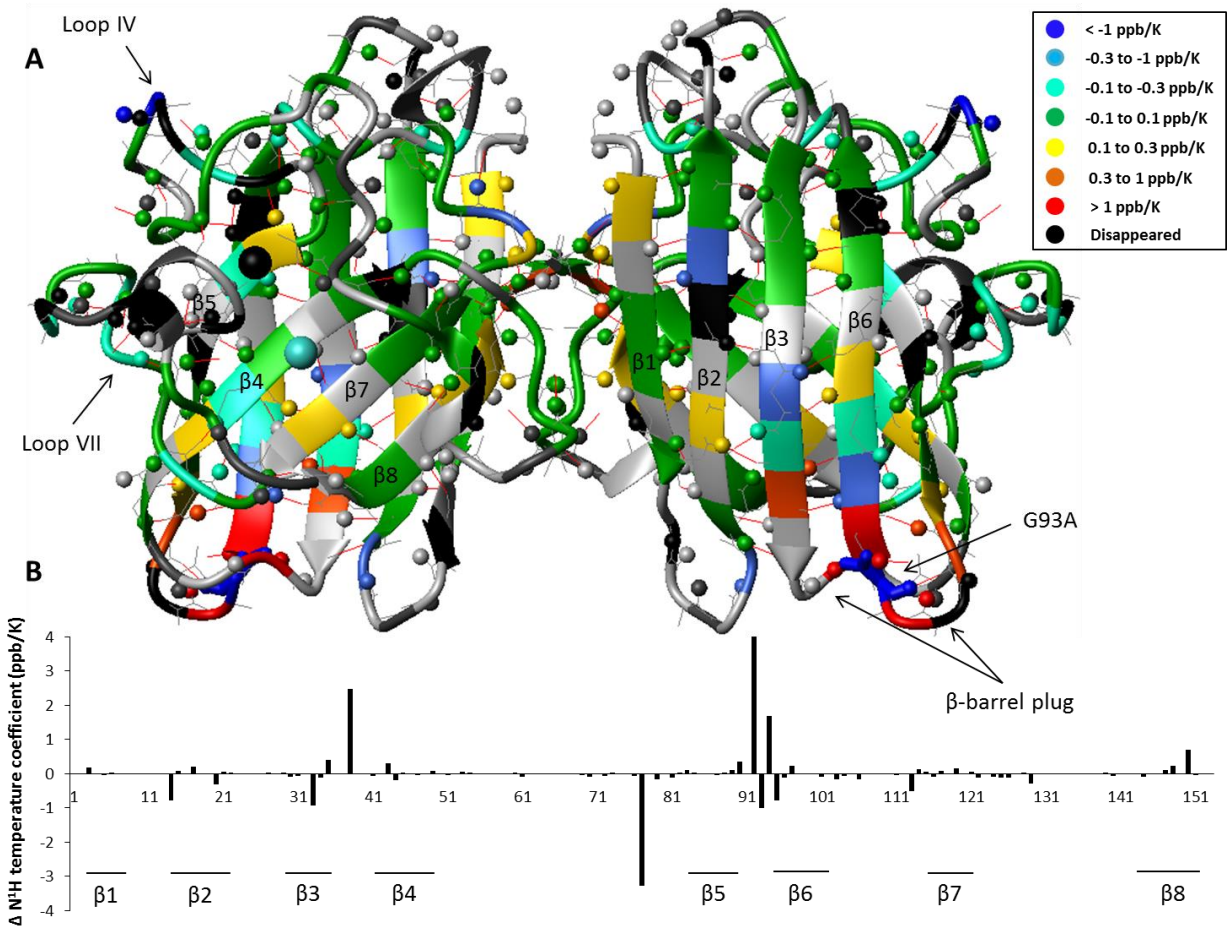

Figure 3.10 - Changes in N^1H temperature coefficients for G93A. (A) Differences in the temperature coefficients between pWT and the ALS mutant G93A mapped onto the 3D ribbon structure of holo SOD1 (PDB 1SOS). The main chain of the mutation site is shown in thick lines and coloured blue. Hydrogen bonds are represented by thin red lines. The bond between the backbone carbonyl C and O is represented by thin grey lines. Red commonly indicates disruption of hydrogen bonding/structure in the mutant relative to pWT, while blue commonly indicates stronger hydrogen bonding/structure formation; there are exceptions depending on the absolute value of the temperature coefficient (see Figure 3.1 and main text). Grey indicates residues for which no data are available. Dark grey indicated residues that disappear in both pWT and G93A. Black indicates residues that disappear in G93A but not in pWT. (B) Values of the N^1H temperature coefficient differences between pWT and G93A. A positive value indicates an increased temperature coefficient for G93A. Horizontal bars indicate β-strands.

In G93A, residues Ile35, Leu38, Asp90, Asp92, Val94 and Gly150 have larger N^1H temperature coefficients by at least 0.3 ppb/K compared to pWT (coloured orange/red in Figure 3.10). Most of these residues also show significant chemical shift changes from pWT at 25°C (Figure 3.4 A). Leu38 is located in loop III, which makes up half of the β-barrel plug. In pWT the amide proton of Leu38 hydrogen bonds

to the oxygen of Gly93 (Figure 3.9) and is the only residue in the loop to participate in a hydrogen bond. It is not surprising that mutation at Gly93 may alter the local conformation and disrupt this hydrogen bond. This was confirmed through comparison of the N^1H temperature coefficient of Leu38, which is significantly increased (by 2.48 ppb/K) in G93A. Unfortunately, there are no other probes in this loop to better understand the change in stability but it seems safe to say that loss of the hydrogen bond will likely increase mobility. There are two hydrogen bonds between Asp90 and Val94, which help to stabilize the tight turn (loop V) between β5 and β6 which makes up the other half of the β-barrel plug. The N^1H temperature coefficients for these residues indicate that these hydrogen bonds are either not formed in G93A or are lost early in the unfolding pathway (only one is lost in pWT), signifying a reduction of local structure in loop V in the mutant. In addition, the significantly increased temperature coefficient of Asp92 (by 4.30 ppb/K) for G93A and the disappearance of the cross peak for Lys91, which is observed at all temperature in pWT, further supports increased dynamics in loop V. Alteration in the structure and dynamics of loop III and V have previously been reported in other NMR studies (see section 3.1.5) (*95*). The increased N^1H temperature coefficient at Ile35 actually represents a strengthening of the hydrogen bond with Ala95. This is because in both pWT and G93A the coefficients fall in the region where the amide proton is likely to be hydrogen bonded and within this range an increased coefficient actually represents a stronger hydrogen bond (see section 3.1.3 and Figure 3.1). This increased stability at this residue could be compensatory for the increased dynamics observed in the β-barrel plug (see discussion). There does not appear to be significant changes in the loops or dimer interface upon mutation, with the exception of an increased temperature coefficient towards the C-terminus, at Gly150, suggestive of an increase in mobility.

As for pWT, amide exchange rates have been measured previously for G93A in the Meiering lab (*6*). Residues with larger N^1H temperature coefficients upon mutation correlate well with those displaying increased exchange rates, confirming increased dynamics in the β-barrel plug. Residues that have smaller N^1H temperature coefficients by greater than 0.3 ppb/K in G93A include Val14, Phe20, Gly33, Glu77,

Ala93, Ala95 and Ile113 (coloured light/dark blue in Figure 3.10). Two of these residues, Gly33 and Ile113, also exhibit decreased exchange rates (Table A1.2.). Three of these residues, Val14, Phe20 and Glu77, did not have measureable exchange rates in either case so a comparison is not possible. Val14 is located in loop I and interacts with Leu38 (*188*). It could be that altered dynamics at Leu38 allow for stronger stabilizing interactions with Val14 decreasing its observed N^1H temperature coefficient. Glu77 is located in loop IV and is in a region that has been proposed to have decreased mobility in mutants (*95, 104*). Lastly, Ala93 and Ala95 have significantly decreased N^1H temperature coefficients, although amide exchange studies reveal increased exchange rates at these residues. Ala93 is the mutated residue and here the reduced temperature coefficient actually represents a weakening of the hydrogen bond (see Figure 3.1; Table A1.1) between the N^1H of Ala93 and the oxygen on Asp90, consistent with the amide exchange results. Ala95 is located in β6 and although the coefficient is smaller in G93A, in both mutant and pWT the temperature coefficient is ≤ -6.5 ppb/K suggesting no formation of the hydrogen bond with oxygen of Ile35. It could be that the increased dynamics in the β-barrel and at Val94 result in some compensatory stabilization at Ala95. This proposal is supported by the strengthening of the hydrogen bond between Ile35 and Ala95 (see above).

There are 11 cross peaks that disappear at increased temperature in G93A but remain visible at all temperatures in pWT. These residues are spread throughout the structure but are mainly found in loops. A greater proportion of residues in loops IV and VII disappear in the mutant compared to pWT, which already has a large number of amides that disappear. Interestingly, the N^1H temperature coefficients for the surrounding residues do not indicate enhanced loss of structure in these loops for the mutant. However, the increased proportion of residues that disappear itself suggest loss of structure allowing for increased conformational, or perhaps more likely chemical exchange. A number of the residues that disappear surround the zinc binding site (Glu78, His80, Ser134, Thr137) suggesting enhanced flexibility in this region. Propagating effects in the metal binding region of G93A have also been observed through amide exchange (*189*).

In summary, the observations described above suggest that in addition to reducing global stability, the G93A mutation reduces the local stability of the β-barrel plug. There is also evidence to suggest the mutant has increased flexibility in loops IV and VII which could lead to enhanced deprotection of the zinc binding site. Increased flexibility in loop VII has been proposed to lead to non-native substrate access to the active site and aberrant chemistry which can be damaging to the protein. Further, both of these loops have been shown to form non-native interactions in the crystal structures of apo mutant SOD1 and thus increased flexibility could lead to unwanted protein association (*89*).

3.3.3.3 E100G

Glu100 is located in β6 and mutation from Glu to Gly decreases the net negative charge of the protein and disrupts a salt bridge between Glu100 and Lys30. E100G is the most globally destabilized mutant studied herein with ΔT_m = -5.2°C. This destabilization may seem surprising since the mutation is located in an edge strand where the main chain of the residue points out toward solvent. However, an interesting computational study identifying the key residues involved in the folding of SOD1 found most of these residues lie on the surface of the protein and not in the hydrophobic core (*206*). Further, each residue is involved in a contact with an oppositely charged amino acid. Disruption of the key electrostatic interaction between Glu100 and Lys30 may be a main cause of the observed decrease in stability. N^1H temperature coefficients were determined for 91 of the 108 amide protons followed in E100G as 17 disappeared at increased temperatures. This allowed for the direct comparison of 81 residues with pWT. The temperature coefficients for E100G indicate a similar pattern of local unfolding to pWT, however, there are distinct differences clustering near the mutation site and distal in the β-barrel plug. Similar to G93A, residues in E100G exhibit both increased and decreased N^1H temperature coefficients compared to pWT, described further below.

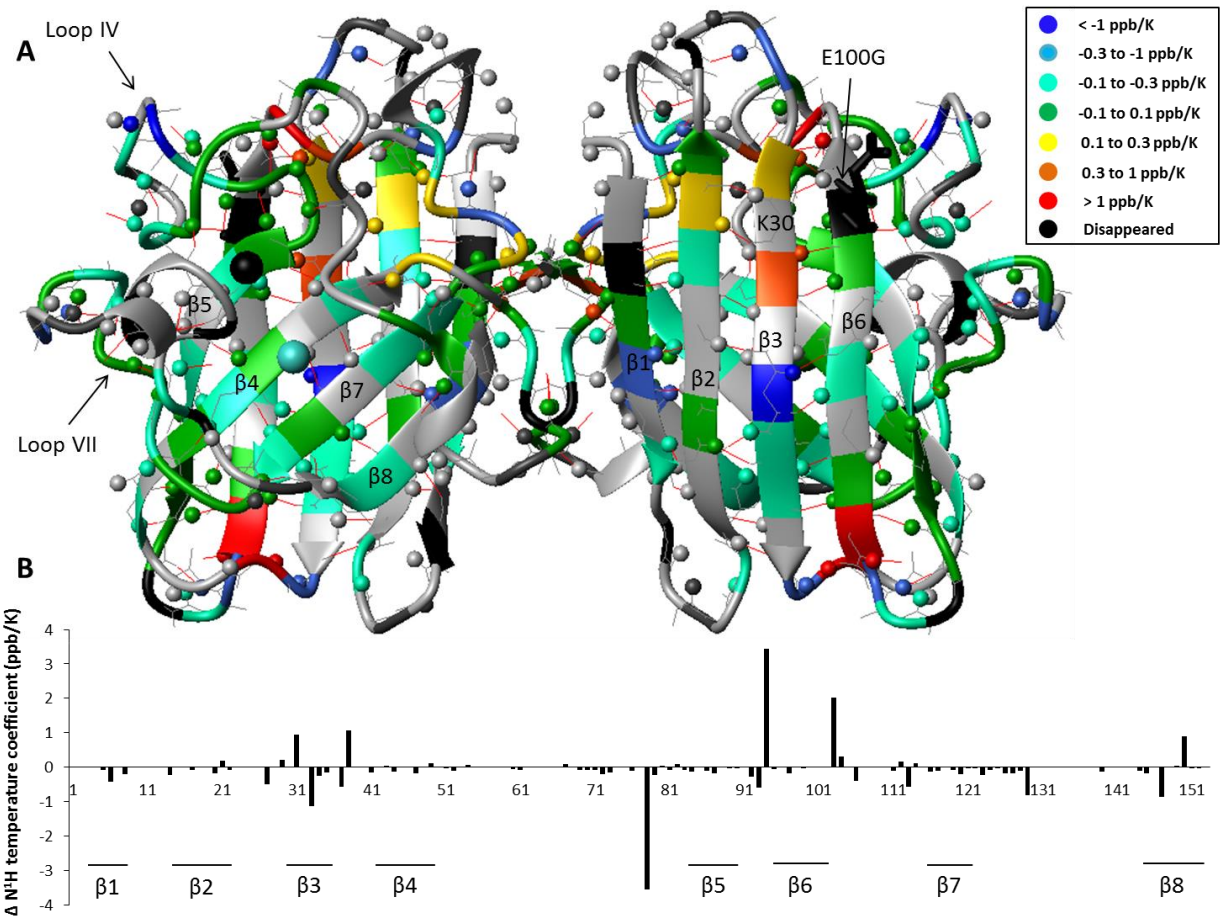

Figure 3.11 - Changes in N^1H temperature coefficients for E100G. (A) Differences in the temperature coefficients between pWT and the ALS mutant E100G mapped onto the 3D ribbon structure of holo SOD1 (PDB 1SOS). The main chain of the mutation site is shown in thick lines and coloured blue. Hydrogen bonds are represented by thin red lines. The bond between the backbone carbonyl C and O is represented by thin grey lines. Red commonly indicates disruption of hydrogen bonding/structure in the mutant relative to pWT, while blue commonly indicates stronger hydrogen bonding/structure formation; there are exceptions depending on the absolute value of the temperature coefficient (see Figure 3.1 and main text). Grey indicates residues for which no data are available. Dark grey indicated residues that disappear in both pWT E100G. Black indicates residues that only disappear in E100G. (B) Absolute values of the N^1H temperature coefficient differences between pWT and E100G. A positive value indicates an increased temperature coefficient for E100G. Horizontal bars indicate β-strands.

In E100G, residues Val31, Leu38, Val94, Val103, Ile104 and Gly150 have significantly more negative (by 0.3 ppb/K) N^1H temperature coefficients compared to pWT (coloured orange/red in Figure 3.11). The edge strand β6 shows local unfolding in pWT (section 3.3.3.1). Upon mutation the extent of unfolding does not appear to change, however, two residues (Val103 and Ile104) in loop VI, which directly follows β6 and the site of the mutation, exhibit significantly different stability. In pWT the amide

protons of Val103 and Ile104 hydrogen bond to the sidechain oxygen of Asp101 (Figure 3.9). The N^1H temperature coefficients indicate that in the mutant there is a strengthening of the hydrogen bond between Val103 and Asp101 and a loss of the hydrogen bond between Ile104 and Asp101. Increased dynamics at Ile104 is supported by previous amide exchange measurements which show that the exchange rate of this amide is ~19 times greater in E100G compared to pWT (Table A1.2 (*6*)). The results here show that there is altered mobility in the N-terminal portion of loop VI in E100G, which has been proposed as an amyloidogenic fragment in SOD1 (*190*). In the crystal structure of pWT, the N^1H of Val29 hydrogen bonds to carbonyl oxygen of Asp101 and vice versa. These hydrogen bonds are lost early in the unfolding pathway of pWT suggesting increased disorder at the end of β3. This loss of structure extends further down into the β3 strand in E100G. The disruption of the salt bridge between Lys30 and position 100 upon mutation removes a stabilizing interaction in this region. This likely influences the hydrogen bond between Val31 and Ile99, which according to the N^1H temperature coefficient of Val31 is lost in E100G but not pWT. Interestingly Gly150, as seen in G93A, has a larger temperature coefficient which could suggest increased mobility in the dimer interface upon mutation.

An interesting finding was that the structural effects caused by mutation appear to propagate into the β-barrel plug. Specifically, the temperature coefficients of Leu38 and Val94 (coloured red in Figure 3.11) increase by 1.07 ppb/K and 3.44 ppb/K, respectively, in the mutant. This suggests a loss of the hydrogen bond between Leu38 and Gly93 which links loops III and V, as well as loss of the hydrogen bond between Val94 and Asp90 which helps to stabilize the tight turn in loop V (based on the -5 ppb/K cut off, Figure 3.1). Interestingly, Gly37 and Gly93 (also located in the β-barrel plug) have decreased N^1H temperature coefficients. This could be due to a compensatory effect due to the increased mobility observed at Leu38, which has been seen in other NMR studies (*108*). The amide proton of Gly93 participates in a hydrogen bond with Asp90 in the pWT crystal structure (PDB 1SOS). The decreased temperature coefficient in this case, however, represents a weakening of the hydrogen bond (since in both G93A and pWT the value lies below the -4.6 ppb/K cut off; see above). The results indicate that while the

extent of destabilization appears to be smaller in E100G, in both G93A and E100G mutation alters the dynamics in the β-barrel plug. Altered dynamics in this region for a number of mutants has been shown both computationally and experimentally (section 3.1.5).

A number of residues (Ala6, Gly27, Gly33, Gly37, Glu78, Gly93, Leu106, Ile113, Gly129 and Gly147 (coloured light/dark blue in Figure 3.11) have significantly reduced N^1H temperature coefficients (by 0.3 ppb/K) in E100G. The reduction in the temperature coefficient however does not alter the predicted hydrogen bonding status, with the exception of Gly33 and Ile113. Based on N^1H temperature coefficients, the hydrogen bond between Gly33 and Val97 is lost in pWT but maintained in both G93A (see section 3.3.3.2) and E100G. Previous amide exchange studies reveal this residue also exhibits a slower exchange rate in both mutants. Ile113 is located in the C-terminal end of loop VI. Amide exchange results are in agreement with a stronger hydrogen bond as the exchange rate of Ile113 is ~2 times slower in the mutant. On the other hand, the reduced N^1H temperature coefficients for 4 of the 10 residues listed above (Ala6, Gly93, Leu106 and Gly147) actually signify a weakened hydrogen bond. Gly93 is in the β-barrel and Leu106 in the N-terminal portion of loop VI, both regions discussed above as having decreased local stability in E100G. Ala6 and Gly147 are both close to the dimer interface indicating that the mutation can have propagating effects on the hydrogen bonding network within the subunit. The remaining four residues (Gly27, Gly37, Glu78, Gly129) indicate some degree of maintenance in the mutant and are spread throughout the polypeptide chain highlighting that there are also propagating stabilizing effects upon mutation. One of these, Glu78, is in a region expected to have increased stability in mutants and neighbours Glu77 which was shown to have increased stability in G93A.

There are 8 peaks that disappear in E100G but remain visible at all temperatures in pWT (Gly10, Gly24, Asn53, Lys91, Gly100, Ser134, Thr137 and Ala140; Table A1.1). Of these 8 residues, 6 (Gly10, Gly24, Lys91, Gly100, Ser134, Thr137 and Ala140) also disappear in G93A. Again the residues are spread throughout the polypeptide chain but mainly found in loops, with the exception of Lys91 and Glu100 which are found in edge strands β5 and β6, respectively. It is noteworthy that 3 of the 8 residues

that disappear in E100G are in loop VII in or near the helix that serves as a cap of the zinc binding site. The increased loss of structure in this region in both mutants suggests that increased flexibility in the loop VII could be a general consequence of mutation.

With the exception of the three residues described earlier there does not appear to be a correlation between amide exchange rates and N^1H temperature coefficients in E100G. Comparison of the amide exchange rates of pWT and E100G reveals very few differences between the two variants. E100G, despite being the most destabilized, is structurally very similar to pWT, evidenced by the small differences in chemical shift changes at 25°C (Figure 3.4 B) and similar exchange behaviour. The lack of correlation could simply be a consequence of the absence of observed differences from pWT in the amide exchange studies suggesting that the determination of N^1H temperature coefficients may be better able to differentiate subtle structural differences.

3.3.3.4 V148I

Val148 is located in β8 and its hydrophobic side chain forms part of the dimer interface. Mutating Val148 to Ile introduces a bulkier hydrophobic side chain at the interface. DSC simulations reveal that V148I is actually more stable than pWT as the T_m is increased by 0.7°C (Figure 3.5). At 24°C a relatively large proportion of residues exhibit significant chemical shift changes, more than for the two destabilized mutants discussed above. The N^1H temperature coefficients were determined for 101 of the 117 residues followed in V148I. At increased temperature the crosspeaks for 16 residues disappeared. It was possible to directly compare the N^1H temperature coefficients for 86 residues with pWT. Analysis of the N^1H temperature coefficients of V148I reveals a similar pattern of local stability as pWT however overall the mutant tends to have smaller coefficients (Figure 3.12), consistent with the increased stability observed by DSC.

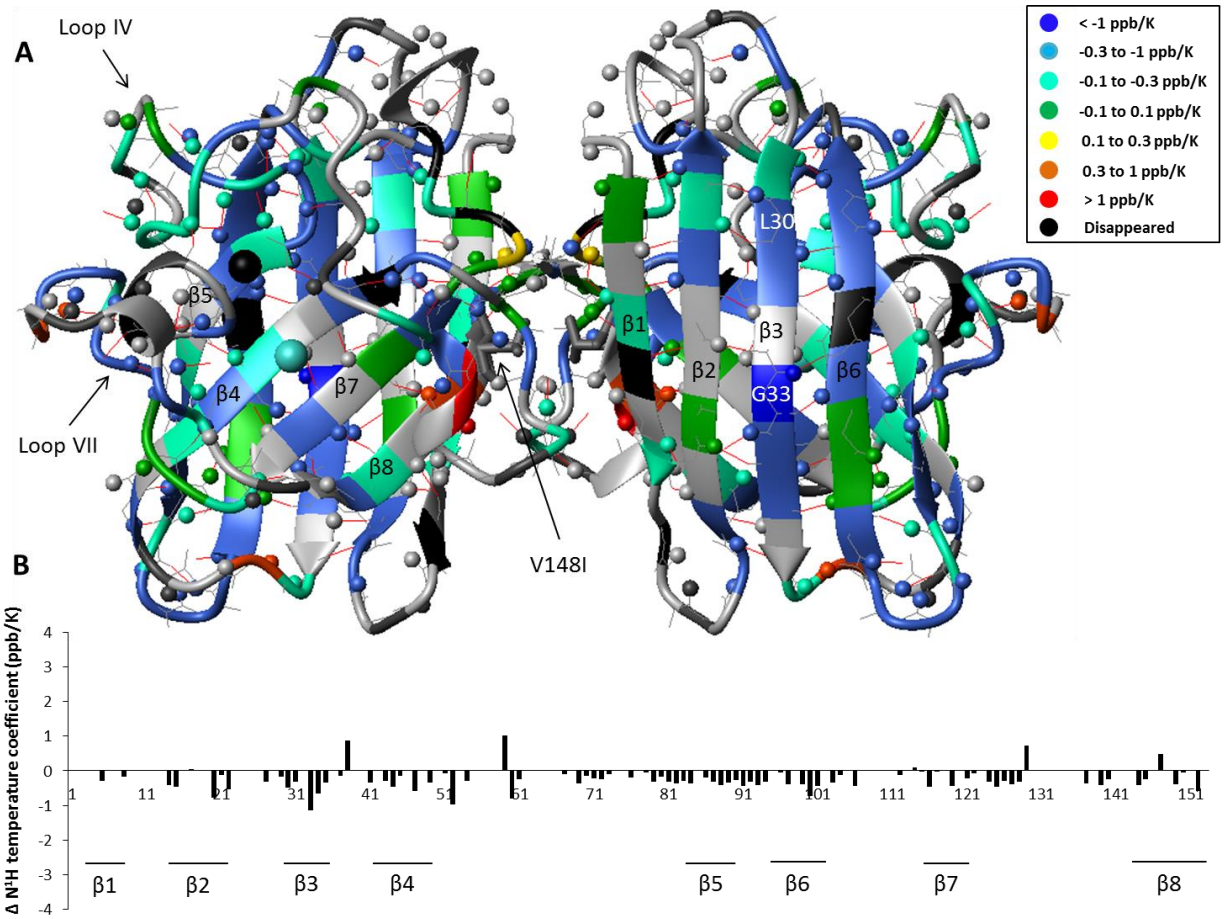

Figure 3.12 - Changes in N^1H temperature coefficients for V148I. (A) Differences in the temperature coefficients between pWT and the ALS mutant V148I mapped onto the 3D ribbon structure of holo SOD1 (PDB 1SOS). The main chain of the mutation site is shown in thick lines and coloured blue. Hydrogen bonds are represented by thin red lines. The bond between the backbone carbonyl C and O is represented by thin grey lines. Red commonly indicates disruption of hydrogen bonding/structure in the mutant relative to pWT, while blue commonly indicates stronger hydrogen bonding/structure formation; there are exceptions depending on the absolute value of the temperature coefficient (see Figure 3.1 and main text). Grey indicates residues for which no data are available. Dark grey indicated residues that disappear in both pWT V148I. Black indicates residues that only disappear in V148I. (B) Absolute values of the N^1H temperature coefficient differences between pWT and V148I. A positive value indicates an increased temperature coefficient for V148I. Horizontal bars indicate β-strands.

There are four residues (Leu38, Ser59, Gly129, and Val147) that have significantly increased (by 0.3 ppb/K) N^1H temperature coefficients in V148I (coloured orange/red in figure 3.12). Two of these, Ser59 and Val147, are close to the site of the mutation in the dimer interface and the other two, Leu38 and Gly129, are distal. Val147 is located in β8 next to the site of the mutation and participates in a hydrogen bond with Leu117 in the pWT crystal structure (Figure 3.9). The increased N^1H temperature coefficient

actually reveals a strengthening of this hydrogen bond. On the other hand, it appears that even in V148I the hydrogen bond between Leu38 and Gly93 is broken, suggesting again weakened interactions in the β-barrel plug. The increased temperature coefficients of Ser59 (loop IV) and Gly129 (loop VII) suggest increased disorder at these specific residues also. In contrast, 45 residues display significantly decreased (by 0.3 ppb/K) N^1H temperature coefficients in V148I. This is a considerably larger proportion than for the other two mutants studied here. Comparison of the absolute N^1H temperature coefficients of pWT and V148I reveals that for 56% of these residues, the decreased temperature coefficient actually represents a weakening of a hydrogen bond (Figure 3.1). In only three cases, Lys30, Gly33, and Ile149 (Figure 3.12), is the decreased temperature coefficient indicative of the preservation of a hydrogen bond lost in pWT. Lys30 and Gly33 are both in β3 and participate in hydrogen bonds with β2 and β6, respectively, suggesting increased stability in β3. Ile149 is next to the site of the mutation and hydrogen bonds to Arg115 (Figure 3.9). The strengthening of the hydrogen bond between Val147 and Leu177, as well as the preservation of the hydrogen bond between Ile149 and Arg115, suggest that there is an increase in the local stability near the mutation.

There are 6 residues (Ala6, Gly10, His48, Ser111, Ile113, Ser134;Table A1.1.) that disappear in V148I that remain visible at all temperatures in pWT. Only 2 of these residues (Gly10 in β1 and Ser134 in loop VII) also disappear in the other mutants. Unlike the other variants studied, in V148I two residues (Ser111 and Ile113) in the C-terminal end of loop VI disappear. This loop forms a portion of the dimer interface. The loss of signal for these residues suggests that this loop has increased disorder in V148I. Thus, although it appears there may be a gain of structure surrounding the mutation site it may be at the expense of the stability of a neighboring region in the dimer interface. The number of residues that disappear in loop VII in V148I is comparable to pWT.

It should be noted that spectral acquisition was completed on a different spectrometer (see section 3.2.2 and 3.2.4) for V148I and while much care was taken to ensure the data were acquired through identical means (sample temperatures, pulse programs, methods of water suppression, etc.) there is some

variability which could in part explain the observed differences. Unfortunately, amide exchange studies have not previously been completed on holo V148I precluding comparison between the two methods.

3.3.5 ^{15}N temperature coefficients

3.3.5.1 pWT

^{15}N temperature coefficients were determined for pWT and the three mutants discussed above. In pWT the temperature coefficients range from -21.5 ppb/K to 28.18 ppb/K. The mutants display a similar range of values which are comparable to what has been reported previously for the B1 domain of protein G (G B1) (*165*). The factors that contribute to ^{15}N temperature coefficients remain unclear (*165*). There does not appear to be a correlation between the sign or magnitude of the temperature coefficient and amino acid type or secondary structure. There is a weak correlation between N^1H and ^{15}N temperature coefficients (Figure 3.13 A) which was also observed for protein G B1. Crystallographic temperature factors, or B-factors, provide information on the relative vibrational motions within a protein (*180*). Residues with large B-factors are commonly found in more flexible regions of a protein. For pWT there is no correlation between B-factors and ^{15}N temperature coefficients (Figure 3.13 B). ^{15}N chemical shifts depend on a number of factors including the conformation and side-chain structure. This makes ^{15}N chemical shifts useful in distinguishing between secondary structural elements in proteins (*207*). ^{15}N chemical shifts can also be affected by electrostatic interactions and hydrogen bonding. Due to the latter, it is surprising that ^{15}N temperature coefficients do not correlate more strongly with hydrogen bonding status (*208*) and consequently N^1H temperature coefficients.

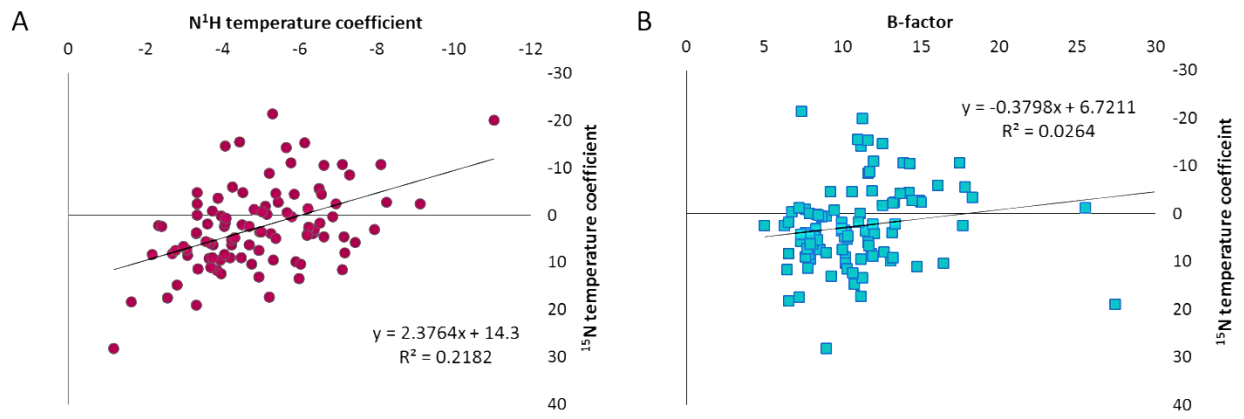

Figure 3.13 - Correlation plots for ^{15}N temperature coefficients of pWT, pH 7.8. (A). Correlation of ^{15}N and N^1H temperature coefficients. (B) Correlation of ^{15}N and B-factors (PDB 1HL5). The line of best fit obtained by linear regression is given by a black solid line. The associate equation and R^2 value is given in the plot area.

The calculated ^{15}N temperature coefficients were mapped onto the 3D ribbon structure of pWT (Figure 3.14). Since the significance, if any, of the sign of the ^{15}N temperature coefficient remains unknown only the magnitude was considered. Unlike for N^1H temperature coefficients, residues at the ends of secondary structural elements, in loops and in the dimer interface display both small and large ^{15}N temperature coefficients. There are small clusters of residues with similar magnitude ^{15}N temperature coefficients in pWT. This is observed near the β-barrel plug with some residues (Gly37, Leu38, Gly41, Lys91, and Val94) displaying large ^{15}N temperature coefficients (≥ 9 ppb/K) however there are also residues with small coefficients (≤ 6 ppb/K) in the region (Asp92, Gly93). Similarly, Asp52 and Asn53, as well as Val5 and Ala6, which lie across the dimer interface, all display large ^{15}N temperature coefficients. In contrast, the top-half of β5, which shows predominantly large N^1H temperature coefficients, is dominated by residues with small ^{15}N temperature coefficients. The residues comprising the hydrophobic core of the dimer interface (described in section 3.3.3.1) also show mainly small ^{15}N temperature dependences. The regions described above have decreased local stability based on N^1H temperature coefficients in pWT. The results indicate that although residues in these regions have similar temperature dependences, there is no clear correlation between the magnitude of the ^{15}N temperature coefficient and the extent of the structural and/or environmental changes it reports on.

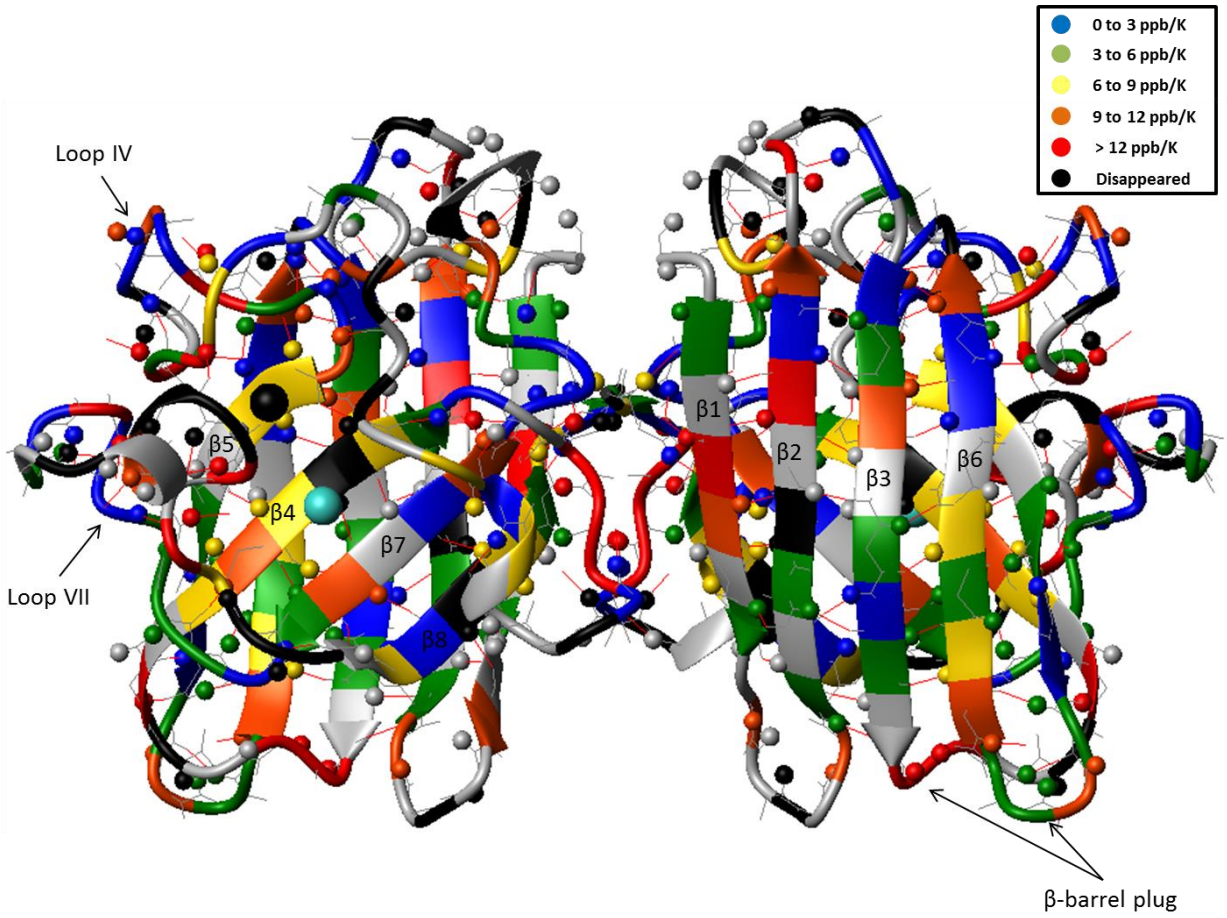

Figure 3.14 - ^{15}N temperature coefficients of pWT at pH 7.8. Hydrogen bonds are represented by red sticks. The carbonyl oxygen is represented by grey sticks. Description of the colour scheme is given in the legend on the right. Grey indicates residues for which no data is available. The ribbon diagram was generated using MOLMOL and PDB file 1SOS.

3.3.5.2 G93A, E100G and V148I

The ^{15}N temperature coefficients of G93A, E100G and V148I were calculated and compared with pWT. Since the uncertainty in ^{15}N chemical shifts was determined to be ± 0.03 ppm, a larger cut-off was chosen for significant temperature coefficient differences (3 ppb/K). The changes in temperature coefficients for each residue were mapped onto the 3D structure for each of the mutants (Figure 3.15). Residues exhibiting different ^{15}N temperature dependences for the most part cluster close to the site of the mutation with V148I showing the highest degree of propagating effects through the structure. A similar pattern of behaviour was seen in V148I for chemical shift changes at 25°C (Figure 3.4 C) and N^{1}H

temperature coefficients (Figure 3.12). It is interesting to note that in most cases the ^{15}N temperature coefficient is reduced in the mutants. This again points to the idea that the magnitude of ^{15}N temperature coefficients may not correlate with the extent of structural and/or environmental changes in the protein.

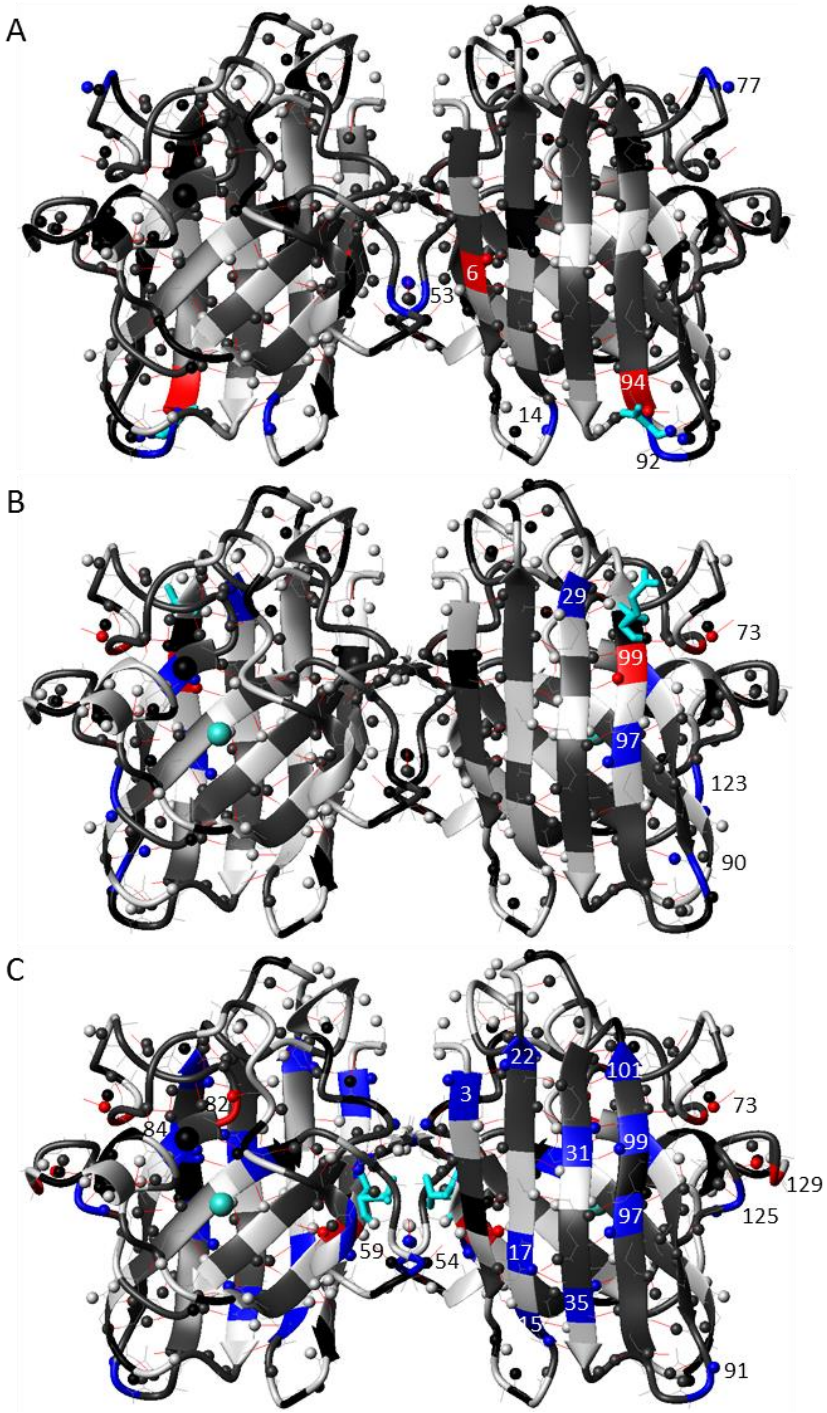

Figure 3.15 - Ribbon diagram of pWT SOD1 indicating residues with significantly different ^{15}N temperature coefficients in (A) G93A (B) E100G and (C) V148I. Residues with ^{15}N temperature coefficients decreased by at least 3 ppb/K compared to pWT are coloured blue. Residues with ^{15}N temperature coefficients increased by at least 3.0 ppb/K compared to pWT are coloured red. Residues numbers are given in for those with significant changes. Dark grey is used to highlight residues with no significant change (i.e. within ± 3.0 ppb/K of pWT). Light grey is used to highlight residues where no data are available. Bound copper (turquoise) and zinc (black) are represented as spheres. The mutated residue is shown in stick representation in cyan. The ribbon diagram was generated using MOLMOL and PDB file 1SOS.

There are 7 residues with significantly different ^{15}N temperature coefficients compared to pWT in G93A. Two of these (Ala6 and Val94; red in Figure 3.15) exhibit increased temperature dependences while the remainder (Val 14, Asn53, Glu77, Asp92 and Gly93; blue in Figure 3.15) have reduced temperature dependences. Most of these residues also have significantly different N^1H temperature coefficients and are local to the mutation site. Three of the residues (Val14, Glu77 and Asn53) are distal from the mutation site. Val14, as described earlier, interacts with Leu38 in the β-barrel plug which has altered dynamics in G93A (*188*). Glu77 is in a region shown to have decreased mobility in mutants (see sections 3.3.3.2 and 3.3.3.3) (*95, 104*). Lastly, Asn53 is in the dimer interface which has been proposed to be weakened in mutants (*81, 93*). The same level of changes in ^{15}N temperature coefficients is observed for E100G. Two residues (Gly73 and Ile99; red in Figure 3.15) display increased temperature dependences and five (Val29, Leu84, Asp90, Val97 and Ala123; blue in Figure 3.15) have reduced values. Here there does not appear to be a correlation between residues displaying different N^1H temperature dependences, however, the residues with altered ^{15}N temperature dependences do cluster close to the site of the mutation. Further, 4 of the 7 residues identified for E100G have altered amide exchange rates (Table A1.2) compared to pWT however in only two cases were the differences large enough to be considered significant (*6*). In V148I, the number of residues with significant differences climbs to 21 with 4 displaying increased temperature coefficients. A large proportion of these residues (17; 81%) also have significantly altered N^1H temperature dependences. It should be noted that the lack of correlation for E100G and the high correlation for V148I between N^1H and ^{15}N temperature dependences in part could be a product of how many residues display significant changes in each mutant.

Taken together, the results indicate that while the factors contributing to ^{15}N temperature coefficients remain unknown, residues with altered coefficients correlate well with those shown to be perturbed through other methods and expected to be structurally affected by mutation. It has been claimed that ^{15}N temperature coefficients are "essentially uninterpretable" (*165*), however, the studies here indicate that ^{15}N temperature dependences likely report on genuine differences in proteins. Further

investigations of the factors that govern ^{15}N temperature coefficients, disentangling the relationship between the sign and magnitude of the coefficients and the related type and extent of conformational deformation, still remains essential to their use in structural analyses.

3.3.6 Non-linear N^1H temperature dependences

3.3.6.1 Theoretical model for curved temperature dependence

The temperature dependence of chemical shifts is expected to be linear since the expansion coefficient of proteins is constant with temperature (see section 3.1.4). In contrast, non-linear behaviour has been observed in a number of proteins well below the global unfolding temperature. Baxter and co-workers proposed that this non-linearity is an indication of the amide group accessing an alternative state (*165*). If an amide proton is able to access another conformation, it will only result in curvature if the two conformations are in fast exchange on the NMR timescale and thus the observed peak is a weighted average of the two states (*158*). One state can be referred to as the ground state (state 1) and the other as the higher energy alternative state (state 2). Each state is assumed to have a linear temperature dependence of chemical shifts as follows:

$$\delta_1(T) = \delta_1^\circ + g_1 T \qquad \text{Eq. 3.2}$$

$$\delta_2(T) = \delta_2^\circ + g_2 T \qquad \text{Eq. 3.3}$$

where δ_1(T) and δ_2(T) are the chemical shifts at a given temperature (T), δ_1° and δ_2° are the initial chemical shifts and g_1 and g_2 are the temperature coefficients of the ground and alternative states, respectively. These two states are separated by a free energy difference, ΔG, given by Eq. 1.1. The observed chemical shift, δ_{obs}, is dependent upon the populations of the ground and alternative state, p_1 and p_2, respectively:

$$\frac{p_2}{p_1} = \exp\left(-\frac{\Delta G}{RT}\right) \qquad \text{Eq. 3.4}$$

Therefore, the observed chemical shift (δ_{obs}) is given by:

$$\delta_{obs} = \delta_1 p_1 + \delta_2 p_2 \quad \text{Eq. 3.5}$$

$$\delta_{obs} = \frac{(\delta_1^{\circ} + g_1 T) + [(\delta_2^{\circ} + g_2 T) e^{(-\Delta G/RT)}]}{1 + e^{(-\Delta G/RT)}} \quad \text{Eq. 3.6}$$

where R is the gas constant. The extent of curvature is dependent upon the differences in δ° and *g*, as well as the ΔG between the two states.

It has been proposed that the alternative state has local structural rearrangement with different hydrogen bonding compared to the ground state resulting in different chemical shifts and/or temperature gradients (*177*). In order to provide a clear understanding of how differences in these values as well as various thermodynamic parameters affect curvature, observed chemical shifts were simulated using typical values (*177*). The residuals (deviations from linearity) were calculated to illustrate the curvature (Figure 3.16). The ground state chemical shift was initially taken to be 8.5 ppm with a temperature coefficient of -2 ppb/K. The shift of the alternative state was set to 8.0 ppm with a temperature coefficient of -7 ppb/K. The thermodynamic parameters for the simulations were taken from Mulder et al., where an excited state of the L99A mutant of T4 lysozyme was characterized (*209*). The values, estimated to represent loss of a hydrogen bond, are ΔG = 2 kcal/mol, ΔH = 7.1 kcal/mol and $T\Delta S$ (25°C) = 5.1 kcal/mol.

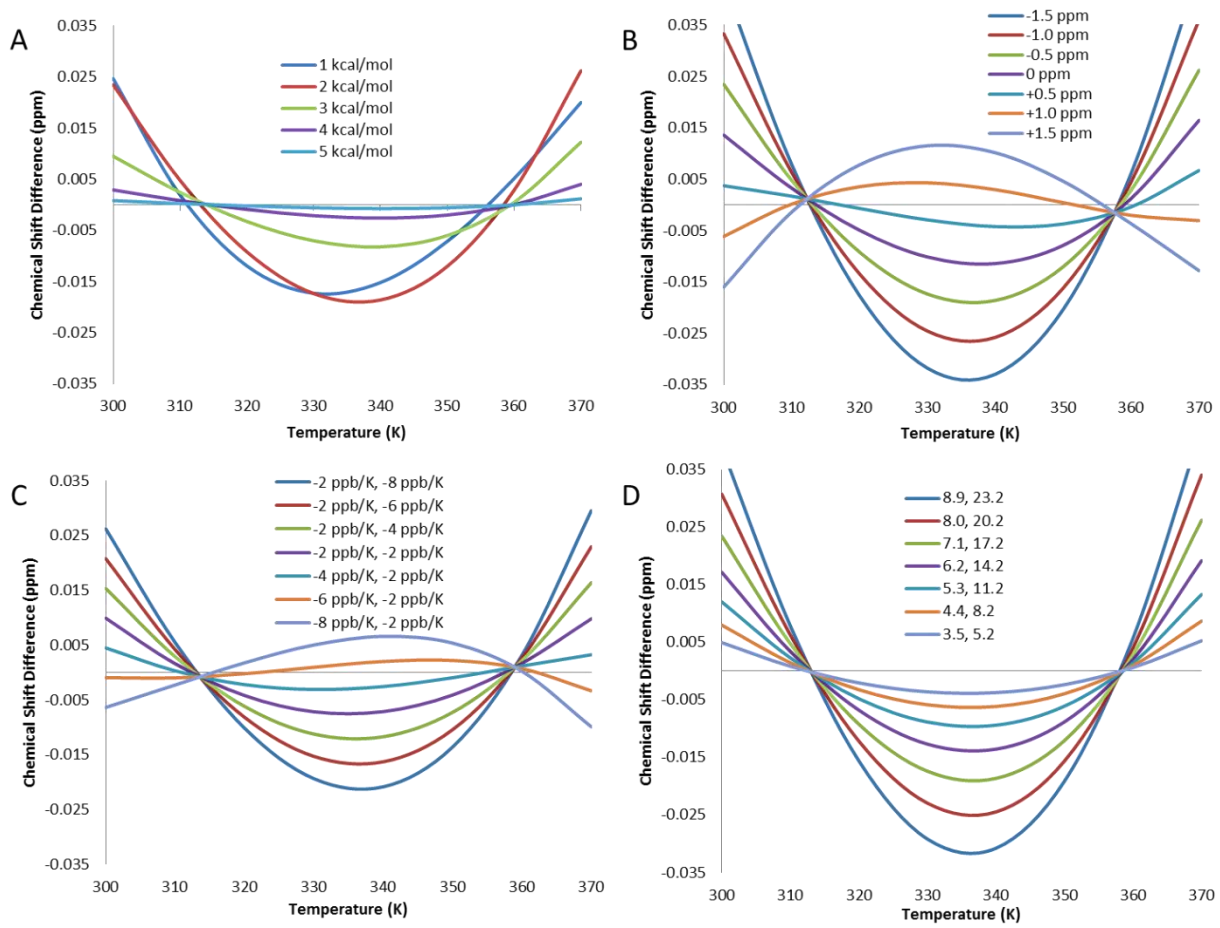

Figure 3.16 - Theoretical curved temperature dependence of N^1H accessing an excited state. (A) Simulations of the dependence of N^1H chemical shift variation with temperature on the difference in free energy between the ground and alternative state. δ_1° = 8.5 ppm, g_1 = -2 ppb/K. δ_2° = 8.0 ppm, g_2 = -7 ppb/K. ΔS = 17.2 cal/mol K^{-1} and ΔH = 6.1, 7.1, 8.1, 9.1 and 10.1 kcal/mol corresponding to ΔG = 1, 2, 3, 4 and 5 kcal/ mol, respectively. The calculated δ_{obs} values were fit using linear regression to a straight line. The deviations from linearity (δ_{linfit} - δ_{obs}) are plotted against temperature. (B) Simulations of the dependence of N^1H chemical shift variation with temperature on the chemical shift difference between the ground and excited state. δ_1° = 8.5 ppm, g_1 = -2 ppb/K. δ_2° is varied from 7 to 10 ppm at 0.5 ppm increments, g_2 = -7 ppb/K. The number given in the figure legend is δ_2° - δ_1°. ΔG = 2 kcal/mol corresponding to ΔH = 7.1 kca/mol and ΔS = 17.2 cal/mol K^{-1}. (C) Simulations of the dependence of N^1H chemical shift variation with temperature on the difference in the *g* between the ground and excited state. The *g* values are given in the figure legend for the ground and alternative states. δ_1° = 8.5 ppm, δ_2° = 8.0 ppm. ΔG = 2 kcal/mol corresponding to ΔH = 7.1 kca/mol and ΔS = 17.2 cal/mol K^{-1}. (D) Simulations of the dependence of N^1H chemical shift variation with temperature on differences in ΔH and ΔS, given in the figure legend as ΔH, ΔS. ΔG is maintained at 2 kcal/mol. δ_1° = 8.5 ppm, g_1 = -2 ppb/K. δ_2° = 8.0 ppm, g_2 = -7 ppb/K.

The simulations reveal that the curvature is a result of the complex interplay between the associated shift differences, temperature coefficients and thermodynamic parameters. The curvature is most pronounced when the difference in free energy between the two states is small and becomes

essentially negligible at $\Delta G \geq 5.0$ kcal/mol (Figure 3.16 A). Other parameters can affect this limit, however. For example, if the chemical shift of the alternative state is shifted upfield by a very large amount or its gradient is significantly more negative, higher energy states may be observed (Figure 3.16 B, C). An increase in ΔH and ΔS will also increase the observed curvature (Figure 3.16 D). In most cases, the curvature is concave (negative value of *a* in Eq. 3.1) however the curvature can be convex (positive value of *a* in Eq. 3.1). The latter happens when the chemical shift of the alternate state is shifted downfield by ≥ 1.0 ppm or the temperature coefficient of the alternative state is much more positive (smaller) than for the ground state. The second scenario may represent the alternative state being more structured (as it is less affected by temperature).

Some assumptions may be made to obtain set limits on the ΔG difference between the two states for residues with observed curvature in proteins. The typical conformation-dependent range of chemical shifts in backbone amide protons is approximately 1-2 ppm (*180*). However, since the alternative state is thought to be the result of a small, local conformational change for up to 5 residues, the difference in chemical shift between the two states is likely smaller. An upfield shift of 0.5 ppm towards random coil for the alternative state (i.e. from 8.5 to 8.0 ppm) was therefore assumed. It has been proposed that the alternative state likely exhibits alternative hydrogen bonding patterns (*180*). Therefore, one can assume a more structured ground state with an average temperature coefficient for a hydrogen bonded proton of -2 ppb/K. The alternative state can be chosen to have an average temperature coefficient for a proton not participating in a hydrogen bond, -7 ppb/K. The thermodynamic parameters can be described as in the study of the excited state of T4 lysozyme (see above) (*209*). The parameters described above are the same as those used in the simulation to illustrate how differences in ΔG affect curvature (Figure 3.16 A). The extent of curvature can be quantified by the quadratic coefficient (*a*) which can be obtained by fitting the residual values (deviations of observed shifts from linearity, $\delta_{linfit} - \delta_{obs}$) to the quadratic equation (see methods). Consistent with Figure 3.16 A, there is a correlation between *a* and ΔG (Figure 3.17). It should be noted that due to the small magnitude of the residual curvature and the experimental uncertainties in

N^1H chemical shifts (0.005 ppm), as well as the assumptions discussed above, this analysis simply provides an estimate of the difference in ΔG between the ground and alternative state.

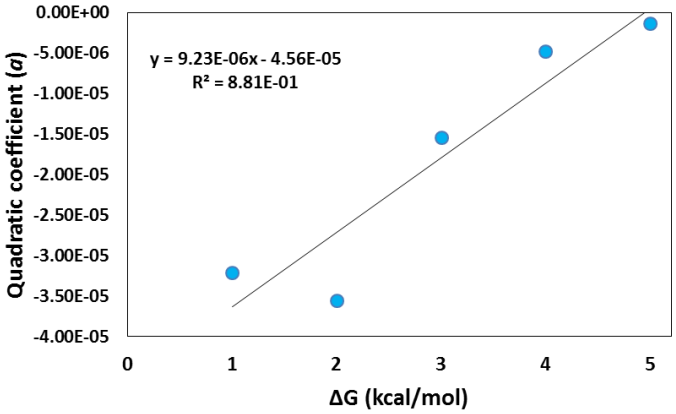

Figure 3.17 - Correlation between the quadratic coefficient (*a*) and the ΔG difference between the ground and alternative state for simulated residual chemical shift values. The line of best fit obtained by linear regression is given by a black solid line. The associate equation and R^2 value is given in the plot area.

3.3.6.2 Residues displaying curved temperature dependences in SOD1

The observed N^1H chemical shifts of pWT at each temperature were fit to a straight line. The residuals (deviations from linearity) were calculated and plotted as a function of temperature (Figure 3.18). For each residue, the residual values were fit to the quadratic equation. To assess curvature, the residuals were visually inspected considering the associated *a* value, the quality of the fit and the uncertainties in the measured N^1H chemical shifts. This method, albeit somewhat subjective, has been used previously to assess curved temperature dependences (*163, 177, 179, 180*). The results indicate that in pWT 50 out of the 153 residues (~33%) are accessing an alternative state. Of these residues displaying curvature, 94% had concave curvature. Simulations (Figure 3.16) reveal that this likely represents a more disordered alternative state in pWT. Residues accessing alternative states have N^1H temperature coefficients spanning the entire range seen in pseudo WT, with approximately half less positive than -5 ppb/K. The majority of residues in pWT are accessing an alternative state estimated to have a free energy difference from the ground state of 2 – 3.5 kcal/mol.

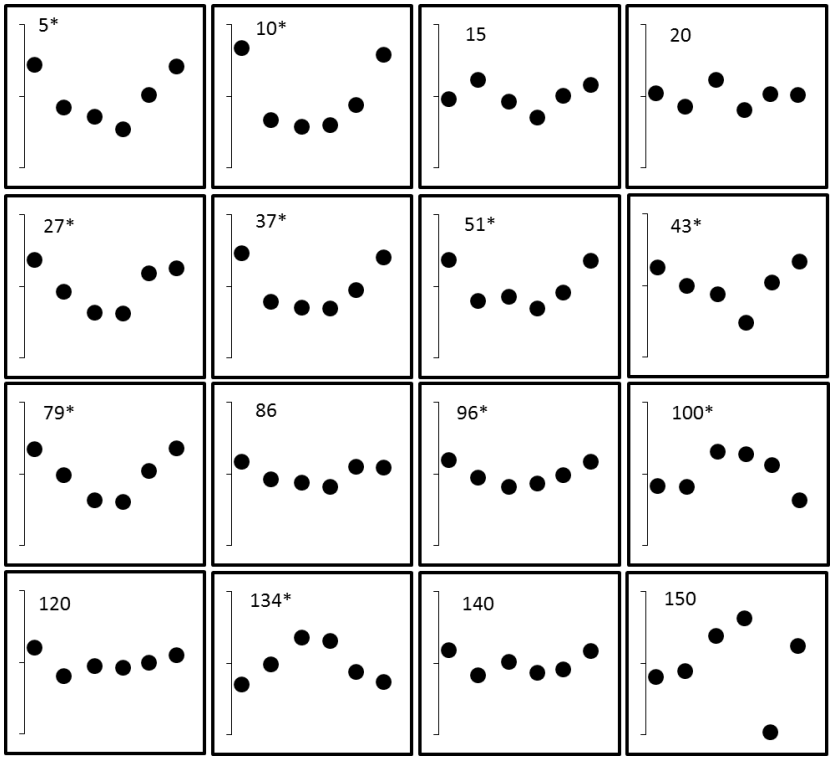

Figure 3.18 - Plots of residual N^1H chemical shift against temperature for representative residues in pWT. The graphs are labelled with residue number and asterisk is used to highlight residues characterized as having curved temperature dependences. The vertical axis has a total range of 0.04 ppm. The horizontal axis covers the temperature range 297-357 K. Scales of the plots are comparable to those used in previous studies (*178-180*).

Residues accessing alternative states are spread throughout the entire polypeptide chain of pWT in both β-strands and loops (Figure 3.19). Based on the crystal structure, the amide proton of 59% of residues in pWT is expected to participate in an intramolecular hydrogen bond. The higher percentage of hydrogen bonded residues accessing alternative states (76%) could suggest that the higher energy state may be achieved through loss of a hydrogen bond. Overall β-sheet 1 (β-strands 1, 2, 3 and 6) shows more conformational heterogeneity than β-sheet 2 (β-strands 4, 5, 7 and 8). This is consistent with the N^1H temperature coefficients indicating that sheet 1 is less stable (see section 3.3.3.1). Specifically, residues accessing alternative states cluster in β3, β4, β6 and to some extent β1. It has previously been shown that regions with decreased stability in proteins tend to be more significantly populated with residues accessing alternative states (*177*). Also, β1, β3 and β6 lose structure first in the unfolding pathway of pWT (section 3.3.3.1), which may reflect increased conformational heterogeneity in these strands.

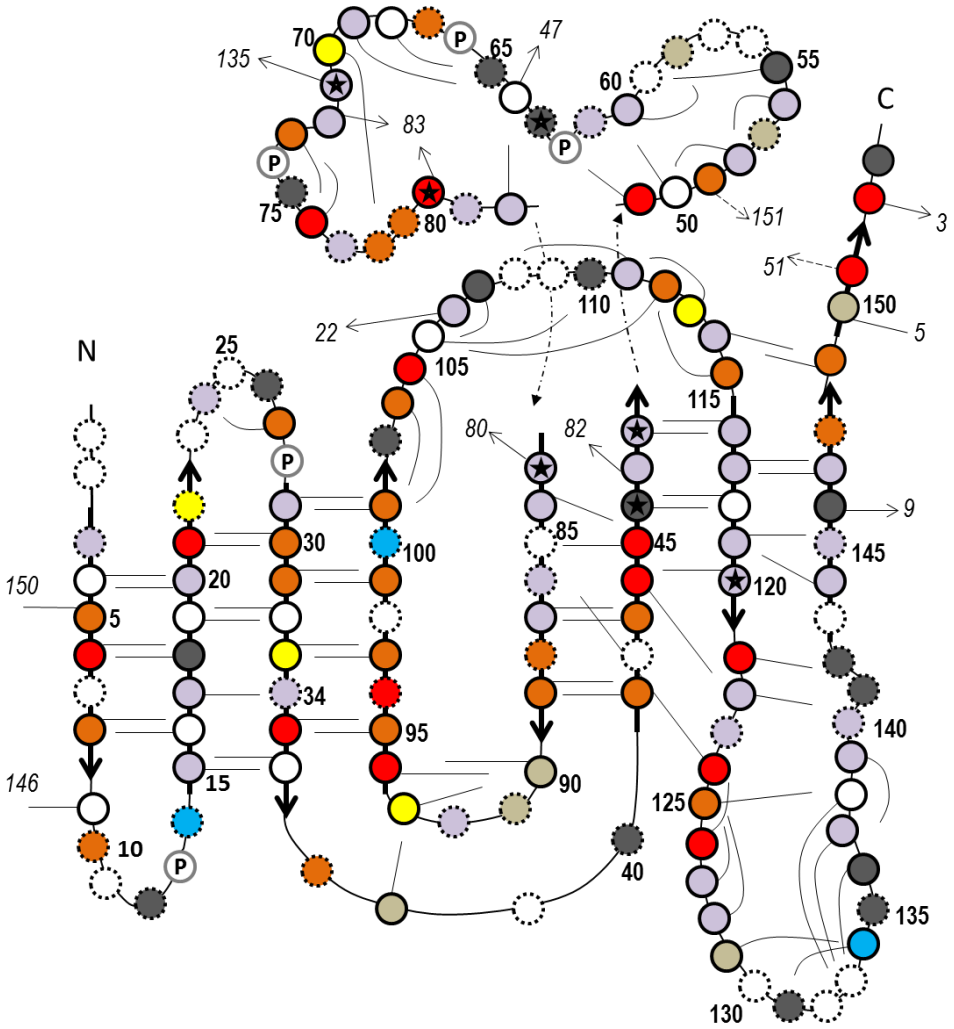

Figure 3.19 - Cartoon representation of pWT highlighting residues with curved N^1H temperature dependences. Each circle represents a residue in the protein. A solid border indicates the amide proton of that residue participates in a hydrogen bond. A dashed border indicates it does not. Circles that lie on top of arrows represent residues in β-strands. Hydrogen bonds are represented as solid black lines connected to the N^1H and pointing towards the oxygen acceptor. Circles with 'P' in the center represent proline residues which have no amide proton. Circles with stars in the center represent metal binding residues. Light purple indicates residues that appear to have linear temperature dependences. Yellow, orange and red indicates residues estimated to access an alternative state with a ΔG of 0 – 2 kcal/mol, 2 – 3.5 kcal/mol, and 3.5 – 5 kcal/mol, respectively. Dark grey indicates residues that disappear at increased temperatures. White indicates residues for which there are no data. Beige is used to indicate residues that do not fall into any of the above categories.

A number of resides in β4 (of sheet 2) appear to be accessing a higher energy state. The N^1H temperature coefficients reveal that β4 is relatively stable with slight loss of structure at the ends of the strand. However, residues in the strand populate alternative conformations estimated between 2 and 5 kcal/mol. Two residues in β4, His46 and His48, are metal binding residues. A definitive explanation for

the increased conformational heterogeneity in β4 cannot be given however one possibility is that altered or weakened metal binding at increased temperatures may affect this strand which contains a greater proportion of metal binding residues than any other strand. Altered or weakened metal binding at increased temperatures is supported by the significant degree of conformational heterogeneity observed in loop IV, specifically near the zinc binding site (residues 63 - 82). Residues in this region are found to have reduced stability based on N^1H temperature coefficients (section 3.3.3.1, Figure 3.8). Loop IV contains three metal binding residues (metal binding residues are marked with stars in Figure 3.19), including His80 which exhibits significant curvature and His63 which disappears at increased temperatures. The zinc binding site is also protected by loop VII. In this loop, five residues have curved temperature dependences and five disappear. Interesting, most of the residues that access an alternative state are located in the N-terminal half of the loop and most of the residues that disappear are in the C-terminal half. This suggests that there is increased disorder in the C-terminal half of the loop and is supported by N^1H temperature coefficients which reveal that many of the hydrogen bonds that tether this half of the loop to the N-terminal half are lost. Taken together, the results suggest that there is a significant amount of conformational heterogeneity in the two long loops (loops IV and VII), especially in the regions that protect the zinc binding site. Overall, the residues accessing alternative states correlate well with regions of the protein expected to have decreased local stability based on N^1H temperature coefficients and previous experimental work (*6, 189*). A negative correlation between local stability and conformation heterogeneity has also been observed in cytochrome *c* (*177*).

Analysis of G93A reveals that 47 (31%) residues have curved temperature dependences which is quite similar to what is seen for pWT (Figure 3.20). As a whole, the results indicate the mutant is able to access higher energy alternative states. Regions of G93A showing conformational heterogeneity are similar to those identified in pWT, with the exception of β4. In this mutant, most residues in β4 appear to have linear temperature dependences with the exception of the first and last in the strand. This does not necessarily mean that these residues are not accessing alternative states but could mean that the strand is

significantly disordered or residues are accessing higher energy conformations (> 5 kcal/mol) not observable by this method (*180*). Analysis of N^1H temperature coefficients reveal that this core strand is stable and so disorder is likely not the cause. Three metal binding residues disappear in G93A (opposed to two that disappear in pWT) which could indicate loss of structure surrounding the metal binding site. Further, loop IV shows less conformational heterogeneity in the zinc binding region (residues 63 – 82) however five residues disappear in this region compared to the three that disappear in pWT. Lack of structure would likely increase both chemical and conformational exchange as it would increase solvent accessibility as well as allow for the population of significantly different conformational states, and as such would likely result in signal loss. The larger number of residues that disappear in loop IV point to increased disorder in the region surrounding the zinc binding site in G93A compared to pWT, which could cause the linear temperature dependences observed in G93A in this region (Figure 3.20). Loop VII shows a similar number of residues accessing alternative states in G93A however six residues in and around the helix in this loop disappear, again pointing to a loss of structure and deprotection of the zinc binding site. Finally, residues 50-53 in the dimer interface appear to be accessing an alternative conformation that differs from pWT since the two of the residues have a different sign of curvature. This result suggest that there may be propagating structural effects in the dimer interface for G93A.

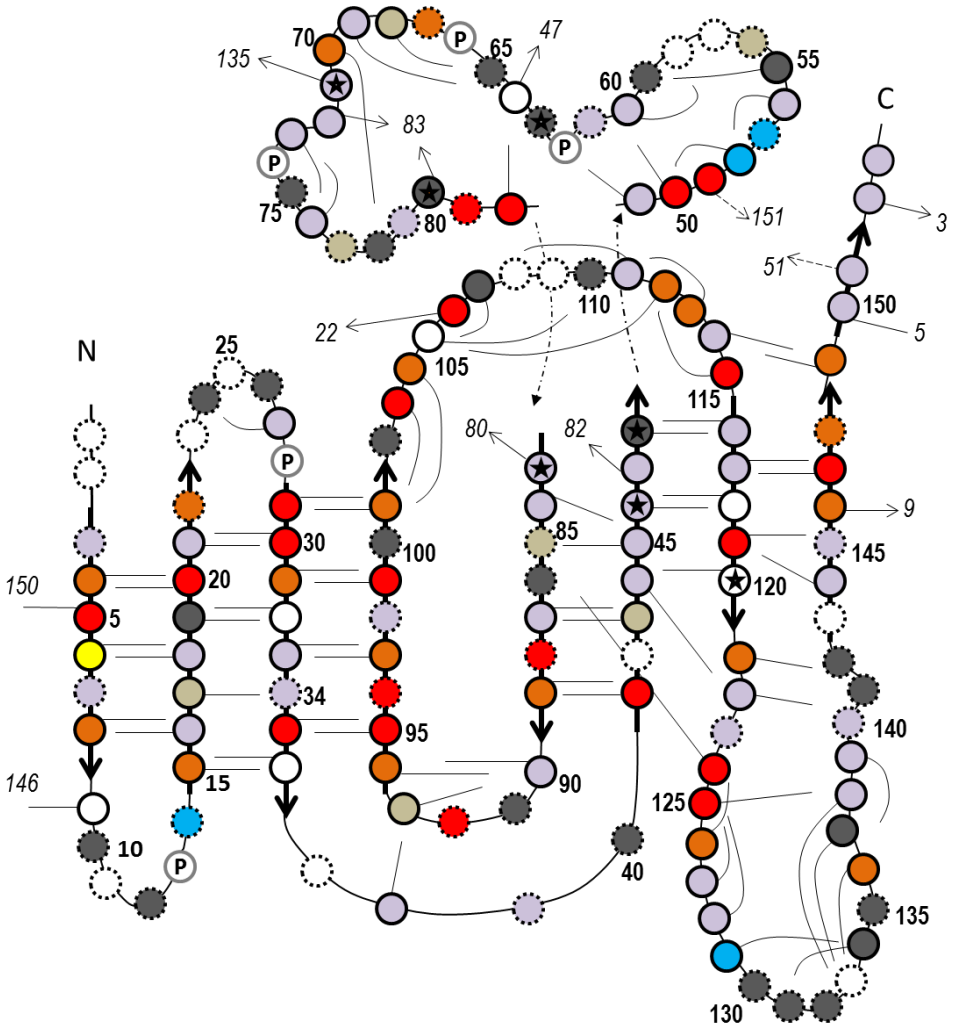

Figure 3.20 - Cartoon representation of G93A highlighting residues with curved N^1H temperature dependences. Each circle represents a residue in the protein. A solid border indicates the amide proton of that residue participates in a hydrogen bond. A dashed border indicates it does not. Circles that lie on top of arrows represent residues in β-strands. Hydrogen bonds are represented as solid black lines connected to the N^1H and pointing towards the oxygen acceptor. Circles with 'P' in the center represent proline residues which have no amide proton. Circles with stars in the center represent metal binding residues. Residues are coloured as in Figure 3.19.

Analysis of the conformational heterogeneity in E100G reveals 47 (31%) of residues access alternative high energy conformations. Again, these residues cluster in the regions identified to have high conformation heterogeneity in pWT but they are estimated to have larger ΔG differences (Figure 3.21). One exception is β3 which is dominated by residues with linear temperature dependences. This strand neighbours the strand that contains the mutation. Again, this could represent one of three situations: the residues are not accessing alternative conformations; the strand is accessing a number of different

conformations (disordered); or the residues are accessing higher energy conformations > 5 kcal/mol. At this point it is difficult to identify which is the case, however, analysis of N^1H temperature coefficients reveals increased loss of structure at β3 compared to pWT (see section 3.3.3.3, Figure 3.11). Loop IV has the largest proportion of residues displaying curved temperature dependences out of the all of the variants analyzed, clustering in the dimer interface (residues 49 - 61) and at the zinc binding site (residues 63 – 82). The results indicate that this loop contains a significant number of residues accessing an alternative state but likely remains more structured in E100G than G93A and similar to pWT. This is supported by 5 residues (His63, Asn65, Lys75, Glu78 and His80; Table A1.1) disappearing in G93A in this loop near the zinc binding site while only 2 disappear in E100G (Asn65, Lys75; Table A1.1). There are 7 residues that display convex curvature (Val14, Gly16, Phe20, Glu40, Asp52, Glu78 and Gly129) in E100G opposed to the 3 in pWT (Val14, Gly100 and Ser134). These residues are spread throughout the polypeptide chain and are found mainly in loops. Simulations suggest that the altered curvature may report on a more structured alternative state. Consistent with this, most of these residues have smaller N^1H temperature coefficients. Interestingly, 3 of the residues (Glu40, Asp52 and Glu78) with convex curvature are directly beside a residue accessing a high energy alterative state and therefore for these residues the altered curvature may represent compensatory stabilization in the mutant (*108*).

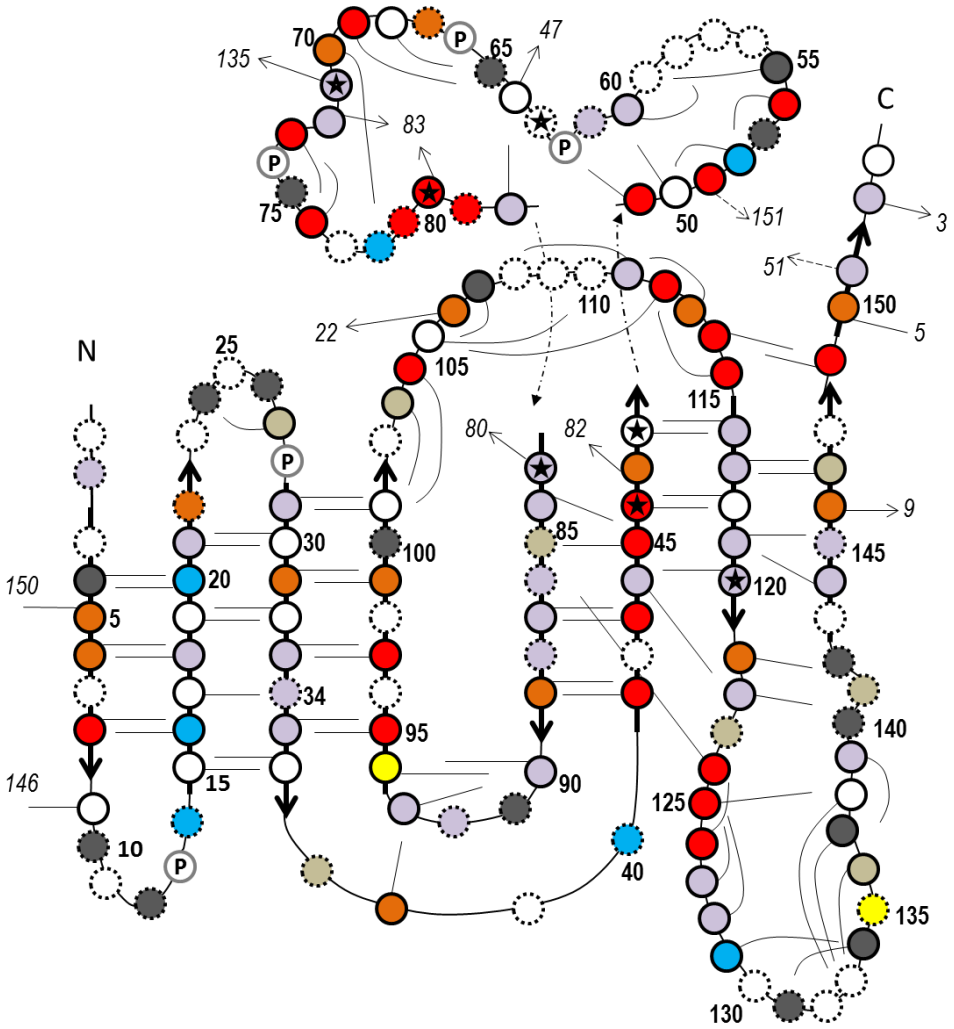

Figure 3.21 - Cartoon representation of E100G highlighting residues with curved N^1H temperature dependences. Each circle represents a residue in the protein. A solid border indicates the amide proton of that residue participates in a hydrogen bond. A dashed border indicates it does not. Circles that lie on top of arrows represent residues in β-strands. Hydrogen bonds are represented as solid black lines connected to the N^1H and pointing towards the oxygen acceptor. Circles with 'P' in the center represent proline residues which have no amide proton. Circles with stars in the center represent metal binding residues. Residues are coloured as in Figure 3.19.

DSC simulations and analysis of N^1H temperature coefficients reveal that the fALS mutant V148I is more stable than pWT (Figure 3.5). In agreement with this, V148I has the smallest number of residues (44, 29%) accessing alternative conformations. As for the other mutants, the residues that do show conformational heterogeneity in this mutant are accessing higher energy states than seen in pWT. Somewhat surprisingly, V148I appears to have the largest proportion of residues accessing alternative states with ΔG of 3.5 - 5 kcal/mol. These residues cluster in the same regions as in pWT, however, as in

G93A, β4 in V148I is dominated by residues with linear temperature dependences. V148I has the largest proportion of residues with convex curvature, most of which have smaller N^1H temperature coefficients compared to WT. Loop VII (which precedes the strand that contains the mutation) exhibits significantly less conformational heterogeneity than in the other variants with only two residues (Glu121 and Gly129) accessing an alternative conformation and only three residues (Asn131, Ser134 and Ser142) disappearing at increased temperatures. This suggests greater stability in the electrostatic loop for this mutant even compared to pWT. Near position 148 in pWT a number of residues have curved temperature dependences however this is not the case in V148I. Although this could indicate increased disorder for the mutant in this region, due to the higher stability of V148I by DSC and stronger hydrogen bonding in this region (determined from N^1H temperature coefficients), it is plausible that these residues simply do not display conformation heterogeneity in V148I.

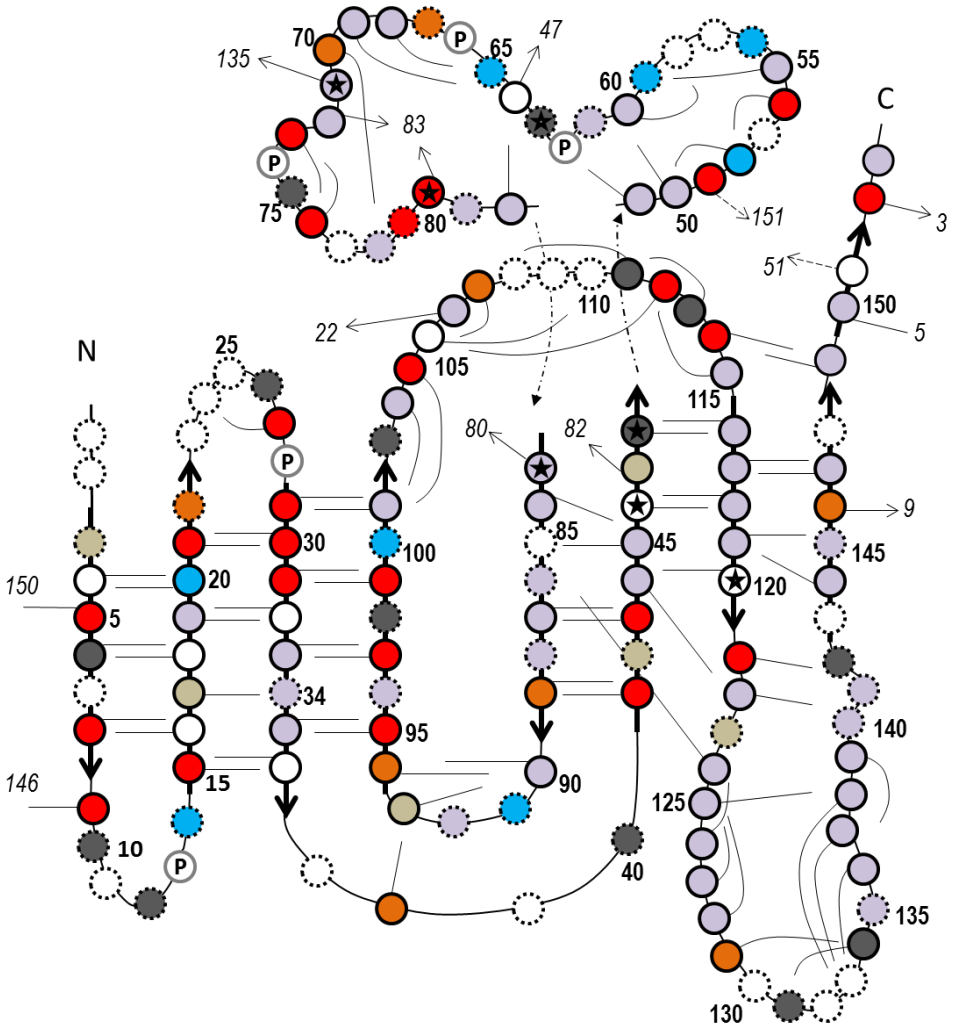

Figure 3.22 - Cartoon representation of V148I highlighting residues with curved N^1H temperature dependences. Each circle represents a residue in the protein. A solid border indicates the amide proton of that residue participates in a hydrogen bond. A dashed border indicates it does not. Circles that lie on top of arrows represent residues in β-strands. Hydrogen bonds are represented as solid black lines connected to the N^1H and pointing towards the oxygen acceptor. Circles with 'P' in the center represent proline residues which have no amide proton. Circles with stars in the center represent metal binding residues. Residues are coloured as in Figure 3.19.

Overall, a similar number of residues show access of higher energy alternative states in pWT and the three disease-associated mutants described above. Comparison of curvature results with N^1H temperature coefficients indicate that regions with decreased local stability also display larger conformational heterogeneity, which is structurally reasonable and has previously been observed for other proteins (*177*). Interestingly, the results show that as a whole, mutants appear to be accessing high energy alternative states compared to pWT. This is true even for V148I which has been shown to have greater

global stability than pWT. It remains unknown whether or not the ability to access higher energy alternative states is a general consequence of mutation, however, the results here point to this being true regardless of global stability.

3.4 Discussion

Considerable information can be obtained from monitoring the temperature dependences of the ^{1}H-^{15}N cross peaks of proteins. Since more is known about the factors that underlie $N^{1}H$ temperature coefficients, these remain the main source of information for structural interpretations (*165*), however, the results here show that differences in ^{15}N temperature coefficients are likely reporting on genuine differences between proteins as well (see section 3.3.5.2). In this analysis, hydrogen bonds are deemed "lost" if they are predicted to form based on crystal structure data but have a high probability of not occurring based on $N^{1}H$ temperature coefficients. Differences in the predicted hydrogen bonding status between crystal structure data and $N^{1}H$ temperature coefficients can be caused by one of two scenarios: (1) the hydrogen bond observed in the crystal structure is simply not formed in solution at any temperature or (2) the hydrogen bond is disrupted early in the thermal unfolding of pWT. NMR temperature dependence studies indicate that the thermal unfolding process of holo pWT begins with "fraying" of the structure at its periphery. In particular, a significant loss of hydrogen bonding is observed at edge strands β5 and β6, as well as in the long loops IV and VII (Figure 3.9). Disruption of the hydrogen bonding network in the dimer interface is also observed which could suggest a weakening of the interface at increased temperatures. Previous NMR relaxation experiments monitoring the backbone dynamics of holo SOD1 indicate that all β-strands in the dimer have equal flexibility at 25°C (*182*). Therefore, the loss of hydrogen bonding observed by temperature coefficients at the β3 - β6 and β5 - β6 interfaces is likely a result of the second scenario indicating hydrogen bonds are lost at increased temperatures and reflect decreased local stability in the edge strands.

Overall, β-sheet 1 (β-strands 1-3, 6) appears to be more perturbed by temperature than β-sheet 2 (β-strands 4, 5, 7 and 8) in holo pWT (Figures 3.8 and 3.9). This is interesting as the opposite has been observed for apo SOD1, with β-sheet 2 having decreased stability (*49*). The conflicting results can be resolved by considering how metal binding affects the structure of SOD1. Out of the 7 metal binding residues in SOD1, 4 are located in β-sheet 2 while none are in β-sheet 1. Upon metal binding, β-strands 4 and 7 become significantly more structured (*120*). Metal binding also favours dimerization which helps to protect the edge strand β8 located in the dimer interface (*54, 189*). The increased structural integrity conferred to β-sheet 2, as compared to β-sheet 1, upon metal binding can explain the observed differences in local unfolding between the holo and apo forms of SOD1.

Curved N^1H temperature dependences can reveal population of an alternative state close in energy to the ground state. A number of studies have found that a significant proportion of residues in proteins access these alternative states, highlighting the dynamic nature of proteins in solution (*163, 176-178, 180*). An interesting finding was the correlation between residues populating alternative conformational states and the unfolding pathway in cytochrome *c* (*177*). The folding of this protein has been studied extensively and regions expected to fold last displayed the highest population of residues with curved temperature dependences. It was proposed that residues displaying curvature may represent the earliest cooperative unfolding unit of a protein. Kinetic studies of holo pWT SOD1 reveal that β5 and β6 are unstructured in the transition state (*126*). Loop IV (discussed further below), which precedes β5, and loop VII are also fairly unstructured in the transition state. These regions are thus likely the last to fold in the SOD1 pathway and here were shown to have the highest population of residues with curved temperature dependences (Figure 3.19). These results are consistent with the results for cytochrome *c* and thus likely represent the earlier cooperative unfolding units in holo pWT.

Analysis of metal binding affinity reveals that copper binds more strongly to SOD1 than zinc (*122*). This is structurally reasonable as zinc-coordinating residues are found mainly in loop IV while copper coordinating ligands are found mainly in core β-strands (Figure 1.4) (*58*). Previous kinetic studies

monitoring the unfolded pathway of holo SOD1 show that the major unfolding pathway involves dimer dissociation to form a monomer intermediate, followed by monomer unfolding (*126*). Both metals remain bound throughout dimer dissociation; with zinc dissociation occurring from the monomer intermediate and copper dissociation later from the unfolded monomer. Monitoring the effect of metals on the unfolding kinetics revealed that the copper binding site is largely structured in the monomer unfolding transition state however the zinc site is only partially formed (*126*). Since most of the copper binding ligands are located in the core β-strands of β-sheet 2, this suggests that the monomer core is likely formed early in the folding pathway. Again, based on N^1H temperature coefficients and curved temperature dependences, the core of the SOD1 monomer is shown to remain fairly structured with little conformational heterogeneity up to 84°C.

As mentioned above, loop IV contains most of the zinc binding residues and upon metal binding becomes highly structured (*120*). The increased flexibility observed in this loop at high temperature may therefore indicate altered/weakened metal binding. This may also explain the increased conformational heterogeneity observed in β-strand 4 (Figure 3.19), which is expected to be structured in the holo state but disordered in the apo state. The majority of residues in loop IV display concave curvature with temperature which commonly represents a less structured alternative state and is consistent with the loss of hydrogen bonding indicated by N^1H temperature coefficients. It is interesting to note that concomitant with the increased disorder in the zinc binding site there is increased disorder at the dimer interface, suggesting coupling between these regions. Metal binding is known to promote dimerization and vice versa (*54*). Thus, disorder in one of these sites could promote disorder in the other. This is consistent with the major unfolding pathway of holo SOD1 which has been shown to involve dimer dissociation followed by rapid zinc loss as the first steps (*125*).

It is important to note there is no indication of metal loss in the NMR experiments conducted here, despite the increased disorder in the metal binding region. In the HSQC spectrum of pWT, Gly61 (located in loop IV) has a well resolved cross peak that shows distinct chemical shift changes upon metal

binding. Considering this, even at the highest temperature studied, metals appear to remain bound to pWT. Lack of metal loss is also consistent with the extremely high affinity of the SOD1 for metals (*122*) and the observation that metals appear to remain bound to globally thermally unfolded SOD1 (*82*). Also, analysis of the pWT HSQC spectrum at 24°C (obtained upon cooling after heating to 84°C) reveals that any spectral changes observed in pWT are reversible. Overall, the results of the NMR temperature dependence studies of pWT not only identify regions of decreased local stability but suggest that the conformational ensemble in solution contains several conformations close in free energy to the native state making the ensemble one with high structural entropy (*210*).

3.4.1 Mutational effects on local unfolding of SOD1

Disease-associated mutants G93A, E100G and V148I all display similar local unfolding patterns to pWT, but also have distinct differences surrounding the mutation site. Interestingly, in all three mutants altered dynamics are observed in the β-barrel plug which could represent a common propagating structural effect upon mutation, however, the extent of destabilization differs between mutants. As may be expected based on the site of mutation, G93A displays the greatest flexibility at the β-barrel plug (Figure 3.10). It appears that mutation from Gly to Ala in loop V significantly disrupts the local hydrogen bonding network decreasing the stability in this region. In addition, G93A exhibits even greater disorder surrounding the zinc binding site when compared to pWT. This is evidenced by the larger proportion of residues that disappear at increased temperature in loops IV and VII in the mutant. Signal loss can be the result of either chemical or conformational exchange (see section 3.3.3.1), both of which can be promoted by loss of structure. Aggregation studies of holo G93A reveal a shorter lag time prior to the onset of aggregation than observed for pWT (*92*). It could be that propagating destabilizing effects in the metal binding region favour zinc loss in G93A, a process known to promote protein aggregation. Destabilization of the metal binding region for G93A has also been observed in amide exchange studies (*189*).

Based on DSC and chemical denaturation (*6*, *149*) (see also section 3.3.2), mutation of Glu to Gly at position 100 destabilizes SOD1 more than the other mutants studied here. Counterintuitively, the H^1N temperature coefficients, conformational heterogeneity and amide exchange rates observed for E100G are most similar to pWT of any of the mutants studied. Gly has a relatively high degree of conformational freedom compared to other amino acids and therefore introducing Gly at the end of β6 likely increases mobility near the site of the mutation. Interestingly, the mutated Gly residue disappears at increased temperature suggesting that there may be a high degree of conformational exchange. In addition, Asp101, which neighbours Gly100, is the acceptor of 3 hydrogen bonds from the N^1Hs of Val29, Val103 and Ile104. In E100G two of these hydrogen bonds are lost, in agreement with increased mobility surrounding the mutation site. The results indicate that the disorder observed at edge strand β6 is increased in E100G, as well as in β3 and loop VI (see section 3.3.3.3).

By DSC, the third mutant, V148I, is globally more stable than pWT (Figure 3.5). The NMR results indicate that upon mutation, almost one third of residues display decreased N^1H temperature coefficients; however, in over half of these, the smaller coefficient is indicative of a weaker hydrogen bond. It appears that introduction of the bulkier hydrophobic side chain into the dimer interface significantly affects the hydrogen bonding network extending throughout the protein. This is physically reasonable as the dimer interface has been identified as a region with high connectivity to distal areas in the protein (*104*). It should be noted however, that since there were differences in data acquisition for V148I (see sections 3.2.2 and 3.2.4), to have the full confidence in the results the variable temperature NMR experiment for V148I should be repeated on the same spectrometer with identical pulse programs, acquisition parameters and temperatures.

The results for both E100G and V148I suggest that local stability may not always be representative of global stability. V148I, for example, despite displaying a significant proportion of residues with weaker hydrogen bonds has increased global stability. NMR relaxation experiments analyzing changes in backbone mobility of the peptidyl-prolyl isomerase Pin1 upon binding of different

ligands revealed an interesting trend in protein stability (*108*). Here, ligand binding results in regions of the protein having both increased and decreased flexibility. It was found that stiffening along a conduit of hydrophobic residues that linked the domain interface to the active site was positively correlated with binding affinity. In addition, in many cases residues with increased flexibility directly neighboured residues with decreased flexibility. A similar trend of both increased and decreased flexibility upon mutation is observed in holo SOD1 mutants. In G93A, for example, the increased dynamics in the β-barrel plug is accompanied by a strengthening of the hydrogen bond between Ile35 and Ala95 (located in β6 next to the β-barrel plug). Also, residues with increased stability upon mutation are not always local to the mutation, but rather for all three mutants can be found at various locations throughout the protein. Increases as well as decreases in local stability upon mutation were also observed in amide exchange experiments of holo SOD1 mutants (*6*). Thus, measurements of global stability do not give the full picture regarding changes in protein structure; as NMR studies reveal that mutations can cause complex changes in local stability that propagate through the structure (*6, 108*), which may provide insight into aggregation mechanisms.

3.4.2 Conclusions and implications for SOD1 aggregation

The thermal unfolding of both WT and mutant SOD1 begins with loss of structure at edge strands β5 and β6. The decreased local stability observed in this region suggests that the edge strands may undergo local unfolding in response to environmental perturbations. Loss of these protective edge strands may expose the hydrophobic core of the SOD1 monomer, which could provide a site for non-native interactions. These edge strands have been proposed to act as "gatekeepers" preventing the aggregation of SOD1 (*52, 105*); however, the location of these strands at the periphery of the structure make them logical candidates for spontaneous unfolding in the rapidly interconverting ensemble of conformers found in solution (*205*). These NMR experiments suggest that upon heating, conformers with disorder at the edge strands become significantly more populated and longer lived. Further, loss of the continuous hydrogen bonding network around the β-barrel cylinder puts SOD1 at risk for edge-to-edge aggregation (see section

1.6.6). The long loops IV and VII also become disordered early in the thermal unfolding, especially for G93A. These loops have been shown previously to form non-native contacts in apo SOD1 assemblies and local unfolding in these loops could lead to protein aggregation (*89*). In pWT, the structural integrity of the β-barrel plug is maintained despite the increased mobility observed at the edge strands. The opposite is true for each of the mutants analyzed here (G93A, E100G and V148I). Specifically, in all 3 mutants increased mobility is observed at Leu38 (the "plug" residue, see section 3.3.3), which fills a cavity formed by surrounding residues (*58, 78*). Loss of structural integrity at the β-barrel plug in combination with the increased mobility at the edge strands suggest an increased opening of the two β-sheets and greater solvent exposure of the hydrophobic interior in mutant SOD1. These findings are in agreement with MD simulations that reveal altered dynamics in the β-barrel plug for A4V, H46R and G37R (*104*), which may point to a common pathway for mutant SOD1 aggregation.

CPMG experiments of the apo monomer variant of WT and mutant SOD1 reveal that generally there appears to be increased structural distortion in an excited state of mutant SOD1s compared to WT (*193*). Analysis of residues with curved temperature dependences reveals a similar trend with holo SOD1 mutants being able to access higher free energy alternative states compared to pWT. Another possibility is that protein aggregation may not be the result of local unfolding but rather occur via non-native association of these transiently populated higher energy conformations. The structure of the alternative state observed in these experiments is unknown, however direction of curvature (see section 3.3.6.1) suggests that for almost every reside the alternative state is more disordered. It could be that aggregation is more likely to occur from higher energy alternative states which are more easily accessed by mutant SOD1.

3.4.3 Future work

In this chapter, NMR temperature-dependence experiments have been described for analyzing the stability and dynamics of SOD1. Analysis of N^1H temperature coefficients have allowed for a residue-

specific picture of the subglobal disruption of structure in SOD1, with identification of regions having decreased local stability. In addition, the dynamic behaviour of SOD1 was characterized by assessing residues displaying curved temperature dependences providing information on high free energy alternative states. The application of these experiments to additional fALS mutants will further aid in the understanding of how point mutations affect the local stability of SOD1. Analysis of common and distinct structural changes between mutants may help to explain their common (aggregation) and distinct (duration) disease characteristics. Further, the study of additional mutants will allow for expansion of the comparative analysis between local and global stability which may help to elucidate the role of local flexibility in protein folding, protein engineering and protein aggregation.

It would also be of interest to analyze how metal loss affects the structure of SOD1. The experiments herein and previous experiments indicate that zinc is likely lost first in the unfolding pathway SOD1. It would be interesting to conduct NMR experiments on apo and copper bound SOD1 to see how the pattern of local unfolding is affected by loss of zinc. It should be noted that these experiments may be more difficult for a number of reasons. First, assignments would need to be completed at 25°C for SOD1 in the altered metal states. Second, since the protein is less structured in more immature or mismetallated forms, peak overlap would present a larger problem increasing the difficulty of following peaks with temperature. Lastly, a smaller temperature range would need to be used to avoid global unfolding as well as smaller temperature increments to ensure accurate tracking of the peaks. However, with careful consideration I believe these experiments would provide important information of how metallation affects the hydrogen bonding network throughout SOD1, local stability, the unfolding pathway and access of high energy alternative states which again would be instrumental in the greater understanding of SOD1 aggregation.

3.5 Insights into SOD1 metal binding from PAR assay and NMR analyses combined

In the apo and holo forms, SOD1 displays striking differences in stability, activity and flexibility (*81, 88*). In most cases the binding of metal cofactors to proteins increases thermodynamic stability, which is especially true for SOD1 (*81, 109*). This is because metal binding results in significant structuring of the protein, especially in β4, β7, loop IV and loop VII (*120*). Mutations on the other hand have been shown to increase the flexibility of SOD1 on both a local and global scale (*104*). It may be true that the increased flexibility caused by mutation predisposes mutants to more easily lose metals; a general consequence proposed to be a result of mutation (*122*). The NMR temperature dependence experiments completed here show decreased local stability surround the zinc binding site but there is no indication of metal loss. Previous studies monitoring the unfolding kinetics of SOD1 reveal that zinc loss precedes copper loss (*125, 126*). These results combined suggest that increased flexibility surrounding the zinc binding site may precede zinc loss and therefore there may be a negative correlation between flexibility in the metal-binding site and metal affinity.

The NMR temperature dependence experiments reveal that the effects of mutations propagate, with residues throughout the structure displaying both increased and decreased flexibility. Based on this result, it is structurally reasonable that regardless of the site of mutation, mutants could display altered/weakened metal binding. In addition, since the zinc binding residues are located in loops shown here to have decreased local stability, the predisposition of mutants to more easily lose zinc upon environmental perturbations is a logical hypothesis. Metal quantitation using the PAR assay (Chapter 2) indicates that mutants may have reduced zinc incorporation compared to copper. Interestingly, G93A which shows even greater disorder in the zinc binding site compared to pWT (based on NMR temperature dependence studies), also displays significantly reduced zinc incorporation (by ~11%) as measured by PAR.

The metal-binding mutant G85R is an interesting variant as the comparative analysis of the correlation between metallation and global stability suggests that the typical stability conferred to SOD1 by metal binding is lost in this mutant (see section 2.3.1.6). NMR temperature dependence studies were attempted to investigate the local stability of this mutant, however, the HSQC at 25°C revealed incomplete metallation and extensive peak overlap prevented any further analysis. A valuable study would be to test if the extent of disorder observed in the zinc binding site of SOD1 mutants from NMR temperature dependence studies correlates with the amount of zinc lost from the protein under native conditions (see section 2.3.1.7 for proposed experiment). Additional mutants would need to be analyzed to improve the reliability of any such correlation; however, the results may provide knowledge on whether the increased disorder observed at the zinc binding site at high temperature is representative of the rapid structural fluctuations occurring in the conformational ensemble present in solution under native conditions.

References

(1) Dobson, C. M. (2004) Principles of protein folding, misfolding and aggregation. *Semin Cell Dev Biol 15*, 3-16.

(2) Levinthal, C. (1968) Are there pathways for protein folding? *Journal of Physcial Chemistry 65*, 44-45.

(3) Daggett, V., and Fersht, A. (2003) The present view of the mechanism of protein folding. *Nat Rev Mol Cell Biol 4*, 497-502.

(4) Dinner, A. R., Sali, A., Smith, L. J., Dobson, C. M., and Karplus, M. (2000) Understanding protein folding via free-energy surfaces from theory and experiment. *Trends Biochem Sci 25*, 331-9.

(5) Radford, S. E. (2000) Protein folding: progress made and promises ahead. *Trends Biochem Sci 25*, 611-8.

(6) Rumfeldt, J. A. (2006) in *Chemistry*, University of Waterloo, Waterloo.

(7) Fersht, A. (1999) *Protein Stability*, W.H. Freeman, New York.

(8) Matthews, C. R. (1993) Pathways of protein folding. *Annu Rev Biochem 62*, 653-83.

(9) Jackson, S. E. (1998) How do small single-domain proteins fold? *Fold Des 3*, R81-91.

(10) Bhuyan, A. K., and Udgaonkar, J. B. (1999) Observation of multistate kinetics during the slow folding and unfolding of barstar. *Biochemistry 38*, 9158-68.

(11) Fersht, A. R., Matouschek, A., and Serrano, L. (1992) The folding of an enzyme. I. Theory of protein engineering analysis of stability and pathway of protein folding. *J Mol Biol 224*, 771-82.

(12) Anfinsen, C. B., Haber, E., Sela, M., and White, F. H., Jr. (1961) The kinetics of formation of native ribonuclease during oxidation of the reduced polypeptide chain. *Proc Natl Acad Sci U S A 47*, 1309-14.

(13) Wang, Q., Zhuravleva, A., and Gierasch, L. M. (2011) Exploring weak, transient protein--protein interactions in crowded in vivo environments by in-cell nuclear magnetic resonance spectroscopy. *Biochemistry 50*, 9225-36.

(14) Hong, J., and Gierasch, L. M. (2010) Macromolecular crowding remodels the energy landscape of a protein by favoring a more compact unfolded state. *J Am Chem Soc 132*, 10445-52.

(15) Gershenson, A., and Gierasch, L. M. (2011) Protein folding in the cell: challenges and progress. *Curr Opin Struct Biol 21*, 32-41.

(16) Hol, E. M., and Scheper, W. (2008) Protein quality control in neurodegeneration: walking the tight rope between health and disease. *J Mol Neurosci 34*, 23-33.

(17) Mahler, H. C., Friess, W., Grauschopf, U., and Kiese, S. (2009) Protein aggregation: pathways, induction factors and analysis. *J Pharm Sci 98*, 2909-34.

(18) Uversky, V. N. (2010) Mysterious oligomerization of the amyloidogenic proteins. *Febs J 277*, 2940-53.

(19) Stefani, M., and Dobson, C. M. (2003) Protein aggregation and aggregate toxicity: new insights into protein folding, misfolding diseases and biological evolution. *J Mol Med (Berl) 81*, 678-99.

(20) Bartolini, M., and Andrisano, V. (2010) Strategies for the inhibition of protein aggregation in human diseases. *Chembiochem 11*, 1018-35.

(21) Soto, C., and Estrada, L. D. (2008) Protein misfolding and neurodegeneration. *Arch Neurol 65*, 184-9.

(22) Ilieva, H., Polymenidou, M., and Cleveland, D. W. (2009) Non-cell autonomous toxicity in neurodegenerative disorders: ALS and beyond. *J Cell Biol 187*, 761-72.

(23) Soto, C. (2003) Unfolding the role of protein misfolding in neurodegenerative diseases. *Nat Rev Neurosci 4*, 49-60.

(24) Bucciantini, M., Giannoni, E., Chiti, F., Baroni, F., Formigli, L., Zurdo, J., Taddei, N., Ramponi, G., Dobson, C. M., and Stefani, M. (2002) Inherent toxicity of aggregates implies a common mechanism for protein misfolding diseases. *Nature 416*, 507-11.

(25) Caughey, B., and Lansbury, P. T. (2003) Protofibrils, pores, fibrils, and neurodegeneration: separating the responsible protein aggregates from the innocent bystanders. *Annu Rev Neurosci 26*, 267-98.

(26) Cohen, F. E., Pan, K. M., Huang, Z., Baldwin, M., Fletterick, R. J., and Prusiner, S. B. (1994) Structural clues to prion replication. *Science 264*, 530-1.

(27) Guijarro, J. I., Sunde, M., Jones, J. A., Campbell, I. D., and Dobson, C. M. (1998) Amyloid fibril formation by an SH3 domain. *Proc Natl Acad Sci U S A 95*, 4224-8.

(28) Khurana, R., Gillespie, J. R., Talapatra, A., Minert, L. J., Ionescu-Zanetti, C., Millett, I., and Fink, A. L. (2001) Partially folded intermediates as critical precursors of light chain amyloid fibrils and amorphous aggregates. *Biochemistry 40*, 3525-35.

(29) Chiti, F., Taddei, N., Bucciantini, M., White, P., Ramponi, G., and Dobson, C. M. (2000) Mutational analysis of the propensity for amyloid formation by a globular protein. *Embo J 19*, 1441-9.

(30) McParland, V. J., Kalverda, A. P., Homans, S. W., and Radford, S. E. (2002) Structural properties of an amyloid precursor of beta(2)-microglobulin. *Nat Struct Biol 9*, 326-31.

(31) Kim, B. E., Nevitt, T., and Thiele, D. J. (2008) Mechanisms for copper acquisition, distribution and regulation. *Nat Chem Biol 4*, 176-85.

(32) Guo, Z., and Eisenberg, D. (2007) The mechanism of the amyloidogenic conversion of T7 endonuclease I. *J Biol Chem 282*, 14968-74.

(33) Knaupp, A. S., Levina, V., Robertson, A. L., Pearce, M. C., and Bottomley, S. P. (2010) Kinetic instability of the serpin Z alpha1-antitrypsin promotes aggregation. *J Mol Biol 396*, 375-83.

(34) Dumoulin, M., Canet, D., Last, A. M., Pardon, E., Archer, D. B., Muyldermans, S., Wyns, L., Matagne, A., Robinson, C. V., Redfield, C., and Dobson, C. M. (2005) Reduced global cooperativity is a common feature underlying the amyloidogenicity of pathogenic lysozyme mutations. *J Mol Biol 346*, 773-88.

(35) Sandelin, E., Nordlund, A., Andersen, P. M., Marklund, S. S., and Oliveberg, M. (2007) Amyotrophic lateral sclerosis-associated copper/zinc superoxide dismutase mutations preferentially reduce the repulsive charge of the proteins. *J Biol Chem 282*, 21230-6.

(36) Schmittschmitt, J. P., and Scholtz, J. M. (2003) The role of protein stability, solubility, and net charge in amyloid fibril formation. *Protein Sci 12*, 2374-8.

(37) Johnson, S. M., Connelly, S., Fearns, C., Powers, E. T., and Kelly, J. W. (2012) The transthyretin amyloidoses: from delineating the molecular mechanism of aggregation linked to pathology to a regulatory-agency-approved drug. *J Mol Biol 421*, 185-203.

(38) Connors, L. H., Lim, A., Prokaeva, T., Roskens, V. A., and Costello, C. E. (2003) Tabulation of human transthyretin (TTR) variants, 2003. *Amyloid 10*, 160-84.

(39) Hammarstrom, P., Jiang, X., Hurshman, A. R., Powers, E. T., and Kelly, J. W. (2002) Sequence-dependent denaturation energetics: A major determinant in amyloid disease diversity. *Proc Natl Acad Sci U S A 99 Suppl 4*, 16427-32.

(40) Hammarstrom, P., Sekijima, Y., White, J. T., Wiseman, R. L., Lim, A., Costello, C. E., Altland, K., Garzuly, F., Budka, H., and Kelly, J. W. (2003) D18G transthyretin is monomeric, aggregation prone, and not detectable in plasma and cerebrospinal fluid: a prescription for central nervous system amyloidosis? *Biochemistry 42*, 6656-63.

(41) Sekijima, Y., Hammarstrom, P., Matsumura, M., Shimizu, Y., Iwata, M., Tokuda, T., Ikeda, S., and Kelly, J. W. (2003) Energetic characteristics of the new transthyretin variant A25T may explain its atypical central nervous system pathology. *Lab Invest 83*, 409-17.

(42) Hurshman, A. R., White, J. T., Powers, E. T., and Kelly, J. W. (2004) Transthyretin aggregation under partially denaturing conditions is a downhill polymerization. *Biochemistry 43*, 7365-81.
(43) Hurshman Babbes, A. R., Powers, E. T., and Kelly, J. W. (2008) Quantification of the thermodynamically linked quaternary and tertiary structural stabilities of transthyretin and its disease-associated variants: the relationship between stability and amyloidosis. *Biochemistry 47*, 6969-84.
(44) Fandrich, M., Forge, V., Buder, K., Kittler, M., Dobson, C. M., and Diekmann, S. (2003) Myoglobin forms amyloid fibrils by association of unfolded polypeptide segments. *Proc Natl Acad Sci U S A 100*, 15463-8.
(45) Canet, D., Last, A. M., Tito, P., Sunde, M., Spencer, A., Archer, D. B., Redfield, C., Robinson, C. V., and Dobson, C. M. (2002) Local cooperativity in the unfolding of an amyloidogenic variant of human lysozyme. *Nat Struct Biol 9*, 308-15.
(46) Dobson, C. M. (2001) The structural basis of protein folding and its links with human disease. *Philos Trans R Soc Lond B Biol Sci 356*, 133-45.
(47) Ding, F., and Dokholyan, N. V. (2008) Dynamical roles of metal ions and the disulfide bond in Cu, Zn superoxide dismutase folding and aggregation. *Proc Natl Acad Sci U S A 105*, 19696-701.
(48) Sinha, N., Tsai, C. J., and Nussinov, R. (2001) A proposed structural model for amyloid fibril elongation: domain swapping forms an interdigitating beta-structure polymer. *Protein Eng 14*, 93-103.
(49) Ding, F., Furukawa, Y., Nukina, N., and Dokholyan, N. V. (2012) Local unfolding of Cu, Zn superoxide dismutase monomer determines the morphology of fibrillar aggregates. *J Mol Biol 421*, 548-60.
(50) Campioni, S., Mannini, B., Zampagni, M., Pensalfini, A., Parrini, C., Evangelisti, E., Relini, A., Stefani, M., Dobson, C. M., Cecchi, C., and Chiti, F. (2010) A causative link between the structure of aberrant protein oligomers and their toxicity. *Nat Chem Biol 6*, 140-7.
(51) Shaw, B. F., Durazo, A., Nersissian, A. M., Whitelegge, J. P., Faull, K. F., and Valentine, J. S. (2006) Local unfolding in a destabilized, pathogenic variant of superoxide dismutase 1 observed with H/D exchange and mass spectrometry. *J Biol Chem 281*, 18167-76.
(52) Nordlund, A., and Oliveberg, M. (2006) Folding of Cu/Zn superoxide dismutase suggests structural hotspots for gain of neurotoxic function in ALS: parallels to precursors in amyloid disease. *Proc Natl Acad Sci U S A 103*, 10218-23.
(53) Das, P., King, J. A., and Zhou, R. (2011) Aggregation of gamma-crystallins associated with human cataracts via domain swapping at the C-terminal beta-strands. *Proc Natl Acad Sci U S A 108*, 10514-9.
(54) Valentine, J. S., Doucette, P. A., and Zittin Potter, S. (2005) Copper-zinc superoxide dismutase and amyotrophic lateral sclerosis. *Annu Rev Biochem 74*, 563-93.
(55) Kato, S., Takikawa, M., Nakashima, K., Hirano, A., Cleveland, D. W., Kusaka, H., Shibata, N., Kato, M., Nakano, I., and Ohama, E. (2000) New consensus research on neuropathological aspects of familial amyotrophic lateral sclerosis with superoxide dismutase 1 (SOD1) gene mutations: inclusions containing SOD1 in neurons and astrocytes. *Amyotroph Lateral Scler Other Motor Neuron Disord 1*, 163-84.
(56) Rosen, D. R., Siddique, T., Patterson, D., Figlewicz, D. A., Sapp, P., Hentati, A., Donaldson, D., Goto, J., O'Regan, J. P., Deng, H. X., and et al. (1993) Mutations in Cu/Zn superoxide dismutase gene are associated with familial amyotrophic lateral sclerosis. *Nature 362*, 59-62.
(57) Van Damme, P., and Robberecht, W. (2009) Recent advances in motor neuron disease. *Curr Opin Neurol 22*, 486-92.

(58) Tainer, J. A., Getzoff, E. D., Beem, K. M., Richardson, J. S., and Richardson, D. C. (1982) Determination and analysis of the 2 A-structure of copper, zinc superoxide dismutase. *J Mol Biol 160*, 181-217.
(59) Valentine, J. S., and Pantoliano, M. W. (1981) *Copper Proteins*, John Wiley & Sons.
(60) Bahadur, R. P., Chakrabarti, P., Rodier, F., and Janin, J. (2003) Dissecting subunit interfaces in homodimeric proteins. *Proteins 53*, 708-19.
(61) Koradi, R., Billeter, M., and Wuthrich, K. (1996) MOLMOL: a program for display and analysis of macromolecular structures. *J Mol Graph 14*, 51-5, 29-32.
(62) Parge, H. E., Hallewell, R. A., and Tainer, J. A. (1992) Atomic structures of wild-type and thermostable mutant recombinant human Cu,Zn superoxide dismutase. *Proc Natl Acad Sci U S A 89*, 6109-13.
(63) Bertini, I., Luchinat, C., and Monnanni, R. (1985) Evidence of the breaking of the copper-imidazolate bridge in copper/cobalt-substitued superoxide dismutase upon reduction of copper (II) centers. *J Am Chem Soc 107*, 2178-2179.
(64) Hall, L. T., Sanchez, R. J., Holloway, S. P., Zhu, H., Stine, J. E., Lyons, T. J., Demeler, B., Schirf, V., Hansen, J. C., Nersissian, A. M., Valentine, J. S., and Hart, P. J. (2000) X-ray crystallographic and analytical ultracentrifugation analyses of truncated and full-length yeast copper chaperones for SOD (LYS7): a dimer-dimer model of LYS7-SOD association and copper delivery. *Biochemistry 39*, 3611-23.
(65) Carroll, M. C., Girouard, J. B., Ulloa, J. L., Subramaniam, J. R., Wong, P. C., Valentine, J. S., and Culotta, V. C. (2004) Mechanisms for activating Cu- and Zn-containing superoxide dismutase in the absence of the CCS Cu chaperone. *Proc Natl Acad Sci U S A 101*, 5964-9.
(66) Seetharaman, S. V., Prudencio, M., Karch, C., Holloway, S. P., Borchelt, D. R., and Hart, P. J. (2009) Immature copper-zinc superoxide dismutase and familial amyotrophic lateral sclerosis. *Exp Biol Med (Maywood) 234*, 1140-54.
(67) Kurobe, N., Suzuki, F., Okajima, K., and Kato, K. (1990) Sensitive enzyme immunoassay for human Cu/Zn superoxide dismutase. *Clin Chim Acta 187*, 11-20.
(68) Klug, D., Rabani, J., and Fridovich, I. (1972) A direct demonstration of the catalytic action of superoxide dismutase through the use of pulse radiolysis. *J Biol Chem 247*, 4839-42.
(69) Steinman, H. M. (1982) Copper-zinc superoxide dismutase from Caulobacter crescentus CB15. A novel bacteriocuprein form of the enzyme. *J Biol Chem 257*, 10283-93.
(70) Rumfeldt, J. A., Stathopulos, P. B., Chakrabarrty, A., Lepock, J. R., and Meiering, E. M. (2006) Mechanism and thermodynamics of guanidinium chloride-induced denaturation of ALS-associated mutant Cu,Zn superoxide dismutases. *J Mol Biol 355*, 106-23.
(71) Lepock, J. R., Frey, H. E., and Hallewell, R. A. (1990) Contribution of conformational stability and reversibility of unfolding to the increased thermostability of human and bovine superoxide dismutase mutated at free cysteines. *J Biol Chem 265*, 21612-8.
(72) Stathopulos, P. B., Rumfeldt, J. A., Scholz, G. A., Irani, R. A., Frey, H. E., Hallewell, R. A., Lepock, J. R., and Meiering, E. M. (2003) Cu/Zn superoxide dismutase mutants associated with amyotrophic lateral sclerosis show enhanced formation of aggregates in vitro. *Proc Natl Acad Sci U S A 100*, 7021-6.
(73) Rakhit, R., Cunningham, P., Furtos-Matei, A., Dahan, S., Qi, X. F., Crow, J. P., Cashman, N. R., Kondejewski, L. H., and Chakrabartty, A. (2002) Oxidation-induced misfolding and aggregation of superoxide dismutase and its implications for amyotrophic lateral sclerosis. *J Biol Chem 277*, 47551-6.
(74) Furukawa, Y., Torres, A. S., and O'Halloran, T. V. (2004) Oxygen-induced maturation of SOD1: a key role for disulfide formation by the copper chaperone CCS. *Embo J 23*, 2872-81.

(75) Hough, M. A., Grossmann, J. G., Antonyuk, S. V., Strange, R. W., Doucette, P. A., Rodriguez, J. A., Whitson, L. J., Hart, P. J., Hayward, L. J., Valentine, J. S., and Hasnain, S. S. (2004) Dimer destabilization in superoxide dismutase may result in disease-causing properties: structures of motor neuron disease mutants. *Proc Natl Acad Sci U S A 101*, 5976-81.

(76) Banci, L., Bertini, I., Cantini, F., D'Amelio, N., and Gaggelli, E. (2006) Human SOD1 before harboring the catalytic metal: solution structure of copper-depleted, disulfide-reduced form. *J Biol Chem 281*, 2333-7.

(77) Getzoff, E. D., Tainer, J. A., Stempien, M. M., Bell, G. I., and Hallewell, R. A. (1989) Evolution of CuZn superoxide dismutase and the Greek key beta-barrel structural motif. *Proteins 5*, 322-36.

(78) Deng, H. X., Hentati, A., Tainer, J. A., Iqbal, Z., Cayabyab, A., Hung, W. Y., Getzoff, E. D., Hu, P., Herzfeldt, B., Roos, R. P., and et al. (1993) Amyotrophic lateral sclerosis and structural defects in Cu,Zn superoxide dismutase. *Science 261*, 1047-51.

(79) Kusaka, H. (1999) [Neuropathology of the motor neuron disease--Bunina body]. *Rinsho Shinkeigaku 39*, 65-6.

(80) Wang, Q., Johnson, J. L., Agar, N. Y., and Agar, J. N. (2008) Protein aggregation and protein instability govern familial amyotrophic lateral sclerosis patient survival. *PLoS Biol 6*, e170.

(81) Doyle, C. M., Rumfeldt, J. A., Broom, H. R., Broom, A., Stathopulos, P. B., Vassall, K. A., Almey, J. J., and Meiering, E. M. (2013) Energetics of oligomeric protein folding and association. *Arch Biochem Biophys 531*, 44-64.

(82) Stathopulos, P. B., Rumfeldt, J. A., Karbassi, F., Siddall, C. A., Lepock, J. R., and Meiering, E. M. (2006) Calorimetric analysis of thermodynamic stability and aggregation for apo and holo amyotrophic lateral sclerosis-associated Gly-93 mutants of superoxide dismutase. *J Biol Chem 281*, 6184-93.

(83) Vassall, K. A., Stubbs, H. R., Primmer, H. A., Tong, M. S., Sullivan, S. M., Sobering, R., Srinivasan, S., Briere, L. A., Dunn, S. D., Colon, W., and Meiering, E. M. (2010) Decreased stability and increased formation of soluble aggregates by immature superoxide dismutase do not account for disease severity in ALS. *Proc Natl Acad Sci U S A 108*, 2210-5.

(84) Rakhit, R., Crow, J. P., Lepock, J. R., Kondejewski, L. H., Cashman, N. R., and Chakrabartty, A. (2004) Monomeric Cu,Zn-superoxide dismutase is a common misfolding intermediate in the oxidation models of sporadic and familial amyotrophic lateral sclerosis. *J Biol Chem 279*, 15499-504.

(85) Khare, S. D., Caplow, M., and Dokholyan, N. V. (2004) The rate and equilibrium constants for a multistep reaction sequence for the aggregation of superoxide dismutase in amyotrophic lateral sclerosis. *Proc Natl Acad Sci U S A 101*, 15094-9.

(86) Doucette, P. A., Whitson, L. J., Cao, X., Schirf, V., Demeler, B., Valentine, J. S., Hansen, J. C., and Hart, P. J. (2004) Dissociation of human copper-zinc superoxide dismutase dimers using chaotrope and reductant. Insights into the molecular basis for dimer stability. *J Biol Chem 279*, 54558-66.

(87) Valentine, J. S. (2002) Do oxidatively modified proteins cause ALS? *Free Radic Biol Med 33*, 1314-20.

(88) Broom, H. R., Primmer, H. A., Rumfeldt, J. A. O., Stathopulos, P. B., Vassall, K. A., Hwang, Y.-M., and Meiering, E. M. (2012) Folding and Aggregation of Cu, Zn-Superoxide Dismutase, in *Amyotrophic Lateral Sclerosis* (Maurer, P. M., Ed.), InTech.

(89) Elam, J. S., Taylor, A. B., Strange, R., Antonyuk, S., Doucette, P. A., Rodriguez, J. A., Hasnain, S. S., Hayward, L. J., Valentine, J. S., Yeates, T. O., and Hart, P. J. (2003) Amyloid-like filaments and water-filled nanotubes formed by SOD1 mutant proteins linked to familial ALS. *Nat Struct Biol 10*, 461-7.

(90) Banci, L., Bertini, I., Durazo, A., Girotto, S., Gralla, E. B., Martinelli, M., Valentine, J. S., Vieru, M., and Whitelegge, J. P. (2007) Metal-free superoxide dismutase forms soluble oligomers under physiological conditions: a possible general mechanism for familial ALS. *Proc Natl Acad Sci U S A 104*, 11263-7.

(91) Mulligan, V. K., Kerman, A., Laister, R. C., Sharda, P. R., Arslan, P. E., and Chakrabartty, A. (2012) Early steps in oxidation-induced SOD1 misfolding: implications for non-amyloid protein aggregation in familial ALS. *J Mol Biol 421*, 631-52.

(92) Hwang, Y. M., Stathopulos, P. B., Dimmick, K., Yang, H., Badiei, H. R., Tong, M. S., Rumfeldt, J. A., Chen, P., Karanassios, V., and Meiering, E. M. (2010) Nonamyloid aggregates arising from mature copper/zinc superoxide dismutases resemble those observed in amyotrophic lateral sclerosis. *J Biol Chem 285*, 41701-11.

(93) Vassall, K. A., Stathopulos, P. B., Rumfeldt, J. A., Lepock, J. R., and Meiering, E. M. (2006) Equilibrium thermodynamic analysis of amyotrophic lateral sclerosis-associated mutant apo Cu,Zn superoxide dismutases. *Biochemistry 45*, 7366-79.

(94) Banci, L., Bertini, I., D'Amelio, N., Gaggelli, E., Libralesso, E., Matecko, I., Turano, P., and Valentine, J. S. (2005) Fully metallated S134N Cu,Zn-superoxide dismutase displays abnormal mobility and intermolecular contacts in solution. *J Biol Chem 280*, 35815-21.

(95) Shipp, E. L., Cantini, F., Bertini, I., Valentine, J. S., and Banci, L. (2003) Dynamic properties of the G93A mutant of copper-zinc superoxide dismutase as detected by NMR spectroscopy: implications for the pathology of familial amyotrophic lateral sclerosis. *Biochemistry 42*, 1890-9.

(96) Lindberg, M. J., Bystrom, R., Boknas, N., Andersen, P. M., and Oliveberg, M. (2005) Systematically perturbed folding patterns of amyotrophic lateral sclerosis (ALS)-associated SOD1 mutants. *Proc Natl Acad Sci U S A 102*, 9754-9.

(97) Lindberg, M. J., Normark, J., Holmgren, A., and Oliveberg, M. (2004) Folding of human superoxide dismutase: disulfide reduction prevents dimerization and produces marginally stable monomers. *Proc Natl Acad Sci U S A 101*, 15893-8.

(98) Furukawa, Y., and O'Halloran, T. V. (2005) Amyotrophic lateral sclerosis mutations have the greatest destabilizing effect on the apo- and reduced form of SOD1, leading to unfolding and oxidative aggregation. *J Biol Chem 280*, 17266-74.

(99) Arnesano, F., Banci, L., Bertini, I., Martinelli, M., Furukawa, Y., and O'Halloran, T. V. (2004) The unusually stable quaternary structure of human Cu,Zn-superoxide dismutase 1 is controlled by both metal occupancy and disulfide status. *J Biol Chem 279*, 47998-8003.

(100) Lynch, S. M., Boswell, S. A., and Colon, W. (2004) Kinetic stability of Cu/Zn superoxide dismutase is dependent on its metal ligands: implications for ALS. *Biochemistry 43*, 16525-31.

(101) Rodriguez, J. A., Shaw, B. F., Durazo, A., Sohn, S. H., Doucette, P. A., Nersissian, A. M., Faull, K. F., Eggers, D. K., Tiwari, A., Hayward, L. J., and Valentine, J. S. (2005) Destabilization of apoprotein is insufficient to explain Cu,Zn-superoxide dismutase-linked ALS pathogenesis. *Proc Natl Acad Sci U S A 102*, 10516-21.

(102) Nekooki-Machida, Y., Kurosawa, M., Nukina, N., Ito, K., Oda, T., and Tanaka, M. (2009) Distinct conformations of in vitro and in vivo amyloids of huntingtin-exon1 show different cytotoxicity. *Proc Natl Acad Sci U S A 106*, 9679-84.

(103) Tanaka, M., Chien, P., Naber, N., Cooke, R., and Weissman, J. S. (2004) Conformational variations in an infectious protein determine prion strain differences. *Nature 428*, 323-8.

(104) Khare, S. D., and Dokholyan, N. V. (2006) Common dynamical signatures of familial amyotrophic lateral sclerosis-associated structurally diverse Cu, Zn superoxide dismutase mutants. *Proc Natl Acad Sci U S A 103*, 3147-52.

(105) Richardson, J. S., and Richardson, D. C. (2002) Natural beta-sheet proteins use negative design to avoid edge-to-edge aggregation. *Proc Natl Acad Sci U S A 99*, 2754-9.

(106) Hallewell, R. A., Imlay, K. C., Lee, P., Fong, N. M., Gallegos, C., Getzoff, E. D., Tainer, J. A., Cabelli, D. E., Tekamp-Olson, P., Mullenbach, G. T., and et al. (1991) Thermostabilization of recombinant human and bovine CuZn superoxide dismutases by replacement of free cysteines. *Biochem Biophys Res Commun 181*, 474-80.
(107) Karch, C. M., Prudencio, M., Winkler, D. D., Hart, P. J., and Borchelt, D. R. (2009) Role of mutant SOD1 disulfide oxidation and aggregation in the pathogenesis of familial ALS. *Proc Natl Acad Sci U S A 106*, 7774-9.
(108) Namanja, A. T., Wang, X. J., Xu, B., Mercedes-Camacho, A. Y., Wilson, K. A., Etzkorn, F. A., and Peng, J. W. (2011) Stereospecific gating of functional motions in Pin1. *Proc Natl Acad Sci U S A 108*, 12289-94.
(109) Wilson, C. J., Apiyo, D., and Wittung-Stafshede, P. (2004) Role of cofactors in metalloprotein folding. *Q Rev Biophys 37*, 285-314.
(110) Dudev, T., and Lim, C. (2008) Metal binding affinity and selectivity in metalloproteins: insights from computational studies. *Annu Rev Biophys 37*, 97-116.
(111) Fenton, D. E. (1995) *Biocoordination Chemistry*, Oxford University Press, Oxford, UK.
(112) Lim, N. C., Freake, H. C., and Bruckner, C. (2004) Illuminating zinc in biological systems. *Chemistry 11*, 38-49.
(113) McCall, K. A., Huang, C., and Fierke, C. A. (2000) Function and mechanism of zinc metalloenzymes. *J Nutr 130*, 1437S-46S.
(114) Andreini, C., Bertini, I., Cavallaro, G., Holliday, G. L., and Thornton, J. M. (2008) Metal ions in biological catalysis: from enzyme databases to general principles. *J Biol Inorg Chem 13*, 1205-18.
(115) Hellinga, H. W. (1996) Metalloprotein design. *Curr Opin Biotechnol 7*, 437-41.
(116) Schmidt, P. J., Rae, T. D., Pufahl, R. A., Hamma, T., Strain, J., O'Halloran, T. V., and Culotta, V. C. (1999) Multiple protein domains contribute to the action of the copper chaperone for superoxide dismutase. *J Biol Chem 274*, 23719-25.
(117) Rosenzweig, A. C. (2001) Copper delivery by metallochaperone proteins. *Acc Chem Res 34*, 119-28.
(118) Lamb, A. L., Torres, A. S., O'Halloran, T. V., and Rosenzweig, A. C. (2001) Heterodimeric structure of superoxide dismutase in complex with its metallochaperone. *Nat Struct Biol 8*, 751-5.
(119) Choi, D. W., and Koh, J. Y. (1998) Zinc and brain injury. *Annu Rev Neurosci 21*, 347-75.
(120) Galaleldeen, A., Strange, R. W., Whitson, L. J., Antonyuk, S. V., Narayana, N., Taylor, A. B., Schuermann, J. P., Holloway, S. P., Hasnain, S. S., and Hart, P. J. (2009) Structural and biophysical properties of metal-free pathogenic SOD1 mutants A4V and G93A. *Arch Biochem Biophys 492*, 40-7.
(121) Potter, S. Z., Zhu, H., Shaw, B. F., Rodriguez, J. A., Doucette, P. A., Sohn, S. H., Durazo, A., Faull, K. F., Gralla, E. B., Nersissian, A. M., and Valentine, J. S. (2007) Binding of a single zinc ion to one subunit of copper-zinc superoxide dismutase apoprotein substantially influences the structure and stability of the entire homodimeric protein. *J Am Chem Soc 129*, 4575-83.
(122) Crow, J. P., Sampson, J. B., Zhuang, Y., Thompson, J. A., and Beckman, J. S. (1997) Decreased zinc affinity of amyotrophic lateral sclerosis-associated superoxide dismutase mutants leads to enhanced catalysis of tyrosine nitration by peroxynitrite. *J Neurochem 69*, 1936-44.
(123) Goto, J. J., Zhu, H., Sanchez, R. J., Nersissian, A., Gralla, E. B., Valentine, J. S., and Cabelli, D. E. (2000) Loss of in vitro metal ion binding specificity in mutant copper-zinc superoxide dismutases associated with familial amyotrophic lateral sclerosis. *J Biol Chem 275*, 1007-14.
(124) Lyons, T. J., Liu, H., Goto, J. J., Nersissian, A., Roe, J. A., Graden, J. A., Cafe, C., Ellerby, L. M., Bredesen, D. E., Gralla, E. B., and Valentine, J. S. (1996) Mutations in copper-zinc superoxide dismutase that cause amyotrophic lateral sclerosis alter the zinc binding site and the redox behavior of the protein. *Proc Natl Acad Sci U S A 93*, 12240-4.

(125) Mulligan, V. K., Kerman, A., Ho, S., and Chakrabartty, A. (2008) Denaturational stress induces formation of zinc-deficient monomers of Cu,Zn superoxide dismutase: implications for pathogenesis in amyotrophic lateral sclerosis. *J Mol Biol 383*, 424-36.
(126) Rumfeldt, J. A., Lepock, J. R., and Meiering, E. M. (2009) Unfolding and folding kinetics of amyotrophic lateral sclerosis-associated mutant Cu,Zn superoxide dismutases. *J Mol Biol 385*, 278-98.
(127) Roberts, B. R., Tainer, J. A., Getzoff, E. D., Malencik, D. A., Anderson, S. R., Bomben, V. C., Meyers, K. R., Karplus, P. A., and Beckman, J. S. (2007) Structural characterization of zinc-deficient human superoxide dismutase and implications for ALS. *J Mol Biol 373*, 877-90.
(128) Rhoads, T. W., Lopez, N. I., Zollinger, D. R., Morre, J. T., Arbogast, B. L., Maier, C. S., DeNoyer, L., and Beckman, J. S. (2011) Measuring copper and zinc superoxide dismutase from spinal cord tissue using electrospray mass spectrometry. *Anal Biochem 415*, 52-8.
(129) Rivera-Mancia, S., Perez-Neri, I., Rios, C., Tristan-Lopez, L., Rivera-Espinosa, L., and Montes, S. (2010) The transition metals copper and iron in neurodegenerative diseases. *Chem Biol Interact 186*, 184-99.
(130) Estevez, A. G., Crow, J. P., Sampson, J. B., Reiter, C., Zhuang, Y., Richardson, G. J., Tarpey, M. M., Barbeito, L., and Beckman, J. S. (1999) Induction of nitric oxide-dependent apoptosis in motor neurons by zinc-deficient superoxide dismutase. *Science 286*, 2498-500.
(131) Das, A., and Plotkin, S. S. (2013) Mechanical probes of SOD1 predict systematic trends in metal and dimer affinity of ALS-associated mutants. *J Mol Biol 425*, 850-74.
(132) Das, A., and Plotkin, S. S. (2013) SOD1 exhibits allosteric frustration to facilitate metal binding affinity. *Proc Natl Acad Sci U S A 110*, 3871-6.
(133) Hayward, L. J., Rodriguez, J. A., Kim, J. W., Tiwari, A., Goto, J. J., Cabelli, D. E., Valentine, J. S., and Brown, R. H., Jr. (2002) Decreased metallation and activity in subsets of mutant superoxide dismutases associated with familial amyotrophic lateral sclerosis. *J Biol Chem 277*, 15923-31.
(134) Ip, P., Mulligan, V. K., and Chakrabartty, A. (2011) ALS-causing SOD1 mutations promote production of copper-deficient misfolded species. *J Mol Biol 409*, 839-52.
(135) Jonsson, P. A., Graffmo, K. S., Andersen, P. M., Brannstrom, T., Lindberg, M., Oliveberg, M., and Marklund, S. L. (2006) Disulphide-reduced superoxide dismutase-1 in CNS of transgenic amyotrophic lateral sclerosis models. *Brain 129*, 451-64.
(136) Lelie, H. L., Liba, A., Bourassa, M. W., Chattopadhyay, M., Chan, P. K., Gralla, E. B., Miller, L. M., Borchelt, D. R., Valentine, J. S., and Whitelegge, J. P. (2011) Copper and zinc metallation status of copper-zinc superoxide dismutase from amyotrophic lateral sclerosis transgenic mice. *J Biol Chem 286*, 2795-806.
(137) Garcia, J. S., Magalhaes, C. S., and Arruda, M. A. (2006) Trends in metal-binding and metalloprotein analysis. *Talanta 69*, 1-15.
(138) Platte, J. A., and Marcy, V. M. (1959) Photometric Determination of Zinc with Zincon. Application to Water Containing Heavy Metals. *Analytical Chemistry 31*, 1226-1228.
(139) Sabel, C. E., Shepherd, J. L., and Siemann, S. (2009) A direct spectrophotometric method for the simultaneous determination of zinc and cobalt in metalloproteins using 4-(2-pyridylazo)resorcinol. *Anal Biochem 391*, 74-6.
(140) Säbel, C. E. (2010) in *Chemical Science*, Laurentian University, Sudbury.
(141) Hunt, J. B., Neece, S. H., Schachman, H. K., and Ginsburg, A. (1984) Mercurial-promoted Zn2+ release from Escherichia coli aspartate transcarbamoylase. *J Biol Chem 259*, 14793-803.
(142) Jezorek, J. R., and Freiser, H. (1979) 4-(Pyridylazo)resorcinol)-based continuous detection system for trace levels of metal ions. *Analytical Chemistry 51*, 373-376.

(143) Marklund, S., and Marklund, G. (1974) Involvement of the superoxide anion radical in the autoxidation of pyrogallol and a convenient assay for superoxide dismutase. *Eur J Biochem 47*, 469-74.
(144) Davydov, D. R., Deprez, E., Hoa, G. H., Knyushko, T. V., Kuznetsova, G. P., Koen, Y. M., and Archakov, A. I. (1995) High-pressure-induced transitions in microsomal cytochrome P450 2B4 in solution: evidence for conformational inhomogeneity in the oligomers. *Arch Biochem Biophys 320*, 330-44.
(145) Fee, J. A. (1973) Studies on the reconstitution of bovine erythrocyte superoxide dismutase. IV. Preparation and some properties of the enzyme in which Co(II) is substituted for Zn(II). *J Biol Chem 248*, 4229-34.
(146) Liochev, S. I., Chen, L. L., Hallewell, R. A., and Fridovich, I. (1998) The familial amyotrophic lateral sclerosis-associated amino acid substitutions E100G, G93A, and G93R do not influence the rate of inactivation of copper- and zinc-containing superoxide dismutase by H2O2. *Arch Biochem Biophys 352*, 237-9.
(147) Dawson, R. M. C., Elliot, D. C., Elliot, W. H., and Jones, K. M. (1989) *Data for Biochemical Research. 3rd Ed.*, Oxford University Press, New York.
(148) Chen, L. L. (1998) in *Biochemistry*, Imperial College of Science, Technology and Medicine, University of London, South Kensington.
(149) Stathopulos, P. B. (2005) in *Biology*, University of Waterloo, Waterloo.
(150) Teilum, K., Olsen, J. G., and Kragelund, B. B. (2011) Protein stability, flexibility and function. *Biochim Biophys Acta 1814*, 969-76.
(151) Bouvignies, G., Vallurupalli, P., Cordes, M. H., Hansen, D. F., and Kay, L. E. (2011) Measuring 1HN temperature coefficients in invisible protein states by relaxation dispersion NMR spectroscopy. *J Biomol NMR 50*, 13-8.
(152) Palmer, A. G., 3rd, Kroenke, C. D., and Loria, J. P. (2001) Nuclear magnetic resonance methods for quantifying microsecond-to-millisecond motions in biological macromolecules. *Methods Enzymol 339*, 204-38.
(153) Henzler-Wildman, K. A., Lei, M., Thai, V., Kerns, S. J., Karplus, M., and Kern, D. (2007) A hierarchy of timescales in protein dynamics is linked to enzyme catalysis. *Nature 450*, 913-6.
(154) Karplus, M., and Kuriyan, J. (2005) Molecular dynamics and protein function. *Proc Natl Acad Sci U S A 102*, 6679-85.
(155) Haupt, C., Weininger, U., Kovermann, M., and Balbach, J. (2011) Local and coupled thermodynamic stability of the two-domain and bifunctional enzyme SlyD from Escherichia coli. *Biochemistry 50*, 7321-9.
(156) Singh, S. M., Cabello-Villegas, J., Hutchings, R. L., and Mallela, K. M. (2010) Role of partial protein unfolding in alcohol-induced protein aggregation. *Proteins 78*, 2625-37.
(157) Kragelund, B. B., Poulsen, K., Andersen, K. V., Baldursson, T., Kroll, J. B., Neergard, T. B., Jepsen, J., Roepstorff, P., Kristiansen, K., Poulsen, F. M., and Knudsen, J. (1999) Conserved residues and their role in the structure, function, and stability of acyl-coenzyme A binding protein. *Biochemistry 38*, 2386-94.
(158) Wuthrich, K. (1986) *NMR of Proteins and Nucleic Acids*, Wiley, New York.
(159) Hansen, D. F., Vallurupalli, P., Lundstrom, P., Neudecker, P., and Kay, L. E. (2008) Probing chemical shifts of invisible states of proteins with relaxation dispersion NMR spectroscopy: how well can we do? *J Am Chem Soc 130*, 2667-75.
(160) Cierpicki, T., and Otlewski, J. (2001) Amide proton temperature coefficients as hydrogen bond indicators in proteins. *J Biomol NMR 21*, 249-61.
(161) Peng, J. W. (2012) Exposing the Moving Parts of Proteins with NMR Spectroscopy. *J Phys Chem Lett 3*, 1039-1051.

(162) Ohnishi, M., and Urry, D. W. (1969) Temperature dependence of amide proton chemical shifts: the secondary structures of gramicidin S and valinomycin. *Biochem Biophys Res Commun 36*, 194-202.
(163) Baxter, N. J., and Williamson, M. P. (1997) Temperature dependence of 1H chemical shifts in proteins. *J Biomol NMR 9*, 359-69.
(164) Andersen, N. H., Neidigh, J. W., Harris, S. M., Gregory, M. L., Zhihong, L., and YTong, H. (1997) Extracting Information from the Temperature Gradients of Polypeptide NH Chemical Shifts. 1. The Importance of Conformational Averaging. *J Am Chem Soc 119*, 8547-8561.
(165) Tomlinson, J. H., and Williamson, M. P. (2012) Amide temperature coefficients in the protein G B1 domain. *J Biomol NMR 52*, 57-64.
(166) McDonald, I. K., and Thornton, J. M. (1994) Satisfying hydrogen bonding potential in proteins. *J Mol Biol 238*, 777-93.
(167) Dyson, H. J., Bolinger, L., Feher, V. A., Osterhout, J. J., Jr., Yao, J., and Wright, P. E. (1998) Sequence requirements for stabilization of a peptide reverse turn in water solution--proline is not essential for stability. *Eur J Biochem 255*, 462-71.
(168) Krebs, D., Maroun, R. G., Sourgen, F., Troalen, F., Davoust, D., and Fermandjian, S. (1998) Helical and coiled-coil-forming properties of peptides derived from and inhibiting human immunodeficiency virus type 1 integrase assessed by 1H-NMR--use of NH temperature coefficients to probe coiled-coil structures. *Eur J Biochem 253*, 236-44.
(169) Wagner, G., and Zuiderweg, E. R. (1983) Two-dimensional double quantum 1H NMR spectroscopy of proteins. *Biochem Biophys Res Commun 113*, 854-60.
(170) Williamson, M. P., and Asakura, T. (1997) Protein chemical shifts. *Methods Mol Biol 60*, 53-69.
(171) Skalicky, J. J., Selsted, M. E., and Pardi, A. (1994) Structure and dynamics of the neutrophil defensins NP-2, NP-5, and HNP-1: NMR studies of amide hydrogen exchange kinetics. *Proteins 20*, 52-67.
(172) Hong, J., Jing, Q., and Yao, L. (2013) The protein amide (1)H(N) chemical shift temperature coefficient reflects thermal expansion of the N-H...O=C hydrogen bond. *J Biomol NMR 55*, 71-8.
(173) Cordier, F., Rogowski, M., Grzesiek, S., and Bax, A. (1999) Observation of through-hydrogen-bond 2hJHC' in a perdeuterated protein. *J Magn Reson 140*, 510-2.
(174) Cordier, F., and Grzesiek, S. (2002) Temperature-dependence of protein hydrogen bond properties as studied by high-resolution NMR. *J Mol Biol 317*, 739-52.
(175) Tilton, R. F., Jr., Dewan, J. C., and Petsko, G. A. (1992) Effects of temperature on protein structure and dynamics: X-ray crystallographic studies of the protein ribonuclease-A at nine different temperatures from 98 to 320 K. *Biochemistry 31*, 2469-81.
(176) Tunnicliffe, R. B., Waby, J. L., Williams, R. J., and Williamson, M. P. (2005) An experimental investigation of conformational fluctuations in proteins G and L. *Structure 13*, 1677-84.
(177) Williamson, M. P. (2003) Many residues in cytochrome c populate alternative states under equilibrium conditions. *Proteins 53*, 731-9.
(178) Chandra, K., Sharma, Y., and Chary, K. V. (2011) Characterization of low-energy excited states in the native state ensemble of non-myristoylated and myristoylated neuronal calcium sensor-1. *Biochim Biophys Acta 1814*, 334-44.
(179) Srivastava, A. K., and Chary, K. V. (2011) Conformational heterogeneity and dynamics in a betagamma-crystallin from Hahella chejuensis. *Biophys Chem 157*, 7-15.
(180) Baxter, N. J., Hosszu, L. L., Waltho, J. P., and Williamson, M. P. (1998) Characterisation of low free-energy excited states of folded proteins. *J Mol Biol 284*, 1625-39.
(181) Delepierre, M., Larvor, M. P., Baleux, F., and Goldberg, M. E. (1991) 1H-NMR conformational analysis of a high-affinity antigenic 11-residue peptide from the tryptophan synthase beta 2 subunit. *Eur J Biochem 201*, 681-93.

(182) Banci, L., Bertini, I., Cramaro, F., Del Conte, R., Rosato, A., and Viezzoli, M. S. (2000) Backbone dynamics of human Cu,Zn superoxide dismutase and of its monomeric F50E/G51E/E133Q mutant: the influence of dimerization on mobility and function. *Biochemistry 39*, 9108-18.
(183) Cheng, J. W., Lepre, C. A., Chambers, S. P., Fulghum, J. R., Thomson, J. A., and Moore, J. M. (1993) 15N NMR relaxation studies of the FK506 binding protein: backbone dynamics of the uncomplexed receptor. *Biochemistry 32*, 9000-10.
(184) Redfield, C., Boyd, J., Smith, L. J., Smith, R. A., and Dobson, C. M. (1992) Loop mobility in a four-helix-bundle protein: 15N NMR relaxation measurements on human interleukin-4. *Biochemistry 31*, 10431-7.
(185) Banci, L., Benedetto, M., Bertini, I., Del Conte, R., Piccioli, M., and Viezzoli, M. S. (1998) Solution structure of reduced monomeric Q133M2 copper, zinc superoxide dismutase (SOD). Why is SOD a dimeric enzyme? *Biochemistry 37*, 11780-91.
(186) Fisher, C. L., Cabelli, D. E., Tainer, J. A., Hallewell, R. A., and Getzoff, E. D. (1994) The role of arginine 143 in the electrostatics and mechanism of Cu,Zn superoxide dismutase: computational and experimental evaluation by mutational analysis. *Proteins 19*, 24-34.
(187) Borchelt, D. R., Lee, M. K., Slunt, H. S., Guarnieri, M., Xu, Z. S., Wong, P. C., Brown, R. H., Jr., Price, D. L., Sisodia, S. S., and Cleveland, D. W. (1994) Superoxide dismutase 1 with mutations linked to familial amyotrophic lateral sclerosis possesses significant activity. *Proc Natl Acad Sci U S A 91*, 8292-6.
(188) Hart, P. J., Liu, H., Pellegrini, M., Nersissian, A. M., Gralla, E. B., Valentine, J. S., and Eisenberg, D. (1998) Subunit asymmetry in the three-dimensional structure of a human CuZnSOD mutant found in familial amyotrophic lateral sclerosis. *Protein Sci 7*, 545-55.
(189) Museth, A. K., Brorsson, A. C., Lundqvist, M., Tibell, L. A., and Jonsson, B. H. (2009) The ALS-associated mutation G93A in human copper-zinc superoxide dismutase selectively destabilizes the remote metal binding region. *Biochemistry 48*, 8817-29.
(190) Khare, S. D., Wilcox, K. C., Gong, P., and Dokholyan, N. V. (2005) Sequence and structural determinants of Cu, Zn superoxide dismutase aggregation. *Proteins 61*, 617-32.
(191) Carr, H. Y., and Purcell, E. M. (1954) Effects of Diffusion on Free Precession in Nuclear Magnetic Resonance Experiments. *Physical Review 94*, 630-638.
(192) Meiboom, S., and Gill, D. (1958) Modified spin-echo method for measuring nuclear relaxation times. *Rev. Sci. Instr. 29*, 688-691.
(193) Teilum, K., Smith, M. H., Schulz, E., Christensen, L. C., Solomentsev, G., Oliveberg, M., and Akke, M. (2009) Transient structural distortion of metal-free Cu/Zn superoxide dismutase triggers aberrant oligomerization. *Proc Natl Acad Sci U S A 106*, 18273-8.
(194) Prudencio, M., Hart, P. J., Borchelt, D. R., and Andersen, P. M. (2009) Variation in aggregation propensities among ALS-associated variants of SOD1: correlation to human disease. *Hum Mol Genet 18*, 3217-26.
(195) Miller, J. F. (1994) Bacterial transformation by electroporation. *Methods Enzymol 235*, 375-85.
(196) Keller, R. (2005), Swiss Federal Institute of Technology.
(197) Morris, G. A., and Freeman, R. (1979) Enhancement of nuclear magnetic resonance signals by polarization transfer. *J Am Chem Soc 101*, 760-762.
(198) Hartel, A. J., Lankhorst, P. P., and Altona, C. (1982) Thermodynamics of stacking and of self-association of the dinucleoside monophosphate m2(6)A-U from proton NMR chemical shifts: differential concentration temperature profile method. *Eur J Biochem 129*, 343-57.
(199) Tiwari, A., and Hayward, L. J. (2003) Familial amyotrophic lateral sclerosis mutants of copper/zinc superoxide dismutase are susceptible to disulfide reduction. *J Biol Chem 278*, 5984-92.
(200) James, T. L. (1998) Fundamentals of NMR, in *Rev. Series 2* pp 1-31, San Francisco.

(201) Zhang, Y.-Z. (1995) in *Structural Biology and Molecular Biophysics*, University of Pennsylvania.
(202) Bai, Y., Milne, J. S., Mayne, L., and Englander, S. W. (1993) Primary structure effects on peptide group hydrogen exchange. *Proteins 17*, 75-86.
(203) Myers, J. K., and Pace, C. N. (1996) Hydrogen bonding stabilizes globular proteins. *Biophys J 71*, 2033-9.
(204) Romero, P., Obradovic, Z., Li, X., Garner, E. C., Brown, C. J., and Dunker, A. K. (2001) Sequence complexity of disordered protein. *Proteins 42*, 38-48.
(205) Kayatekin, C., Zitzewitz, J. A., and Matthews, C. R. (2008) Zinc binding modulates the entire folding free energy surface of human Cu,Zn superoxide dismutase. *J Mol Biol 384*, 540-55.
(206) Khare, S. D., Ding, F., and Dokholyan, N. V. (2003) Folding of Cu, Zn superoxide dismutase and familial amyotrophic lateral sclerosis. *J Mol Biol 334*, 515-25.
(207) Saito, H., Ando, I., and Ramamoorthy, A. (2011) Chemical shift tensor - the heart of NMR: Insights into biological aspects of proteins. *Prog Nucl Magn Reson Spectrosc 57*, 181-228.
(208) Tomlinson, J. H., Green, V. L., Baker, P. J., and Williamson, M. P. (2010) Structural origins of pH-dependent chemical shifts in the B1 domain of protein G. *Proteins 78*, 3000-16.
(209) Mulder, F. A., Mittermaier, A., Hon, B., Dahlquist, F. W., and Kay, L. E. (2001) Studying excited states of proteins by NMR spectroscopy. *Nat Struct Biol 8*, 932-5.
(210) Shortle, D., Simons, K. T., and Baker, D. (1998) Clustering of low-energy conformations near the native structures of small proteins. *Proc Natl Acad Sci U S A 95*, 11158-62.

Appendix 1 – Residues specific variable temperature NMR data for holo SOD1s

Table A1.1 - N^1H and ^{15}N temperature coefficients of holo SOD1s. The N^1H of residues that participate in a hydrogen bond are marked with a 'y' and those that do not with an 'n' (based on crystal structure data, PDB 1SOS). UA represents unassigned residues. OL represents residues with overlapping cross peaks. D represents residues that disappear at increased temperature. PRO represents proline residues which have no amide proton.

Residue	#	Structure	H-bond	N^1H Temperature Coefficient (ppb/K)				^{15}N Temperature Coefficient (ppb/K)			
				pWT	G93A	E100G	V148I	pWT	G93A	E100G	V148I
ALA	1	N	n	UA	UA	UA	UA	UA	UA	UA	UA
THR	2	N	n	UA	UA	-8.93	UA	UA	UA	-14.31	UA
LYS	3	B1	n	-6.51	-6.69	OL	-6.52	-5.63	-2.7	OL	1.16
ALA	4	B1	y	OL	-2.83	D	OL	OL	10.81	D	OL
VAL	5	B1	y	-5.65	-5.61	-5.57	-5.36	-14.24	-13.76	-13.09	-12.42
ALA	6	B1	y	-4.2	-4.21	-3.78	D	9.04	3.83	9.77	D
VAL	7	B1	n	OL	-6.71	OL	OL	OL	4.86	OL	OL
LEU	8	B1	y	-5.26	-5.23	-5.05	-5.09	3.84	4	6.58	6.19
LYS	9	loop I	y	OL	OL	OL	-5.49	OL	OL	OL	1.38
GLY	10	loop I	n	-5.9	D	D	D	9.79	D	D	D
ASP	11	loop I	n	UA	UA	UA	UA	UA	UA	UA	UA
GLY	12	loop I	n	D	D	D	D	D	D	D	D
PRO	13	loop I	n	PRO	PRO	PRO	PRO	PRO	PRO	PRO	PRO
VAL	14	B2	n	-7.11	-6.32	-6.89	-6.71	-10.69	-6.81	-8.53	-7.83
GLN	15	B2	y	-3.31	-3.4	OL	-2.85	3.94	4.65	OL	8.23
GLY	16	B2	y	OL	-3.01	OL	OL	OL	10.78	OL	OL
ILE	17	B2	y	-3.31	-3.52	-3.21	-3.37	3.64	3.16	4.81	6.69
ILE	18	B2	y	D	-4.64	-5.44	OL	D	4.01	-9.33	OL
ASN	19	B2	y	OL	D	OL	-3.49	OL	D	OL	11.1
PHE	20	B2	y	-2.81	-2.49	-2.64	-2.04	14.69	13.59	15.24	15.74
GLU	21	B2	y	-4.5	-4.55	-4.69	-4.36	2.06	2.79	2.38	3.22
GLN	22	B2	y	-6.63	-6.64	-6.56	-6.11	-10.49	-9.48	-9.15	-6.7
LYS	23	loop II	n	UA	UA	UA	UA	UA	UA	UA	UA
GLU	24	loop II	n	-3.32	D	D	OL	18.99	D	D	OL
SER	25	loop II	n	UA	UA	UA	UA	UA	UA	UA	UA
ASN	26	loop II	n	D	D	D	D	D	D	D	D
GLY	27	loop II	y	-6.21	-6.25	-5.7	-5.91	-1.31	-0.28	-3.27	-2.46
PRO	28	loop II	n	PRO	PRO	PRO	PRO	PRO	PRO	PRO	PRO
VAL	29	B3	y	-6.93	-6.97	-7.15	-6.76	-2.46	-2.13	1.25	-1.06
LYS	30	B3	y	-4.96	-4.87	OL	-4.47	3.55	2.87	OL	5.53
VAL	31	B3	y	-3.95	-3.87	-4.9	-3.63	9.57	12.06	7.51	13.56
TRP	32	B3	y	OL	OL	OL	OL	OL	OL	OL	OL
GLY	33	B3	y	-5	-4.06	-3.87	-3.86	3.52	5.13	3.17	2.81
SER	34	B3	n	-3.34	-3.22	-3.09	-2.68	-0.03	0.17	0.21	0.74
ILE	35	B3	y	-3.33	-3.73	-3.17	-2.98	-4.77	-5.34	-2.06	0.48
LYS	36	B3	y	OL	OL	OL	OL	OL	OL	OL	OL
GLY	37	loop III	n	-5.21	OL	-4.65	-5.06	17.31	OL	16.14	14.76
LEU	38	loop III	y	-4.45	-6.93	-5.52	-5.31	-15.54	-16.51	-12.61	-13.64
THR	39	loop III	n	OL	-12.73	OL	OL	OL	0.26	OL	OL
GLU	40	loop III	n	D	D	-5.48	D	D	D	4.09	D

GLY	41	B4	y	-6.14	-6.08	-5.99	-5.81	-15.33	-16.87	-14.98	-14.57
LEU	42	B4	n	OL	OL	OL	-8.16	OL	OL	OL	2.73
HIS	43	B4	y	-4.94	-5.24	-4.98	-4.65	7.42	7.11	8.21	6.69
GLY	44	B4	y	-3.87	-3.67	-3.74	-3.4	11.75	10.92	8.95	11.02
PHE	45	B4	y	-3.76	-3.79	-3.78	-3.61	6.27	5.11	7.98	8.14
HIS	46	B4	y	D	-3.58	-3.05	OL	D	12.8	12.59	OL
VAL	47	B4	y	-4.05	-4	-3.88	-3.48	8.34	8.38	10.63	13
HIS	48	B4	y	-6.34	D	OL	D	3.97	D	OL	D
GLU	49	B4	y	-4.05	-4.13	-4.15	-3.7	2.41	2.03	3.57	3.81
PHE	50	loop IV	y	OL	-5.15	OL	-5.28	OL	7.82	OL	7.44
GLY	51	loop IV	n	-5.29	-5.26	-5.25	-5.22	-21.47	-21.72	-20.46	-18.86
ASP	52	loop IV	y	-2.57	-2.55	-2.47	-1.6	17.41	15.57	17.99	20.03
ASN	53	loop IV	n	-11.04	-11.11	D	OL	-20	-14.53	D	OL
THR	54	loop IV	y	-3.33	-3.37	-3.4	-3.05	-2.35	-2.66	-0.17	11.34
ALA	55	loop IV	y	D	D	D	-6.31	D	D	D	-8.45
GLY	56	loop IV	y	OL	-3.6	OL	-4.41	OL	9.91	OL	-0.89
CYS	57	loop IV	n	UA	UA	UA	UA	UA	UA	UA	UA
THR	58	loop IV	n	UA	UA	UA	UA	UA	UA	UA	UA
SER	59	loop IV	n	-2.17	D	OL	-3.17	8.29	D	OL	11.53
ALA	60	loop IV	y	-3.97	-3.98	-3.92	-3.17	0.12	0.24	1.05	-2.27
GLY	61	loop IV	n	-4.22	-4.13	-4.13	-3.98	6.31	6.16	3.98	4.46
PRO	62	loop IV	n	PRO	PRO	PRO	PRO	PRO	PRO	PRO	PRO
HIS	63	loop IV	n	D	D	OL	D	D	D	OL	D
PHE	64	loop IV	y	UA	UA	UA	UA	UA	UA	UA	UA
ASN	65	loop IV	n	D	D	D	-4.46	D	D	D	8.19
PRO	66	loop IV	n	PRO	PRO	PRO	PRO	PRO	PRO	PRO	PRO
LEU	67	loop IV	n	-6.57	-6.56	-6.67	-6.48	-4.42	-3.6	-3.76	-3.13
SER	68	loop IV	y	OL	-3.38	OL	-2.87	OL	-7.84	OL	0.37
ARG	69	loop IV	y	-5.45	-5.4	-5.35	-5.08	-2.8	-2.51	-0.63	-0.46
LYS	70	loop IV	y	-7.17	-7.08	-7.1	-7.02	7.98	8.69	9.42	9.66
HIS	71	loop IV	y	-4.95	-4.93	-4.85	-4.72	13.08	13.86	12.24	14.19
GLY	72	loop IV	y	-4.52	-4.46	-4.32	-4.28	-4.69	-3.82	-5.41	-5.51
GLY	73	loop IV	y	-5.98	-6.01	-5.82	-5.88	13.36	12.19	9.89	9.88
PRO	74	loop IV	n	PRO	PRO	PRO	PRO	PRO	PRO	PRO	PRO
LYS	75	loop IV	n	D	D	D	D	D	D	D	D
ASP	76	loop IV	y	-4.69	-4.62	-4.57	-4.5	2.44	0.6	2.66	2.8
GLU	77	loop IV	n	-8.1	-4.83	OL	OL	-10.69	6.47	OL	OL
GLU	78	loop IV	n	-9.13	D	-5.57	-9.07	-2.41	D	0.57	-0.76
ARG	79	loop IV	n	-4.07	-3.91	-3.84	-3.75	-14.65	-13.82	-13.36	-13.4
HIS	80	loop IV	n	-4.23	D	-4.27	-4.05	5.28	D	7.62	7.88
VAL	81	loop IV	y	-3.74	-3.63	-3.66	-3.42	-0.92	-0.62	0.38	2.07
GLY	82	loop IV	y	-5.31	-5.33	-5.4	-4.95	9.43	7.69	7.84	6.36
ASP	83	B5	y	-3.1	-3.2	-3.02	-2.81	8.56	8.39	8.4	10.41
LEU	84	B5	y	-2.7	-2.74	-2.55	-2.34	8.2	8.09	11.25	11.44
GLY	85	B5	n	OL	-4.19	-4.05	OL	OL	0.39	-5.88	OL
ASN	86	B5	n	-6.37	D	-6.25	-6.17	3.07	D	4.12	4.47
VAL	87	B5	y	-4.32	-4.28	-4.14	-4.01	4.73	6.9	5.14	5.19
THR	88	B5	n	-6.85	-6.86	-6.86	-6.44	0.4	1.26	1.88	2.99
ALA	89	B5	y	-6.53	-6.64	-6.49	-6.18	1.7	-0.22	1.26	3.01
ASP	90	loop V	y	-5.86	-6.21	-5.83	-5.6	-4.35	-3.73	1.33	-2.86

LYS	91	loop V	n	-6.02	D	D	-5.59	10.27	D	D	14.38
ASP	92	loop V	n	-3.88	-8.18	-3.61	-3.57	-3.52	3.39	-1.9	-1.8
GLY	93	loop V	y	-4.24	-3.24	-3.64	-3.82	-5.95	-1.59	-8.65	-7.79
VAL	94	B6	y	-3.64	-5.33	-7.08	-3.32	9.18	-2.96	6.42	11.56
ALA	95	B6	y	-7.3	-6.51	-7.24	-7.31	-8.42	-8.74	-6.82	-5.63
ASP	96	B6	n	-6.2	-6.07	OL	-6.15	4.15	2.61	OL	5.7
VAL	97	B6	y	-5.21	-5.45	-5.03	-4.82	-8.9	-9.48	-5.79	-4.76
SER	98	B6	n	OL	-3.55	OL	D	OL	7.98	OL	D
ILE	99	B6	y	-5.11	-5.11	-5.1	-4.72	-1.85	-2.4	-6.11	1.81
GLU	100	B6	n	-8.24	D	D	-7.52	-2.81	D	D	-4.78
ASP	101	B6	y	-5.77	-5.67	OL	-5.34	-11.09	-10.44	OL	-7.79
SER	102	loop VI	n	D	D	OL	D	D	D	OL	D
VAL	103	loop VI	y	-2.34	-2.18	-4.37	-1.99	2.13	1.82	3.55	4.99
ILE	104	loop VI	y	-4.74	-4.69	-5.06	-4.63	10.36	9.44	11.34	10
SER	105	loop VI	y	OL	OL	OL	OL	OL	OL	OL	OL
LEU	106	loop VI	y	-3.67	-3.5	-3.27	-3.24	6	6.33	6.92	7.56
SER	107	loop VI	y	D	D	D	-4.63	D	D	D	14.47
GLY	108	loop VI	n	UA	UA	UA	UA	UA	UA	UA	UA
ASP	109	loop VI	n	UA	UA	UA	UA	UA	UA	UA	UA
HIS	110	loop VI	n	D	D	OL	OL	D	D	OL	OL
SER	111	loop VI	y	-3.7	-3.66	-3.58	D	11.05	9.37	8.52	D
ILE	112	loop VI	y	-5.39	-5.37	-5.56	-5.26	-4.64	-5.3	-4.89	-4.97
ILE	113	loop VI	y	-5.15	-4.62	-4.57	D	-0.15	1.28	2.39	D
GLY	114	loop VI	y	-6.24	-6.36	-6.35	-6.34	2.47	2.33	1.08	2.9
ARG	115	B7	n	-4.06	-4.1	-4.07	-4.04	1.74	0.8	0.99	1.5
THR	116	B7	y	-3.74	-3.65	-3.61	-3.29	9.02	9.61	8.73	10.13
LEU	117	B7	y	-4.08	-4.16	-3.98	-4.05	0.64	0.62	1.29	3.02
VAL	118	B7	y	OL	OL	OL	-3.21	OL	OL	OL	8.24
VAL	119	B7	y	-3.36	-3.51	-3.27	-2.92	11.3	10.24	13.27	13.7
HIS	120	B7	y	-3.56	OL	-3.35	OL	5.52	OL	7.28	OL
GLU	121	loop VII	y	-5.78	-5.84	-5.76	-5.57	0.25	-0.32	1.02	2.46
LYS	122	loop VII	y	-5.38	-5.26	-5.38	-5.3	4.86	6.03	5.26	4.87
ALA	123	loop VII	n	-7.95	-7.93	-7.7	-7.96	3.05	2.44	6.26	4.98
ASP	124	loop VII	y	-7.16	-7.07	-7.06	-6.84	4.53	5.09	6.89	7.17
ASP	125	loop VII	y	-5.66	-5.55	-5.64	-5.21	-0.45	0.68	2.32	3.66
LEU	126	loop VII	y	-4.81	-4.69	-4.63	-4.53	-1.27	-1.65	-1.25	-0.27
GLY	127	loop VII	y	-1.63	-1.62	-1.45	-1.24	18.28	16.91	15.62	15.62
LYS	128	loop VII	y	-2.43	-2.44	-2.33	-2.1	2.43	2.06	2.25	3.41
GLY	129	loop VII	y	-7.44	-7.14	-6.62	-8.17	5.79	4.74	5.63	-5.56
GLY	130	loop VII	n	UA	D	UA	UA	UA	D	UA	UA
ASN	131	loop VII	n	D	D	D	D	D	D	D	D
GLU	132	loop VII	n	OL	D	OL	OL	OL	D	OL	OL
GLU	133	loop VII	n	OL	OL	OL	OL	OL	OL	OL	OL
SER	134	loop VII	y	-7.11	D	D	D	11.6	D	D	D
THR	135	loop VII	n	D	D	-3.28	D	D	D	6.05	D
LYS	136	loop VII	y	D	-3.47	-2.82	-3	D	4.72	7.73	1.99
THR	137	loop VII	y	-3.97	D	D	-3.6	12.34	D	D	9.65
GLY	138	loop VII	y	OL	-3.49	OL	-3.56	OL	13.59	OL	8.19
ASN	139	loop VII	y	-1.16	-1.19	-1.04	-0.75	28.18	26.88	25.46	26.23
ALA	140	loop VII	n	-2.78	-2.72	D	-2.54	7.49	8.16	D	8.64

GLY	141	loop VII	n	D	D	-5.93	-6.4	D	D	-6.61	-1.42
SER	142	loop VII	n	D	D	D	D	D	D	D	D
ARG	143	B8	n	UA	UA	UA	UA	UA	UA	UA	UA
LEU	144	B8	y	-4.49	-4.41	-4.38	-4.08	8.92	10.78	9.34	11.86
ALA	145	B8	n	-3.6	-3.58	-3.43	-3.36	1.79	3.02	1.84	1.88
CYS	146	B8	y	D	-5.96	-6	-5.8	D	12.36	8.9	12.83
GLY	147	B8	y	-3.08	-3.19	-2.22	-3.56	7.36	6.17	5.29	2.4
VAL	148	B8	n	-6.19	-6.4	OL	OL	4.3	3.07	OL	OL
ILE	149	B8	y	-4.68	-4.66	-4.72	-4.28	6.26	4.4	6.84	9.39
GLY	150	B8	y	-5.03	-5.73	-5.92	-4.99	-0.74	-2.59	-0.99	-0.03
ILE	151	B8	n	-6.62	-6.57	-6.58	OL	4.64	4.36	5.93	OL
ALA	152	C	y	-2.98	-2.96	-2.94	-2.41	6.66	8.27	8.82	11.97
GLN	153	C	n	D	-8.05	OL	-7.54	D	-9.54	OL	-4.69

Table A1.2 - Amide exchange rates for holo SOD1s at 25°C, pH 7.8. Values taken from Rumfeldt, 2006 (JR thesis). Residues that were not assigned, exchanged in the dead time, too fast to measure, had a measureable exchange rate, and were too slow to measure are represented by NA, DT, too fast, measureable and too slow, respectively.

		pWT			**G93A**			**E100G**		
amino acid		**Category**		**k_{ex} (min^{-1})**	**Category**		**k_{ex} (min^{-1})**	**Category**		**k_{ex} (min^{-1})**
ALA	1	NA			NA			NA		
THR	2	NA			NA			DT	≥	1.00E-01
LYS	3	DT	≥	5.00E-01	DT	≥	1.00E-01	DT	≥	1.00E-01
ALA	4	too slow	≤	6.00E-06	too slow	≤	6.00E-06	too slow	≤	6.00E-06
VAL	5	too slow	≤	6.00E-06	too slow	≤	6.00E-06	too slow	≤	6.00E-06
ALA	6	too slow	≤	6.00E-06	too slow	≤	6.00E-06	too slow	≤	6.00E-06
VAL	7	measureable	□	6.25E-03	measurable	=	9.38E-04	measurable	=	1.67E-03
LEU	8	too slow	≤	6.00E-06	too slow	≤	6.00E-06	too slow	≤	6.00E-06
LYS	9	DT	≥	5.00E-01	DT	≥	1.00E-01	DT	≥	1.00E-01
GLY	10	DT	≥	5.00E-01	DT	≥	1.00E-01	DT	≥	1.00E-01
ASP	11	NA			NA			DT	≥	1.00E-01
GLY	12	DT	≥	5.00E-01	DT	≥	1.00E-01	DT	≥	1.00E-01
PRO	13	proline			proline			proline		
VAL	14	DT	≥	5.00E-01	DT	≥	1.00E-01	DT	≥	1.00E-01
GLN	15	measureable	□	5.75E-03	measurable	=	1.13E-03	measurable	=	4.61E-03
GLY	16	DT	≥	5.00E-01	DT	≥	1.00E-01	DT	≥	1.00E-01
ILE	17	DT	≥	5.00E-01	DT	≥	1.00E-01	DT	≥	1.00E-01
ILE	18	too slow	≤	6.00E-06	too slow	≤	6.00E-06	too slow	≤	6.00E-06
ASN	19	too slow	≤	6.00E-06	too slow	≥	6.00E-06	too slow	≤	6.00E-06
PHE	20	too slow	≤	6.00E-06	too slow	≤	6.00E-06	too slow	≤	6.00E-06
GLU	21	too slow	≤	6.00E-06	too slow	≤	6.00E-06	too slow	≤	6.00E-06
GLN	22	DT	≥	5.00E-01	DT	≥	1.00E-01	DT	≥	1.00E-01
LYS	23	DT	≥	5.00E-01	DT	≥	1.00E-01	DT	≥	1.00E-01
GLU	24	DT	≥	5.00E-01	DT	≥	1.00E-01	DT	≥	1.00E-01
SER	25	NA			NA			NA		
ASN	26	DT	≥	5.00E-01	DT	≥	1.00E-01	DT	≥	1.00E-01
GLY	27	DT	≥	5.00E-01	DT	≥	1.00E-01	DT	≥	1.00E-01
PRO	28	proline			proline			proline		
VAL	29	measureable	□	7.96E-05	too slow	≤	6.00E-06	measurable	=	1.23E-03

LYS	30	too slow	≤	6.00E-06	too slow	≤	6.00E-06	too slow	≤	6.00E-06
VAL	31	too slow	≤	6.00E-06	too slow	≤	6.00E-06	too slow	≤	6.00E-06
TRP	32	too slow	≤	6.00E-06	too slow	≤	6.00E-06	too slow	≤	6.00E-06
GLY	33	measureable	□	4.93E-03	measurable	=	6.91E-04	measurable	=	3.11E-03
SER	34	measureable	□	1.23E-02	measurable	=	1.21E-02	measurable	=	1.30E-02
ILE	35	measureable	□	3.11E-05	measurable	=	4.46E-05	too slow	≤	6.00E-06
LYS	36	measureable	□	4.17E-05	measurable	=	2.29E-04	measurable	=	1.94E-05
GLY	37	DT	≥	5.00E-01	DT	≥	1.00E-01	DT	≥	1.00E-01
LEU	38	measureable	□	1.85E-04	measurable	=	7.31E-04	measurable	=	1.14E-04
THR	39	DT	≥	5.00E-01	DT	≥	1.00E-01	DT	≥	1.00E-01
GLU	40	DT	≥	5.00E-01	DT	≥	1.00E-01	DT	≥	1.00E-01
GLY	41	measureable	□	3.28E-02	too fast	≈	5.00E-02	too fast	≈	5.00E-02
LEU	42	DT	≥	5.00E-01	DT	≥	1.00E-01	DT	≥	1.00E-01
HIS	43	too slow	≤	6.00E-06	measurable	=	2.09E-05	too slow	≤	6.00E-06
GLY	44	too slow	≤	6.00E-06	too slow	≤	6.00E-06	too slow	≤	6.00E-06
PHE	45	too slow	≤	6.00E-06	measurable	=	1.21E-05	too slow	≤	6.00E-06
HIS	46	too slow	≤	6.00E-06	too slow	≤	6.00E-06	too slow	≤	6.00E-06
VAL	47	too slow	≤	6.00E-06	too slow	≤	6.00E-06	too slow	≤	6.00E-06
HIS	48	too slow	≤	6.00E-06	too slow	≤	6.00E-06	too slow	≤	6.00E-06
GLU	49	too slow	≤	6.00E-06	too slow	≤	6.00E-06	too slow	≤	6.00E-06
PHE	50	measureable	□	6.81E-04	measurable	=	1.56E-04	measurable	=	2.88E-04
GLY	51	measureable	□	2.38E-03	measurable	=	2.77E-03	measurable	=	1.76E-03
ASP	52	measureable	□	2.52E-03	measurable	=	1.26E-03	measurable	=	1.62E-03
ASN	53	DT	≥	5.00E-01	DT	≥	1.00E-01	DT	≥	1.00E-01
THR	54	DT	≥	5.00E-01	too fast	≈	5.00E-02	DT	≥	1.00E-01
ALA	55	DT	≥	5.00E-01	DT	≥	1.00E-01	DT	≥	1.00E-01
GLY	56	DT	≥	5.00E-01	DT	≥	1.00E-01	DT	≥	1.00E-01
CYS	57	NA			NA			NA		
THR	58	NA			NA			NA		
SER	59	DT	≥	5.00E-01	DT	≥	1.00E-01	DT	≥	1.00E-01
ALA	60	too fast	≈	5.00E-02	too fast	≈	5.00E-02	too fast	≈	5.00E-02
GLY	61	DT	≥	5.00E-01	DT	≥	1.00E-01	DT	≥	1.00E-01
PRO	62	proline			proline			proline		
HIS	63	DT	≥	5.00E-01	DT	≥	1.00E-01	DT	≥	1.00E-01
PHE	64	NA			NA			NA		
ASN	65	DT	≥	5.00E-01	DT	≥	1.00E-01	DT	≥	1.00E-01
PRO	66	proline			proline			proline		
LEU	67	DT	≥	5.00E-01	DT	≥	1.00E-01	DT	≥	1.00E-01
SER	68	DT	≥	5.00E-01	DT	≥	1.00E-01	too fast	≈	5.00E-02
ARG	69	measureable	□	2.72E-02	measurable	=	6.63E-03	too fast	≈	5.00E-02
LYS	70	DT	≥	5.00E-01	too fast	≈	5.00E-02	DT	≥	1.00E-01
HIS	71	measureable	□	2.14E-04	measurable	=	1.14E-04	measurable	=	1.68E-04
GLY	72	too slow	≤	6.00E-06	too slow	≤	6.00E-06	too slow	≤	6.00E-06
GLY	73	measureable	□	2.49E-04	measurable	=	4.26E-05	measurable	=	3.50E-04
PRO	74	proline			proline			proline		
LYS	75	DT	≥	5.00E-01	DT	≥	1.00E-01	DT	≥	1.00E-01
ASP	76	too fast	≈	5.00E-02	too fast	≈	5.00E-02	DT	≥	1.00E-01
GLU	77	DT	≥	5.00E-01	DT	≥	1.00E-01	DT	≥	1.00E-01
GLU	78	DT	≥	5.00E-01	DT	≥	1.00E-01	DT	≥	1.00E-01
ARG	79	too fast	≈	5.00E-02	measurable	=	1.45E-02	measurable	=	3.06E-02

HIS	80	too slow	≤	6.00E-06	measurable	=	1.48E-05	too slow	≤	6.00E-06
VAL	81	DT	≥	5.00E-01	DT	≥	1.00E-01	DT	≥	1.00E-01
GLY	82	too slow	≤	6.00E-06	too slow	≤	6.00E-06	too slow	≤	6.00E-06
ASP	83	too slow	≤	6.00E-06	measurable	=	1.59E-05	too slow	≤	6.00E-06
LEU	84	too slow	≤	6.00E-06	too slow	≤	6.00E-06	too slow	≤	6.00E-06
GLY	85	too slow	≤	6.00E-06	measurable	=	1.64E-05	too slow	≤	6.00E-06
ASN	86	DT	≥	5.00E-01	too fast	≈	5.00E-02	DT	≥	1.00E-01
VAL	87	too slow	≤	6.00E-06	measurable	=	2.73E-05	too slow	≤	6.00E-06
THR	88	DT	≥	5.00E-01	DT	≥	1.00E-01	DT	≥	1.00E-01
ALA	89	measureable	□	4.16E-04	measurable	=	2.48E-04	measurable	=	2.38E-04
ASP	90	too fast	≈	5.00E-02	DT	≥	1.00E-01	too fast	≈	5.00E-02
LYS	91	DT	≥	5.00E-01	DT	≥	1.00E-01	DT	≥	1.00E-01
ASP	92	DT	≥	5.00E-01	DT	≥	1.00E-01	DT	≥	1.00E-01
GLY	93	measureable	□	2.29E-02	DT	≥	1.00E-01	measurable	=	1.52E-02
VAL	94	measureable	□	9.85E-03	DT	≥	1.00E-01	measurable	=	6.63E-03
ALA	95	measureable	□	2.29E-03	measurable	=	4.77E-03	measurable	=	1.55E-03
ASP	96	DT	≥	5.00E-01	DT	≥	1.00E-01	DT	≥	1.00E-01
VAL	97	measureable	□	5.51E-04	measurable	=	1.09E-04	measurable	=	4.13E-04
SER	98	DT	≥	5.00E-01	DT	≥	1.00E-01	DT	≥	1.00E-01
ILE	99	measureable	□	2.21E-03	measurable	=	1.94E-04	measurable	=	8.08E-03
GLU	100	DT	≥	5.00E-01	DT	≥	1.00E-01	DT	≥	1.00E-01
ASP	101	measureable	□	9.47E-03	measurable	=	2.19E-03	NA		
SER	102	DT	≥	5.00E-01	DT	≥	1.00E-01	DT	≥	1.00E-01
VAL	103	measureable	□	8.32E-03	measurable	=	9.12E-03	measurable	=	4.93E-03
ILE	104	measureable	□	1.40E-05	measurable	=	1.17E-05	measurable	=	2.63E-04
SER	105	DT	≥	5.00E-01	DT	≥	1.00E-01	DT	≥	1.00E-01
LEU	106	DT	≥	5.00E-01	DT	≥	1.00E-01	DT	≥	1.00E-01
SER	107	DT	≥	5.00E-01	DT	≥	1.00E-01	DT	≥	1.00E-01
GLY	108	NA			NA			NA		
ASP	109	NA			NA			DT	≥	1.00E-01
HIS	110	NA			DT	≥	1.00E-01	DT	≥	1.00E-01
SER	111	DT	≥	5.00E-01	DT	≥	1.00E-01	DT	≥	1.00E-01
ILE	112	measureable	□	6.41E-05	too slow	≤	6.00E-06	measurable	=	4.76E-05
ILE	113	measureable	□	1.07E-04	measurable	=	2.47E-05	measurable	=	5.26E-05
GLY	114	too slow	≤	6.00E-06	too slow	≤	6.00E-06	too slow	≤	6.00E-06
ARG	115	too slow	≤	6.00E-06	too slow	≤	6.00E-06	too slow	≤	6.00E-06
THR	116	too slow	≤	6.00E-06	too slow	≤	6.00E-06	too slow	≤	6.00E-06
LEU	117	too slow	≤	6.00E-06	too slow	≤	6.00E-06	too slow	≤	6.00E-06
VAL	118	too slow	≤	6.00E-06	too slow	≤	6.00E-06	too slow	≤	6.00E-06
VAL	119	too slow	≤	6.00E-06	measurable	=	1.65E-05	too slow	≤	6.00E-06
HIS	120	NA			NA			too slow	≤	6.00E-06
GLU	121	measureable	□	2.49E-03	measurable	=	3.69E-04	measurable	=	1.28E-03
LYS	122	measureable	□	4.98E-04	measurable	=	8.44E-05	measurable	=	3.23E-04
ALA	123	DT	≥	5.00E-01	DT	≥	1.00E-01	DT	≥	1.00E-01
ASP	124	too slow	≤	6.00E-06	too slow	≤	6.00E-06	too slow	≤	6.00E-06
ASP	125	measureable	□	5.15E-04	measurable	=	1.64E-04	measurable	=	5.13E-04
LEU	126	measureable	□	1.38E-04	measurable	=	2.39E-05	measurable	=	6.23E-05
GLY	127	measureable	□	5.90E-04	measurable	=	8.13E-05	measurable	=	3.90E-04
LYS	128	too fast	≈	5.00E-02	measurable	=	1.10E-02	too fast	≈	5.00E-02
GLY	129	DT	≥	5.00E-01	DT	≥	1.00E-01	DT	≥	1.00E-01

GLY	130	NA			DT	≥	1.00E-01	DT	≥	1.00E-01
ASN	131	DT	≥	5.00E-01	DT	≥	1.00E-01	DT	≥	1.00E-01
GLU	132	NA			NA			NA		
GLU	133	DT	≥	5.00E-01	DT	≥	1.00E-01	DT	≥	1.00E-01
SER	134	DT	≥	5.00E-01	DT	≥	1.00E-01	DT	≥	1.00E-01
THR	135	DT	≥	5.00E-01	DT	≥	1.00E-01	DT	≥	1.00E-01
LYS	136	DT	≥	5.00E-01	DT	≥	1.00E-01	DT	≥	1.00E-01
THR	137	DT	≥	5.00E-01	DT	≥	1.00E-01	DT	≥	1.00E-01
GLY	138	measureable	□	2.99E-02	measurable	=	5.21E-03	measurable	=	1.80E-02
ASN	139	too fast	≈	5.00E-02	measurable	=	1.35E-02	measurable	=	3.43E-02
ALA	140	DT	≥	5.00E-01	DT	≥	1.00E-01	DT	≥	1.00E-01
GLY	141	DT	≥	5.00E-01	DT	≥	1.00E-01	DT	≥	1.00E-01
SER	142	DT	≥	5.00E-01	DT	≥	1.00E-01	DT	≥	1.00E-01
ARG	143	NA			NA			NA		
LEU	144	measureable	□	1.89E-04	measurable	=	4.23E-05	measurable	=	5.28E-05
ALA	145	too slow	≤	6.00E-06	too slow	≤	6.00E-06	too slow	≤	6.00E-06
CYS	146	too fast	≈	5.00E-02	too fast	≈	5.00E-02	too fast	≈	5.00E-02
GLY	147	too slow	≤	6.00E-06	measurable	=	1.70E-05	too slow	≤	6.00E-06
VAL	148	DT	≥	5.00E-01	DT	≥	1.00E-01	DT	≥	1.00E-01
ILE	149	too slow	≤	6.00E-06	too slow	≤	6.00E-06	too slow	≤	6.00E-06
GLY	150	too slow	≤	6.00E-06	too slow	≤	6.00E-06	too slow	≤	6.00E-06
ILE	151	measureable	□	1.24E-03	measurable	=	4.68E-04	measurable	=	7.76E-04
ALA	152	measureable	□	1.98E-03	measurable	=	8.95E-04	measurable	=	1.17E-03
GLN	153	measureable	□	1.56E-02	measurable	=	9.15E-03	measurable	=	7.92E-03

Table A1.3 - pWT residual curvature. The quadratic coefficient (*a*) obtained by fitting residual data to the quadratic equation and associated R^2 value is given. Only residues for which crosspeaks were observed at all temperature are included.

	24°C	36.5°C	49.5°C	61.5°C	72.5°C	84°C		
Res	R1	R2	R3	R4	R5	R6	*a*	R^2
1								
2								
3	0.0068	-0.0098	0.0025	-0.0002	-0.0022	0.0029	-6.53E-06	0.9970
4								
5	0.0089	-0.0031	-0.0055	-0.0091	0.0004	0.0083	-1.83E-05	0.9998
6	0.0056	-0.0013	-0.0019	-0.0100	0.0015	0.0061	-1.30E-05	0.9996
7								
8	0.0101	-0.0041	-0.0065	-0.0094	0.0023	0.0077	-1.92E-05	0.9996
9								
10	0.0135	-0.0066	-0.0084	-0.0080	-0.0023	0.0118	-2.50E-05	0.9996
11								
12								
13								

14	-0.0063	-0.0005	0.0080	0.0040	0.0034	-0.0085	1.55E-05	0.9994
15	-0.0006	0.0046	-0.0015	-0.0059	0.0003	0.0031	-4.39E-06	0.9996
16								
17	0.0001	-0.0026	0.0034	-0.0021	0.0042	-0.0030	2.57E-06	0.9997
18								
19								
20	0.0008	-0.0027	0.0046	-0.0038	0.0008	0.0004	-4.60E-07	0.9997
21	0.0062	-0.0033	-0.0048	-0.0025	0.0006	0.0038	-1.04E-05	0.9999
22	0.0144	-0.0049	-0.0081	-0.0184	0.0052	0.0118	-2.94E-05	0.9968
23								
24	0.0037	-0.0042	-0.0004	0.0000	-0.0009	0.0018	-4.34E-06	0.9998
25								
26								
27	0.0075	-0.0015	-0.0073	-0.0076	0.0037	0.0052	-1.51E-05	0.9993
28								
29	0.0042	-0.0029	-0.0011	-0.0010	-0.0047	0.0055	-7.93E-06	0.9991
30	0.0081	-0.0033	-0.0058	-0.0090	0.0060	0.0039	-1.46E-05	0.9991
31	0.0119	-0.0018	-0.0132	-0.0083	0.0009	0.0104	-2.48E-05	0.9998
32								
33	0.0165	0.0006	-0.0114	-0.0281	0.0005	0.0219	-4.29E-05	0.9970
34	0.0035	-0.0027	-0.0001	-0.0070	0.0069	-0.0006	-4.83E-06	0.9993
35	0.0065	-0.0044	-0.0007	-0.0074	0.0006	0.0053	-1.18E-05	0.9997
36								
37	0.0093	-0.0042	-0.0060	-0.0062	-0.0009	0.0081	-1.75E-05	0.9999
38	-0.0050	-0.0040	0.0071	0.0200	-0.0174	-0.0006	1.43E-05	0.9936
39								
40								
41	0.0089	-0.0042	-0.0050	-0.0084	0.0027	0.0061	-1.62E-05	0.9994
42								
43	0.0051	0.0000	-0.0024	-0.0104	0.0008	0.0069	-1.35E-05	0.9994
44	0.0032	-0.0015	-0.0028	-0.0019	0.0012	0.0017	-5.45E-06	1.0000
45	0.0062	-0.0042	-0.0041	-0.0020	0.0012	0.0029	-9.23E-06	0.9998
46								
47	0.0045	-0.0026	-0.0023	-0.0036	0.0014	0.0027	-7.59E-06	0.9999
48	0.0032	-0.0045	0.0010	-0.0008	0.0000	0.0010	-3.11E-06	0.9995

49	0.0045	-0.0015	-0.0021	-0.0035	-0.0044	0.0069	-1.05E-05	0.9998
50								
51	0.0075	-0.0040	-0.0029	-0.0061	-0.0018	0.0073	-1.44E-05	0.9998
52	-0.0006	-0.0011	0.0014	0.0048	-0.0059	0.0014	1.70E-06	0.9996
53	0.0033	-0.0011	-0.0017	0.0031	-0.0138	0.0102	-9.34E-06	0.6033
54	0.0036	-0.0024	-0.0007	-0.0024	-0.0024	0.0042	-6.95E-06	0.9999
55								
56								
57								
58								
59	-0.0404	0.0661	0.0040	-0.0307	-0.0140	0.0151	1.17E-05	0.9618
60	0.0036	-0.0044	-0.0001	-0.0024	0.0045	-0.0012	-2.84E-06	0.9995
61	0.0044	-0.0028	-0.0007	-0.0042	-0.0010	0.0043	-8.27E-06	0.9999
62								
63								
64								
65								
66								
67	0.0108	-0.0038	-0.0083	-0.0069	-0.0026	0.0107	-2.17E-05	0.9999
68								
69	0.0042	-0.0022	-0.0011	-0.0052	0.0005	0.0038	-8.26E-06	0.9998
70	0.0144	-0.0057	-0.0110	-0.0098	0.0009	0.0113	-2.70E-05	0.9994
71	-0.0018	0.0040	0.0017	-0.0034	-0.0052	0.0048	-2.56E-06	0.9990
72	0.0009	-0.0040	-0.0009	0.0111	-0.0070	-0.0001	3.02E-06	0.9981
73	0.0086	-0.0025	-0.0053	-0.0078	-0.0030	0.0101	-1.88E-05	0.9998
74								
75								
76	0.0057	-0.0012	-0.0032	-0.0081	0.0009	0.0060	-1.28E-05	0.9998
77	0.0020	-0.0046	0.0011	-0.0028	0.0107	-0.0064	2.44E-06	0.9891
78	0.0076	-0.0009	-0.0096	-0.0048	0.0024	0.0053	-1.52E-05	0.9953
79	0.0070	-0.0002	-0.0072	-0.0078	0.0010	0.0071	-1.61E-05	0.9999
80	0.0070	-0.0053	-0.0014	-0.0039	-0.0028	0.0064	-1.19E-05	0.9997
81	0.0024	0.0003	-0.0034	-0.0010	-0.0016	0.0033	-5.93E-06	1.0000
82	0.0020	0.0003	0.0012	-0.0062	-0.0031	0.0058	-7.45E-06	0.9994
83	0.0026	-0.0025	0.0003	-0.0026	0.0009	0.0013	-3.77E-06	0.9999
84	0.0044	-0.0027	-0.0018	-0.0039	0.0010	0.0029	-7.62E-	0.9999

							06	
85								
86	0.0034	-0.0015	-0.0023	-0.0035	0.0021	0.0018	-6.11E-06	0.9998
87	0.0035	-0.0018	0.0001	-0.0044	-0.0023	0.0050	-7.85E-06	0.9998
88	0.0080	-0.0030	-0.0052	-0.0081	0.0021	0.0062	-1.56E-05	0.9994
89	0.0116	-0.0023	-0.0122	-0.0072	-0.0004	0.0105	-2.38E-05	0.9997
90	0.0031	0.0015	0.0004	-0.0106	-0.0024	0.0082	-1.18E-05	0.9985
91	-0.0078	0.0066	0.0064	-0.0066	0.0068	-0.0055	1.01E-05	0.9966
92	0.0035	-0.0014	-0.0018	-0.0051	0.0028	0.0021	-6.78E-06	0.9998
93	0.0128	-0.0016	-0.0088	-0.0125	-0.0095	0.0196	-3.18E-05	0.9991
94	0.0061	-0.0038	0.0018	-0.0107	-0.0002	0.0069	-1.28E-05	0.9993
95	0.0092	-0.0014	-0.0083	-0.0087	-0.0004	0.0096	-2.04E-05	0.9999
96	0.0038	-0.0010	-0.0036	-0.0026	-0.0002	0.0035	-7.80E-06	1.0000
97	0.0096	-0.0039	-0.0067	-0.0089	0.0034	0.0064	-1.78E-05	0.9995
98								
99	0.0070	-0.0032	-0.0027	-0.0087	0.0017	0.0059	-1.38E-05	0.9996
100	-0.0032	-0.0036	0.0062	0.0056	0.0025	-0.0074	1.21E-05	0.9974
101	0.0099	-0.0026	-0.0077	-0.0117	0.0053	0.0069	-1.98E-05	0.9988
102								
103	0.0089	-0.0047	-0.0041	-0.0089	0.0029	0.0060	-1.60E-05	0.9997
104	0.0045	-0.0012	-0.0009	-0.0065	-0.0031	0.0072	-1.13E-05	0.9997
105								
106	0.0082	-0.0061	-0.0009	-0.0117	0.0085	0.0022	-1.25E-05	0.9984
107								
108								
109								
110								
111	0.0034	-0.0022	-0.0013	-0.0034	0.0015	0.0019	-5.76E-06	0.9999
112	0.0084	-0.0053	-0.0034	-0.0058	-0.0005	0.0065	-1.46E-05	0.9997
113	0.0163	-0.0014	-0.0093	-0.0158	-0.0208	0.0309	-4.40E-05	0.9937
114	0.0039	-0.0024	-0.0005	-0.0011	-0.0071	0.0071	-8.71E-06	0.9987
115	0.0068	-0.0033	-0.0031	-0.0035	-0.0056	0.0087	-1.39E-05	0.9997
116	-0.0001	-0.0023	0.0021	0.0025	-0.0011	-0.0011	2.61E-06	0.9999
117	-0.0006	-0.0010	0.0029	0.0012	-0.0032	0.0008	1.43E-06	0.9998
118								

119	0.0036	-0.0017	-0.0024	-0.0034	0.0023	0.0016	-6.11E-06	0.9999
120	0.0041	-0.0038	-0.0010	-0.0014	0.0000	0.0021	-5.58E-06	0.9999
121	0.0046	-0.0011	-0.0013	-0.0065	-0.0025	0.0069	-1.13E-05	0.9997
122	0.0034	-0.0023	-0.0023	0.0004	-0.0022	0.0029	-5.41E-06	0.9998
123	0.0058	-0.0059	-0.0052	0.0018	0.0060	-0.0025	-4.20E-06	0.9934
124	0.0033	-0.0005	-0.0016	-0.0052	-0.0003	0.0043	-8.12E-06	0.9997
125	0.0065	-0.0016	-0.0043	-0.0080	0.0013	0.0061	-1.40E-05	0.9997
126	0.0027	0.0013	-0.0042	-0.0056	0.0041	0.0017	-7.04E-06	0.9995
127	0.0009	-0.0048	0.0060	-0.0032	0.0035	-0.0023	2.11E-06	0.9996
128	0.0052	-0.0065	0.0020	-0.0049	0.0030	0.0011	-5.84E-06	0.9995
129	-0.0003	-0.0087	-0.0005	0.0095	0.0203	-0.0203	1.79E-05	0.9730
130								
131								
132								
133								
134	-0.0060	-0.0002	0.0073	0.0063	-0.0023	-0.0051	1.34E-05	0.9993
135								
136								
137	0.0029	-0.0011	0.0003	-0.0041	-0.0031	0.0052	-7.25E-06	0.9998
138								
139	0.0010	0.0001	-0.0001	-0.0027	0.0001	0.0016	-2.93E-06	1.0000
140	0.0037	-0.0034	0.0005	-0.0026	-0.0016	0.0034	-6.08E-06	0.9999
141								
142								
143								
144	0.0035	-0.0011	-0.0005	-0.0062	0.0000	0.0043	-8.14E-06	0.9998
145	0.0037	-0.0027	-0.0005	-0.0034	-0.0004	0.0032	-6.54E-06	0.9999
146								
147	0.0013	0.0015	-0.0025	-0.0021	-0.0014	0.0032	-5.03E-06	0.9999
148	0.0183	-0.0135	-0.0119	-0.0039	0.0036	0.0074	-2.56E-05	0.9955
149	0.0111	-0.0038	-0.0087	-0.0086	0.0004	0.0095	-2.19E-05	0.9999
150	-0.0038	-0.0020	0.0076	0.0125	-0.0192	0.0049	6.90E-06	0.9928
151	0.0046	-0.0006	-0.0037	-0.0049	-0.0011	0.0056	-1.08E-05	0.9999
152	0.0042	-0.0015	-0.0033	-0.0018	-0.0021	0.0045	-8.44E-06	1.0000
153								

Table A1.4 - G93A residual curvature. The quadratic coefficient (*a*) obtained by fitting residual data to the quadratic equation and associated R^2 value is given. Only residues for which crosspeaks were observed at all temperature are included.

	24°C	36.5°C	49.5°C	61.5°C	72.5°C	84°C		
Res	R1	R2	R3	R4	R5	R6	*a*	R^2
1								
2								
3	0.0054	-0.0076	0.0015	-0.0025	0.0036	-0.0004	-4.26E-06	0.9977
4	0.0067	-0.0010	-0.0048	-0.0084	0.0001	0.0075	-1.54E-05	0.9999
5	0.0063	-0.0042	-0.0021	-0.0041	-0.0012	0.0053	-1.09E-05	0.9998
6	0.0158	-0.0082	-0.0090	-0.0112	0.0000	0.0125	-2.88E-05	0.9996
7	0.0010	-0.0003	0.0014	-0.0048	0.0009	0.0017	-3.14E-06	0.9994
8	0.0075	-0.0033	-0.0054	-0.0049	0.0001	0.0059	-1.39E-05	0.9999
9								
10								
11								
12								
13								
14	-0.0083	0.0033	0.0071	0.0035	0.0016	-0.0072	1.56E-05	0.9998
15	0.0069	-0.0029	-0.0042	-0.0057	-0.0005	0.0063	-1.36E-05	1.0000
16	0.0023	-0.0017	-0.0008	-0.0017	0.0008	0.0011	-3.53E-06	1.0000
17	0.0028	-0.0005	0.0038	-0.0081	-0.0082	0.0103	-1.09E-05	0.9987
18	0.0039	-0.0035	-0.0009	-0.0024	0.0011	0.0017	-5.46E-06	0.9998
19								
20	0.0097	-0.0089	-0.0033	-0.0030	0.0022	0.0034	-1.24E-05	0.9995
21	0.0025	-0.0037	0.0021	-0.0002	-0.0037	0.0030	-3.33E-06	0.9996
22	0.0115	-0.0059	-0.0053	-0.0107	0.0009	0.0094	-2.15E-05	0.9990
23								
24								
25								
26								
27	0.0045	-0.0029	-0.0001	-0.0048	-0.0019	0.0052	-9.01E-06	0.9996
28								
29	0.0043	-0.0002	-0.0039	-0.0043	-0.0013	0.0054	-1.02E-05	0.9999
30	0.0061	-0.0022	-0.0036	-0.0067	0.0013	0.0052	-1.22E-05	0.9998
31	0.0085	-0.0023	-0.0047	-0.0099	-0.0009	0.0095	-1.87E-05	0.9998
32								
33	-0.0008	0.0000	0.0012	-0.0022	0.0047	-0.0030	2.48E-06	0.9997
34	0.0019	-0.0007	0.0004	-0.0050	0.0012	0.0021	-4.62E-06	0.9999
35	0.0049	-0.0020	-0.0025	-0.0059	0.0017	0.0038	-9.62E-06	0.9999
36								
37								

38	-0.0018	0.0061	-0.0021	-0.0070	0.0043	0.0005	-2.21E-06	0.9969
39	0.0047	-0.0029	-0.0014	-0.0050	0.0016	0.0031	-8.16E-06	0.9984
40								
41	0.0050	-0.0014	-0.0045	-0.0042	0.0015	0.0036	-9.64E-06	0.9999
42								
43	0.0059	-0.0059	0.0020	-0.0066	0.0004	0.0041	-9.15E-06	0.9991
44	0.0017	-0.0006	0.0007	-0.0040	-0.0008	0.0030	-4.57E-06	0.9999
45	0.0044	-0.0044	0.0002	-0.0021	-0.0012	0.0031	-6.28E-06	0.9998
46	-0.0088	-0.0109	-0.0114	0.0739	-0.0198	-0.0231	4.51E-05	0.9617
47	0.0044	-0.0040	0.0010	-0.0048	-0.0003	0.0036	-7.41E-06	0.9997
48								
49	0.0052	-0.0028	-0.0014	-0.0056	-0.0004	0.0051	-1.02E-05	0.9999
50	0.0030	-0.0008	-0.0028	-0.0023	0.0006	0.0023	-5.87E-06	1.0000
51	0.0043	-0.0008	-0.0032	-0.0041	-0.0013	0.0051	-9.70E-06	1.0000
52	-0.0022	0.0006	0.0024	0.0011	-0.0003	-0.0016	4.25E-06	1.0000
53	-0.0020	0.0008	0.0003	0.0013	0.0037	-0.0041	5.07E-06	0.9642
54	0.0040	-0.0025	0.0007	-0.0065	0.0001	0.0042	-8.19E-06	0.9998
55								
56	0.0015	0.0042	0.0034	-0.0135	-0.0085	0.0131	-1.39E-05	0.9976
57								
58								
59								
60	0.0013	-0.0008	0.0013	-0.0042	0.0006	0.0017	-3.23E-06	0.9999
61	0.0047	-0.0043	-0.0009	-0.0021	0.0001	0.0026	-6.61E-06	0.9998
62								
63								
64								
65								
66								
67	0.0085	-0.0029	-0.0062	-0.0056	-0.0032	0.0093	-1.77E-05	0.9999
68	0.0133	-0.0264	0.0126	0.0013	-0.0004	-0.0003	-4.85E-06	0.9925
69	0.0046	-0.0033	-0.0005	-0.0050	0.0012	0.0031	-7.72E-06	0.9997
70	0.0119	-0.0049	-0.0080	-0.0097	0.0011	0.0096	-2.27E-05	0.9994
71	0.0034	-0.0025	0.0014	-0.0065	0.0009	0.0032	-6.73E-06	0.9995
72	0.0008	-0.0044	0.0015	0.0062	-0.0023	-0.0017	3.42E-06	0.9994
73	0.0035	-0.0020	-0.0002	-0.0040	-0.0016	0.0043	-7.27E-06	0.9998
74								
75								
76	0.0051	-0.0060	0.0010	-0.0022	-0.0004	0.0025	-6.15E-06	0.9995
77	-0.0053	0.0059	0.0151	-0.0186	-0.0052	0.0082	-2.41E-06	0.9917
78								
79	0.0052	-0.0031	-0.0020	-0.0037	-0.0012	0.0048	-9.55E-06	0.9999
80								

81	0.0053	-0.0025	-0.0038	-0.0031	0.0005	0.0037	-9.30E-06	1.0000
82	0.0049	-0.0001	-0.0044	-0.0060	0.0000	0.0057	-1.17E-05	0.9999
83	0.0000	-0.0004	0.0000	0.0008	0.0002	-0.0006	7.55E-07	1.0000
84	0.0011	-0.0025	0.0009	0.0013	-0.0012	0.0003	-2.47E-07	0.9999
85	0.0107	-0.0121	-0.0016	0.0004	-0.0021	0.0046	-1.22E-05	0.9984
86								
87	0.0008	-0.0021	0.0032	-0.0019	-0.0014	0.0013	-9.81E-07	0.9998
88	0.0051	-0.0010	-0.0031	-0.0061	-0.0010	0.0061	-1.17E-05	0.9998
89	0.0087	0.0003	-0.0069	-0.0133	0.0003	0.0109	-2.20E-05	0.9989
90	0.0024	-0.0016	-0.0013	-0.0006	-0.0013	0.0023	-4.22E-06	0.9999
91								
92	0.0058	-0.0018	-0.0051	-0.0030	-0.0014	0.0055	-1.15E-05	0.9999
93	0.0037	-0.0032	-0.0043	0.0021	0.0030	-0.0013	-2.92E-06	0.9996
94	0.0085	-0.0035	-0.0058	-0.0056	-0.0016	0.0080	-1.66E-05	0.9999
95	0.0069	-0.0039	-0.0046	-0.0045	0.0025	0.0035	-1.13E-05	0.9995
96	0.0055	-0.0018	-0.0028	-0.0055	-0.0017	0.0064	-1.19E-05	0.9999
97	0.0079	-0.0026	-0.0044	-0.0095	0.0011	0.0074	-1.66E-05	0.9997
98	0.0032	-0.0026	-0.0019	-0.0012	0.0022	0.0003	-3.88E-06	0.9999
99	0.0055	-0.0017	-0.0032	-0.0052	-0.0018	0.0064	-1.19E-05	0.9999
100								
101	0.0110	-0.0073	-0.0061	-0.0059	0.0023	0.0059	-1.73E-05	0.9991
102								
103	0.0074	-0.0053	-0.0016	-0.0055	-0.0009	0.0060	-1.26E-05	0.9998
104	0.0060	-0.0009	-0.0049	-0.0058	-0.0018	0.0073	-1.38E-05	1.0000
105								
106	0.0071	-0.0040	-0.0035	-0.0072	0.0039	0.0036	-1.21E-05	0.9996
107								
108								
109								
110								
111	-0.0001	0.0019	-0.0007	-0.0023	-0.0009	0.0020	-2.45E-06	0.9999
112	0.0061	-0.0013	-0.0042	-0.0073	0.0002	0.0064	-1.36E-05	0.9999
113	0.0065	-0.0017	-0.0028	-0.0070	-0.0043	0.0095	-1.54E-05	0.9997
114	0.0030	-0.0019	-0.0007	-0.0028	-0.0002	0.0026	-5.42E-06	0.9999
115	0.0067	-0.0040	-0.0034	-0.0043	0.0001	0.0049	-1.15E-05	0.9999
116	0.0012	-0.0019	0.0006	0.0001	-0.0005	0.0005	-9.54E-07	1.0000
117	0.0020	-0.0014	-0.0006	-0.0012	-0.0004	0.0016	-3.38E-06	1.0000
118								
119	0.0041	-0.0011	-0.0038	-0.0036	0.0014	0.0030	-8.08E-06	1.0000
120								
121	0.0070	-0.0023	-0.0042	-0.0070	-0.0006	0.0072	-1.47E-05	0.9999
122	0.0040	-0.0041	0.0005	-0.0024	-0.0007	0.0027	-5.78E-06	0.9997
123	0.0043	-0.0042	-0.0034	-0.0003	0.0060	-0.0023	-3.18E-06	0.9958

124	0.0062	-0.0035	-0.0025	-0.0061	0.0017	0.0043	-1.11E-05	0.9993
125	0.0070	-0.0057	-0.0029	-0.0022	0.0004	0.0035	-9.86E-06	0.9995
126	0.0074	-0.0036	-0.0035	-0.0075	0.0016	0.0056	-1.38E-05	0.9998
127	0.0017	-0.0029	0.0000	0.0008	0.0016	-0.0011	-2.63E-07	0.9999
128	-0.0003	-0.0022	0.0030	0.0010	-0.0002	-0.0013	2.76E-06	0.9999
129	-0.0050	-0.0056	0.0045	0.0111	0.0141	-0.0191	2.31E-05	0.9892
130								
131								
132								
133								
134								
135								
136	0.0095	-0.0052	-0.0013	-0.0096	-0.0052	0.0119	-1.98E-05	0.9994
137								
138	-0.0018	-0.0217	0.0439	-0.0126	-0.0084	0.0005	1.36E-05	0.9813
139	0.0017	-0.0015	0.0011	-0.0039	0.0017	0.0010	-2.99E-06	0.9999
140	0.0017	-0.0027	0.0018	-0.0036	0.0041	-0.0013	-9.52E-07	0.9997
141								
142								
143								
144	0.0033	-0.0022	-0.0005	-0.0061	0.0051	0.0003	-5.16E-06	0.9994
145	0.0035	-0.0036	0.0008	-0.0029	0.0003	0.0020	-4.92E-06	0.9998
146	0.0096	-0.0043	-0.0049	-0.0082	-0.0012	0.0091	-1.88E-05	0.9998
147	0.0042	-0.0020	-0.0014	-0.0044	-0.0008	0.0045	-8.58E-06	1.0000
148	0.0068	-0.0037	-0.0010	-0.0096	0.0016	0.0059	-1.32E-05	0.9989
149	0.0089	-0.0017	-0.0083	-0.0090	0.0034	0.0068	-1.82E-05	0.9996
150	0.0018	-0.0022	0.0022	-0.0043	0.0012	0.0012	-2.98E-06	0.9996
151	0.0019	-0.0007	-0.0011	-0.0017	-0.0004	0.0020	-3.90E-06	1.0000
152	0.0022	-0.0001	0.0004	-0.0038	-0.0048	0.0061	-7.30E-06	0.9997
153	0.0037	-0.0033	0.0000	-0.0023	-0.0012	0.0031	-5.92E-06	0.9992

Table A1.5 - E100G residual curvature. The quadratic coefficient (*a*) obtained by fitting residual data to the quadratic equation and associated R^2 value is given. Only residues for which crosspeaks were observed at all temperature are included.

	24°C	36.5°C	49.5°C	61.5°C	72.5°C	84°C		
Res	R1	R2	R3	R4	R5	R6	*a*	R^2
1								
2	-0.0018	0.0042	0.0011	-0.0038	-0.0034	0.0038	-2.20E-06	0.9925
3								
4								
5	0.0071	-0.0039	-0.0033	-0.0038	-0.0035	0.0074	-1.35E-05	0.9997
6	0.0098	-0.0037	-0.0039	-0.0119	-0.0009	0.0106	-2.10E-05	0.9997

7								
8	0.0065	-0.0020	-0.0076	0.0010	-0.0049	0.0070	-1.26E-05	0.9993
9								
10								
11								
12								
13								
14	-0.0073	-0.0018	0.0087	0.0093	0.0012	-0.0101	1.96E-05	0.9993
15								
16								
17	-0.0029	-0.0025	0.0037	0.0064	0.0016	-0.0064	1.05E-05	0.9998
18	-0.0048	0.0058	0.0010	0.0000	-0.0022	0.0001	4.09E-06	0.9993
19								
20	-0.0022	-0.0017	0.0019	0.0065	0.0000	-0.0045	7.99E-06	0.9999
21	0.0067	-0.0053	-0.0053	0.0007	0.0016	0.0016	-8.25E-06	0.9994
22	0.0125	-0.0038	-0.0122	-0.0076	0.0018	0.0093	-2.39E-05	0.9993
23								
24								
25								
26								
27	-0.0209	0.0414	-0.0158	-0.0049	-0.0051	0.0053	4.84E-06	0.9622
28								
29	0.0042	-0.0015	-0.0045	0.0000	-0.0020	0.0038	-7.66E-06	0.9996
30								
31	0.0100	-0.0046	-0.0083	-0.0047	0.0010	0.0066	-1.74E-05	0.9997
32								
33	0.0050	-0.0037	-0.0061	0.0018	0.0038	-0.0008	-5.11E-06	0.9994
34	0.0014	-0.0006	-0.0028	0.0035	-0.0029	0.0015	-1.98E-06	0.9998
35	0.0041	-0.0029	-0.0030	0.0002	-0.0010	0.0025	-6.10E-06	0.9999
36								
37	-0.0237	0.0518	-0.0217	-0.0102	-0.0048	0.0087	4.48E-07	0.9592
38	0.0069	-0.0015	-0.0062	-0.0052	-0.0013	0.0072	-1.48E-05	1.0000
39								
40	-0.0265	0.0206	0.0164	0.0040	-0.0037	-0.0107	3.62E-05	0.9924
41	0.0047	-0.0026	-0.0035	-0.0010	-0.0013	0.0037	-8.02E-06	0.9999
42								
43	0.0047	-0.0019	-0.0057	0.0009	-0.0013	0.0033	-7.96E-06	0.9997
44	0.0028	-0.0033	-0.0029	0.0065	-0.0050	0.0019	-2.38E-06	0.9992
45	0.0060	-0.0036	-0.0067	0.0032	-0.0027	0.0038	-8.84E-06	0.9995
46	0.0059	-0.0046	-0.0063	0.0044	-0.0016	0.0022	-7.11E-06	0.9994
47	0.0087	-0.0032	-0.0097	0.0010	-0.0051	0.0082	-1.60E-05	0.9994
48								
49	0.0048	-0.0004	-0.0064	-0.0010	-0.0021	0.0051	-1.03E-05	0.9999

50								
51	0.0052	-0.0028	-0.0021	-0.0028	-0.0040	0.0065	-1.05E-05	0.9997
52	-0.0031	-0.0024	0.0035	0.0092	-0.0024	-0.0048	1.05E-05	0.9997
53								
54	0.0064	-0.0034	-0.0077	0.0018	0.0000	0.0028	-9.39E-06	0.9996
55								
56								
57								
58								
59								
60	0.0022	-0.0021	-0.0021	0.0031	-0.0024	0.0014	-2.48E-06	0.9998
61	0.0035	-0.0036	-0.0044	0.0043	0.0014	-0.0012	-2.03E-06	0.9994
62								
63								
64								
65								
66								
67	0.0106	-0.0031	-0.0089	-0.0057	-0.0045	0.0117	-2.21E-05	0.9996
68								
69	0.0056	-0.0028	-0.0054	-0.0004	-0.0007	0.0037	-9.18E-06	0.9998
70	0.0131	-0.0070	-0.0074	-0.0093	0.0012	0.0095	-2.31E-05	0.9988
71	0.0010	-0.0011	-0.0002	0.0009	-0.0019	0.0013	-1.39E-06	0.9999
72	-0.0003	-0.0016	-0.0038	0.0117	-0.0031	-0.0028	4.98E-06	0.9985
73	0.0052	-0.0019	-0.0047	-0.0002	-0.0047	0.0063	-1.04E-05	0.9995
74								
75								
76	0.0050	-0.0036	-0.0021	-0.0017	-0.0014	0.0039	-8.07E-06	0.9999
77								
78	-0.0306	0.0074	0.0350	0.0165	-0.0081	-0.0202	5.78E-05	0.9944
79	0.0082	-0.0042	-0.0092	0.0019	-0.0017	0.0050	-1.29E-05	0.9994
80	0.0061	-0.0037	-0.0043	-0.0003	-0.0027	0.0050	-1.01E-05	0.9998
81	0.0057	-0.0034	-0.0050	0.0014	-0.0033	0.0046	-9.17E-06	0.9997
82	-0.0011	0.0010	-0.0002	0.0013	-0.0005	-0.0006	1.71E-06	1.0000
83	0.0030	-0.0042	-0.0015	0.0036	-0.0011	0.0001	-1.72E-06	0.9997
84	0.0048	-0.0045	-0.0017	0.0009	-0.0036	0.0040	-6.95E-06	0.9998
85	-0.0313	0.0516	-0.0131	-0.0025	-0.0055	0.0008	1.81E-05	0.9686
86	0.0016	-0.0020	-0.0003	0.0010	-0.0012	0.0009	-1.58E-06	0.9998
87	0.0024	-0.0018	-0.0027	0.0019	-0.0011	0.0012	-3.09E-06	0.9999
88	0.0043	-0.0038	-0.0011	-0.0022	0.0009	0.0019	-5.95E-06	0.9996
89	0.0138	-0.0047	-0.0122	-0.0078	-0.0007	0.0116	-2.66E-05	0.9997
90	0.0034	-0.0039	-0.0028	0.0055	-0.0040	0.0018	-3.04E-06	0.9987
91								
92	0.0036	-0.0048	-0.0008	0.0042	-0.0048	0.0026	-3.47E-06	0.9994

93	0.0040	-0.0020	-0.0034	0.0031	-0.0084	0.0067	-8.01E-06	0.9992
94	0.0415	-0.0114	-0.0445	-0.0222	0.0075	0.0290	-7.83E-05	0.9871
95	0.0051	-0.0027	-0.0028	-0.0024	-0.0024	0.0053	-9.72E-06	0.9997
96								
97	0.0083	-0.0049	-0.0083	0.0007	0.0000	0.0041	-1.24E-05	0.9993
98								
99	0.0071	-0.0020	-0.0074	-0.0023	-0.0018	0.0065	-1.38E-05	0.9998
100								
101								
102								
103	0.0127	-0.0262	0.0560	-0.0661	0.0035	0.0202	-2.61E-05	0.9248
104	0.0066	-0.0040	-0.0049	-0.0004	-0.0025	0.0052	-1.09E-05	0.9997
105								
106	0.0081	-0.0041	-0.0067	-0.0026	0.0000	0.0053	-1.37E-05	0.9999
107								
108								
109								
110								
111	0.0006	-0.0016	0.0008	0.0021	-0.0028	0.0010	-8.61E-08	0.9999
112	0.0061	-0.0028	-0.0042	-0.0016	-0.0042	0.0068	-1.17E-05	0.9997
113	0.0089	-0.0035	-0.0080	-0.0005	-0.0072	0.0102	-1.75E-05	0.9992
114	0.0059	-0.0039	-0.0054	0.0017	-0.0016	0.0033	-8.49E-06	0.9992
115	0.0067	-0.0026	-0.0075	-0.0011	0.0007	0.0038	-1.13E-05	0.9998
116	-0.0008	-0.0014	0.0006	0.0065	-0.0047	-0.0003	3.40E-06	0.9995
117	0.0043	-0.0048	-0.0035	0.0040	-0.0001	0.0001	-3.36E-06	0.9995
118								
119	0.0035	-0.0028	-0.0053	0.0057	-0.0017	0.0006	-3.21E-06	0.9995
120	0.0013	-0.0029	-0.0004	0.0047	-0.0025	-0.0001	5.41E-07	0.9997
121	0.0080	-0.0024	-0.0083	-0.0032	-0.0009	0.0067	-1.54E-05	0.9998
122	0.0038	-0.0038	-0.0008	0.0010	-0.0036	0.0035	-5.39E-06	0.9995
123	-0.0009	-0.0036	-0.0018	0.0081	0.0089	-0.0108	1.05E-05	0.9916
124	0.0063	-0.0034	-0.0052	-0.0037	0.0042	0.0019	-9.62E-06	0.9987
125	0.0083	-0.0046	-0.0089	-0.0023	0.0073	0.0003	-1.10E-05	0.9979
126	0.0062	-0.0021	-0.0063	-0.0036	0.0020	0.0037	-1.12E-05	0.9998
127	0.0021	-0.0054	-0.0023	0.0097	-0.0007	-0.0034	3.34E-06	0.9994
128	0.0025	-0.0020	-0.0024	0.0030	-0.0031	0.0021	-3.25E-06	0.9998
129	-0.0126	-0.0058	0.0071	0.0320	0.0057	-0.0265	4.28E-05	0.9866
130								
131								
132								
133								
134								
135	0.0122	-0.0002	-0.0058	-0.0089	-0.0283	0.0309	-3.69E-05	0.9931

136	-0.0018	-0.0054	0.0000	0.0115	0.0091	-0.0134	1.50E-05	0.9984
137								
138								
139	0.0050	-0.0054	-0.0049	0.0060	-0.0009	0.0002	-3.78E-06	0.9996
140								
141	-0.0208	0.0386	-0.0126	-0.0035	-0.0062	0.0045	7.07E-06	0.9643
142								
143								
144	0.0042	-0.0009	-0.0049	-0.0002	-0.0028	0.0047	-8.63E-06	0.9998
145	0.0046	-0.0036	-0.0042	0.0030	-0.0021	0.0024	-5.86E-06	0.9997
146	0.0130	-0.0073	-0.0084	-0.0061	-0.0006	0.0094	-2.23E-05	0.9994
147	-0.0350	0.0709	-0.0289	-0.0093	-0.0050	0.0074	7.77E-06	0.9617
148								
149	0.0055	0.0002	-0.0082	-0.0025	0.0002	0.0049	-1.18E-05	0.9998
150	0.0086	-0.0038	-0.0078	-0.0046	0.0028	0.0047	-1.47E-05	0.9994
151	0.0032	-0.0025	-0.0021	0.0012	-0.0026	0.0027	-4.75E-06	0.9996
152	0.0041	-0.0051	-0.0014	0.0046	-0.0052	0.0029	-4.16E-06	0.9994
153								

Table A1.6 - V148I residual curvature. The quadratic coefficient (*a*) obtained by fitting residual data to the quadratic equation and associated R^2 value is given. Only residues for which crosspeaks were observed at all temperature are included.

	24.5°C	30°C	37°C	43°C	48°C	55°C	61°C	67°C	72.5°C	77.5°C	82°C	87.5°C		
Res	R1	R2	R3	R4	R5	R6	R7	R8	R9	R10	R11	R12	*a*	R^2
1														
2														
3	0.0056	0.0018	-0.0011	-0.0059	-0.0026	-0.0026	-0.0034	-0.0002	0.0011	0.0114	0.0028	-0.0069	-3.98E-06	0.9964
4														
5	0.0047	0.0014	0.0016	-0.0003	0.0008	-0.0070	-0.0048	-0.0027	-0.0060	-0.0009	0.0057	0.0074	-1.05E-05	0.9994
6														
7														
8	0.0076	-0.0003	0.0007	-0.0045	-0.0011	-0.0030	-0.0043	-0.0025	-0.0024	0.0020	0.0038	0.0039	-9.25E-06	0.9998
9	0.0104	-0.0017	0.0026	-0.0060	-0.0025	-0.0062	-0.0038	-0.0004	-0.0025	0.0000	0.0051	0.0050	-1.16E-05	0.9993
10														
11														
12														
13														
14	-0.0107	-0.0035	-0.0027	0.0014	0.0088	0.0095	0.0066	0.0066	0.0009	-0.0007	-0.0042	-0.0120	1.90E-05	0.9994

15	0.0090	0.0004	0.0002	-0.0046	-0.0039	-0.0052	-0.0030	0.0012	-0.0023	0.0003	0.0033	0.0047	-1.03E-05	0.9998
16														
17	0.0053	0.0029	0.0000	-0.0019	0.0012	-0.0057	-0.0046	-0.0045	-0.0079	-0.0098	0.0288	-0.0036	-1.08E-05	0.9960
18														
19	0.0030	0.0019	0.0002	-0.0044	-0.0009	-0.0036	-0.0012	0.0032	0.0001	0.0006	0.0006	0.0006	-3.65E-06	0.9998
20	0.0006	-0.0045	-0.0011	-0.0010	-0.0003	0.0021	0.0042	0.0063	0.0032	-0.0001	-0.0036	-0.0057	6.64E-06	0.9998
21	0.0122	0.0014	-0.0005	-0.0124	-0.0033	-0.0021	-0.0020	0.0001	-0.0028	0.0003	0.0024	0.0065	-1.27E-05	0.9991
22	0.0080	0.0055	0.0004	-0.0079	-0.0005	-0.0066	-0.0069	-0.0033	-0.0027	0.0006	0.0049	0.0084	-1.49E-05	0.9995
23														
24														
25														
26														
27	0.0055	0.0031	-0.0016	-0.0037	-0.0013	-0.0040	-0.0031	-0.0003	-0.0016	-0.0003	0.0039	0.0035	-8.20E-06	0.9998
28														
29	0.0100	0.0009	-0.0028	-0.0061	0.0000	-0.0036	-0.0029	-0.0032	-0.0023	0.0008	0.0031	0.0060	-1.12E-05	0.9992
30	0.0048	0.0014	0.0008	-0.0037	-0.0021	-0.0027	-0.0022	-0.0008	-0.0012	0.0004	0.0010	0.0045	-7.09E-06	0.9999
31	0.0131	-0.0047	0.0036	-0.0098	-0.0021	-0.0037	-0.0032	-0.0006	-0.0015	0.0013	0.0017	0.0059	-1.16E-05	0.9992
32														
33	0.0002	-0.0019	0.0008	-0.0011	0.0015	0.0002	-0.0017	0.0024	0.0013	0.0019	-0.0007	-0.0029	1.91E-06	0.9999
34	0.0020	-0.0006	-0.0016	-0.0004	0.0011	-0.0020	-0.0017	0.0035	-0.0001	0.0014	-0.0019	0.0004	-7.95E-07	0.9999
35	-0.0007	-0.0040	-0.0041	-0.0067	-0.0057	0.0421	-0.0065	-0.0041	-0.0044	-0.0024	-0.0031	-0.0004	8.25E-06	0.9929
36														
37	0.0077	0.0020	-0.0007	-0.0058	-0.0021	-0.0048	-0.0039	0.0001	0.0004	0.0000	0.0049	0.0022	-9.31E-06	0.9997
38	0.0096	0.0045	-0.0030	-0.0045	-0.0022	-0.0057	-0.0072	-0.0038	-0.0019	0.0015	0.0063	0.0062	-1.45E-05	0.9998
39														
40														
41	0.0066	0.0048	-0.0012	-0.0047	-0.0018	-0.0058	-0.0043	-0.0029	-0.0027	0.0022	0.0048	0.0050	-1.16E-05	0.9998
42	0.0065	0.0017	-0.0017	-0.0043	0.0028	-0.0046	-0.0032	-0.0048	-0.0046	-0.0024	0.0146	-0.0001	-9.27E-06	0.9898
43	0.0080	0.0005	-0.0023	-0.0019	-0.0032	-0.0040	-0.0026	-0.0012	-0.0006	0.0021	0.0019	0.0034	-8.56E-06	0.9999

44	0.0049	0.0003	-0.0028	-0.0019	-0.0010	-0.0021	-0.0012	-0.0004	0.0010	0.0019	0.0014	-0.0002	-3.91E-06	0.9999
45	0.0051	0.0003	-0.0002	-0.0056	-0.0007	-0.0013	-0.0026	0.0020	-0.0007	0.0022	0.0017	-0.0001	-4.37E-06	0.9998
46														
47	-0.0012	-0.0013	0.0021	-0.0015	-0.0010	0.0014	-0.0002	-0.0068	0.0122	0.0037	0.0058	-0.0132	-4.67E-06	0.9983
48														
49	0.0036	0.0023	0.0001	-0.0027	-0.0023	-0.0015	-0.0034	0.0007	-0.0025	-0.0001	0.0020	0.0038	-6.31E-06	0.9999
50	0.0090	-0.0009	-0.0031	-0.0045	0.0000	-0.0022	-0.0036	0.0001	-0.0029	0.0007	0.0077	-0.0003	-7.63E-06	0.9991
51	0.0097	0.0001	-0.0018	-0.0028	0.0000	-0.0048	-0.0059	-0.0039	-0.0025	0.0003	0.0046	0.0070	-1.23E-05	0.9997
52	-0.0063	0.0000	0.0005	0.0003	0.0012	0.0017	0.0034	0.0071	0.0025	0.0004	-0.0041	-0.0067	-9.55E-06	0.9999
53														
54	0.0090	0.0014	-0.0003	-0.0042	-0.0036	-0.0052	-0.0032	-0.0012	-0.0018	-0.0021	0.0039	0.0073	-1.20E-05	0.9999
55	0.0033	0.0031	-0.0028	-0.0028	0.0020	-0.0029	-0.0030	-0.0010	-0.0012	-0.0004	0.0023	0.0032	-5.73E-06	0.9997
56	-0.0125	-0.0076	0.0002	0.0061	0.0090	0.0058	0.0077	0.0095	0.0034	-0.0027	-0.0038	-0.0150	-2.27E-05	0.9998
57														
58														
59	-0.0091	-0.0055	0.0020	0.0003	0.0053	0.0068	0.0071	0.0063	0.0040	0.0001	-0.0065	-0.0108	-1.74E-05	0.9999
60	0.0054	0.0001	-0.0024	-0.0051	-0.0010	-0.0015	-0.0002	0.0021	0.0018	0.0009	0.0004	-0.0009	-3.01E-06	0.9998
61	0.0043	-0.0015	0.0013	-0.0033	-0.0002	-0.0024	-0.0020	0.0014	-0.0004	0.0007	0.0015	0.0007	-3.61E-06	0.9998
62														
63														
64														
65	-0.0297	-0.0051	0.0174	0.0149	0.0135	0.0040	0.0015	0.0001	-0.0013	-0.0027	-0.0061	-0.0065	2.49E-05	0.9951
66														
67	0.0125	0.0040	-0.0026	-0.0072	-0.0037	-0.0063	-0.0069	-0.0034	-0.0009	0.0006	0.0072	0.0067	-1.67E-05	0.9994
68	-0.0010	0.0024	-0.0010	-0.0029	0.0006	0.0003	-0.0006	0.0035	0.0018	-0.0006	0.0002	-0.0025	-1.36E-06	0.9999
69	0.0039	0.0040	-0.0019	-0.0061	-0.0006	-0.0035	0.0003	0.0011	-0.0017	0.0008	0.0017	0.0018	-5.49E-06	0.9996
70	0.0132	0.0067	0.0002	-0.0086	-0.0047	-0.0072	-0.0100	-0.0068	-0.0043	0.0005	0.0067	0.0142	-2.29E-05	0.9995
71	0.0003	-0.0026	-0.0019	0.0111	-0.0036	-0.0160	0.0180	-0.0010	-0.0029	-0.0015	-0.0011	0.0011	-8.98E-07	0.9952
72	0.0014	-0.0030	-0.0053	-0.0077	-0.0012	-0.0015	0.0351	-0.0002	-0.0057	-0.0042	-0.0027	-0.0052	-9.49E-06	0.9928
73	0.0063	0.0011	-0.0004	-0.0054	-0.0008	-0.0023	-0.0023	-0.0002	-0.0025	0.0001	0.0024	0.0041	-7.61E-06	0.9997

74														
75														
76	0.0069	-0.0007	-0.0005	-0.0032	-0.0027	-0.0025	-0.0022	-0.0009	0.0005	0.0009	0.0024	0.0018	-6.61E-06	0.9998
77														
78	0.0040	0.0053	-0.0025	-0.0026	-0.0030	-0.0048	0.0001	-0.0020	-0.0028	0.0018	0.0047	0.0019	-7.72E-06	0.9945
79	0.0089	0.0024	-0.0011	-0.0053	-0.0031	-0.0046	-0.0067	0.0011	-0.0014	0.0008	0.0047	0.0042	-1.15E-05	0.9998
80	0.0047	0.0035	-0.0002	-0.0022	-0.0016	-0.0063	-0.0043	-0.0003	-0.0005	0.0002	0.0016	0.0055	-8.97E-06	0.9999
81	0.0064	0.0007	-0.0005	-0.0027	-0.0019	-0.0052	-0.0044	0.0024	-0.0003	-0.0005	0.0038	0.0021	-7.54E-06	0.9998
82	0.0009	0.0018	-0.0001	-0.0005	-0.0003	-0.0032	-0.0016	0.0020	-0.0011	-0.0009	0.0026	0.0005	-2.59E-06	0.9999
83	0.0026	-0.0027	0.0024	-0.0022	-0.0013	-0.0022	0.0003	0.0027	0.0014	0.0003	-0.0006	-0.0009	-5.75E-07	0.9999
84	0.0050	0.0003	0.0006	-0.0051	-0.0029	-0.0025	-0.0012	0.0041	0.0003	-0.0004	0.0018	0.0001	-4.19E-06	0.9998
85														
86	0.0043	0.0025	0.0001	-0.0046	-0.0016	-0.0040	-0.0007	0.0006	-0.0022	0.0009	0.0018	0.0030	-6.50E-06	0.9997
87	0.0046	0.0026	0.0002	-0.0055	-0.0026	-0.0030	-0.0028	0.0035	-0.0005	0.0004	0.0011	0.0021	-6.00E-06	0.9997
88	0.0042	0.0008	-0.0006	-0.0039	0.0018	-0.0026	-0.0010	-0.0013	-0.0027	-0.0010	0.0018	0.0045	-5.80E-06	0.9996
89	0.0097	0.0049	-0.0006	-0.0064	-0.0023	-0.0069	-0.0076	-0.0023	-0.0032	-0.0001	0.0058	0.0090	-1.62E-05	0.9997
90	0.0038	0.0011	-0.0003	-0.0046	0.0013	-0.0031	0.0004	0.0003	-0.0023	-0.0004	0.0022	0.0025	-4.83E-06	0.9997
91	-0.0101	-0.0017	0.0008	0.0036	0.0056	0.0041	0.0039	0.0036	0.0000	0.0009	-0.0015	-0.0092	-1.34E-05	0.9998
92	0.0026	0.0010	-0.0043	-0.0054	-0.0033	-0.0036	-0.0047	0.0362	-0.0044	-0.0043	-0.0046	-0.0052	-4.64E-06	0.9935
93	0.0068	0.0049	0.0009	-0.0038	-0.0019	-0.0060	-0.0076	-0.0022	-0.0052	-0.0123	0.0242	0.0023	-1.46E-05	0.9968
94	0.0111	0.0040	-0.0005	-0.0051	-0.0078	-0.0063	-0.0039	-0.0025	-0.0016	-0.0003	0.0035	0.0094	-1.61E-05	0.9999
95	0.0061	0.0021	-0.0014	-0.0029	0.0005	-0.0020	-0.0045	-0.0051	-0.0041	-0.0008	0.0061	0.0060	-1.02E-05	0.9990
96	0.0050	0.0023	-0.0020	-0.0065	0.0027	-0.0017	-0.0032	-0.0018	-0.0015	0.0017	0.0028	0.0021	-6.36E-06	0.9993
97	0.0074	0.0020	0.0010	-0.0046	-0.0038	-0.0038	-0.0045	-0.0021	-0.0014	0.0014	0.0034	0.0050	-1.07E-05	0.9999
98														
99	0.0078	0.0039	-0.0015	-0.0045	-0.0022	-0.0055	-0.0046	-0.0026	-0.0015	-0.0002	0.0043	0.0065	-1.22E-05	0.9999

100	-0.0084	-0.0047	-0.0076	-0.0004	0.0060	0.0130	0.0142	0.0084	0.0002	0.0026	-0.0065	-0.0168	-2.28E-05	0.9945
101	0.0020	0.0067	0.0001	-0.0057	-0.0004	-0.0061	-0.0018	0.0015	-0.0048	0.0025	0.0032	0.0029	-7.43E-06	0.9992
102														
103	0.0088	-0.0031	0.0017	-0.0039	-0.0029	-0.0052	-0.0028	0.0016	0.0018	0.0008	0.0005	0.0027	-7.33E-06	0.9997
104	0.0089	0.0025	-0.0002	-0.0066	-0.0039	-0.0036	-0.0020	-0.0025	-0.0039	0.0009	0.0038	0.0065	-1.21E-05	0.9998
105														
106	0.0024	0.0017	-0.0003	-0.0025	-0.0008	-0.0028	-0.0019	0.0019	0.0012	-0.0001	0.0000	0.0013	-3.29E-06	0.9999
107	0.0100	0.0017	0.0010	-0.0054	-0.0026	-0.0073	-0.0058	-0.0022	-0.0026	0.0022	0.0031	0.0078	-1.42E-05	0.9998
108														
109														
110														
111	0.0069	0.0017	0.0014	-0.0016	-0.0012	-0.0035	-0.0044	-0.0014	-0.0077	-0.0063	-0.0083	0.0244	-1.52E-05	0.9975
112	0.0069	0.0011	0.0020	-0.0052	-0.0016	-0.0067	-0.0039	-0.0009	-0.0019	0.0007	0.0038	0.0040	-9.61E-06	0.9996
113														
114	0.0078	0.0030	-0.0026	-0.0063	-0.0001	-0.0048	-0.0025	-0.0012	-0.0009	-0.0007	0.0035	0.0048	-9.93E-06	0.9994
115	0.0059	-0.0002	-0.0008	-0.0027	-0.0010	-0.0036	-0.0015	-0.0014	-0.0005	0.0022	0.0008	0.0027	-6.20E-06	0.9999
116	0.0002	-0.0048	-0.0071	-0.0075	-0.0050	0.0407	-0.0027	-0.0001	-0.0021	-0.0056	-0.0026	-0.0036	-1.10E-05	0.9930
117	0.0054	-0.0037	0.0006	-0.0033	-0.0017	0.0007	-0.0013	0.0028	-0.0014	0.0033	-0.0002	-0.0013	-1.73E-06	0.9996
118	0.0108	-0.0067	0.0005	-0.0065	0.0004	-0.0024	-0.0023	0.0017	0.0022	0.0031	-0.0017	0.0008	-5.03E-06	0.9992
119	0.0017	0.0018	0.0010	-0.0052	-0.0019	0.0003	0.0001	0.0018	0.0009	-0.0008	-0.0003	0.0008	-2.05E-06	0.9999
120														
121	0.0096	0.0011	-0.0031	-0.0052	-0.0011	-0.0054	-0.0025	-0.0005	-0.0010	0.0001	0.0047	0.0033	-1.01E-05	0.9995
122	0.0074	0.0003	-0.0011	-0.0046	-0.0012	-0.0046	-0.0011	-0.0006	-0.0006	0.0008	0.0027	0.0026	-7.59E-06	0.9997
123	0.0055	0.0028	-0.0022	-0.0056	0.0005	-0.0045	-0.0049	-0.0023	-0.0010	0.0142	0.0051	-0.0076	-5.24E-06	0.9871
124	0.0036	0.0041	0.0009	-0.0058	-0.0001	-0.0023	-0.0040	-0.0028	-0.0023	0.0004	0.0034	0.0049	-8.43E-06	0.9994
125	0.0032	0.0017	-0.0021	-0.0031	0.0018	-0.0019	-0.0019	0.0012	-0.0024	-0.0005	0.0008	0.0033	-4.31E-06	0.9998
126	0.0010	0.0022	-0.0017	-0.0026	0.0027	-0.0023	-0.0021	0.0010	-0.0008	0.0015	0.0019	-0.0009	-1.84E-06	0.9998

127	-0.0011	-0.0038	0.0022	0.0000	-0.0002	0.0008	0.0007	0.0045	0.0038	0.0015	-0.0033	-0.0050	5.52E-06	0.9999
128	0.0017	0.0003	0.0002	-0.0001	-0.0037	-0.0007	-0.0010	0.0027	0.0003	0.0007	-0.0010	0.0005	-1.56E-06	0.9999
129	0.0115	0.0067	-0.0009	-0.0066	-0.0015	-0.0080	-0.0068	-0.0125	-0.0063	0.0048	0.0057	0.0139	-2.17E-05	0.9956
130														
131														
132														
133														
134														
135	0.0031	0.0024	-0.0005	-0.0043	-0.0019	-0.0028	-0.0016	0.0016	0.0019	0.0013	0.0027	-0.0020	-3.39E-06	0.9998
136	0.0054	-0.0010	-0.0013	-0.0030	-0.0001	-0.0015	-0.0022	0.0021	-0.0003	-0.0004	-0.0022	0.0044	-4.63E-06	0.9998
137	0.0017	0.0010	0.0005	-0.0018	-0.0029	-0.0024	0.0003	0.0040	-0.0027	0.0033	-0.0002	-0.0009	-1.62E-06	0.9998
138	0.0061	0.0057	-0.0025	-0.0086	-0.0014	-0.0026	-0.0027	0.0013	-0.0021	0.0000	0.0037	0.0033	-8.93E-06	0.9996
139	0.0011	-0.0009	-0.0005	-0.0027	0.0005	-0.0001	0.0007	0.0025	0.0025	0.0017	-0.0030	-0.0020	1.61E-06	0.9999
140	0.0032	-0.0026	-0.0006	-0.0015	-0.0013	-0.0014	0.0007	0.0038	0.0040	0.0003	-0.0034	-0.0012	6.80E-07	0.9998
141	0.0011	0.0001	0.0009	-0.0032	0.0017	-0.0014	0.0005	-0.0006	-0.0017	0.0012	0.0012	0.0001	-1.39E-06	0.9997
142														
143														
144	0.0030	-0.0003	0.0008	-0.0043	0.0002	-0.0027	-0.0009	0.0019	0.0036	-0.0009	-0.0005	0.0001	-2.07E-06	0.9997
145	0.0022	0.0009	-0.0019	-0.0027	-0.0006	-0.0014	0.0008	0.0030	0.0006	-0.0002	0.0014	-0.0020	-7.33E-07	0.9999
146	0.0135	0.0057	-0.0012	-0.0077	-0.0047	-0.0086	-0.0071	-0.0056	-0.0024	-0.0005	0.0062	0.0124	-2.11E-05	0.9998
147	0.0018	-0.0107	0.0011	0.0031	0.0052	0.0020	0.0000	0.0030	-0.0005	-0.0013	-0.0006	-0.0031	5.67E-06	0.9994
148														
149	0.0050	0.0025	-0.0028	-0.0042	0.0003	-0.0040	-0.0004	0.0002	-0.0022	0.0013	0.0007	0.0033	-6.18E-06	0.9998
150	-0.0012	-0.0025	0.0023	-0.0014	0.0016	0.0014	0.0018	0.0022	-0.0021	-0.0011	0.0012	-0.0022	-3.06E-06	0.9998
151														
152	0.0086	0.0024	-0.0037	-0.0038	-0.0030	-0.0041	-0.0043	0.0016	-0.0005	0.0004	0.0023	0.0041	-9.68E-06	0.9999
153	0.0029	0.0035	-0.0005	-0.0035	0.0007	-0.0043	-0.0023	-0.0002	-0.0036	0.0007	0.0035	0.0031	-6.48E-06	0.9992

Appendix 2 – Pulse programs for NMR

A2.1 Edited ^{1}H-^{15}N HSQC Pulse Program (gradients; 600 MHz spectrometer)

```
;invifpf3gpsi
;avance-version
;2D H-1/X correlation via double inept transfer
;   using sensitivity improvement
;phase sensitive using Echo/Antiecho-TPPI
gradient selection
;with decoupling during acquisition
;using f3 - channel
;using flip-back pulse
;A.G. Palmer III, J. Cavanagh, P.E. Wright & M.
Rance, J. Magn.
;   Reson. 93, 151-170 (1991)
;L.E. Kay, P. Keifer & T. Saarinen, J. Am.
Chem. Soc. 114,
;   10663-5 (1992)
;J. Schleucher, M. Schwendinger, M. Sattler, P.
Schmidt, O. Schedletzky,
;   S.J. Glaser, O.W. Sorensen & C. Griesinger,
J. Biomol. NMR 4,
;   301-306 (1994)
;S. Grzesiek & A. Bax, J. Am. Chem. Soc. 115,
12593-12594 (1993)
;modified by jgaspar to include delay prior to
aquisition

define list<gradient> EA=<EA>

;$Id: Grad1.incl,v 1.7 2002/06/12 09:04:22 ber
Exp $
# 22 "C:/Bruker/XWIN-
NMR/exp/stan/nmr/lists/pp/invifpf3gpsid31" 2

# 1 "C:/Bruker/XWIN-
NMR/exp/stan/nmr/lists/pp/Delay.incl" 1
;Delay.incl  -  include file for commonly used
delays
;version 00/02/07


;general delays

define delay DELTA
define delay DELTA1
define delay DELTA2
define delay DELTA3
define delay DELTA4
define delay DELTA5
define delay DELTA6
define delay DELTA7
define delay DELTA8

define delay TAU
define delay TAU1
define delay TAU2
define delay TAU3
define delay TAU4
define delay TAU5


;delays for centering pulses

define delay CEN_HN1
define delay CEN_HN2
define delay CEN_HN3
define delay CEN_HC1
define delay CEN_HC2
define delay CEN_HC3
define delay CEN_HC4
define delay CEN_HP1
define delay CEN_HP2
define delay CEN_CN1
define delay CEN_CN2
define delay CEN_CN3
define delay CEN_CN4
define delay CEN_CP1
define delay CEN_CP2

;loop counters

define loopcounter COUNTER
define loopcounter SCALEF
define loopcounter FACTOR1
define loopcounter FACTOR2
define loopcounter FACTOR3

;$Id: Delay.incl,v 1.11 2002/06/12 09:04:22 ber
Exp $
# 23 "C:/Bruker/XWIN-
NMR/exp/stan/nmr/lists/pp/invifpf3gpsid31" 2
```

```
"p2=p1*2"

"p22=p21*2"

"d0=3u"

"d11=30m"

"d26=1s/(cnst4*4)"

"DELTA=p16+d16+p2+d0*2"
"DELTA1=p16+d16+8u"

"CEN_HN1=(p21-p1)/2"
"CEN_HN2=(p22-p2)/2"

"l3=(td1/2)"

1 ze
  d31
  d11 pl16:f3
2 d1 do:f3
  6m
3 d11
  18m
4 (p1 ph1)
  d26 pl3:f3
  (CEN_HN2 p2 ph2) (p22 ph6):f3
  d26 setnmr2|0 setnmr0|34|32|33
  (p1 ph2)
  4u pl0:f1
  (p11:sp1 ph1:r):f1
  4u
  p16:gp1
  d16 pl1:f1
  (p21 ph3):f3
  d0
  p2 ph7
  d0
  p16:gp2*EA
  d16
  (p22 ph4):f3
  DELTA
  (CEN_HN1 p1 ph1) (p21 ph4):f3
  d24
  (CEN_HN2 p2 ph1) (p22 ph1):f3
  d24
  (CEN_HN1 p1 ph2) (p21 ph5):f3
  d26
  (CEN_HN2 p2 ph1) (p22 ph1):f3
  d26
  (p1 ph1)
  DELTA1
  (p2 ph1)
  4u
  p16:gp3
  d16 pl16:f3
  4u setnmr2^0 setnmr0^34^32^33
  go=2 ph31 cpd3:f3
  d1 do:f3 wr #0 if #0 zd
  3m ip5 igrad EA
  3m ip5
  lo to 3 times 2
  d11 id0
  3m ip3
  3m ip3
  3m ip6
  3m ip6
  3m ip31
  3m ip31
  lo to 4 times l3
exit

ph1=0
ph2=1
ph3=0 2
ph4=0 0 2 2
ph5=1 1 3 3
ph6=0
ph7=0 0 2 2
ph31=2 0 0 2

;pl0 : 120dB
;pl1 : f1 channel - power level for pulse (default)
;pl3 : f3 channel - power level for pulse (default)
;pl16: f3 channel - power level for CPD/BB
decoupling
;sp1: f1 channel - shaped pulse  90 degree
;p1 : f1 channel -  90 degree high power pulse
;p2 : f1 channel - 180 degree high power pulse
;p11: f1 channel -  90 degree shaped pulse
;p16: homospoil/gradient pulse                [1
msec]
;p21: f3 channel -  90 degree high power pulse
;p22: f3 channel - 180 degree high power pulse
;d0 : incremented delay (2D)                  [3
usec]
;d1 : relaxation delay; 1-5 * T1
;d11: delay for disk I/O                      [30
msec]
;d16: delay for homospoil/gradient recovery
;d24: 1/(4J)YH for YH
```

; 1/(8J)YH for all multiplicities
;d26: 1/(4J(YH))
;d31: delay between experiments in multizg
;cnst4: = J(YH)
;l3: loop for phase sensitive 2D using E/A
method : l3 = td1/2
;in0: 1/(2 * SW(X)) = DW(X)
;nd0: 2
;NS: 1 * n
;DS: >= 16
;td1: number of experiments
;MC2: echo-antiecho
;cpd3: decoupling according to sequence defined
by cpdprg3
;pcpd3: f3 channel - 90 degree pulse for
decoupling sequence

;use gradient ratio: gp 1 : gp 2 : gp 3
; 50 : 80 : 20.1 for
C-13
; 50 : 80 : 8.1 for
N-15

;for z-only gradients:
;gpz1: 50%
;gpz2: 80%
;gpz3: 20.1% for C-13, 8.1% for N-15

;use gradient files:
;gpnam1: SINE.100
;gpnam2: SINE.100
;gpnam3: SINE.100

A2.2 ^{1}H-^{15}N HSQC Pulse Program (presat; 600 MHz spectrometer)

```
;hsqcf3phpr
;avance-version (02/05/31)
;HSQC
;2D H-1/X correlation via double inept transfer
;phase sensitive
;with decoupling during acquisition
;using f3 - channel
;G. Bodenhausen & D.J. Ruben, Chem. Phys.
Lett. 69, 185 (1980)

;$Id: Avance1.incl,v 1.7.2.3 2003/02/25
14:48:47 ber Exp $
# 12 "C:/Bruker/XWIN-
NMR/exp/stan/nmr/lists/pp/hsqcf3phpr" 2

# 1 "C:/Bruker/XWIN-
NMR/exp/stan/nmr/lists/pp/Delay.incl" 1
;Delay.incl  -  include file for commonly used
delays
;version 00/02/07

;general delays

define delay DELTA
define delay DELTA1
define delay DELTA2
define delay DELTA3
define delay DELTA4
define delay DELTA5
define delay DELTA6
define delay DELTA7
define delay DELTA8

define delay TAU
define delay TAU1
define delay TAU2
define delay TAU3
define delay TAU4
define delay TAU5

;delays for centering pulses

define delay CEN_HN1
define delay CEN_HN2
define delay CEN_HN3
define delay CEN_HC1
define delay CEN_HC2
define delay CEN_HC3
define delay CEN_HC4
define delay CEN_HP1
define delay CEN_HP2
define delay CEN_CN1
define delay CEN_CN2
define delay CEN_CN3
define delay CEN_CN4
define delay CEN_CP1
define delay CEN_CP2

;loop counters

define loopcounter COUNTER
define loopcounter SCALEF
define loopcounter FACTOR1
define loopcounter FACTOR2
define loopcounter FACTOR3

;$Id: Delay.incl,v 1.11 2002/06/12 09:04:22 ber
Exp $
# 13 "C:/Bruker/XWIN-
NMR/exp/stan/nmr/lists/pp/hsqcf3phpr" 2

"p2=p1*2"

"p22=p21*2"

"d0=3u"

"d11=30m"

"d12=20u"

"d13=4u"

"d26=1s/(cnst4*4)"

"DELTA=d0*2+p2"

# 1 "mc_line 35 file C:/Bruker/XWIN-
NMR/exp/stan/nmr/lists/pp/hsqcf3phpr
expanding definition part of mc command before
ze"
define delay MCWRK
define delay MCREST
define loopcounter ST1CNT
"ST1CNT = td1 / (2)"
"MCWRK = 0.250000*d11"
"MCREST = d11 - d11"
```

```
# 35 "C:/Bruker/XWIN-
NMR/exp/stan/nmr/lists/pp/hsqcf3phpr"
1 ze
# 1 "mc_line 35 file C:/Bruker/XWIN-
NMR/exp/stan/nmr/lists/pp/hsqcf3phpr
expanding definition of mc command after ze"
# 36 "C:/Bruker/XWIN-
NMR/exp/stan/nmr/lists/pp/hsqcf3phpr"
  d11 pl16:f3
# 1 "mc_line 37 file C:/Bruker/XWIN-
NMR/exp/stan/nmr/lists/pp/hsqcf3phpr
expanding start label for mc command"
2 MCWRK  * 3 do:f3
LBLSTS1, MCWRK
LBLF1, MCREST
# 38 "C:/Bruker/XWIN-
NMR/exp/stan/nmr/lists/pp/hsqcf3phpr"
3 d12 pl9:f1
  d1 cw:f1 ph29
  d13 do:f1
  d12 pl1:f1
  p1 ph1
  d26 pl3:f3
  (center (p2 ph2) (p22 ph9):f3 )
  d26
  (p1 ph3)
  (p21 ph6):f3
  d0
  (p2 ph8)
  d0
  (p22 ph7):f3
  DELTA
  (p21 ph7):f3
  (p1 ph4)
  d26
  (center (p2 ph2) (p22 ph5):f3 )
  d26 pl16:f3
  go=2 ph31 cpd3:f3
# 1 "mc_line 59 file C:/Bruker/XWIN-
NMR/exp/stan/nmr/lists/pp/hsqcf3phpr
expanding mc command in line"
  MCWRK  do:f3 wr #0 if #0 zd ip6  MCWRK
ip9  MCWRK  ip29
  lo to LBLSTS1 times 2
  MCWRK id0
  lo to LBLF1 times ST1CNT
# 60 "C:/Bruker/XWIN-
NMR/exp/stan/nmr/lists/pp/hsqcf3phpr"
exit

ph1=0
ph2=0
ph3=1
ph4=1
ph5=0 0 0 0 0 0 0 0 2 2 2 2 2 2 2 2
ph6=0 2
ph7=0 0 0 0 2 2 2 2
ph8=0 0 2 2
ph9=0 0 0 0 0 0 0 0 2 2 2 2 2 2 2 2
ph29=0
ph31=0 2 0 2 2 0 2 0

;pl1 : f1 channel - power level for pulse (default)
;pl3 : f3 channel - power level for pulse (default)
;pl9 : f1 channel - power level for presaturation
;pl16: f3 channel - power level for CPD/BB
decoupling
;p1 : f1 channel -  90 degree high power pulse
;p2 : f1 channel - 180 degree high power pulse
;p21: f3 channel -  90 degree high power pulse
;p22: f3 channel - 180 degree high power pulse
;d0 : incremented delay (2D)                [3 usec]
;d1 : relaxation delay; 1-5 * T1
;d11: delay for disk I/O                     [30
msec]
;d12: delay for power switching             [20 usec]
;d13: short delay                           [4 usec]
;d26 : 1/(4J)YH
;cnst4: = J(YH)
;in0: 1/(2 * SW(X)) = DW(X)
;nd0: 2
;NS: 4 * n
;DS: 16
;td1: number of experiments
;FnMODE: States-TPPI, TPPI, States or QSEC
;cpd3: decoupling according to sequence defined
by cpdprg3
;pcpd3: f3 channel - 90 degree pulse for
decoupling sequence

;$Id: hsqcf3phpr,v 1.1 2002/06/12 09:04:54 ber
Exp $
```

A2.3 ^{1}H-^{15}N HSQC Pulse Program (500 MHz spectrometer)

```
;invietgpsi
;avance-version (00/04/28)
;HSQC
;2D H-1/X correlation via double inept transfer
;   using sensitivity improvement
;phase sensitive using Echo/Antiecho-TPPI
gradient selection
;with decoupling during acquisition
;using trim pulses in inept transfer
;A.G. Palmer III, J. Cavanagh, P.E. Wright & M.
Rance, J. Magn.
;   Reson. 93, 151-170 (1991)
;L.E. Kay, P. Keifer & T. Saarinen, J. Am.
Chem. Soc. 114,
;   10663-5 (1992)
;J. Schleucher, M. Schwendinger, M. Sattler, P.
Schmidt, O. Schedletzky,
;   S.J. Glaser, O.W. Sorensen & C. Griesinger,
J. Biomol. NMR 4,
;   301-306 (1994)

# 1 "C:/Bruker/XWIN-
NMR/exp/stan/nmr/lists/pp/Avance.incl" 1
;Avance.incl
;version  00/07/27

;switch between high and low stage oh H
amplifier
;use 2H channel for lock or pulse (lockswitch)
;allow for 2H decoupling (lockswitch)
;turn lock-hold on/off (BSMS)
;switch between 1H or 19F output (H amplifier)
;select output for 19F (amplifier)
;homospoil on/off (BSMS)
;for Q-switch probes
;for mixing probe
;gating pulse for RX22, ADC and HPPR
;not active
;$Id: Avance1.incl,v 1.5 2000/08/16 13:26:55
ber Exp $
# 19 "C:/Bruker/XWIN-
NMR/exp/stan/nmr/lists/pp/invietgpsi" 2
# 1 "C:/Bruker/XWIN-
NMR/exp/stan/nmr/lists/pp/Grad.incl" 1
;Grad.incl  -  include file for Gradient
Spectroscopy
;avance-version (00/07/27)
;gradient pulse for gs-syntax
;blank/unblank gradient amplifier and turn lock-
hold on/off
;blank/unblank gradient amplifier
;for RCB board (BSMS)

define list<gradient> EA=<EA>

;$Id: Grad1.incl,v 1.6 2000/10/16 11:47:19 ber
Exp $
# 20 "C:/Bruker/XWIN-
NMR/exp/stan/nmr/lists/pp/invietgpsi" 2

# 1 "C:/Bruker/XWIN-
NMR/exp/stan/nmr/lists/pp/Delay.incl" 1
;Delay.incl  -  include file for commonly used
delays
;
;version 00/02/07

;general delays

define delay DELTA
define delay DELTA1
define delay DELTA2
define delay DELTA3
define delay DELTA4
define delay DELTA5
define delay DELTA6
define delay DELTA7
define delay DELTA8

define delay TAU
define delay TAU1
define delay TAU2
define delay TAU3
define delay TAU4
define delay TAU5

;delays for centering pulses

define delay CEN_HN1
define delay CEN_HN2
define delay CEN_HN3
define delay CEN_HC1
define delay CEN_HC2
define delay CEN_HC3
define delay CEN_HC4
define delay CEN_HP1
define delay CEN_HP2
```

```
define delay CEN_CN1
define delay CEN_CN2
define delay CEN_CN3
define delay CEN_CN4
define delay CEN_CP1
define delay CEN_CP2

;loop counters

define loopcounter COUNTER
define loopcounter SCALEF
define loopcounter FACTOR1
define loopcounter FACTOR2
define loopcounter FACTOR3

;$Id: Delay.incl,v 1.10 2000/05/08 11:39:02 eng
Exp $
# 21 "C:/Bruker/XWIN-
NMR/exp/stan/nmr/lists/pp/invietgpsi" 2

"p2=p1*2"

"p4=p3*2"

"d0=3u"

"d4=1s/(cnst2*4)"

"d11=30m"

"d13=4u"

"DELTA=p16+d16+50u+p2+d0*2"
"DELTA1=d13+p16+d16+4u"

# 1 "mc_line 42 file C:/Bruker/XWIN-
NMR/exp/stan/nmr/lists/pp/invietgpsi expanding
definition part of mc command before ze"
; dimension 2 aq-mode (F2) undefined (F1)
Echo-Antiecho
define delay MCWRK
define delay MCREST
define loopcounter ST1CNT
"ST1CNT = td1 / ( 2 ) "
"MCWRK  = 0.166667 *  d1"
"MCREST =  d1 -  d1"
# 42 "C:/Bruker/XWIN-
NMR/exp/stan/nmr/lists/pp/invietgpsi"
1 ze
  d11 pl12:f2
# 1 "mc_line 44 file C:/Bruker/XWIN-
NMR/exp/stan/nmr/lists/pp/invietgpsi expanding
start label for mc command"
2       MCWRK*2  do:f2
LBLSTS1,       MCWRK*4
LBLF1,       MCREST
# 45 "C:/Bruker/XWIN-
NMR/exp/stan/nmr/lists/pp/invietgpsi"
3 (p1 ph1)
  d4 pl2:f2
  (p2 ph1) (p4 ph6):f2
  d4
  p28 ph1
  d13
  (p1 ph2) (p3 ph3):f2
  d0
  p2 ph7
  d0
  50u setnmr2|0 setnmr0|34|32|33
  p16:gp1*EA
  d16
  (p4 ph4):f2
  DELTA
  (p1 ph1) (p3 ph4):f2
  d24
  (p2 ph1) (p4 ph1):f2
  d24
  (p1 ph2) (p3 ph5):f2
  d4
  (p2 ph1) (p4 ph1):f2
  d4
  (p1 ph1)
  DELTA1
  (p2 ph1)
  d13
  p16:gp2
  d16 pl12:f2
  4u setnmr2^0 setnmr0^34^32^33
  go=2 ph31 cpd2:f2
# 1 "mc_line 76 file C:/Bruker/XWIN-
NMR/exp/stan/nmr/lists/pp/invietgpsi expanding
mc command in line "
  MCWRK  do:f2 wr #0 if #0 zd   igrad EA
MCWRK  ip5*2
  lo to LBLSTS1 times 2
  MCWRK  id0  MCWRK  ip3*2  MCWRK
ip6*2  MCWRK  ip31*2
  lo to LBLF1 times ST1CNT
# 77 "C:/Bruker/XWIN-
NMR/exp/stan/nmr/lists/pp/invietgpsi"
exit
```

```
ph1=0
ph2=1
ph3=0 2
ph4=0 0 2 2
ph5=1 1 3 3
ph6=0
ph7=0 0 2 2
ph31=0 2 2 0

;pl1 : f1 channel - power level for pulse (default)
;pl2 : f2 channel - power level for pulse (default)
;pl12: f2 channel - power level for CPD/BB
decoupling
;p1 : f1 channel -  90 degree high power pulse
;p2 : f1 channel - 180 degree high power pulse
;p3 : f2 channel -  90 degree high power pulse
;p4 : f2 channel - 180 degree high power pulse
;p16: homospoil/gradient pulse
;p28: f1 channel - trim pulse
;d0 : incremented delay (2D)                [3 usec]
;d1 : relaxation delay; 1-5 * T1
;d4 : 1/(4J)XH
;d11: delay for disk I/O                     [30
msec]
;d13: short delay                           [4 usec]
;d16: delay for homospoil/gradient recovery
;d24: 1/(4J)XH for XH
;     1/(8J)XH for all multiplicities
;cnst2: = J(XH)
;in0: 1/(2 * SW(X)) = DW(X)
;nd0: 2
;NS: 1 * n
;DS: >= 16
;td1: number of experiments
;FnMODE: echo-antiecho
;cpd2: decoupling according to sequence defined
by cpdprg2
;pcpd2: f2 channel - 90 degree pulse for
decoupling sequence

;use gradient ratio:        gp 1 : gp 2
;                            80 : 20.1    for C-13
;                            80 :  8.1    for N-15

;for z-only gradients:
;gpz1: 80%
;gpz2: 20.1% for C-13, 8.1% for N-15

;use gradient files:
;gpnam1: SINE.100
;gpnam2: SINE.100

;$Id: invietgpsi,v 1.6 2000/05/08 11:40:23 eng
Exp $
```

A2.4 ^{15}N-3D NOESY Pulse Program

```
;noesyhsqcfpf3gpsi3d
;avance-version (03/06/18)
;NOESY-HSQC
;3D sequence with
;   homonuclear correlation via dipolar coupling
;   dipolar coupling may be due to noe or
chemical exchange
;   H-1/X correlation via double inept transfer
;      using sensitivity improvement
;phase sensitive (t1)
;phase sensitive using Echo/Antiecho-TPPI
gradient selection (t2)
;with decoupling during acquisition
;using flip-back pulse
;using f3 - channel
;(use parameterset NOESYHSQCFPF3GPSI3D)
;
;O. Zhang, L.E. Kay, J.P. Olivier & J.D.
Forman-Kay,
;   J. Biomol. NMR 4, 845 - 858 (1994)
;A.G. Palmer III, J. Cavanagh, P.E. Wright & M.
Rance, J. Magn.
;   Reson. 93, 151-170 (1991)
;L.E. Kay, P. Keifer & T. Saarinen, J. Am.
Chem. Soc. 114,
;   10663-5 (1992)
;J. Schleucher, M. Schwendinger, M. Sattler, P.
Schmidt, O. Schedletzky,
;   S.J. Glaser, O.W. Sorensen & C. Griesinger,
J. Biomol. NMR 4,
;   301-306 (1994)

prosol relations=<triple>

# 1 "C:/Bruker/XWIN-
NMR/exp/stan/nmr/lists/pp/Avance.incl" 1
;Avance.incl
;
;avance-version (03/02/17)

;$Id: Avance1.incl,v 1.7.2.3 2003/02/25
14:48:47 ber Exp $
# 30 "C:/Bruker/XWIN-
NMR/exp/stan/nmr/lists/pp/noesyhsqcfpf3gpsi3
d" 2

# 1 "C:/Bruker/XWIN-
NMR/exp/stan/nmr/lists/pp/Grad.incl" 1
;Grad.incl  -  include file for Gradient
Spectroscopy
;
;avance-version (02/05/31)


define list<gradient> EA=<EA>

;$Id: Grad1.incl,v 1.7 2002/06/12 09:04:22 ber
Exp $
# 31 "C:/Bruker/XWIN-
NMR/exp/stan/nmr/lists/pp/noesyhsqcfpf3gpsi3
d" 2

# 1 "C:/Bruker/XWIN-
NMR/exp/stan/nmr/lists/pp/Delay.incl" 1
;Delay.incl  -  include file for commonly used
delays
;
;version 00/02/07

;general delays

define delay DELTA
define delay DELTA1
define delay DELTA2
define delay DELTA3
define delay DELTA4
define delay DELTA5
define delay DELTA6
define delay DELTA7
define delay DELTA8

define delay TAU
define delay TAU1
define delay TAU2
define delay TAU3
define delay TAU4
define delay TAU5

;delays for centering pulses

define delay CEN_HN1
define delay CEN_HN2
define delay CEN_HN3
define delay CEN_HC1
define delay CEN_HC2
define delay CEN_HC3
define delay CEN_HC4
```

```
define delay CEN_HP1
define delay CEN_HP2
define delay CEN_CN1
define delay CEN_CN2
define delay CEN_CN3
define delay CEN_CN4
define delay CEN_CP1
define delay CEN_CP2

;loop counters

define loopcounter COUNTER
define loopcounter SCALEF
define loopcounter FACTOR1
define loopcounter FACTOR2
define loopcounter FACTOR3

;$Id: Delay.incl,v 1.11 2002/06/12 09:04:22 ber Exp $
# 32 "C:/Bruker/XWIN-NMR/exp/stan/nmr/lists/pp/noesyhsqcfpf3gpsi3d" 2

"p2=p1*2"

"p22=p21*2"

"d0=3u"

"d10=3u"

"d11=30m"

"d12=20u"

"d13=4u"

"d26=1s/(cnst4*4)"

"p19=300u"

"DELTA1=d13+p19+d16+4u"
"DELTA3=d24-p16-d16"
"DELTA4=d26-p16-d16"
"DELTA=p16+d16+p2+d10*2"
"DELTA2=p22+d0*2"

"TAU=d8-p16-d16"

aqseq 321

# 1 "mc_line 74 file C:/Bruker/XWIN-NMR/exp/stan/nmr/lists/pp/noesyhsqcfpf3gpsi3d expanding definition part of mc command before ze"
; dimension 3 aq-mode (F2) Echo-Antiecho (F1) States-TPPI  F2->F1
define delay MCWRK
define delay MCREST
define loopcounter ST1CNT
"ST1CNT = td1 / (2)"
define loopcounter ST2CNT
"ST2CNT = td2 / (2)"
"MCWRK = 0.100000*d11"
"MCREST = d11 - d11"
# 74 "C:/Bruker/XWIN-NMR/exp/stan/nmr/lists/pp/noesyhsqcfpf3gpsi3d"
1 ze
# 1 "mc_line 74 file C:/Bruker/XWIN-NMR/exp/stan/nmr/lists/pp/noesyhsqcfpf3gpsi3d expanding definition of mc command after ze"
# 75 "C:/Bruker/XWIN-NMR/exp/stan/nmr/lists/pp/noesyhsqcfpf3gpsi3d"
  d11 pl16:f3
# 1 "mc_line 76 file C:/Bruker/XWIN-NMR/exp/stan/nmr/lists/pp/noesyhsqcfpf3gpsi3d expanding start label for mc command"
2 MCWRK  * 2 do:f3
LBLSTS2, MCWRK  * 4
LBLF2, MCWRK  * 3
LBLSTS1, MCWRK
LBLF1, MCREST
# 77 "C:/Bruker/XWIN-NMR/exp/stan/nmr/lists/pp/noesyhsqcfpf3gpsi3d"
3 d12
  d1
  (p1 ph8)
  DELTA2 pl3:f3
  (p2 ph9)
  d0
  (p22 ph1):f3

  d0
  (p1 ph10)
  TAU setnmr2|0 setnmr0|34|32|33
  p16:gp1
  d16
  (p1 ph11)
  d26
```

```
  (center (p2 ph1) (p22 ph6):f3 )
  d26
  (p1 ph2)

  4u pl0:f1
  (p11:sp1 ph12):f1
  4u
  p16:gp2
  d16 pl1:f1

  (p21 ph3):f3
  d10
  (p2 ph7)

  d10
  p16:gp3*EA
  d16
  (p22 ph4):f3
  DELTA
  (center (p1 ph1) (p21 ph4):f3 )
  p16:gp4
  d16
  DELTA3
  (center (p2 ph1) (p22 ph1):f3 )
  DELTA3
  p16:gp4
  d16
  (center (p1 ph2) (p21 ph5):f3 )
  p16:gp5
  d16
  DELTA4
  (center (p2 ph1) (p22 ph1):f3 )
  DELTA4
  p16:gp5
  d16
  (p1 ph1)
  DELTA1
  (p2 ph1)
  d13
  p19:gp6
  d16 pl16:f3
  4u setnmr2^0 setnmr0^34^32^33
  go=2 ph31 cpd3:f3
# 1 "mc_line 145 file C:/Bruker/XWIN-
NMR/exp/stan/nmr/lists/pp/noesyhsqcfpf3gpsi3
d expanding mc command in line"
  MCWRK  do:f3 wr #0 if #0 zd igrad EA
MCWRK  ip5*2
  lo to LBLSTS2 times 2
  MCWRK id10  MCWRK  ip3*2  MCWRK
ip6*2  MCWRK  ip31*2
  lo to LBLF2 times ST2CNT
  MCWRK rd10  MCWRK  ip8  MCWRK  ip9
  lo to LBLSTS1 times 2
  MCWRK id0
  lo to LBLF1 times ST1CNT
# 148 "C:/Bruker/XWIN-
NMR/exp/stan/nmr/lists/pp/noesyhsqcfpf3gpsi3
d"
exit

ph1=0
ph2=1
ph3=0 2
ph4=0 0 2 2
ph5=1 1 3 3
ph6=0
ph7=0 0 2 2
ph8=0 0 0 0 2 2 2 2
ph9=1 1 1 1 3 3 3 3
ph10=0 0 0 0 0 0 0 0 0 0 0 0 0 0 0 0
    2 2 2 2 2 2 2 2 2 2 2 2 2 2 2 2
ph11=0 0 0 0 0 0 0 0 2 2 2 2 2 2 2 2
ph12=2 2 2 2 2 2 2 2 0 0 0 0 0 0 0 0
ph31=0 2 2 0 2 0 0 2 2 0 0 2 0 2 2 2 0
    2 0 0 2 0 2 2 0 0 2 2 0 2 0 0 2

;pl0 : 120dB
;pl1 : f1 channel - power level for pulse (default)
;pl3 : f3 channel - power level for pulse (default)
;pl16: f3 channel - power level for CPD/BB
decoupling
;sp1 : f1 channel - shaped pulse  90 degree
;sp13: f2 channel - shaped pulse 180 degree
(adiabatic)
;p1 : f1 channel -  90 degree high power pulse
;p2 : f1 channel - 180 degree high power pulse
;p8 : f2 channel - 180 degree shaped pulse for
inversion (adiabatic)
;p11: f1 channel -  90 degree shaped pulse
;p16: homospoil/gradient pulse                [1
msec]
;p19: homospoil/gradient pulse
[300 usec]
;p21: f3 channel -  90 degree high power pulse
;p22: f3 channel - 180 degree high power pulse
;d0 : incremented delay (F1 in 3D)
[3 usec]
;d1 : relaxation delay; 1-5 * T1
;d8 : mixing time
;d10: incremented delay (F2 in 3D)
[3 usec]
```

```
;d11: delay for disk I/O                  [30
msec]
;d12: delay for power switching
[20 usec]
;d13: short delay                    [4 usec]
;d16: delay for homospoil/gradient recovery
;d24: 1/(4J)YH for YH
;     1/(8J)YH for all multiplicities
;d26: 1/(4J(YH))
;cnst4: = J(YH)
;in0: 1/(2 * SW(H)) = DW(H)
;nd0: 2
;in10: 1/(2 * SW(X)) = DW(X)
;nd10: 2
;NS: 8 * n
;DS: >= 16
;td1: number of experiments in F1
;td2: number of experiments in F2
;FnMODE: States-TPPI (or TPPI) in F1
;FnMODE: echo-antiecho in F2
;cpd3: decoupling according to sequence defined
by cpdprg3
;pcpd3: f3 channel - 90 degree pulse for
decoupling sequence

;use gradient ratio:        gp 1 : gp 2 : gp 3 :  gp 4
: gp 5 : gp 6
;                            30 :  -50 :   80 :    11 :
5 : 8.1*x

;   with x = p16/p19

;for z-only gradients:
;gpz1: 30%
;gpz2: -50%
;gpz3: 80%
;gpz4: 11%
;gpz5: 5%
;gpz6: 27% (8.1% *p16(=1 ms)/p19(=300 us))

;use gradient files:
;gpnam1: SINE.100
;gpnam2: SINE.100
;gpnam3: SINE.100
;gpnam4: SINE.100
;gpnam5: SINE.100
;gpnam6: SINE.50

                              ;preprocessor-flags-
start
;LABEL_CN: for C-13 and N-15 labeled
samples start experiment with
;          option -DLABEL_CN (eda:
ZGOPTNS)
                              ;preprocessor-flags-
end


;$Id: noesyhsqcfpf3gpsi3d,v 1.1.2.3 2003/06/18
15:27:56 ber Exp
```